Faculty of Engineering

Department of Civil Engineering and Architecture

PhD in Design, Modelling and Simulation in engineering

Cycle XXXVIII

Ph.D. Thesis

Entrainment and Deposition of Large Wood in Rivers: Insights from Numerical Modelling, Flume Experiments and Field Observations

Ph.D. Candidate

Ennouini Wafae

Advisors

Prof. Stefano Sibilla

Prof. Elisabetta Persi

Prof. Gabriella Petaccia

Ph.D. coordinator

Prof. Ferdinando Auricchio

May 2026

"All models are wrong, but some are useful. However, the approximate nature of the model must always be borne in mind."

George E. P. Box, 1987

Acknowledgements

This thesis is the result of three years of research that would not have been possible without the support, guidance, and generosity of many people. Looking back, I realize that every chapter of this work carries the imprint of someone who helped me along the way.

First and foremost, I wish to express my deepest gratitude to my supervisors, who guided me through every stage of this journey. To Prof. Stefano Sibilla, for his rigorous scientific guidance, his constant availability, and the trust he placed in me from the very beginning. His ability to see the broader picture while maintaining attention to detail shaped the way I approach research. To Prof. Elisabetta Persi, whose expertise in large wood modelling laid the foundation upon which this entire thesis was built. Her patience in explaining complex concepts, her sharpness in reviewing my work, and her genuine encouragement during the most difficult moments were invaluable. I am deeply grateful for the countless discussions that pushed me to think more critically and write more clearly. To Prof. Gabriella Petaccia, for her support, her sharp scientific eye, and her insightful contributions to many components of this research. Her deep knowledge of the ORSA2D numerical framework was essential to the model developments in this thesis, and I am grateful for her availability and encouragement along the way.

Thank you to Prof. Diego Ravazzolo, whose scientific contributions and constant support were essential to this research. His expertise, practical insights, and willingness to help at every stage of this work made a real difference in the quality of the final result. My thanks also go to Prof. Andrea Fenocchi, for giving me the opportunity to work on an engineering consultancy during my PhD, an experience that enriched my research with a practical perspective I would not have gained otherwise.

I wish to sincerely thank Prof. Lorenzo Picco and Prof. Pierfranco Costabile for accepting to serve as reviewers of this thesis. Their careful and thorough reading of the manuscript, along with their constructive comments and suggestions, contributed significantly to improving the quality and clarity of the final version.

I also wish to thank Prof. Luca Mao, Prof. Lorenzo Picco, and Prof. Diego Ravazzolo for generously sharing the Tagliamento River field data that made model application to a real case study possible.

A special acknowledgement goes to the colleagues who made my international research stay in France both scientifically enriching and personally memorable. I am particularly grateful to Dr. Borbála Hortobágyi. Her guidance during the fieldwork campaign, her patience in explaining the intricacies of RFID tracking, and her generosity in sharing data and knowledge were essential to the development

of Chapters 8 and 9. I also wish to express my gratitude to Prof. Hervé Piégay at ENS de Lyon, who welcomed me into his research group and gave me the opportunity to participate in the field campaign.

To all my colleagues at the University of Pavia, thank you for being there when things got hard, and for celebrating with me when things went right. A PhD can be an isolating experience, but you made sure it never felt that way. I carry your friendship with me beyond these walls.

To my friends, from Morocco, from Italy, and from every corner of the world in between. You became the closest thing to family I have outside my own. You showed me that home is not a place you come from but something you build with the people around you. I will carry a piece of each of you with me, no matter where life takes us next.

To my family, my parents and my siblings for their unconditional love and unwavering support from the very beginning. Everything I have achieved started with the foundation you gave me. No distance has ever diminished your presence in my life, and I hope this thesis makes you proud.

And to Danilo for standing beside me through every frustration, every late night, every moment of doubt, and every small victory along the way. Thank you for your patience when deadlines consumed my weekends, for your calm when I lost mine, and for your love that made even the hardest days feel lighter. You gave me strength when I needed it most.

Abstract

Large wood (LW) plays a dual role in river systems: it improves habitat complexity and geomorphic diversity but can also exacerbate flood risks by obstructing flow and damaging infrastructure. Understanding and predicting LW entrainment, transport, and deposition remains a significant challenge due to the complex interplay between hydraulic forces, wood properties, and channel morphology. This thesis contributes to the efforts of modelling of LW dynamics in rivers by developing, validating, and applying an enhanced version of the two-way coupled Eulerian–Lagrangian model ORSA2D_WT.

This research integrates model refinement, laboratory experimentation, and field monitoring into a coherent framework. First, the entrainment and arrest routines of ORSA2D_WT are revised to incorporate orientation-dependent sliding and rolling thresholds, and stochastic deposition processes induced by vegetation entrapment. These improvements address key limitations of earlier model formulation, where entrainment was treated as purely buoyancy driven. Second, controlled flume experiments were conducted to quantify hydrodynamic coefficients for rolling and sliding motion under shallow water conditions. Measured drag and side force coefficients are shown to vary strongly with orientation and bed proximity and are incorporated into the model to improve its physical realism. Third, the enhanced model was validated against flume-based entrainment experiments, where dimensionless critical water depths and velocities were compared across a range of wood orientations. Sensitivity analyses revealed the importance of drag coefficient variability and frictional anisotropy in reproducing observed thresholds. The improved model successfully captured the transition between sliding and rolling regimes, aligning with previous experimental datasets. Fourth, the thesis extends the application of ORSA2D_WT to two natural river systems. In the Tagliamento River (Italy), simulations of the flood event were compared against RFID and GPS field-tracked LW trajectories. The results demonstrated that the improved entrainment formulations enhanced the capacity to replicate observed transport trajectories and mobility rate. Sensitivity analyses further highlighted the role of wood density and initial orientation in controlling transport distances within a braided river morphology. In the Allier River (France), a field monitoring campaign was carried out using RFID-tagged logs, grain-size surveys, and wood density sampling during a research stay. This data provided a good dataset on wood mobilization during floods in a large gravel-bed river. The enhanced ORSA2D_WT model was applied to an 8 *km* study reach, calibrated against post-the March 2024 flood event. Simulations underscored the role of riparian vegetation and floodplain roughness in entrapping LW, consistent with field observations.

Overall, the enhanced ORSA2D_WT framework increases the robustness and realism of LW transport simulations, bridging the gap between laboratory, numerical, and field approaches. The results contribute to the understanding of LW dynamics.

Table of contents

List of Figures

List of Tables

Chapter 1

Introduction

1.1. Motivation

LW, generally defined as wood pieces longer than 1–2 *m* and with a diameter larger than 0.1 *m* (Gurnell et al., 2002; Piégay and Gurnell, 1997), is a fundamental component of fluvial ecosystems. When naturally recruited from riparian vegetation or upstream reaches, LW contributes to habitat diversity, flow resistance, and channel morphology (Wohl, 2013; Gurnell, 2014). It creates hydraulic complexity by forming pools, retaining sediments, and providing shelter and feeding areas for aquatic organisms (Gregory et al., 2003; Montgomery et al., 2003). For these reasons, LW introduction has become a widely used practice in river restoration projects aiming to recover ecological integrity (Roni and Beechie, 2013). However, LW also represents a potential hazard, especially during floods. Mobilized logs can accumulate against critical infrastructure such as bridges, culverts, and weirs, leading to partial or complete blockages (Lange and Bezzola, 2006; Ruiz-Villanueva et al., 2014a). Such accumulations may elevate upstream water levels, enhance scour processes, and, in extreme cases, cause structural failure (Diehl, 1997; Kramer and Wohl, 2017). Post-flood surveys have documented significant damage linked to LW jams, particularly in mountain rivers with high wood recruitment (Follett and Wohl, 2024; Ruiz-Villanueva et al., 2018)

Since LW mobilization typically takes place during high-flow events when direct observations are challenging, it is difficult to predict transport dynamics. To fill this gap an effort has been made in the last decade to develop numerical models to simulate LW transport at a river reach scale, offering insights to supplement sparse field data. Modeling approaches often rely on one-way coupling (Pascal et al., 2023 and Sansen et al., 2025), while other models (Kang and Kimura, 2018; Ruiz-Villanueva et al., 2014a), including the ORSA2D_WT model used in this work (Persi et al., 2019b) are two-way coupled, allowing the flow to drive the motion of LW, and considering the reaction forces exerted by LW pieces on the flow. Such advancements in the modeling methodology are motivated by the broader goal of forecasting LW-related risks during floods, in which including the effect of LW on the flow is essential.

Focusing on the ORSA2D_WT model, its earlier version was limited by oversimplified entrainment and arrest routines. It was developed to consider entrainment only on a floatation-based criterion, considering constant entrainment drag forces and friction. Additionally, LW arrest was not totally developed, lacking more accurate procedures in case of interaction with existing vegetation or LW accumulations. Such gaps contrasted with literature evidence which demonstrated the importance of including rolling and sliding incipient motion dynamics, or the coefficients variability with LW yaw angle and bed proximity. These simplifications questioned the predictive reliability of the model, particularly under shallow flow conditions and in structurally complex channels. Addressing these

gaps by incorporating more physically based entrainment thresholds, orientation-dependent hydrodynamic and frictional parameters, and stochastic arrest formulations is therefore essential for producing more realistic simulations of LW dynamics during flood events.

1.2. Objectives and Methodology

The aim of this thesis is to improve the mechanistic understanding and predictive modelling of LW transport in the ORSA2D_WT model. To achieve this, the goal of this research was to integrate model improvement, laboratory experimentation, and field data within a coherent framework. The work is designed not only to refine the physical representation of LW entrainment and arrest processes in the ORSA2D_WT model, but also to test these improvements through controlled experiments and real-case river applications. This thesis's research questions, aims, and methodologies are summarized in Table 1.1.

Table 1.1 Research questions, aims, and their methodology.

Research Question	Research Aim	Methodology
What are the physical thresholds and mechanisms governing LW entrainment and arrest?	To refine entrainment and arrest mechanisms in the ORSA2D_WT model	Model improvement by implementation of a flotation parameter, and sliding–rolling criteria, and vegetation entrapment
How can hydrodynamic coefficients of LW motion be experimentally quantified and incorporated into modelling motion by rolling and sliding under shallow water conditions?	Measuring drag and side force coefficients through controlled flume experiments of near bed conditions	Laboratory flume experiments with logs under varying orientations using a hydrodynamic balance to measure drag and side forces
To what extent can the improved ORSA2D_WT model reproduce LW mobility observed in laboratory environments?	To validate the improved model against laboratory results	Numerical simulations and sensitivity analyses compared with experimental data
In what ways do wood properties (density, size, orientation) and environmental factors (channel morphology, riparian vegetation, flow variability) influence the transport and deposition of LW in rivers, and what are the main limitations of modeling these processes in real-world settings?	To apply and evaluate the model capacity in natural river case studies (Tagliamento and Allier Rivers)	Numerical simulations compared against field monitoring data with RFID and GPS tagged logs

1.3. Thesis structure

This dissertation is organized into chapters that progressively build from background information, through model development and validation, to real-world application. Below are a brief outline of each chapter and its contribution to the overall goal of the thesis.

Chapter 2 – Literature Review: This chapter reviews the current state of knowledge on LW in rivers, establishing the context and rationale for the study. It begins by defining LW and its various classifications, then discusses the dualistic role of wood in river systems (ecological benefits versus flood and structural risks). Key processes such as wood recruitment, entrainment, transport dynamics, and deposition mechanisms are examined with reference to previous studies. The chapter also surveys existing approaches to modeling LW transport – from early empirical formulas to numerical models and highlights their limitations. Additionally, methods for field monitoring of LW (e.g. tagging and tracking techniques) are summarized.

Chapter 3 – Eulerian–Lagrangian Modeling of LW Transport (ORSA2D_WT): Chapter 3 introduces the numerical modeling framework that is the starting point of this research. It presents the ORSA2D_WT model, describing its mathematical foundation and computational implementation. The model's two-way coupled structure, combining a 2D shallow-water hydrodynamic solver with a Lagrangian module for tracking LW pieces is explained. Governing equations for log motion (translation and rotation) are outlined. The chapter discusses how the model handles entrainment (flotation-based criteria) and arrest under baseline conditions, as formulated in prior work (Persi 2018). By summarizing the original capabilities and assumptions of ORSA2D_WT, Chapter 3 provides a baseline against which the contributions of this thesis (developed in Chapter 4 and beyond) can be understood. It also includes notes on the numerical solution approach and any computational considerations (e.g. time-stepping, coupling strategy) relevant to later applications.

Chapter 4 – Improving Entrainment and Deposition Modeling: In this chapter, the focus is on the enhancements added to the modeling framework. Chapter 4 details the development of an improved entrainment and arrest model for LW within ORSA2D_WT. It introduces a refined theoretical framework for incipient motion of LW, distinguishing between different entrainment modes (sliding versus rolling) and incorporating the effects of channel bed conditions (friction angles). The chapter also describes how wood deposition (arrest) is modeled. A notable addition in this thesis is a sub-algorithm for entrapment by vegetation, which simulates the possibility of LW getting caught on floodplain trees or LW accumulations already in place. The implementation of these features into the ORSA2D_WT code is explained, and their expected impact on simulation realism is discussed.

Chapter 5 – Hydrodynamic Coefficients from Flume Experiments: Chapter 5 transitions to the experimental component of the research. It documents the laboratory experiments conducted to measure hydrodynamic coefficients. The chapter describes the experimental setup in a laboratory flume and then presents the results in terms of measured drag and side coefficients measured for cylinders at near-bed conditions and with various orientations to the flow.

Chapter 6 – Entrainment Model Validation: Chapter 6 provides a thorough validation of the newly implemented entrainment and transport model against experimental results. Here, the enhanced ORSA2D_WT model is systematically tested on scenarios that mimic the laboratory setups.

Chapter 7 – Model Application to the Tagliamento River: Chapter 7 marks the shift from controlled experiments to real-world application. It introduces the Tagliamento River in Italy as a case study site, a braided river with a history of LW transport during floods. The results in terms of entrainment ratio and simulated transport trajectories are compared against field data (RFID and GPS trajectories) and discrepancies in the observed versus simulated behavior are discussed. Finally, the effect of wood density and initial orientation of LW elements is assessed through a sensitivity analysis

Chapter 8 – Field Monitoring of LW in the Allier River: This chapter focuses on the field data collection campaign carried out on the Allier River in France during the abroad Ph.D. stay in 2024. It provides an overview of the river's key characteristics, outlines the methodology used to monitor LW dynamics in the field, and presents an analysis of the collected data.

Chapter 9 – Model Application to the Allier River: In the final chapter, the thesis integrates the model and field data within the Allier River case study. The enhanced ORSA2D_WT model was configured for an 8 *km* reach of the monitored river. The hydraulic model of the March 2024 flood event was calibrated against flood marks collected in the field, and simulations of LW transport were then carried out with a particular focus on the role of riparian vegetation as an entrapment mechanism.

Finally, the thesis concludes with a **Conclusions and Recommendation** section that synthesizes the main findings and contributions of the current thesis. It revisits the objectives stated in this introduction and discusses how each was addressed. The conclusions also acknowledge the remaining limitations and offer recommendations for future work.

Chapter 2

Literature Review

2.1. Abstract

This chapter provides a comprehensive review of the state of knowledge on large wood (LW) in river systems, with particular focus on its definitions, classifications, ecological functions, hydraulic implications, and modelling approaches. LW, also referred to as large woody debris (LWD) or coarse woody debris (CWD), plays a dual role in fluvial environments: it enhances habitat complexity and geomorphic diversity, but also poses potential risks during floods by obstructing flow and threatening infrastructure. The review synthesizes existing literature on entrainment mechanisms, transport dynamics, deposition, and entrapment processes, highlighting the physical, hydraulic, and geomorphic factors that govern wood mobility. Different modelling frameworks are examined, ranging from empirical formulations to coupled numerical approaches, with discussion of their strengths and limitations. The chapter also summarizes field-based monitoring techniques, including tagging and tracking methods, which provide critical data for model calibration and validation. By identifying knowledge gaps in the understanding of LW processes, this review establishes the scientific foundation for the modelling developments and applications presented in the subsequent chapters.

2.2. Large wood in river systems: Definitions and Classification

Large Wood (LW), commonly referred to in earlier literature as Large Woody Debris (LWD) or Coarse Woody Debris (CWD), refers to dead woody pieces present within river systems (Harmon et al., 1986) and large enough to interact significantly with the flow of water, sediment dynamics, and channel morphology. A widely accepted definition, particularly in hydrological and ecological studies, defines LW as woody material with dimensions of at least 10 cm in diameter and 1 m in length (Nakamura and Swanson, 1994; Wohl et al., 2010). Although the terms LWD and CWD are still frequently encountered in the literature, recent studies increasingly prefer the use of LW to avoid the negative connotation associated with the word "debris," which may implicitly undervalue its ecological and geomorphic functions within river systems.

However, these dimensions vary considerably depending on the study area, river size and geomorphic context. For instance, in the foothills of the Cascade Range and Willapa Hills, Bilby and Ward (1991) defined LW as woody pieces exceeding 10 cm in diameter and 2 *m* in length, reflecting the larger size of trees and fluvial transport capacity in these forested regions. Meanwhile, in steep, headwater alpine streams, where wood pieces tend to be shorter and fragmented, Comiti et al. (2006) used lower thresholds of 0.3 *m* in length and 0.05 *m* in diameter to capture functionally significant wood pieces.

These variations highlight the importance of context when defining LW. Smaller streams may be significantly influenced by small wood pieces, while larger rivers require larger logs or wood pieces to produce comparable impacts. Moreover, some studies differentiate between "large wood" (LW) and "small woody debris" (SWD), with the latter often referring to pieces below standard LW thresholds but still contributing to stream processes (Merten et al., 2013). Although the terms LWD and CWD are still frequently encountered in the literature, recent studies increasingly prefer the use of LW to avoid the negative connotation associated with the word "debris," which may implicitly undervalue its ecological and geomorphic functions within river systems.

The term LW encompasses a wide range of material types, including:

- Whole trees with roots and branches.
- Trunks or logs, main structure of the tree without roots or branches.
- Large branches.
- Root wads.

LW classification is typically based on physical attributes, origin, spatial position, and mobility.

2.2.1. Classification by origin

Different inputs can be considered for LW. Focusing on natural inputs, in literature we can distinguish nonautogenic wood which can be moved by in-situ tree mortality or bank erosion (Erskine et al., 2012; Latterell and Naiman, 2007; Picco et al., 2016), or allogenic wood, introduced from upland areas through landslides, windthrow, or mass wasting (Hyatt and Naiman, 2001). Natural hazards (e.g., storms, floods, fire) may also contribute to periodic LW recruitment. For example, Picco et al., (2016) observed significant wood recruitment during a single flood event, with 690 trees recruited, while Lucía et al. (2015) found that a flash flood event was responsible for recruiting 70-80% of LW, primarily through channel widening processes. Anthropogenic inputs, on the other hand, may have different sources, they can be sourced from restoration projects, for example, engineered log jams (ELJs) are increasingly used in restoration projects (Addy and Wilkinson, 2016). However, during flood events these ELJs could be mobilized, or they can be sourced from accidental sources like wood waste from logging or construction sites, bridge debris, or damaged woody infrastructure during extreme weather events.

2.2.2. Classification by position in the river system

LW can be also classified based on its position within the river system. LW can be an in-channel wood, characterized by its direct interactions with low or high flows and can be responsible for hydraulic divergences such as increased roughness, turbulence, and backwater effects (Blanckaert et al., 2014). Floodplain or overbank LW, on the other hand, is found outside the main channel area, can be either free or buried, and it can be mobilized during overbank high flows or stored long-term, depending on geomorphic context (Wohl, 2020).

2.3. Benefits and Risks of large wood in rivers

2.3.1. Ecological and geomorphological benefits

LW has a great impact on the health and functioning of river ecosystems: actually, it provides habitat for freshwater and riparian organisms, including macroinvertebrates, amphibians, and fish (Anlanger et al., 2022; Elosegi et al., 2016; Mitchell et al., 2012; Poledniková and Galia, 2021; Vera et al., 2014). LW creates also hydraulic heterogeneity through flow resistance induction, the generation of pools (Stewart et al., 2012), and the modification of sediment transport processes (Schalko and Weitbrecht, 2022), enhancing ecological heterogeneity and integrity. Geomorphologically, wood structures like log steps and jams can control the channel shape by stabilizing the bank, encouraging sediment accumulation, and directing flow line paths. LW has the long-term effect of maintaining or restoring natural meandering processes, most notably in dynamic, gravel-bed rivers. These phenomena are most useful where natural fluvial processes have been disrupted in incised or degraded streams. From a restoration viewpoint, the installation of LW in stream channels is now a standard practice for river restoration projects (Grabowski et al., 2019) to facilitate ecological connectivity and hydrological functioning. If properly designed and executed, engineered log jams (ELJs) have the potential to replicate the functions of naturally occurring wood to establish dynamic equilibrium of sediment transport and flow regulation. Figure 2.1 highlights key ecological and geomorphological functions of LW, including habitat creation, sediment retention, flow deflection, and channel stability enhancement.

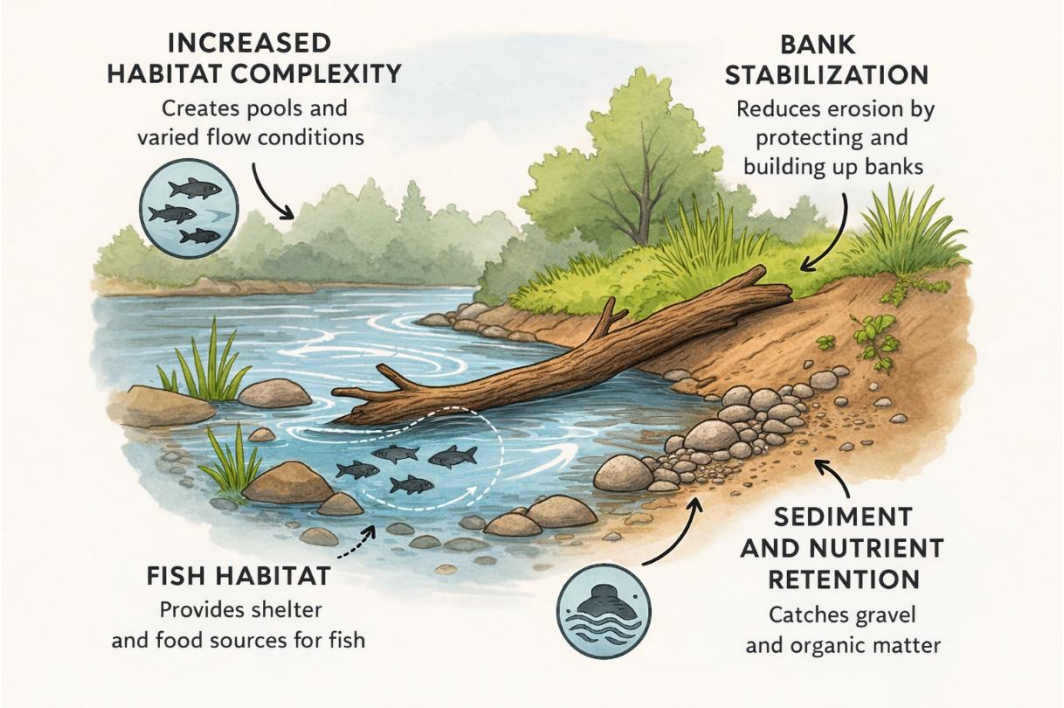

Figure 2.1 Benefits of LW in Streams. (Generated using AI).

2.3.2. Hydraulic and flood-related risks

Despite these advantages, LW represents a major hazard source especially in flood-prone zones and anthropized catchments. The main point of concern is the possibility of obstruction. During high-flow events, LW can become mobile if entrainment thresholds are exceeded. Mobilized wood can accumulate hydraulic structures including bridges (Figure 2.2), culverts, and weirs, causing partial or complete blockage (Ruiz-Villanueva et al., 2014b) Such blockages can lead to a local backwater, which can exacerbate the flood upstream and increase the potential for structural failure (Ruiz-Villanueva et al., 2017; Schalko et al., 2017) . This risk is critical for urban or semi-urban areas, where infrastructure and human safety are at stake directly. Wood jams at bridge piers proved to have a substantial impact on flow hydraulics, and particularly on hydraulic capacity and scour potential, both of which can compromise structural stability (Elliot et al., 2012; Panici and de Almeida, 2018; Zhang et al., 2023, 2022). In addition, the entrainment and transport of LW during floods make flood modeling and risk assessment a dynamic and unpredictable task. Traditional flood models that do not take LW into consideration can underestimate the water levels as well as the potential of damage in extreme occurrences (Addy and Wilkinson, 2019; Rasche et al., 2019; Ruiz-Villanueva et al., 2014c; Zischg et al., 2018). The interplay between wood and flow can become highly nonlinear and scale-dependent, making prediction exercises difficult.

Figure 2.2 (a) A log jam spans nearly bank-to-bank in Four Mile Creek beneath Hubbell Avenue in Des Moines (Source: Timothy Meinch/The Register), (b) Peachtree Creek, Atlanta, Debris from floods cause bridge problems (Source: South Atlantic Water Science Centre).

2.3.3. Global perspectives

The role of LW in river systems has been documented worldwide, yet its implications differ markedly depending on regional geomorphology, climate, and societal priorities. The following case studies highlight how LW is perceived and managed in diverse contexts, ranging from ecological restoration in North America to hazard mitigation in Asia and Europe, and from estuarine dynamics in Australia to hydropower challenges in South America. Taken together, these examples illustrate that while LW contributes to ecosystem health and morphological processes, it also presents complex trade-offs with flood safety, navigation, and infrastructure resilience. In the Pacific northwest region, specifically in Washington and Oregon, LW is deliberately introduced to rivers to restore salmon habitats, with documented ecological successes in projects for Skagit River and Elwha River. However, these attempts have also triggered fears of a higher flood risk in the areas and navigation obstacles on high flows (Buscombe et al., 2024; Skagit Watershed Council, 2017). On the other hand, Japan's steep terrain and abundant typhoons lead to increasing LW transport during heavy storms (Seo et al., 2012). For example, when the island of Hokkaido was hit by Typhoon Etau in 2003, 50,000 m^3 of LW were mobilized by landslides and flood into Nibutani Dam (Murakami et al., 2008). A recognizable and persistent efforts for minimizing LW related flood risk in Japanese large rivers is also documented (Nakagawa and Takahashi, 2001; Okamoto et al., 2020; Yano et al., 2016). In Europe, LW transport during floods poses great risks in Alpine catchments as this has the potential of blocking bridges and contributing to increased flood risk (Erpicum et al., 2024; Piton et al., 2024) . LW recruitment mainly takes place due to channel widening and bank erosion with volumes rising to 1270 $m^3 km^{-1}$ as reported by Lucía et al. (2015) for the Magra river basin in north-western Italy. Drainage area and channel slope are the major factors affecting LW recruitment, whereas deposition patterns are more complicated (Lucía et al., 2015). Other methods for estimating LW potential and transport dynamics have also been developed, such as hazard index maps (Mazzorana et al., 2009), and GIS-based approaches to estimate LW flux during extreme events (Piton et al., 2024). Numerical Modeling and scaled flume experiments have improved knowledge about LW dynamics (Ruiz-Villanueva et al., 2014b). In southeastern Australian estuaries, LW dominates, originating from various sources such as floods, bank erosion, and human activities. Unlike river systems where discharge is the major driver of LW transport, wind and tidal forces contribute to the transport and stranding of LW in estuarine environment (Hinwood and McLean, 2017). Tidal action is of special importance, helping to trap LW on inter-tidal bars and shoals. However, the wide and deep nature of estuaries channels exclude (to a great extent) the formation of log jams, compared to riverine systems. Notwithstanding this, LW contributes significantly to localized scour and sediment accretion, thus altering the estuarine habitats. In South America, one of the major tributaries of the Amazon River, the Madeira

River, carries significant amounts of LW material, especially during flood events. This causes enormous operational problems to facilities such as the Jirau Hydroelectric Power Plant, where massive LW accumulation potentially interferes with the efficient operation of turbines. Though log boom barriers are used to hold the wood, the structures may fail to provide the desired retention efficiency under dynamic flow conditions. To improve understanding and management of LW transport in that area, a recent study (Caldatto et al., 2024) used the PART module of Delft3D software to obtain hydrodynamic and particle tracking simulations of LW transport, treating LW as Lagrangian particles. These simulations were calibrated and verified with actual observed flow data. The results allowed the determination of how flow conditions, modes of plant operation, and the presence of log booms affect movements of transported LW and its accumulation areas. Such global examples demonstrate the need for sensitive-to-context approaches of LW management. Although LW positively helps to increase the quantity of river health and impact its morphology, uncontrolled wood transport during extreme events may cause serious hazards.

The synthesis of these global perspectives highlights that while the occurrence and movement of LW are natural components of river dynamics, their implications for flood risk and channel stability are profoundly context dependent. Across diverse hydroclimatic and geomorphic settings, a common gap emerges, as the lack of predictive tools to quantify how wood is entrained, transported, and retained under varying flow and boundary conditions. This gap underpins the focus of the present thesis.

2.4. Entrainment of large wood in rivers

In the context of fluvial systems, incipient motion or, in other terms, the entrainment of LW is the initial mobilization of LW from a static condition and into the process of active transport. LW is typically stacked along riverbanks, floodplains, bars, or resting on the bottom of the river. Entrainment is the initial phase in the dynamic life cycle of wood in river systems, followed by transport and deposition.

2.4.1. Physical processes of large wood entrainment

LW in rivers typically becomes mobile during high-flow events, when the hydraulic forces can overcome the resisting forces (weight, friction, and any anchoring) on a log. Early work by Braudrick and Grant, (2000) combined theory and flume experiments to identify the primary factors controlling LW incipient motion. They found that piece orientation relative to flow, presence of rootwads, wood density, and log diameter are the dominant factors influencing stability. LW oriented parallel to the flow and those with rootwads tend to be more stable (requiring higher flows to move), whereas logs facing obliquely or perpendicular to flow are more easily rolled or pushed downstream. Notably,

Braudrick and Grant (2000) observed that for logs shorter than the channel width, log length did not significantly affect the threshold of movement. This implies that in larger rivers where individual pieces can freely rotate and float, length alone is not a limiting factor for entrainment unless the log can span the channel. In smaller channels, however, field observations confirm that piece length relative to channel width is critical: longer logs often become wedged or stored until extreme floods occur (Bocchiola et al., 2008). In fact, most mobile pieces in small streams are shorter than the bankfull channel width (Braudrick and Grant, 2000), underscoring the importance of channel geometry in wood mobility. Another aspect of LW entrainment is buoyancy. Freshly fallen wood is usually less dense than water (typical wood densities are around 400–700 $kg\ m^{-3}$), so that many logs float once sufficiently submerged. The buoyant lift can dramatically reduce the friction with the bed, causing a sudden onset of motion when water depth reaches a critical portion of the log's diameter. Braudrick and Grant, (2000) defined a "buoyant depth" threshold – essentially the flow depth at which a log will start to float – as an upper limit of stability for a given log. For example, a cylindrical log (~500 $kg\ m^{-3}$ density) without rootwads will begin to float when the flow depth submerges enough of its diameter to counteract its weight. Logs denser than water (e.g. waterlogged or very heavy wood) behaves more like bed sediment, requiring drag and lift forces to initiate sliding or rolling along the bed. Recent flume experiments by Chen et al. (2020) illustrate these modes: lighter (buoyant) logs tended to initiate motion by floating upward, whereas heavier (Waterlogged) logs had to be pushed or rolled by the flow. They also proved how log orientation affects the mode of motion, logs aligned with flow mostly slide downstream once entrained, whereas those diagonal or perpendicular to flow tend to roll. The entrainment depth required to mobilize a piece can thus depend on its orientation and density. Furthermore, channel bed and bank roughness play an important role in pinning and resisting LW entrainment. In this context Crosato et al., (2013) integrated flume data for cylindrical and square section logs to propose an entrainment threshold formula based on simple parameters: flow depth/velocity, log geometry (size, density), and median bed sediment size. This emphasizes that the channel physical roughness is part of the incipient motion criterion for LW. LW and sediment transport processes are often intertwined. Mobile LW elements can alter local hydraulics, causing zones of flow separation that promote sediment deposition (for instance, upstream of a log jam) or focused scour (Galia et al., 2024). Conversely, sediment can influence wood mobility: a log partly buried in accumulated sediment will have a higher resistance to movement until that sediment is eroded. In gravel-bed rivers, LW often becomes wedged amid gravel bars; the wood may remain stable until either flow increases enough to wash out the anchoring gravels or the log is buoyed up and floated off the bar. Field observations have shown that wood pieces with rootwads tend to collect more sediment and form more stable log accumulations than pieces without (Pöppl et al., 2021). The

rootwads can act like a "hook" digging into the bed or bank, making the piece harder to entrain. In predicting incipient motion, these wood–sediment interactions introduce complexity: the critical condition for entrainment might depend on concurrent sediment transport and morphological adjustments.

2.4.2. Modeling approaches for large wood entrainment

Over the past 3 decades numerous studies have attempted to understand the mechanisms controlling the entrainment of LW, employing a combination of field observations, flume experiments, and theoretical modeling. In 2000, Braudrick and Grant asked an important question "When do logs move in rivers?". To answer this question, they examined entrainment thresholds of LW in rivers by a combination of theoretical approach and flume experiments. The authors considered circular cylindrical logs in uniform flow on smooth immobile planar stream bed; furthermore, they assumed that a cylinder initiates the entrainment by sliding. According to the authors, LW entrainment is governed by a balance of streamwise force components, both downstream (net gravity and hydrodynamic drag) and upstream oriented (friction). The effect of hydrodynamic lift on the normal force component (which triggers friction) was neglected. Building on this foundation, Bocchiola et al. (2006) performed controlled flume experiments on cylindrical wooden dowels (320–740 $kg\ m^{-3}$ density) to refine the entrainment threshold model. They introduced a distinction between two mechanisms of motion – sliding and rolling – depending on a log's orientation to flow, an effect overlooked in earlier models. If a piece of wood is aligned parallel to the flow direction, sliding is the dominant mode of movement, whereas if it is positioned perpendicular to the flow, rolling becomes the primary motion mechanism. Later, Crosato et al. (2013) built upon Bocchiola et al. (2006)'s model and modified it for wood entrainment under lowland river conditions, with generally lower channel slopes, subcritical flows, and different bed characteristics. They conducted flume experiments in a 14 m × 0.4 m straight flume with a horizontal bed, testing both cylindrical logs (like Bocchiola, et al., 2006) and square-section logs, at various orientations (parallel and perpendicular) and with two bed types (smooth wooden bed and rough gravel bed). In applying Bocchiola et al. (2006) approach to lowland scenarios, Crosato et al. (2013) introduced few simplifications. First, recognizing that bed slope in lowland rivers is small (often negligible), they dropped the downslope weight component from the equations. Second, they examined the extreme case of a log-oriented perpendicular to flow, which in Bocchiola et al. (2006) formulation would normally be treated as a rolling case. However, Crosato et al. (2013) opted to simplify the physics of rolling by treating it as a form of high friction sliding. In other words, for a log crossing the flow, they assumed it "slides" with an effectively larger friction resistance (since it must overcome a tipping moment). In their analysis, a square log perpendicular to flow was interpreted as if rolling could be approximated as sliding with a very large

friction coefficient to mimic the resistance to rolling. This allowed them to use a sliding-type force balance for both parallel and perpendicular cases, adjusting parameters accordingly. Crosato et al. (2013) tested the predictive ability of this simplified threshold formula against their experimental data. They found that using the results obtained with the undisturbed submergence ratio as a predictor (S) for the initiation of motion were quite poor. In theory, one would expect the predictor to be $S < 1$ for a log to move (the water depth should reach a certain fraction of the log's diameter to provide enough buoyant lift and drag), yet in their experiments the critical submergence ratio varied widely, from S = 0.61 up to 1.44. In some cases, logs began moving when the flow depth was significantly less than the log diameter (low S), and in others movement only occurred when the log was deeply submerged (S >1). This scatter indicated that simply using S (based on global depth) ignores important local physics – essentially confirming Bocchiola's point that the local depth around the log (and other flow disturbances) matter. Crosato et al. (2013) attempted an empirical correction: they defined a correction factor $C_r = \frac{h_r}{h}$ to relate the effective local depth to the overall depth. Interestingly, when they plotted C_r against the observed S for their data, they found approximately $C_r = 1/S$. In other words, cases where the undisturbed depth was insufficient (S <1) corresponded to local flow depth amplification around the log (C_r>1), and vice versa. They interpreted this result as a sign that the conceptual model needed improvement as balancing depth and buoyancy alone (even with corrections) is too crude when ignoring detailed flow structure like 3D flow effects, such as flow acceleration under the log and streamline curvature around it, which differ depending on log shape and orientation. Additionally, experiments by Crosato et al. (2013) addressed the influence of a mobile bed: they observed that if the sand bed was allowed to scour around the log, the log could start moving at lower flows than on a fixed bed, because local scour increases the water depth beneath the log, effectively lifting it sooner. This underscores that in natural rivers, bed scouring around LW can facilitate its entrainment even at flow conditions below those of initiation of motion.

Chen et al. (2020) followed the work of Bocchiola et al. (2006) and Crosato et al. (2013), expanding the experimental scope and refining the modelling framework to make it more generally applicable. They took a comprehensive look at how entrainment thresholds depend jointly upon log orientation, log density, and channel bed roughness. They conducted flume tests with 48 cylindrical logs, systematically varying length, diameter, density, and initial orientation of each log relative to the flow. The range of wood densities spanned both lighter than water (fresh, buoyant wood) and denser than water (waterlogged wood) cases, thereby examining a broader density range than the one investigated by Bocchiola et al. (2006) (which was 320–740 $kg\ m^{-3}$). They also tested multiple bed conditions, including different roughnesses (achieved by using beds with different grain sizes or

materials) to see how a smooth and rough bed alters the incipient motion. Crucially, instead of treating orientation in binary terms (parallel versus. perpendicular), Chen et al. (2020) considered a series of orientation angles, including oblique angles in between. This allowed them to identify how the mode of movement transitions from sliding to rolling as the log's angle changes. As observed before they found that log orientation is a controlling factor for the mechanism of entrainment: logs initially aligned to the flow tended to slide along the bed when mobilized, whereas logs at oblique or transverse angles primarily rolled out of their resting position. This matches Bocchiola et al. (2006) observation of two regimes, but Chen et al. (2020) were able to observe the gradient between these extremes. For instance, a log at 45° to the flow might begin to both pivot and translate, depending on exact forces, but in general any significant deviation from alignment caused rolling to dominate. They quantified how the critical flow depth (or velocity) required for entrainment varies with orientation – notably, logs parallel to flow required deeper flows (greater submergence) to start moving than logs oriented more obliquely. Physically, a parallel log has a smaller projected area to the flow and experiences less drag, and it also has a larger contact area along the bed (maximizing friction), so it is the harder to move. In contrast, a perpendicular log catches more flow and can pivot more easily once lift reduces its effective weight. Chen et al. (2020) also examined bed roughness effects systematically. They reported that the entrainment threshold (often measured as a critical flow depth h, or critical velocity) is sensitive to bed roughness: a rougher bed increases resistance to motion, requiring a larger flow to entrain a given log. This aligns with Crosato et al. (2013) findings that on a gravel bed logs stayed immobile until higher discharges were reached compared to a smooth bed configuration. Roughness elements can delay the initiation of rolling by "blocking" the log for the same flow conditions. Chen et al. (2020)'s data provided a cautionary note that one cannot universally apply a single critical submergence or floatation criterion without considering bed conditions. In fact, they found that floatation-based thresholds from prior global data (e.g. the idea that a log moves when the flow depth exceeds some fraction of its diameter or its buoyant depth) could be misleading on different beds, showing that on a smoother bed the log floats earlier, while on a very rough bed, the required threshold could be higher. Thus, they urge caution and calibration when applying floatation thresholds across different river types.

2.4.3. Challenges and uncertainties in predicting large wood entrainment

Predicting the incipient motion of LW in rivers is fraught with uncertainty due to many interrelated factors. A primary challenge is the high variability in log properties – wood pieces differ in size, shape, and density, which leads to widely varying entrainment thresholds. For instance, longer or larger-diameter logs (or those with rootwads and branches) tend to require higher flow forces to dislodge, whereas smaller or lower-density (more buoyant) logs can mobilize at much lower flow

depths (Braudrick and Grant, 2000; Haga et al., 2002). The orientation of a log relative to the flow is another critical factor: logs aligned parallel to flow present less drag and often remain stable until higher flows, while logs placed obliquely or perpendicular to the current experience greater torque and tend to roll or pivot into motion under weaker flows (Braudrick and Grant, 2000; Bocchiola et al., 2006). Moreover, local flow disturbances caused by the log itself may add complexity. A LW element can locally alter the flow, for example, causing upstream backwater effect or flow acceleration around the log, so the forces at incipient motion deviate from what simple uniform-flow assumptions predict. Experiments show that the effective water depth" responsible for LW motion" a partially submerged log is often different from the undisturbed flow depth, especially at a low submergence, therefore a good estimation of the water depth is essential for the accuracy of such force balance-based models. Log–bed interactions and channel bed roughness further contribute to uncertainty. The friction and contact conditions between a log and the riverbed can vary greatly, e.g. a rough, coarse bed provides higher resistance to sliding (static friction coefficients on gravel can be up to 40% higher than the ones on a smooth wood bed (Crosato et al., 2013) meaning the same log might remain immobile on a rough bed but move on a smooth bed under identical flow. In natural settings, logs are often partially buried, caught behind boulders, or braced against banks/vegetation, so extra force is needed to overcome these obstacles before movement begins (Davidson et al., 2015). All these factors make general predictions difficult, and simplified models face limitations. Early force-balance models (Braudrick and Grant, 2000) assumed idealized conditions – a uniform cylindrical log on a flat bed with incipient motion by sliding – and thus could not account for rolling motion or complex log geometries. Later studies introduced separate sliding versus rolling mechanisms and considered a broader range of wood orientations and buoyancies (Bocchiola et al., 2006; Chen et al., 2020), but even these improved models remain highly sensitive to input parameters and local conditions. Predictions can hinge on uncertain values like drag coefficients, the number of contact points, or the definition of an "effective" flow depth in the presence of the log. As a result, thresholds derived from lab experiments or simple formulas often do not transfer reliably to field settings with different bed conditions or log types.

In summary, the incipient entrainment of LW depends on a complex interplay of LW characteristics, channel hydraulics, and boundary conditions. The current predictive approaches struggle to capture this complexity. This leads to significant uncertainty in forecasting exactly when a given log will start moving and highlights the need for calibration and validation of such models (Merten et al., 2010).

2.5. Deposition mechanisms of large wood

LW deposition refers to the process by which LW carried by the flow is removed from transport and comes to rest within the river environment. In other words, it is the natural retention, or storage, of wood in channels and floodplains once flow forces can no longer keep the wood moving. Understanding this process is fundamental because LW deposition influences channel morphology, habitat complexity, and flood hazard. The likelihood and location of deposition are not random but result from the interaction of three factors: (i) hydrodynamic conditions that govern when and where wood can exit the main flow, (ii) geomorphic and structural controls that provide sites where wood may lodge, and (iii) the physical characteristics and orientation of individual logs. These factors interact, producing the specific mechanisms of entrapment observed in rivers, including bridging, jamming, snagging, deposition in low-velocity zones, and burial by sediment.

2.5.1. Controls on large wood deposition

The likelihood of LW deposition is governed by flow velocity, depth, and turbulence. High flows transport wood but also create the conditions for deposition once velocities diminish. Studies have noted that wood transport is typically "uncongested" (free-floating single pieces) during rising and peak flows and then transitions to deposition on the falling limb of the hydrograph (MacVicar and Piégay, 2012; Ravazzolo et al., 2015a). Deposition often occurs when flow velocities drop below a critical value needed to carry the wood, or when logs encounter low-energy environments (eddies, slackwater). Flow structure is important: for instance, large eddies in the lee of channel obstructions can effectively capture wood. Peak flow magnitude and duration set the stage for wood entrapment – longer duration floods can carry wood farther downstream, whereas short, flashy floods may leave more wood stored locally as water levels fall rapidly (Bertoldi et al., 2013). Turbulence and secondary currents also influence deposition: in meandering single-thread rivers, secondary flows may push floating LW toward the banks (promoting snagging), whereas in braided rivers complex flow around bars causes repeated deposition and re-entrainment of wood (Kramer and Wohl, 2017). Field tracking has shown that in low-obstruction channels, logs can travel at speeds approaching the surface water velocity, indicating minimal deposition until flows decelerate (MacVicar and Piégay, 2012). In summary, high-energy flows are needed to mobilize and distribute wood, but deposition is favored by hydraulic heterogeneity, the zones of flow separation, expansions, or smooth velocity gradients are where LW can exit the main current. Furthermore, the physical characteristics of the channel exert a strong control on wood entrapment. Channel morphology dictates both the availability of trapping sites and the residence time of LW. In confined, steep channels with few overbank areas, wood tends to be flushed downstream quickly and has shorter residence or retention times, whereas in unconfined

or low-slope rivers with wide floodplains, LW can remain stored for long periods (Kramer and Wohl, 2017). Similarly, braided rivers present many bars and splitting flows that repeatedly deflect and deposit LW, leading to shorter travel distances (Ravazzolo et al., 2015a). By contrast, single-thread channels with continuous flow often convey LW further before it finds a depositional refuge (Bertoldi et al., 2013). The relative size of wood to the channel is also crucial: when log length approaches or exceeds the channel width, pieces are more likely to jam or brace against the banks, greatly promoting deposition (Merten et al., 2011). Moreover, man-made structures frequently create prime wood entrapment sites. Bridges are notorious for accumulating driftwood; logs can wedge against piers or lodges beneath bridge decks, rapidly forming large jams (Wyss et al., 2021). Laboratory and field tests have characterized how logs interact with bridge piers, typically involving an impact and rotation phase, followed by either lodging or release depending on friction and drag balance (Lyn et al., 2003). Sharp bends, culverts, and grade-control structures are other locations where flow convergence or physical narrowing induces LW deposition. Many rivers in developed areas now have debris retention structures (like rack structures or engineered log jams) designed specifically to intercept LW before it reaches vulnerable infrastructure (Schalko et al., 2020). These structures capitalize on the same principles of deposition: by providing an obstruction in the flow, they create a sheltered area or physical barrier where LW will accumulate. In summary, structural controls, whether natural (trees, rocks, bars and boulders) or artificial (bridges, debris racks), are often the initial triggers for LW deposition in rivers, as they present the resistance needed to halt a moving log. Moreover, the orientation of LW elements relative to the flow heavily influences whether it will continue its transport or become entrapped. Orientation relative to flow dictates the hydrodynamic forces on a log. Flume experiments have shown that logs floating perpendicular to the flow experience greater drag and tend to be caught or grounded faster, whereas logs aligned parallel to flow experience lower drag and can more easily be transported further downstream (Bocchiola et al., 2006; Chen et al., 2020). Wood size, density, and shape further influence deposition. Lighter (less dense) wood floats high and might ride over some obstacles but can also strand at higher elevations as floods recede. Denser or water-logged wood floats low in the water (or partially submerged), making it more likely to ground in shallow areas (Ruiz-Villanueva et al., 2016a). Similarly, large-diameter logs require higher water depths to continue floating, so, as water level falls, LW elements with larger diameter will lose their buoyancy and deposit (often at higher elevations on banks) (Kramer and Wohl, 2017). Branching complexity can increase the chance of entrapment by vegetation or other wood. In essence, the physical attributes of each piece, its length, diameter, attached root/branch network, and buoyancy, contribute to its "disposition probability" in a given river setting (Kramer and Wohl, 2017). This is why certain pieces (e.g. a long log with a broad root fan) often serve as the key-element of a

jam, while smaller or smoother pieces might pass through until captured by larger logs (Merten et al., 2011).

2.5.2. Mechanisms of large wood deposition

The interplay between hydraulic, geomorphic, and LW-specific factors manifest in several characteristic deposition mechanisms. Long logs can span across channels or between boulders, forming "bridges" that trap additional wood. A single key piece (often a large log with root wad or branches) can lodge between banks or against obstructions, creating a stable anchor that causes other drifting pieces to accumulate and form LW jams (Merten et al., 2011). Channel-spanning jams are especially effective at trapping wood, although during extreme floods they may be overtopped or mobilized, allowing some wood to pass through (Kramer and Wohl, 2017). Once a jam is established, the entrapped wood is harder to remobilize than individual free logs (Kramer and Wohl, 2017). Moreover, wood frequently deposits by snagging on rough elements or structures. For example, living riparian trees and fallen logs protruding into flow are extremely effective at capturing LW, often catching large "key" logs that then rack up additional pieces. Man-made structures (bridge piers, weirs) likewise intercept wood; during floods, logs can pivot and lodge against bridge piers, initiating accumulations that block the channel (Schalko, 2018; Wyss et al., 2021). Lower flow velocities promote more stable accumulations at structures, whereas higher velocities can prevent piling or even flush out jams (Lyn et al., 2003; Panici and de Almeida, 2018). LW can also be entrapped by sediment. During lower flows, logs may become partially buried (e.g. by bedload deposition or overbank silts). Such burial anchoring is one of the most effective mechanisms for LW retention (Kramer and Wohl, 2017; Merten et al., 2011; Wohl and Goode, 2008). Once a log is buried it remains in place until a sufficiently large flood scours it out (Kramer and Wohl, 2017). Over time, vegetation can grow around or even on deposited logs, further anchoring them in place. This interplay among wood, sediment, and vegetation creates semi-permanent wood storage sites in many rivers (Gurnell et al., 2016). Finally, hydrodynamic conditions have an important role as well by strongly controlling where LW comes to rest. LW commonly deposits in zones of flow recirculation or reduced velocity, such as floodplains, point bars, or on the inside of meander bends (Gurnell et al., 2002; Martin et al., 2018). According to MacVicar and Piégay, (2012) and Ravazzolo et al., (2015a) most wood depositions occur during the falling limb of the flood hydrograph, when hydraulic deceleration occurs (Piégay et al., 1999).

2.6. Numerical modelling of large wood in rivers

Numerical modelling may help in understanding and predicting LW transport. Several models have been developed to simulate LW dynamics, each adopting different methodologies. Over the past 10–15 years, substantial progress has been made in numerically modeling of LW dynamics in rivers. This section reviews the main approaches, including their capabilities and limitations.

2.6.1. Two-dimensional models (Eulerian–Lagrangian)

These models integrate wood dynamics directly into a two-dimensional (depth-averaged) hydraulic model. One of the first models of this kind is the Iber-Wood model developed by Ruiz-Villanueva et al. (2014a), where the Iber 2D hydrodynamic solver (Poupeau et al., 2010) of the Shallow Water Equations (SWE) is coupled with a kinematic Lagrangian model to account for LW displacement and rotation, providing insights into wood entrainment, accumulation and deposition processes. Similarly, Persi et al. (2018) integrated a Discrete Element Method dynamic Lagrangian approach tracking the motion of rigid bodies based on hydrodynamic forces, with an Eulerian solution of the SWE to simulate cylindrical wood transport in 2D streams in the ORSA2D_WT model. It was further extended to account for a two-way coupling (Persi et al., 2019b), where the flow drives the motion of wood, and the additional drag force exerted by LW pieces on the flow is considered. This allows phenomena like slow-down behind LW or increased backwater levels to be represented. Each LW piece experiences hydrodynamic drag, buoyancy, friction and gravity forces, as well as added mass and pressure gradient forces. The model computes a force balance on each piece at every time-step to determine its acceleration, rotation, and potential deposition. Collision algorithms enable logs to bounce off solid banks or each other (these collisions are usually treated as inelastic or partially elastic). Kang and Kimura, (2018) developed a modelling approach in which a piece of wood, with or without roots, was represented as an assemblage of spheres. LW motion is driven by hydrodynamic forces through floating, sliding, or rolling, initially neglecting collisions, which were incorporated in a later study (Kang et al., 2021). The model is two-way coupled as well, accounting for the drag force exerted by the wood on the flow. Finally, Xiong et al. (2022) developed an innovative fully coupled modeling system, integrating a high-performance 2D hydrodynamic model with a 3D Discrete Element Method (DEM) model, to simulate the transport of multiple debris within highly convective flows and to directly quantify the resultant impact forces on structures. A slightly simpler approach keeps the hydraulics and wood dynamics partially coupled: the flow field is computed by a 2D hydraulic model, but the wood pieces do not exert feedback forces on the flow (i.e., the coupling is one-way: flow influences wood, but wood does not alter flow). Wood pieces are again treated as

Lagrangian particles (often cylinders) that can float, translate, rotate, and interact via collisions. Examples of these models are those developed by Pascal et al. (2023) and Sansen et al. (2025).

2.6.2. Three-dimensional CFD-based models

To capture the full physics of wood–fluid interaction, LW motion can be integrated in fully 3D solutions of the Navier-Stokes equations. To overcome the difficulties posed by the simultaneous presence of free surfaces and moving objects, one possible approach is the use of Lagrangian CFD methods such as Smoothed Particle Hydrodynamics (SPH), a meshless method where both fluid and solid are represented by particles. Amicarelli et al. (2015) for example, used SPH to model floating rigid bodies as collections of particles and allowed them to interact with a particle-based fluid. Omidvar et al. (2013) extended a 3D SPH model to simulate floating bodies with substantial heave motion by introducing a variable particle mass distribution within an arbitrary Lagrangian–Eulerian framework. The method employed an embedded Riemann solver and locally refined particle resolution around the body, achieving computational savings of up to 80% compared to uniformly fine particle distributions. Validation against laboratory experiments included a forced 2D wedge and a 3D heaving cone, where SPH reproduced forces and free-surface evolution with close agreement, particularly at low-frequency motions. Another approach developed by Lai and Bountry, (2022) and Lai and Bandrowski, (2014) coupled rigid-body (in their case in-stream LW structures) dynamics with a 3D RANS (Reynolds-averaged Navier–Stokes) flow solver using their 3D model U2RANS. The model was tested and validated against experimental data (Lai and Bountry, 2022). However, such models can represent complex LW-flow behaviors but are extremely computationally intensive and require fine-scale calibration; thus, their application has been limited up to now to simplified experiments rather than to real large-scale river reaches.

2.7. Field tracking of large wood in rivers

2.7.1. Tracking methods and technologies

Field observations remain indispensable for validating and refining numerical models. Over the past two decades, researchers have employed a wide range of technologies – from simple tags to high-tech sensors – to monitor LW movement in situ. This section reviews the main tracking techniques (RFID tags, GPS and radio telemetry, and "Smart Wood" sensor logs), discusses the challenges in collecting and interpreting field data, and highlights key studies that have advanced our field understanding of LW dynamics.

Early efforts to track LW in rivers were often manual or qualitative, for example, marking logs with paint or numbered tags and then searching for them after floods (Moulin, 2005; Wohl and Goode, 2008), or using time-lapse photography and videography to observe wood floating as done by Ruiz-Villanueva et al. (2016b) . Another approach is using active or passive RFID tags (Passive Radio Frequency Identification). These are small, electronic tags that can be attached to or embedded in logs. Each tag carries a unique ID and can be detected by a handheld or stationary RFID receiver when it is within range (typically a few meters). This technology significantly advanced the study of LW dynamics, enabling detailed measurements of entrainment, transport paths, and deposition (MacVicar et al., 2009; Ravazzolo et al., 2015a; Schenk et al., 2014; Wyżga et al., 2017). However, this technology comes with the limitation that one should approach within a few meters of each log to be tracked. Moreover, when logs become buried in sediment or lodged underwater, detection becomes more difficult. Despite these challenges, RFID technology has allowed the compilation of quantitative datasets on wood travel distances, redistribution rates, and storage locations that were previously unattainable (Ruiz-Villanueva et al., 2016b). A more advanced approach is using GPS devices. A prominent example is a study on the Tagliamento River (Ravazzolo et al., 2015a), where logs fitted with GPS receivers and GSM transmitters were tracked. These GPS devices were programmed to obtain a position at set intervals and transmit the data via mobile phone networks when possible. The Tagliamento experiments revealed the potential of GPS devices: during floods, they captured detailed data on the dynamics of LW, including the timing of entrainment, travel speeds, and stop locations during the transport. The latest generation of LW tracking, "Smart-Wood", involves instrumenting logs with multiple sensors to record their motion dynamics in detail (Spreitzer et al., 2019). The main idea behind this approach is implanting inertial measurement units (IMUs) in real logs. Each IMU sensor package includes a 3-axis accelerometer, gyroscope, magnetometer, on-board processor, memory, and a wireless transmitter. These units are capable of logging high-frequency data on the log acceleration (impacts, movement), rotation (orientation changes via

gyroscope), and heading (from magnetometer) during transport. In their latest study, Spreitzer et al. (2024) deployed Smart-Wood logs (~4.3 *m* long, ~0.33 *m* diameter) in three Swiss rivers to capture quantitative dynamics of LW movement during floods. The results revealed consistent patterns such as logs rotations (due to helical flow patterns) and recording distinct impact events when hitting obstacles like bridge piers or riverbanks.

2.7.2. Challenges in data collection and interpretation

Tracking LW in the field is inherently difficult, and several challenges have been identified. The most significant challenge is finding the tagged logs after floods. In dense forests or braided rivers, logs can be transported into side channels, vegetation, or buried in sediments, making recovery very time-consuming if not impossible. RFID-tagged logs that are buried or floating out of the main reach may not be detected unless one conducts very intensive surveys. Similarly, a GPS logger that detached or a radio tag that ran out of battery might lead to a lost log (and therefore lost data). Many studies (Charles et al., 2024.; MacVicar and Piégay, 2012a; Ravazzolo et al., 2015a) report a recovery rate ranging between 96% and 33% of tagged logs, introducing survivorship bias in the data (the logs that are found might not be representative of those not found – for example, easily found ones might be those that stranded near access points). This can be mitigated by tagging large numbers of logs to begin with, accepting that some fraction will never be traced. Methods like RFID give essentially two data points for each log; the location where it was tagged (initial position) and the location where it was found later. What happened in between is usually unknown. A log might have moved in one flood or in multiple incremental steps; it might have been temporarily stored in an intermediate location, etc. Without continuous tracking, interpretation requires assumptions. GPS tracking and sensor logs improve this by giving time series, but these are still limited in their use. Thus, piecing together a full narrative of a log's journey is impossible. We often must speculate on the event that may have entrained and transported a specific log, but the exact timing and path remain unknown. Finally, field tracking experiments are subject to natural conditions. Floods may not occur as conveniently or frequently as needed for study, or conversely, a flood may be so large that it sweeps all tagged logs out of the study area. Animal interference (beavers moving tagged logs), equipment failures (water damage to electronics), and safety concerns (needing to avoid being in the field during dangerous high flows) all complicate data collection.

Despite these challenges, field tracking studies have yielded critical insights that inform and validate models. One of the early studies to use active radio transmitters in a systematic way was by Haga et al. (2002). By tracking logs in steep headwater streams, this study highlighted the importance of piece anchoring and local retention: many logs moved only until they encountered the first stable

obstruction, often traveling short distances. It emphasized piece size and channel width as factors in entrapment. Martin and Benda (2001) showed a field experiment that introduced marked logs to a stream and monitored their redistribution over years. It provided evidence for episodic movement (logs mostly move during intense floods) and that jams can be breakpoints that halt further transport until they fail. MacVicar and Piégay (2012) combined video monitoring of floating wood during floods with field inventories along the Rhône River in France. Their work offered a direct measurement of floating wood velocity and confirmed that in an uncongested, single-thread river, wood pieces can move at speeds comparable to the surface flow. Importantly, it documented most wood being deposited near peak flow and not much after. Ravazzolo et al. (2015a) were among the first to use combined RFID and GPS tracking in a braided river environment on the Tagliamento River. It demonstrated that modern technologies could allow one to track wood even in a complex, multi-thread system. The study findings underscored the role of channel morphology: in the braided Tagliamento river, wood dispersal was widespread, and wood often deposited on mid-channel bars, contrasting with behavior in narrower rivers. It also showed that active tags can be used in tracking with acceptable cost-time effort ratio.

In reviewing these studies, a common theme is the interplay between field data and numerical modeling. Field tracking provides the ground truth needed to test and validate model. Conversely, models can help interpret field data by filling spatio-temporal gaps, for instance, running a simulation between known start and end points of a log's path to see what likely happened in between. Both are evolving together: as tracking methods get better, they feed more information to models; and as models get better, they can pose new questions to be answered by field experiments.

Chapter 3

Eulerian Lagrangian Modeling of Large Wood Transport: ORSA2D_WT Model

3.1. Abstract

This chapter introduces the ORSA2D_WT model, a two-way coupled Eulerian–Lagrangian framework for simulating LW transport in rivers. The model integrates a 2D shallow-water solver with a discrete Lagrangian module to describe the translation, rotation, entrainment, and deposition of individual wood elements. The governing equations account for buoyancy, drag, side forces, and collision dynamics, while also incorporating simplified entrainment and arrest routines. Emphasis is placed on the representation of flow–LW interactions, including the feedback of wood on hydraulics through additional drag and side effects. The chapter details the numerical implementation of each sub-model, highlighting assumptions and limitations, such as utilizing hydrodynamic coefficients accounting only for floating and simplified entrainment thresholds. By providing a baseline description of the ORSA2D_WT model, this chapter establishes the foundation for subsequent improvements, experimental validation, and real-world applications developed in the following chapters.

3.2. Governing equations in ORSA2D_WT

ORSA2D_WT is a two-dimensional (2D) numerical model developed to simulate the motion of floating rigid logs in open-channel flows. Each log is represented as a solid cylinder with fixed mass and geometry. The logs are assumed to remain partially submerged according to their buoyancy and move only in the horizontal plane, as vertical accelerations are negligible once flotation equilibrium is reached. The model is designed for high–Reynolds–number flow conditions (Re > 10^4), where viscous and history effects are of secondary importance. Accordingly, hydrodynamic forces are expressed through empirical coefficients, primarily drag and side-force coefficients. The governing equations for LW dynamics, originally formulated by Persi (2018), are based on Newton's second law and expressed through an Eulerian–Lagrangian framework. This approach allows coupling between the Eulerian flow field (computed from the 2D hydrodynamic solver) and the Lagrangian motion of each log. The formulation is derived from the Maxey–Riley equation, an extension of the Basset–Boussinesq–Oseen (BBO) equations, adapted for a semi-submerged cylindrical body. This provides a physically consistent basis for representing added mass and fluid acceleration effects. To capture the influence of local velocity gradients along a log's length, each log is conceptually divided into four segments along its main axis. Hydrodynamic forces are computed at each segment, allowing spatial variations in the Eulerian velocity field to be reflected in the Lagrangian response of the log. The model simulates translation, rotation, entrainment, arrest, and collisions of LW elements during flood events.

3.2.1. Translation model

The main forces acting on each log include drag, added mass, pressure gradient, and side-force contributions, as summarized in Eq. (3.1):

$$\boldsymbol{F}_{total} = \boldsymbol{F}_D + \boldsymbol{F}_{AM} + \boldsymbol{F}_{PG} + \boldsymbol{F}_S \tag{3.1}$$

Where $\boldsymbol{F}_D$ is the drag force, $\boldsymbol{F}_S$ the side force, $\boldsymbol{F}_{PG}$ the pressure-gradient force, and $\boldsymbol{F}_{AM}$ the added mass force.

The drag and side forces account for the main hydrodynamic resistance acting on the log due to its motion relative to the surrounding flow. These forces act in directions parallel and perpendicular to the flow, respectively, and together they represent the hydrodynamic resistance and lateral deviations that govern the translation of a LW element on the water surface as expressed in equations 3.2 and 3.3.

$$\boldsymbol{F}_D = \frac{1}{2} C_D \rho_f A' \boldsymbol{V}|\boldsymbol{V}| \tag{3.2}$$

$$\boldsymbol{F}_S = \frac{1}{2} C_s \rho_f A' \boldsymbol{V}|\boldsymbol{V}| \times \boldsymbol{i}_z \tag{3.3}$$

Where V is the relative velocity, A' the area on which the force acts, ρ_f is the density of the fluid, C_D and C_S are the drag and side-force coefficients, respectively. And where $\boldsymbol{i}_z$ is the unit vector normal to the 2D flow plane. The values of these coefficients were derived by Persi (2018) and Persi et al. (2019a), who conducted a series of laboratory experiments to estimate the drag and side-force coefficients of a semi-submerged floating LW elements. More detailed information on the experimental setup and coefficient derivation can be found in the cited studies.

When the log accelerates, it also accelerates a portion of the surrounding fluid, producing an additional inertial effect known as the added mass force, defined as:

$$\boldsymbol{F}_{AM} = \frac{1}{2} C_{AM} m_f \left(\frac{D\boldsymbol{V}_f}{Dt} - \frac{D\boldsymbol{V}_b}{dt} \right) \tag{3.4}$$

Where m_f is the log mass, $\boldsymbol{V}_b$ is the velocity vector of the body, $\boldsymbol{V}_f$ is the velocity vector of the undisturbed flow at the body center and C_{AM} is the added mass coefficient, which depends on the log's geometry and submergence ratio, defined by Persi (2018) as 1.41 for a LW element with a density of 774 kg/m^3 .

In addition, the force exerted on a volume of fluid equal to the body volume in the undisturbed flow must be considered, leading to the pressure gradient force:

$$\boldsymbol{F}_{PG} = m_f \left(\frac{D\boldsymbol{V}_f}{Dt} \right) \tag{3.5}$$

Expanding Eq. (3.1), the translation equation implemented in the discrete element module of ORSA2D_WT becomes:

$$\left(m_b + \frac{1}{2} C_{AM} m_f \right) \frac{d\boldsymbol{V}_b}{dt}$$

$$= \frac{1}{2} \rho_f C_D A \left(\boldsymbol{V}_f - \boldsymbol{V}_b \right) \left| \boldsymbol{V}_f - \boldsymbol{V}_b \right| \tag{3.6}$$

$$+ \frac{1}{2} \rho_f C_s A \left(\boldsymbol{V}_f - \boldsymbol{V}_b \right) \left| \boldsymbol{V}_f - \boldsymbol{V}_b \right| \times \boldsymbol{i}_z$$

$$+ \rho_f \left(1 + \frac{1}{2} C_{AM} \right) Vol \frac{D\boldsymbol{V}_f}{Dt}$$

3.2.2. Rotation model

The rotational motion of each LW element in ORSA2D_WT is governed by the balance of angular momentum around its center of mass, accounting for both the hydrodynamic torque distribution and the added inertia effects. The general form of the rotation equation, adapted from Persi (2018), is expressed as:

$$I\frac{d\boldsymbol{\omega}_b}{dt} = \boldsymbol{T}_{CM} + \boldsymbol{T}_{AI} = \sum \boldsymbol{r} \times \boldsymbol{F} + \frac{1}{2} C_{AI} I \left(\frac{D\boldsymbol{\omega}_f}{Dt} - \frac{d\boldsymbol{\omega}_b}{dt}\right) \tag{3.7}$$

Where I is the moment of inertia, $\boldsymbol{\omega}_b$ is the angular velocity, $\boldsymbol{T}_{CM}$ represents the torque due to the distribution of hydrodynamic forces acting along the body, and $\boldsymbol{T}_{AI}$ is the added inertia torque, accounting for the difference in angular acceleration between the log and the surrounding flow, $\boldsymbol{r}$ is the position vector of the applied force F with respect to the LW's center of mass, C_{AI} is the added inertia coefficient, and ω_f is the local angular velocity of the fluid.

Equation 3.7 can be further expanded as:

$$\begin{aligned} I\frac{d\boldsymbol{\omega}_b}{dt} = & \left[-b_{CMy}\left(\frac{1}{2}\rho_f C_D A(\mu_f - \mu_b)\right)|\boldsymbol{V}_f - \boldsymbol{V}_b|\right] \\ & + \frac{1}{2}\rho_f C_S A(v_f - v_b)|\boldsymbol{V}_f - \boldsymbol{V}_b| \\ & + \rho_f\left(1 + \frac{1}{2}C_{AM}\right) Vol\frac{D\mu_f}{Dt} - \frac{1}{2}\rho_f C_{AM} Vol\frac{D\mu_b}{dt} \\ & + b_{CMx}\left(\frac{1}{2}\rho_f C_D A(v_f - v_b)\right)|\boldsymbol{V}_f - \boldsymbol{V}_b| \\ & + \frac{1}{2}\rho_f C_S A(\mu_f - \mu_b)|\boldsymbol{V}_f - \boldsymbol{V}_b| \\ & + \rho_f\left(1 + \frac{1}{2}C_{AM}\right) Vol\frac{Dv_f}{Dt} - \frac{1}{2}\rho_f C_{AM} Vol\frac{Dv_b}{dt} \\ & + \frac{1}{2}C_{AI} I\left(\frac{D\boldsymbol{\omega}_f}{Dt} - \frac{d\boldsymbol{\omega}_b}{dt}\right) \end{aligned} \tag{3.8}$$

3.2.3. Collision model

Collisions between floating LW elements or between LW elements and channel boundaries are essential for accurately reproducing LW transport processes. ORSA2D_WT implements the collision model of Hecker (1997), based on an impulse–momentum formulation. During a collision, an instantaneous impulse J acts along the normal contact, modifying the post-collision linear and angular velocities according to momentum conservation and restitution laws:

$$J = \frac{-(1-e)\boldsymbol{V}_{rel}^{i} \cdot \boldsymbol{n}}{\frac{1}{m_{b1}} + \frac{1}{m_{b2}} + \frac{(\boldsymbol{r_1} \times \boldsymbol{n})^2}{I_1} + \frac{(\boldsymbol{r_2} \times \boldsymbol{n})^2}{I_2}} \tag{3.9}$$

when two moving bodies are involved in the collision, or as:

$$J = \frac{-(1-e)\boldsymbol{V}_{rel}^{i} \cdot \boldsymbol{n}}{\frac{1}{m_{b1}} + \frac{(\boldsymbol{r_1} \times \boldsymbol{n})^2}{I_1}} \tag{3.10}$$

when a cylinder impacts a rigid wall.

In equations (3.9) and (3.10), $\boldsymbol{V}_{rel}^{i}$ is the relative velocity between the bodies, $\boldsymbol{n}$ is the unit vector normal to the hit body, with components $\boldsymbol{n}_x$ and $\boldsymbol{n}_y$, $\boldsymbol{r_i}$ are the distances between the impact point and the center of mass of the bodies, I_i are the moments of inertia and m_{bi} are the masses of the bodies, with I is the inelastic restitution coefficient.

3.2.4. Entrainment and Arrest model

In its standard form, ORSA2D_WT entrainment model is based on a flotation parameter, as developed by Braudrick and Grant (2000): this flotation parameter is based on a balance of downstream force components (Buoyancy F_B, Gravity F_G and Drag forces F_D) and upstream force component which correspond to the Friction force F_F. Persi (2018) implemented this approach by first evaluating the net weight of a log under partially or fully submerged conditions (Eq.3.11). The log is assumed to rest on the channel bed: if the water depth exceeds the log diameter, the body is considered fully submerged, whereas for shallower flows, only the submerged portion of the volume is accounted for. When the resulting net weight is negative, the log is buoyant and therefore floats; in this case, the equations of transport are directly applied.

$$\boldsymbol{W} = m_b \boldsymbol{g} - Vol_{sub} \rho_f \boldsymbol{g} \tag{3.11}$$

where m_b is the mass of the body, g stands for the gravitational acceleration, Vol_{sub} is the submerged volume, calculated taking into account the submerged part of each body and ρ_f is the density of the

fluid. The first term on the right-hand side is the real weight of the body, and the second term is the buoyancy force. Conversely, when the net weight is positive, floating is not guaranteed, and the force balance by (Braudrick and Grant, 2000) is calculated, requiring the computation of the effect of gravity (F_G) on a sloping bottom, the static friction (F_F) between the bottom and the body and the drag force (F_D) on the body as follow:

$$\boldsymbol{F}_G = \boldsymbol{W}\ sin\,\alpha \tag{3.12}$$

$$\boldsymbol{F}_F = \mu_f \boldsymbol{W}\ \cos\alpha \frac{\boldsymbol{V}}{|\boldsymbol{V}|} \tag{3.13}$$

$$\boldsymbol{F}_D = \frac{1}{2} C_{D_{app}} \rho_f A' \boldsymbol{V}|\boldsymbol{V}| \tag{3.14}$$

where α is the horizontal angle of the channel bottom, μ_f is the coefficient of friction between the bottom and the body, C_{D_app} is the apparent drag coefficient, which is specific for the incipient motion computation, A' the area on which the force acts and V the relative velocity. The area A' is different according to the body shape and to the water level. The apparent drag coefficient used in the model is the one proposed by Bocchiola et al. (2006), who averaged a series of experiments on sand and gravel beds, with wooden cylinders parallel and perpendicular to the flow. The resulting average drag coefficient value is 1.41.

The friction coefficient contributes to defining the mobility of the rigid body and depends mainly on the roughness of both the bottom and the body surface. Since the interest is in wooden elements, the incipient motion is computed with friction coefficients depending on the bottom material and varies for artificial and real channels, as shown in Table 3.1.

Table 3.1 Coefficient of friction for incipient motion, between wooden elements and different bed material as in (Persi, 2018). References: a (Crosato et al., 2013); b (Murase, 1984); c (Ishikawa, 1989).

Bed material	$\boldsymbol{\mu_f}$
Wood	0.47^a
Wet metal	0.20^b
Gravel	0.64^a
Sand	0.47^c

Once the forces included in the model are computed adopting the appropriate drag and friction coefficients, the floating parameter can be calculated as the ratio between the forces in favor to (gravity and drag) and those opposed to the motion (friction):

$$\frac{F_G + F_D}{F_F} \tag{3.15}$$

If the ratio is higher than 1, the body floats, otherwise, the equations of motion are not computed.

This same condition is also used to evaluate the arrest, which requires verification of the incipient motion condition at every time step. When the net weight of a log becomes positive, the model recomputes the force balance to determine whether the flow is still capable of sustaining movement. In this situation, the log is already in motion, and therefore the contact mechanics differ, friction is no longer static but dynamic, implying that the friction coefficient must be reduced accordingly (Rabinowicz, 1951). The specific values adopted for the dynamic friction coefficients in ORSA2D_WT are listed in Table 3.2

Table 3.2 Coefficient of kinematic friction, between wooden elements and different materials (Persi, 2018). References: a value approximated from (Blau, 2001); b (Murase 1984); c value obtained by reducing the static coefficient by 25% (Murase 1984).

Bed material	μ_f
Wood	0.30^a
Wet metal	0.15^b
Gravel	0.48^a
Sand	0.35^c

3.3. Numerical modelling and Model implementation

3.3.1. SWE hydrodynamic solver module

The fluid motion is governed by the depth-averaged Shallow Water Equations (SWE). Denoting water depth by h and unit-width discharges by q_x and q_y, the continuity and momentum equations are:

$$\frac{\partial h}{\partial t} + \frac{\partial q_x}{\partial x} + \frac{\partial q_y}{\partial y} = 0\,,$$

$$\frac{\partial q_x}{\partial t} + \frac{\partial}{\partial x}\left(\frac{q_x^2}{h} + \frac{1}{2}gh^2\right) + \frac{\partial}{\partial y}\left(\frac{q_x q_y}{h}\right) = gh\left(S_{0x} - S_{fx}\right)\,, \tag{3.16}$$

$$\frac{\partial q_y}{\partial t} + \frac{\partial}{\partial y}\left(\frac{q_y^2}{h} + \frac{1}{2}gh^2\right) + \frac{\partial}{\partial x}\left(\frac{q_x q_y}{h}\right) = gh\left(S_{0y} - S_{fy}\right)\,,$$

where g is gravity, S_{0x} and S_{0y} are bed slopes in *x and y* and S_{fx} and S_{fy} are friction slopes from bed resistance. The first line is mass conservation; the others are momentum in *x and y* directions.

ORSA2D_WT stems from the ORSA2D SWE model (Petaccia and Natale, 2013, 2020; Petaccia et al., 2010), which discretizes Eq. 3.29 on a mesh of finite-volume cells (structured or unstructured). Fluxes at cell faces are computed by Roe's approximate Riemann solver (1st-order accurate). The

bed-slope source term is up winded as in Bermúdez and Vázquez (1994), and the friction term is treated semi-implicitly. An entropy fix (Harten–Hyman) is applied to avoid non-physical rarefactions. In practice, ORSA2D_WT marches the solution forward in time using an explicit finite-volume scheme with a global time step. Time stepping is constrained by the Courant–Friedrichs–Lewy condition. A single time step Δt is chosen to satisfy:

$$\Delta t = CFL \frac{\Delta x}{a} \tag{3.17}$$

where Δx is the smallest cell size, a the maximum wave speed in the domain, and a CFL≤1.

Furthermore, ORSA2D_WT includes a wetting–drying algorithm: cells with water height below a predefined small threshold are treated as dry, and updates are modified to prevent negative depths. This allows flood fronts to advance onto dry areas and retreat without numerical instability. The bed slope source terms S_{0x} and S_{0y} and friction terms S_{fx} and S_{fy} are included as algebraic source terms in (2.30). As noted, the bed slope is upwind-discretized and the friction term (e.g. through Manning or Chézy formulations) is computed semi-implicitly at each time step. Physically, ghS_0 represents the driving gravity force and ghS_f the resistance from bed roughness. These contributions ensure the flow responds to channel slope and friction.

3.3.2. Discrete element method (DEM)

As explained in detail in section 3.3, floating logs are treated as rigid bodies whose motion follows Newton's laws. For each log, the translation and rotation equations are solved in the Lagrangian frame. The translational equation includes hydrodynamic drag, side forces, added-mass effects, and gravity/buoyancy (modified for partial submergence). The formulation is an extension of the Maxey–Riley equations to large bodies. Because velocity gradients across a body can vary significantly, each log is subdivided into 4 segments along its main axis. The hydrodynamic force (drag, side force, added mass) is computed on each segment using the local fluid velocity (Figure 3.5). then summed to yield the net forces.

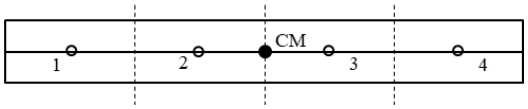

Figure 3.1 Scheme of the division of the transported body. Forces are evaluated at the center of each segment (points 1 to 4); the corresponding volume is highlighted by dashed lines (Persi 2018).

Furthermore, at each time step, the code must find the local flow velocity at each segment center. A "point-in-cell" algorithm is used. Simple nearest-centroid assignment can fail on unstructured meshes; instead ORSA2D_WT uses a hybrid method inspired by Soukal et al. (2012) . First, the nearby triangle is identified (often by nearest-cell-center), then a brief "walk" search is performed to locate the exact cell containing the point. A rotation/test procedure (Eq. 3.7–3.8 in Persi, 2018) is used to determine if the point lies to one side of the current triangle, and if not, it steps to a neighboring triangle, repeating until the correct cell is found. Once the cell is identified, the undisturbed flow velocity V_f (from the SWE solution) is interpolated at the segment center. This ensures that the force on each segment depends on the correct local velocity, avoiding spurious jumps caused by coarse mesh assignment. Moreover, the check for collisions in log–log and log–wall interactions is explicitly handled. At each step, all pairs of logs (and each log against channel boundaries) are tested for overlap. A collision is detected when the distance between two-cylinder centerlines falls below half of the sum of their lengths. Because collisions are only detected at discrete time steps, some degree of overlap may already be present. In such cases, the code first repositions the bodies to remove interpenetration: for log–wall contacts only the log is shifted back, while for log–log collisions one log (the "colliding" body) is moved aside. Once repositioning is completed, the post-impact velocities are updated using the impulse–momentum formulation detailed in Persi (2018) Section 2.5. Time integration of the DEM is done with an explicit 4th-order Runge–Kutta (RK4) scheme. At each time step, the algorithm updates the log position (x, y), orientation ϑ, and velocities (u, v, ω). More details about the RK4 procedure are available in Persi (2018) Section 3.4.5.

3.3.3. SWE-DEM two-way coupling

In congested wood transport, logs can significantly alter the flow (backwater effect), which one-way coupling ignores. In other words, as logs accumulate or obstruct the channel, they raise the upstream water level. Two-way coupling was introduced to capture this feedback (Persi et al., 2019b). ORSA2D_WT two-way coupling scheme adds the log forces back into the SWE momentum equations as source terms of opposite sign, ensuring momentum conservation. Implementing two-way coupling allows the model to simulate situations where logs slow down the flow and cause upstream ponding, which is important for flood risk and transport prediction.

In practice, the hydrodynamic forces (drag, side) acting on each log are applied, reversed, to the flow as distributed sources. Persi et al. (2019b) derived the form of the source-term vector $\boldsymbol{S}$ to be added to the momentum equations.

$$\frac{q_x}{\partial t}+\frac{\partial}{\partial x}\left(\frac{q_x^2}{h}+\frac{1}{2}gh^2\right)+\frac{\partial}{\partial y}\left(\frac{q_x q_y}{h}\right)=gh\left(S_{0x}-S_{fx}\right)+S_{sorg\_x} \tag{3.18}$$

$$\frac{\partial q_y}{\partial t}+\frac{\partial}{\partial y}\left(\frac{q_y^2}{h}+\frac{1}{2}gh^2\right)+\frac{\partial}{\partial x}\left(\frac{q_x q_y}{h}\right)=gh\left(S_{0y}-S_{fy}\right)+S_{sorg\_y} \tag{3.19}$$

where S_{sorg_x} and S_{sorg_y} represent the momentum loss due to LW presence. To conserve momentum, equal and opposite forces $-F_D$, $-F_S$ are applied to the SWE as source terms.

For each log, the ORSA2D_WT computes drag and side forces at four segment centers as explained in section 2.4.2. These forces are collected into matrices F_x, F_y, which store per-segment contributions. In the implementation of the coupling procedure, three different strategies were tested, depending on the number of cells on which the opposite of the hydrodynamic forces were applied (Persi et al., 2019b). However, for the applications in this thesis research, the 1 step strategy was adopted, applying the source terms only in the four cells containing the log segment centers (Figure 3.6). Each force is assigned to its host cell, producing a sparse but computationally efficient correction.

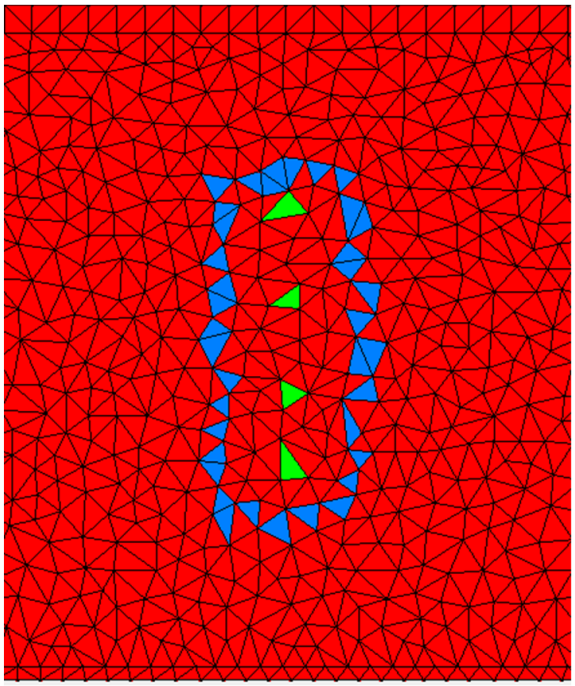

Figure 3.2 1-step strategy for two-way coupling: green cells contain the segment centers; blue cells contain the log boundary.

The final source vectors are constructed as:

$$S_{sorg_x}=-\frac{F_{D,x}+F_{S,x}}{\rho_w A}\ ;\ S_{sorg_y}=-\frac{F_{D,y}+F_{S,y}}{\rho_w A} \tag{3.20}$$

With A the projected area of the wood piece normal to the direction of the force.

In benchmarking the two-way coupling algorithm, Persi et al. (2019b) found that the 1Step method was the fastest and easiest to implement, with only marginal loss of precision (≈1.5% error vs. distributing the force on all the cells within the log area) and concluded that the simplest 1Step coupling often suffices for modelling purposes.

3.4. Limitations and possible improvements in ORSA2D_WT

The ORSA2D_WT model currently simulates large wood transport by computing drag and side forces, added mass, and pressure-gradient forces on floating logs (Persi et al., 2019c) . This Eulerian–Lagrangian approach treats logs as freely buoyant cylinders, following the Maxey–Riley framework for small particles modified for large bodies. However, in reality, LW often moves in contact with the bed or banks at low flow. As highlighted by several authors (Bocchiola et al., 2006; Braudrick and Grant, 2000; Chen et al., 2020; Crosato et al., 2013), in such conditions logs can initiate motion by rolling, sliding or pivoting, their behavior being also affected by LW orientation: logs aligned parallel to the flow tend to slide, whereas oblique or transverse logs tend to roll. Under very shallow water conditions, logs typically remain partially in contact with the surface (bed/banks), so the onset of motion is governed by critical tilting or sliding thresholds. This is not represented in the current model, leading to underestimation of entrainment potential at lower flows. An improved model would therefore need explicit sliding- and rolling-initiation criteria to account for motion of logs that are only partially buoyant. A related limitation concerns the hydrodynamic coefficients used in the model. ORSA2D_WT model is parameterized with drag and side coefficients calibrated for free-floating cylinders (Persi et al., 2019a), but the effective forces differ when a log is partly in contact with the surface. In shallow flow, the submerged volume and exposed area of a log change dynamically, so drag and side coefficients should depend on the degree of contact. Some recent studies address this issue: for example, Hlavňa et al. (2024) introduced a correction factor k to the original Braudrick and Grant (2000) model for semi-submerged logs resting on slopes. In ORSA2D_WT the absence of such a factor means that buoyancy and drag may be not accurately computed when a log is in contact with a surface. To improve accuracy, the model should incorporate accurate coefficients that account for bed proximity. In short, the ORSA2D_WT model must be extended with surface-contact hydrodynamics and bed-interaction effects for shallow flows. Another shortfall of the current entrainment modeling is the treatment of friction. Laboratory tests show that the “friction angle” of a cylindrical log depends on its orientation: a log aligned with the flow typically has a higher sliding threshold than one placed obliquely (Chen et al., 2020). In other words, a parallel log encounters a higher resistance to finally slide, whereas an angled log more easily rolls and encounters less resistance. Current models generally use a single μ friction coefficient, regardless of orientation

relative to the flow. ORSA2D_WT should therefore be enhanced with orientation-dependent friction coefficients: for example, assigning a lower effective μ for logs oriented normal to flow (favoring rolling) and a higher μ for those aligned with flow (favoring sliding). This extension would allow the model to reproduce the observed orientation effects on mobility, as well as to include static friction when logs transiently rest on the bed.

Perhaps, the most fundamental limitation lies in how arrest is handled. In the current formulation, arrest is essentially a reversed entrainment criterion or balance of forces: when driving forces are insufficient to overcome resistance, the log is assumed to stop. Alternatively, a log can stop if it has more than two points of contact. This procedure, regulated through the collision subroutine, requires the definition of boundaries against which LW can collide and is computationally expensive. Furthermore, field and experimental evidence indicates that wood arrest is seldom a deterministic reverse of entrainment. Instead, debris often becomes irreversibly trapped by channel features. This simplification does not reflect the complexity of natural systems, where arrest is often the result of stochastic entrapment processes rather than a deterministic force balance. Logs frequently become trapped by interlocking with other pieces of wood, wedging against banks, or bridging across structural obstacles. Experiments by Bocchiola et al. (2008) demonstrated that jams form around "key logs" that snag or span a channel, with subsequent pieces accumulating in a highly stochastic manner. Arrest in nature is therefore more often the outcome of chance encounters and physical interlocking than a predictable reduction in hydrodynamic force. Especially important but currently neglected process is entrapment by vegetation. Riparian and in-channel and bank vegetation, such as pioneer trees, rootwads, and vegetated islands, provides natural anchor points for logs. Gurnell et al. (2002) and Abbe and Montgomery (2003) highlighted how vegetation acts as a primary mechanism for wood retention, with stems and branches snagging moving logs and initiating the formation of stable jams. In braided rivers like the Tagliamento river, vegetated islands frequently trap floating logs, anchoring accumulations that persist over multiple flood events (Bertoldi et al., 2010). ORSA2D_WT does not currently represent arrest by vegetation, which limits its ability to predict wood retention in vegetated floodplains. Including vegetation as probabilistic arrest elements, with entrapment likelihood depending on vegetation density and heights, would bring the model closer to observed field behavior. In summary, the ORSA2D_WT entrainment and arrest routines remain oversimplified, treating all logs as fully floating bodies with fixed coefficients, neglecting sliding/rolling thresholds, orientation effects, and contact motion in very shallow water conditions. Improving the model will require (1) adding initiation criteria for rolling and sliding; (2) estimation of hydrodynamic coefficients to account for partial submergence and bed proximity; (3) using orientation-dependent friction; and (4)

modeling arrest as a stochastic entrapment process (e.g. lodging against vegetation) rather than a force balance. Addressing these limitations, should yield more realistic predictions of LW dynamics.

Chapter 4

Improving Entrainment and Arrest Mechanisms in ORSA2D_WT model

4.1. Abstract

This chapter presents the improvements made to the entrainment and arrest module of the ORSA2D_WT model to provide a more physically based description of LW dynamics. While the original model relied primarily on simplified flotation thresholds and deterministic arrest routines, new formulations are introduced to distinguish between different initiation mechanisms, namely flotation or sliding, and rolling based on log orientation. These refinements address the strong dependence of entrainment thresholds on the geometry and positioning of wood pieces, as highlighted in previous laboratory studies, thereby extending the model's applicability to a wider range of hydraulic conditions, particularly in shallow flows where entrainment by flotation may underestimate the initial motion. In addition to entrainment, the representation of arrest and deposition has been enhanced through the inclusion of stochastic entrapment mechanisms. Specifically, vegetation entrapment is introduced as a condition based sub-module, imitating the ability of riparian trees and floodplain vegetation to capture mobile LW. This extension allows the model to better reflect field observed processes, where logs frequently become lodged against vegetation. The numerical implementation of these improvements is therefore described. By embedding these improvements, the revised model overcomes some limitations of the original version, where entrainment was treated as a buoyancy-driven process and arrest as a purely deterministic outcome. The improvements increase the realism and robustness of LW simulations, ultimately enhancing the model's predictive reliability for flood risk assessments. This chapter thus provides a first step in improving ORSA2D_WT model.

4.2. Improved entrainment and arrest model

Entrainment of LW in rivers is governed by the balance between the hydrodynamic forces generated by the flow and the resisting forces arising from gravity, buoyancy, and bed friction. In the original ORSA2D_WT model (Persi, 2018), entrainment was represented by a floatation ratio as proposed by Braudrick and Grant, (2000) as explained in detail in section 3.1.4. Braudrick and Grant, (2000) did not consider pre-flotation mechanisms such as rolling and sliding, which laboratory studies have shown to be critical at lower flow stages (Bocchiola et al., 2006; Chen et al., 2020; Crosato et al., 2013). For this reason, the entrainment model in ORSA2D_WT was modified. This extension allows the model to explicitly account for both the flotation threshold, governing the transition to buoyant motion, and the sliding–rolling threshold, which controls entrainment of negatively buoyant or partially submerged logs. Haga et al. (2002) introduced a dimensionless model for LW entrainment to differentiate between incipient motion by sliding, rolling or floating based on a dimensionless force parameter, defined as:

$$\Psi = \frac{F}{R} \tag{4.1}$$

Where F is the hydrodynamic force (F_D) and R is the resisting force ($F_F - F_G$). Based on this model, LW elements will start moving when the hydrodynamic force is greater than the resistance force. Considering this force balance along with the ratio between water depth (h) and log diameter (D_{log}), the authors could determine the motion type as follows:

A log is stable if $\Psi \leq 1$ and $\frac{h}{D_{log}} < 1$ (4.2)

A log is sliding or rolling if $\Psi > 1$ and $\frac{h}{D_{log}} < 1$ (4.3)

A log will float if $\frac{h}{D_{log}} \geq 1$ (4.4)

Figure 4.1 shows an example of the relationship between the transport mode and the corresponding dimensionless water depth h*and the dimensionless force Ψ.

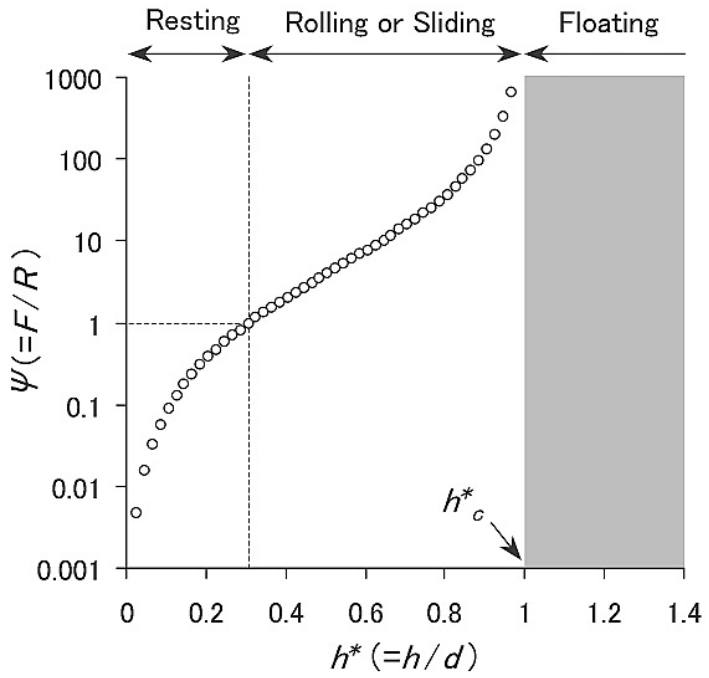

Figure 4.1 An example of the relationship between log transport mode, the dimensionless water depth h*and the dimensionless force Ψ. Source: Haga et al. (2002).

Building on this foundation, Bocchiola et al. (2006) performed controlled flume experiments on cylindrical wooden dowels to refine the entrainment threshold model. They introduced a distinction between the mechanisms of incipient motion (rolling and sliding) accounting for the orientation of LW with respect to the flow (Figure 4.2).

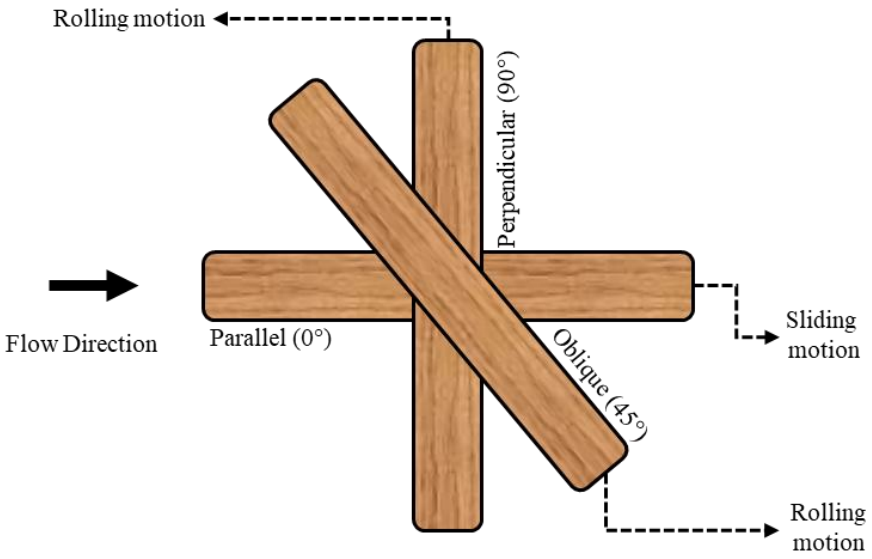

Figure 4.2 Plan view of log's orientation with respect to the flow direction and the corresponding initial motion for each configuration.

Bocchiola et al. (2006) introduced a dimensionless threshold parameter, Y_W^* representing the ratio of hydrodynamic support to log weight, for a cylindrical log of diameter D_{log} in water with density ρ_w. The parameter is defined using a representative local water depth h around the log of a density ρ_{log}.

$$Y_W^* = \frac{\rho_w h}{\rho_{log} D_{log}} \tag{4.5}$$

At incipient motion, Y_W^* is related to the hydrodynamic drag on the log. Bocchiola et al. (2006) proved that at the threshold of motion, Y_W^* satisfies the following relation:

$$Y_W^* = \frac{1}{1 + C_D X_{S,R}^*} \tag{4.6}$$

where C_D is an entrainment drag coefficient and $X_{S,R}^*$ is a dimensionless force ratio that differs for sliding versus rolling cases. The term $X_{S,R}^*$ encapsulates the balance of forces, or moments, driving motion. In particular, Bocchiola et al. (2006) derived the following expressions for $X_{S,R}^*$ in the two modes (Eq. 4.7 holds for sliding, while Eq. 4.8 for rolling):

$$X_S^* = \frac{1}{2}\frac{U_w^2}{g L_{log}}(\cos\alpha \tan\emptyset - \sin\alpha) \tag{4.7}$$

$$X_R^* = \frac{1}{2}\frac{U_w^2}{g D_{log}}(\cos\alpha \tan\delta - \sin\alpha) \tag{4.8}$$

With, U_w the flow velocity (undisturbed by the log), g gravity, L_{log} the log's length, $\emptyset$ a sliding dry friction angle between the log and the bed, and α the slope of the channel.

In Eq. 4.8, D_{log} is the log's diameter, and δ is the rolling dry friction angle between the log and the bed.

Moreover, Bocchiola et al. (2006) acknowledged that the presence of a partially submerged log disturbs the local flow depth. The undisturbed flow depth h may not represent the water depth "felt" by the log. They introduced a representative depth, h_r, related to the Y_W^* parameter, and empirically related it to the undisturbed depth via an equation fitted to their experiments:

$$\frac{h_r}{h} = a_{S,R}\left(Y_W^{b_{S,R}}\right) \tag{4.9}$$

In which, a and b change with log's orientation therefore changes with the mode of entrainment mechanism (subscript $\underline{S}$ stands for sliding, R for rolling). These parameters are 0.84 and 0.77 for the rolling case, and 0.91 and 0.78 for sliding case.

By implementing this approach in the ORSA2D_WT, the entrainment module is enabled to model a sliding-rolling motion threshold in addition to a floatation threshold. The implementation of this approach is shown in the following paragraph.

4.2.1. Flotation threshold

The simplest entrainment mechanism is flotation, which occurs when buoyancy exceeds the log weight. This condition can be expressed through the relative buoyancy index, Y_W^*, as expressed in Eq. (4.5). Flotation occurs when Y_W^* exceeds unity, indicating the log is fully buoyant and moves without bed contact. However, the water depth around the log is disturbed as the log is immersed, which results in the buoyancy force to be less than that occurring under hydrostatic conditions. Chen et al. (2020)'s experiments results show an average flotation threshold of $Y^* = 1.24$, with the floatation threshold value increasing up to 1.26 for finer channel bed material, while with coarse bed material decreasing to 1.21. For the sake of simplicity, an average threshold of 1.24 was adopted in the model.

4.2.2. Sliding and rolling thresholds

The present model adopts the generalized stability criterion proposed by Chen at al. (2020), that modifies the original one suggested by Bocchiola et al. (2006) Eq. (4.6):

$$\mathrm{Y_w^*} = \frac{1.24}{1 + \mathrm{C_d X_{S,R}^*}} \tag{4.10}$$

where C_d is the entrainment drag coefficient and $X_{S,R}^*$ is the dimensionless ratio already presented (Eq (4.7) and (4.8)).

Frictional resistance plays an important role in both sliding and rolling thresholds. In ORSA2D_WT, friction coefficients were originally applied as static values depending only on bed material (e.g., wood–sand μ=0.47, wood–gravel μ=0.64 and μ=0.20 for smoother artificial beds such as wet metal) and the occurrence of static or dynamic friction (in entrainment or arrest conditions, respectively). These coefficients, derived from classical experimental studies (Ishikawa, 1989; Murase, 1984; Crosato et al., 2013), provided a practical way to distinguish between substrates, but did not incorporate the effects of log orientation. However, Chen et al. (2020) demonstrated that friction angles vary strongly with log orientation. A log initially parallel to the flow will require a higher friction angle to initiate its motion (typically $\varphi \approx$ 18–19°), consistently with sliding as the dominant

mode of entrainment. In contrast, when the log is initially oriented oblique or transverse to the flow direction it requires significantly lower friction angles ($\varphi \approx 5$–$9°$), reflecting the dominance of rolling as the governing motion process. Figure 4.3 illustrates this systematic decline in friction angle with increasing orientation, for the two tested bed-types, confirming that entrainment thresholds are strongly reduced when logs are not aligned with the flow.

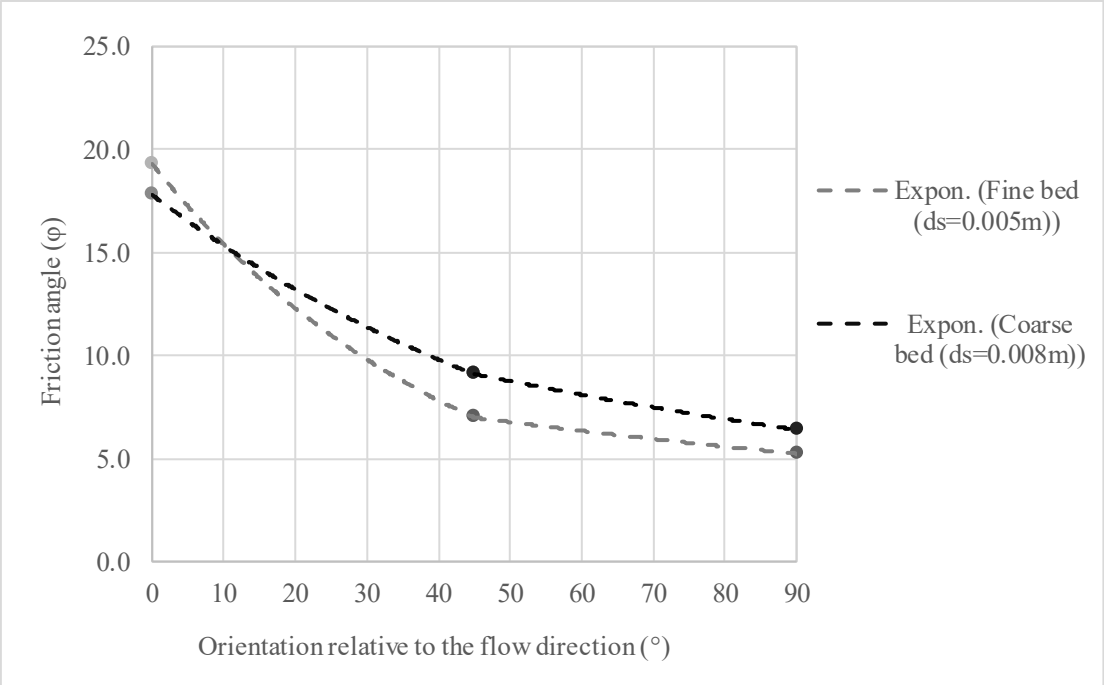

Figure 4.3 Friction angle values as found by Chen et al. (2020) for fine bed (in grey) and coarse bed (in black) materials in function of the log's orientation relative to the flow.

The drag coefficient, C_d, depends on a variety of factors including the orientation of the wooden element, its shape (the log can be represented by a regular smooth/rough cylinder, as well as a more complex element with branches and roots), the aspect ratio (length to diameter ratio), the Froude number, and the relative submergence of the element (Gippel et al., 1996). Several studies have analyzed the drag acting on LW under various flow and structural conditions (Abbe and Montgomery, 1996; Alonso, 2004; Braudrick and Grant, 2000; D'Aoust and Millar, 2000; Gippel et al., 1992; Gippel et al., 1996; Hygelund and Manga, 2003; Manga and Kirchner, 2000; Shields and Alonso, 2012; Shields and Gippel, 1995; Wallerstein et al., 2001, 2002). These studies report a wide range of drag coefficient values, reflecting differences in wood orientation, geometry, complexity, submergence, and flow conditions. For example, D'Aoust and Millar (2000) assumed a C_d of 0.3 when estimating anchoring thresholds for LW, whereas Hygelund and Manga (2003) measured field values as high as C_d = 3.0. Manners et al. (2007) reported C_d values reaching 9.0 for complex log jams in alpine rivers. Experimental studies have further emphasized the critical influence of

orientation on C_d. Morinaga et al. (2012) measured drag coefficients between 1.0–1.2 for vertical rooted logs. Shields and Alonso (2012) reported a broad range of C_d, from 0.05 to 1.29 for simple cylindrical forms and up to 6.27 for complex, non-cylindrical structures. In laboratory flume experiments, Persi et al. (2019a) found C_d values between 0.2 – 1.25 depending on the submergence ratio and the wooden logs orientation with respect to the flow. Similarly, Innocenti et al. (2023) found C_d values between 0.35–1.0 for wooden dowels tested at various orientations in sharp river bends. These findings underscore the strong dependency of C_d on orientation, with parallel alignment consistently yielding lower drag than perpendicular or oblique positioning. Additional factors such as blockage ratio, submergence level, flow unsteadiness, surface roughness, and log complexity further modulate drag forces on LW in riverine environments. The drag coefficient, incorporated in the model for entrainment as well as for the initial rolling and sliding motion, was experimentally determined using a hydrodynamic balance, as discussed in detail in Chapter 5.

The model adopted for entrainment under sliding or rolling modes is also employed to verify the arrest of rigid bodies, ensuring that the transition from motion to rest is consistently represented (the limits of this strategy, which does not consider the arrest due to the interaction with bed material or vegetation, have been already discussed in Section 3.4). For this reason, the incipient motion condition is evaluated at each computational time step, allowing the model to determine whether a body remains in motion under the prevailing hydrodynamic forces or comes to rest due to resisting forces. Overall, the improved formulation allows the simulation of LW motion through rolling and sliding under shallow-water conditions, before the flow depth becomes sufficient to initiate flotation. This enhancement reduces the systematic underestimation of entrainment thresholds that typically arise when models assume flotation as the sole mechanism responsible for the onset of motion. Finally, accounting for motion by sliding and rolling requires an update of the translational equation (Eq 3.6) to distinguish between the case of a floating log and that of a log moving in contact with the channel bed or banks. This distinction is essential, as the governing forces and resistance terms differ significantly between the two situations. Further details on the formulation and its implementation are provided in Section 4.4.

4.3. Numerical implementation of the entrainment and arrest model

The entrainment and arrest model in ORSA2D_WT built upon the classical force-balance approach (Braudrick and Grant, 2000; Bocchiola et al., 2006; Chen et al., 2020), was extended to account for both flotation and contact-driven motion (sliding and rolling). The procedure is performed at each computational time step, taking advantage of the body localization and subdivision strategies described in Persi (2018). The first step is the evaluation of the Y^* floatation parameter (Eq 4.5). To obtain a meaningful value, the representative water depth h is computed as the average of the local water depths evaluated at the center of mass of the four sub-segments into which the log is divided. This averaging procedure ensures that spatial variations of the flow field along the log's main axis are incorporated in the flotation criterion, thereby providing a more realistic estimate of the buoyant contribution acting on the body.

Then, if $Y^* \geq 1.24$ the LW element can float, the equations of translation and rotation are directly applied. Otherwise, if the condition is not satisfied, the element is either stable or mobilized through sliding or rolling depending on its initial orientation. In this case, the stability curve (Eq. 4.10) is evaluated. According to this criterion, a log is stable if the (Y^*, $X^*_{S,R}$) point lies below the stability curve defined by Eq. 4.10, otherwise, the hydrodynamic forces overcome resistance forces, and the log is entrained. In such conditions, the log is set in motion by sliding if it is initially aligned with the flow, or by rolling if it is oblique or perpendicular, and this motion persists until the water depth is sufficient to satisfy the flotation condition and buoyancy becomes the dominant mechanism.

An important parameter to determine the dimensionless drag to friction ratio $X^*_{S,R}$ (Eqs 4.7 and 4.8), is the friction angle. An orientation-dependent friction as proposed by Chen et al. (2020) was introduced by interpolating experimental data obtained for fine-bed (d_s = 0.005 m) and coarse-bed (d_s = 0.008m) conditions. To implement this in ORSA2D_WT, we adopted the average of fine- and coarse-bed results as a representative friction–orientation curve. This averaging reduces sensitivity to a particular bed material while preserving the observed decline in resistance with increasing orientation angle. A further extension was made to account for the full range of orientations from 0° to 360°, since in ORSA2D_WT logs can rotate freely during motion. To ensure continuity across the entire circle, the empirical functions derived from Chen et al. (2020) data were mirrored and fitted with exponential curves (Figure 4.4). This provides smooth periodic variation of friction angles, with maxima at 0° and 180° (parallel alignment) and minima around 90° and 270° (transverse alignment). In this way, the model accounts not only for the difference between parallel and transverse logs, but also for logs in any intermediate orientation.

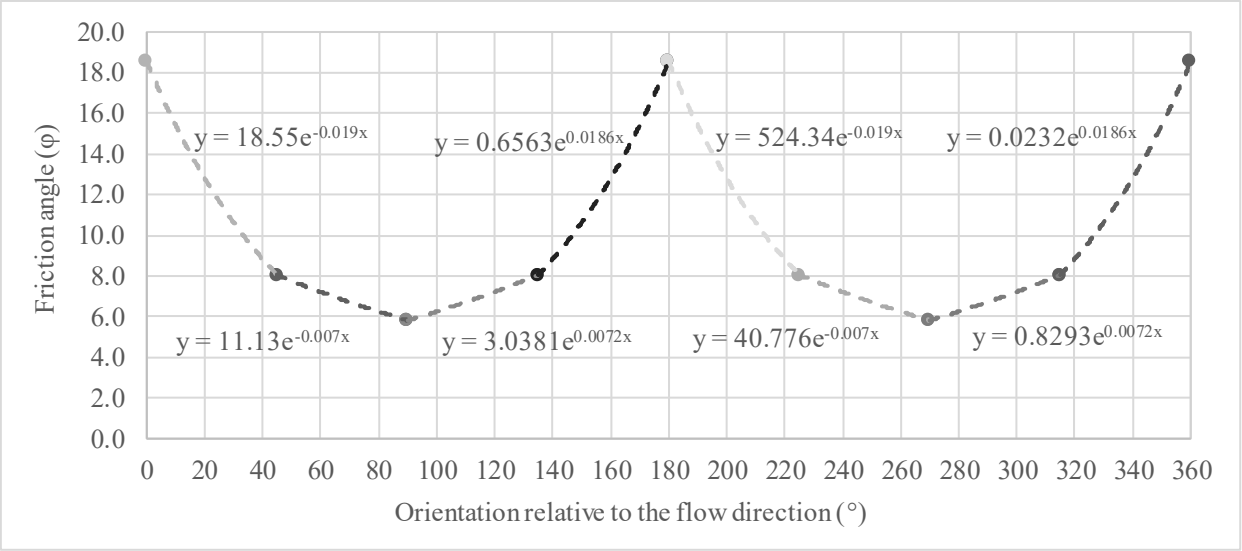

Figure 4.4 Averaged friction angle values as found by Chen et al. (2020) in function of the log's orientation relative to the flow.

4.4. Extension of the translation equations for rolling and sliding motion

In the original formulation of ORSA2D_WT (Persi, 2018), the translational equations of motion were written under the assumption that entrainment occurs primarily through flotation (Section 3.1.1). Once a log becomes buoyant, it is transported as a semi-submerged rigid body, and the governing force balance includes only hydrodynamic contributions. However, this assumption neglects the frequent occurrence of shallow-water conditions, in which LW remains in contact with the bed and moves through sliding or rolling. To account for these processes, the translational equations were updated to explicitly distinguish between two regimes:

1. Case (i): motion in contact with the bed (rolling/sliding), when the flotation index $Y^* < 1.24$ is not satisfied.
2. Case (ii): motion by flotation, when the log is fully supported by buoyancy $Y^* \geq 1.24$ and no longer interacts with the bed.

This distinction allows the model to dynamically switch between contact-driven motion and buoyancy-driven transport at each computational time step. When the log is partially submerged but not buoyant, it is supported by the channel bed and subjected to additional resistance forces. The translational balance therefore becomes:

$$\boldsymbol{F}_{total} = \boldsymbol{F}_D + \boldsymbol{F}_{AM} + \boldsymbol{F}_{PG} + \boldsymbol{F}_S + \boldsymbol{F}_G + \boldsymbol{F}_F \tag{4.11}$$

where $\boldsymbol{F}_G$ is the downslope component of the net body weight W (as expressed in Eq 4.12) on a bed with slope α and it is expressed as:

$$\boldsymbol{F}_G = \boldsymbol{W} \sin\alpha \tag{4.12}$$

Here α is the horizontal angle of the channel bottom.

$\boldsymbol{F}_F$ is the bed friction, expressed as a Coulomb-type resisting force, with the kinematic friction coefficient μ depending on the motion state.

$$\boldsymbol{F}_F = \mu\, W \cos\alpha \frac{\boldsymbol{V}_b}{|\boldsymbol{V}_b|} \tag{4.13}$$

and $\boldsymbol{V}_b$ being the velocity vector of the body. The kinematic friction coefficients were derived by first converting the static friction angles into a friction coefficient ($\mu = \tan(\delta, \emptyset)$, where δ is the static rolling friction angle and $\emptyset$ is the static sliding friction angle). These values were then reduced by 25% to account for the lower resistance during motion, following the procedure suggested by Murase (1984). Therefore, expanding Eq. (4.11), the translation equation implemented in the discrete element module of ORSA2D_WT in the case of bodies moving in contact with the bed becomes:

$$\begin{aligned}
&\left(m_b + \frac{1}{2} C_{AM} m_f\right) \frac{d\boldsymbol{V}_b}{dt} \\
&= \frac{1}{2} \rho_f C_D A \left(\boldsymbol{V}_f - \boldsymbol{V}_b\right) \left|\boldsymbol{V}_f - \boldsymbol{V}_b\right| \\
&+ \frac{1}{2} \rho_f C_s A \left(\boldsymbol{V}_f - \boldsymbol{V}_b\right) \left|\boldsymbol{V}_f - \boldsymbol{V}_b\right| \times \boldsymbol{i}_z \\
&+ \rho_f \left(1 + \frac{1}{2} C_{AM}\right) Vol \frac{D\boldsymbol{V}_f}{Dt} \\
&+ \boldsymbol{W} \sin\alpha - \mu\, W \cos\alpha \frac{\left(\boldsymbol{V}_f - \boldsymbol{V}_b\right)}{\left|\boldsymbol{V}_f - \boldsymbol{V}_b\right|}
\end{aligned} \tag{4.14}$$

where $\boldsymbol{i}_z$ is the unit vector normal to the 2D flow plane.

It is important to note that in the case of motion in contact with the bed, the hydrodynamic coefficients associated with drag (C_D) and side force (C_s) differ from those used for a log floating at the free surface (Persi et al., 2019a). This distinction arises because the boundary modifies the flow field around the log, altering the effective force coefficients. For the rolling–sliding regime, the coefficients adopted in the model were determined from dedicated experiments designed to measure the drag and side forces acting on semi-submerged cylinders in contact with a boundary. Further details on the experimental setup, methodology, and the resulting coefficients are presented in Chapter 5.

4.5. Modeling entrapment by vegetation

4.5.1. Large wood transport and entrapment by vegetation

Many studies highlight that a substantial portion of LW transported during floods is not carried indefinitely but is entrapped by features in the channel and floodplain, including living trees and dense vegetation. Wood tends to accumulate along channel margins and forested floodplain areas – the greater the contact between the active channel and woody vegetation, the more wood is retained (Gurnell et al., 2002). In medium-sized channels, for example, wood jams can form when smaller floating pieces lodge behind larger key obstacles (such as boulders or stable logs), and standing trees often serve as such key elements that capture mobile wood (Gurnell et al., 2002). Fundamentally, living woody vegetation (standing trees, shrubs) acts as a natural "filter" that can snag driftwood, greatly influencing how far wood travels during floods.

The height and density of riparian vegetation are critical factors in wood retention. Tall trees that protrude above floodwaters are particularly effective at arresting floating logs. If water depth remains below canopy height, the standing trees act as a physical barrier that wood cannot easily bypass, causing logs to pile up against trunks and branches. Indeed, researchers have hypothesized that live standing trees can snare drifting wood on the rising limb of a flood, effectively removing wood from transport before the peak flow occurs (Kramer and Wohl, 2017). By contrast, when vegetation is completely submerged by extreme floods, wood may overtop the canopy, reducing retention efficiency. Vegetation density likewise modulates trapping: a dense stand of trees or shrubs presents a tight network of obstacles that increases the probability of wood collision and capture, whereas widely spaced trees might let some logs pass through gaps. Field evidence supports this intuitive pattern. For instance, Beckman and Wohl, (2014) observed that when logs come in contact with stable elements like living trees or stumps on the banks, those logs tend to remain in place rather than continuing moving. Similarly, Galia and Máčka (2023) found that live trees and shrubs can pin a considerable fraction of the total wood load within channels (in some rivers, 15–30% of all LW volume was found lodged against living vegetation). However, that study also noted that the proportion of wood retained by vegetation does not increase in a simple linear way with vegetation density alone – the flood disturbance regime and site conditions also play a role. This suggests that while abundant riparian vegetation generally promotes wood retention, factors like flood magnitude, wood supply, and channel morphology interact with vegetation characteristics to determine actual outcomes.

A growing body of literature has documented the role of living vegetation in trapping LW during floods. Galia and Máčka (2023) conducted field inventories across 16 European river reach and demonstrated that woody vegetation is not only a source of wood recruitment but also "plays a crucial role as retention elements for mobilized wood during floods". They observed wood pieces of various sizes pinned against live trees and found that stable vegetated patches within the channel were hot spots for wood deposition. Interestingly, they did not find a strong bias in the size of wood that gets trapped – in most sites, the dimensions of wood caught by trees were not significantly smaller than free-floating pieces, implying that even quite large logs can be halted by vegetation given the right conditions. Earlier research by MacVicar and Piégay (2012), using video monitoring of wood transport, noted that live vegetation can intercept wood early in the flood hydrograph. Their observations indicate that entrapment by standing trees on floodplains may explain why wood transport often tapers off before the flood's peak flow – essentially, many logs get parked in the vegetated overbank areas as water rises, rather than continuing to travel with the highest discharge (Kramer and Wohl, 2017).

Physical experiments have reinforced these field findings by illuminating the mechanics of wood-vegetation interactions. For example, a recent flume study (Igarashi and Tanaka, 2024) simulated floating debris transport through a stand of model trees. The experiments showed that the first row of vegetation facing the flow can trap a high percentage of incoming wood, especially for denser (high specific gravity) logs which tend to ride lower in the water and get caught in the vortex formed in front of the trees. Once past the frontline trees, whether debris gets further detained within a vegetated patch depends on the debris' flexibility. Accounting for realistic LW deposition patterns is critical for both scientific understanding and practical management. Accurate models of wood dynamics need to reflect where wood actually comes to rest; otherwise, they risk misrepresenting how far wood travels, how jams form, and the resultant impacts on flood risk. In reality, LW is repeatedly stored and remobilized in a stop-and-go fashion through a river system. If we ignore the fact that a large quantity of wood ends up stranded along vegetated banks, islands, and floodplains during floods, we may overestimate the downstream wood flux and fail to predict local accumulations that can alter flow patterns. In terms of flood hazard, unrealistic wood deposition modeling can be dangerous: undetected wood jam locations might lead to unexpected backwater effects or structure blockages in real events. Thus, incorporating realistic deposition (e.g. wood trapping on floodplain trees) improves model accuracy in predicting both the LW transport trajectories and the feedback on flow. This is essential for designing mitigation measures (like bridge protection, wood retention structures) and for ecological restoration, where LW placement is used deliberately, in both cases, it is important to understand how and where LW naturally tends to accumulate.

4.5.2. Implementing entrapment by vegetation in ORSA2D_WT

In ORSA2D_WT, vegetation is represented via a Canopy Height Model (CHM) that gives the height of vegetation above ground. The CHM is derived from high-resolution terrain data: specifically subtracting the bare-earth Digital Terrain Model (DTM) from the surface model (DSM) which includes trees and structures. In practice:

$$CHM(x,y) = DSM(x,y) - DTM(x,y) \tag{4.15}$$

where the DSM is typically obtained from airborne LiDAR or photogrammetric surveys. This ensures CHM (x, y) represents the local vegetation canopy height at each horizontal coordinate (x, y). The resulting CHM raster is then overlaid on the ORSA2D_WT computational grid: each grid cell is assigned a CHM value (by computing the average within the cell). In fact, every model cell carries a vegetation height above ground. LW entrapment is then detected by comparing CHM and h (the average water depth at the center of mass of the wooden element). Intuitively, if vegetation protrudes above the water surface, it can snag logs; conversely if the flow submerges the vegetation, logs can float past. We therefore apply a simple rule-based criterion: a grid cell (x, y) is flagged as a potential LW entrapment zone whenever the vegetation height exceeds the water depth, i.e.

$$CHM(x,y) > h(x,y) \tag{4.16}$$

Equivalently, define a binary entrapment indicator

$$E(x,y) = \begin{cases} 1, & CHM(x,y) > h(x,y) \\ 0, & otherwise \end{cases} \tag{4.17}$$

Cells with E =1 are marked as entrapment cells. The overall algorithm can be summarized as follows:

1. Compute CHM**:** Derive a high-resolution CHM from LiDAR or similar data by Eq. (4.15). This raster gives the canopy height at each point.

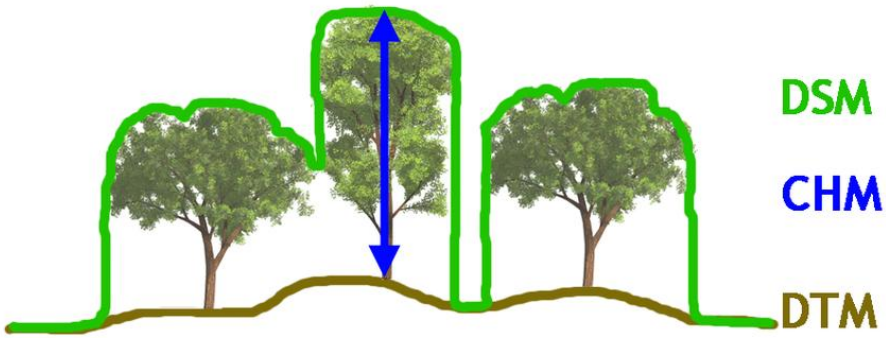

Figure 4.5 Representation of DSM, CHM and DTM.

2. Map to model grid**:** Interpolate CHM raster onto the ORSA2D_WT grid so that each grid cell (x, y) has a representative CHM value.
3. Entrapment criterion**:** At each time step the routine locate the LW element and evaluate if $CHM(x, y) > h(x, y) + D_{Log}$. If true, set the entrapment flag $E(x, y) = 1$; otherwise, $E(x, y) = 0$. In other words, a cell is flagged when its vegetation height exceeds the flood depth (logs would snag on vegetation above water).
4. Finally, if desired a spatial map of entrapment zones can be produced by plotting all cells with $E(x, y) = 1$. This binary raster or GIS layer highlight locations where LW is likely to accumulate due to vegetation.

Overall, the CHM -based rule provides a simple first-order estimate of where LW may be entrapped by vegetation. It assumes rigid, fixed vegetation (non-erodible trees/shrubs) and neglects finer factors like wood-vegetation drag and debris bridging. Nevertheless, by incorporating actual canopy heights in ORSA2D_WT, this method yields a simple estimation of potential LW retention and entrapment. Such entrapment mechanism can enhance risk assessments (e.g. where woody jams may block channels) and guide the placement of mitigation measures under specific flood scenarios.

Chapter 5

Hydrodynamic coefficients of bodies under rolling–sliding motion

5.1. Abstract

This chapter focuses on the experimental quantification of hydrodynamic coefficients governing LW motion under rolling–sliding conditions. Recent studies have demonstrated that drag and side coefficients parameters are strongly dependent on bed proximity. To address this limitation, a series of controlled flume experiments were conducted using a dedicated hydrodynamic balance to directly measure drag and side forces acting on cylindrical wooden dowels under varying orientation conditions. The experimental design is presented in detail, including channel configuration, flow conditions, calibration procedures, and measurement strategy, ensuring reproducibility and reliability of results.

The experiments provide systematic datasets of hydrodynamic coefficients for different log orientations relative to flow, highlighting their non-linear variability with angle and bed proximity. Results confirm that drag coefficients are minimized when logs are aligned with the flow and maximized when oriented transversely, while side-force coefficients increase significantly under oblique configurations. Furthermore, the influence of bed proximity was found to alter force distributions, with near-bed conditions amplifying resistance forces compared to fully floating configurations. These findings demonstrate that the assumption of constant coefficients in existing modelling approaches is inadequate for capturing the complexity of LW dynamics. The measured coefficients are subsequently analyzed, discussed in the context of existing literature, and interpolated to provide parameterizations suitable for numerical implementation in the ORSA2D_WT model. By supplying empirically derived values for drag and side forces, this chapter establishes an experimental foundation for model calibration and validation.

5.2. Experimental set-up

5.2.1. Channel characteristics

The experimental campaign was performed in a laboratory flume at the Hydraulics division of the Department of Civil Engineering and Architecture (DICAr) at the University of Pavia. The flume (Figures 5.1 and 5.2) has a total length of 6.00 *m* and a width of 1.00 *m*, with a horizontal metallic bottom and Plexiglas sides of 0.70 *m* height. Steady free-surface flow was established under controlled laboratory conditions. Upstream of the flume, the head tank collects water delivered by the hydraulic pumps. The supply conduit feeding the tank is equipped with a valve (Figure 4.3), which allows precise regulation of the inflow and consequently of the flow depth required for the tests.

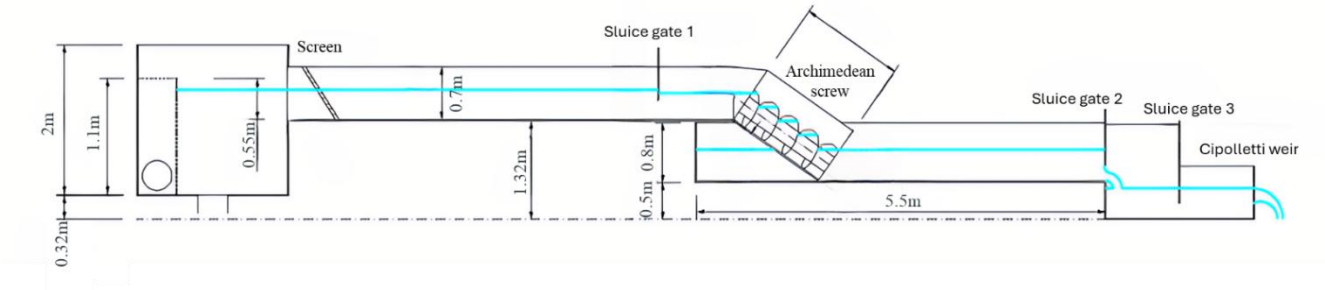

Figure 5.1 Longitudinal section of the channel used for the experiment.

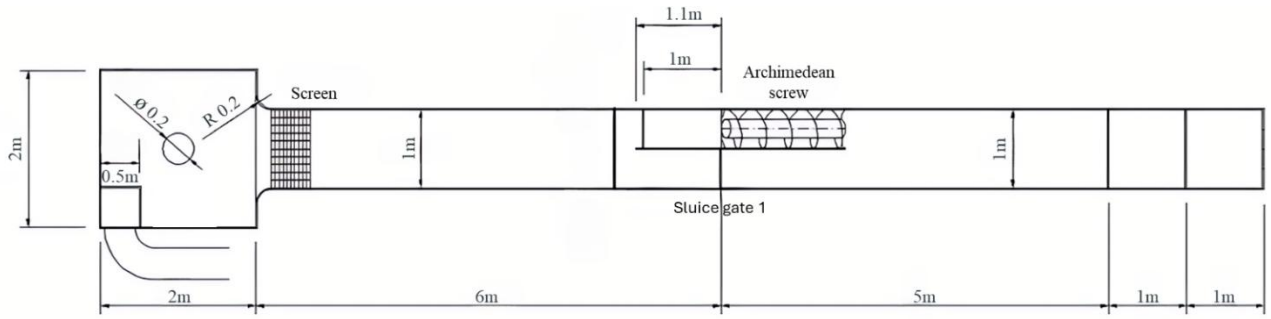

Figure 5.2 Plan view of the channel used for the experiment.

The discharge was measured using a Cipolletti weir located downstream of the flume. At the beginning of each test, the head above the weir crest was recorded, and the flow rate was determined using the standard Cipolletti equation:

$$Q = 0.415L\sqrt{2g}H^{\frac{3}{2}} \tag{5.1}$$

where:

- Q is the discharge [$l\ s^{-1}$],
- L is the crest length of the Cipolletti weir [m],
- H is head above the crest [m],
- g is the gravitational acceleration (9.81 $m\ s^{-2}$).

Knowing Q, and with the imposed water depth h in the channel and its width B, the mean velocity can be obtained as:

$$V = \frac{Q}{A} = \frac{Q}{hB} \tag{5.2}$$

5.2.2. The Hydrodynamic balance

The hydrodynamic balance (Figure 5.3a) is a lever-based force transducer specifically designed to measure the horizontal hydrodynamic forces on a submerged cylindrical body in an open-channel flow (Persi et al., 2019a). In particular, it measures the drag force (parallel to the flow) and the side (cross flow) force acting on the cylinder. The balance is mounted on the flume support frame: a horizontal aluminum beam and two vertical guide columns hold the balance in position and allow its height (submergence) to be adjusted. A steel plate at the base carries a spherical joint that serves as the lever fulcrum (Figure 5.3c). From this fulcrum a connecting vertical rod protrudes into the flow, supporting the test cylinder at its downstream end. The connecting rod itself is made in two segments to minimize flexure and flow disturbance. The upper segment (nearest to the fulcrum) is a steel bar 10 mm in diameter and 0.10 m long; the lower segment is aluminum, 6 mm in diameter and 0.29 m long, with a threaded end to attach the cylinder. The bar diameters were chosen to keep the lever stiff under the largest expected forces. The aluminum tip is relatively thin to reduce blockage effects and local disturbance of the flow around the cylinder. Above the spherical fulcrum, a custom 3D-printed loading block ("presser") is fixed to the steel bar, roughly 0.08 m upstream of the joint. This presser transmits the net horizontal forces from the cylinder into four L-shaped lever arms. Each of these four vertical levers converts the horizontal input force into a vertical load on an underlying load cell. In other words, the horizontal drag or side forces acting on the cylinder cause the presser to push on the L-levers, which then pull up or push down on the load cells. Because the Phidgets load cells are sensitive only to vertical loading, this lever geometry ensures that each cell experiences a vertical strain proportional to either the drag or side component of the force. Four micro-load-cells (Phidgets 0–780 g shear cells) are arranged in a square layout under the four levers. These miniature load cells each have a full-scale capacity of 780 g (~7.65 N) and high sensitivity: manufacturer data report creep

of only about 1.6 g/hour and repeatability error on the order of ±0.39 g. The load cells are mounted on independent 3D-printed bases and oriented horizontally so that the L-levers apply vertical loads to them. In practice, cell 2 (the "drag cell") reacts almost exclusively to the streamwise (drag) force, while cells 1 and 3 (the "side cells") capture the transverse component of force. The fourth cell (cell 0) is left unloaded by flow forces and instead serves as a structural stabilizer to prevent any lateral shifting of the mechanism. In this way the drag and side forces are effectively decoupled: the drag cell and one side cell are mechanically independent, and the pair of side cells share the lateral load symmetrically.

All four load cells connect to a single Phidget Bridge 4-input interface board. This 24-bit analog-to-digital converter allows sampling of each channel. A MATLAB script (using the Phidgets libraries) controls the acquisition: the user sets the test duration (typically ~30 s) and the sampling interval (e.g. 8 ms per sample) via the software. During a run, the bridge outputs real-time digital voltage ratios (mV/V) from each cell. These voltage signals are recorded, averaged on the test duration and later converted to forces using the calibration curves.

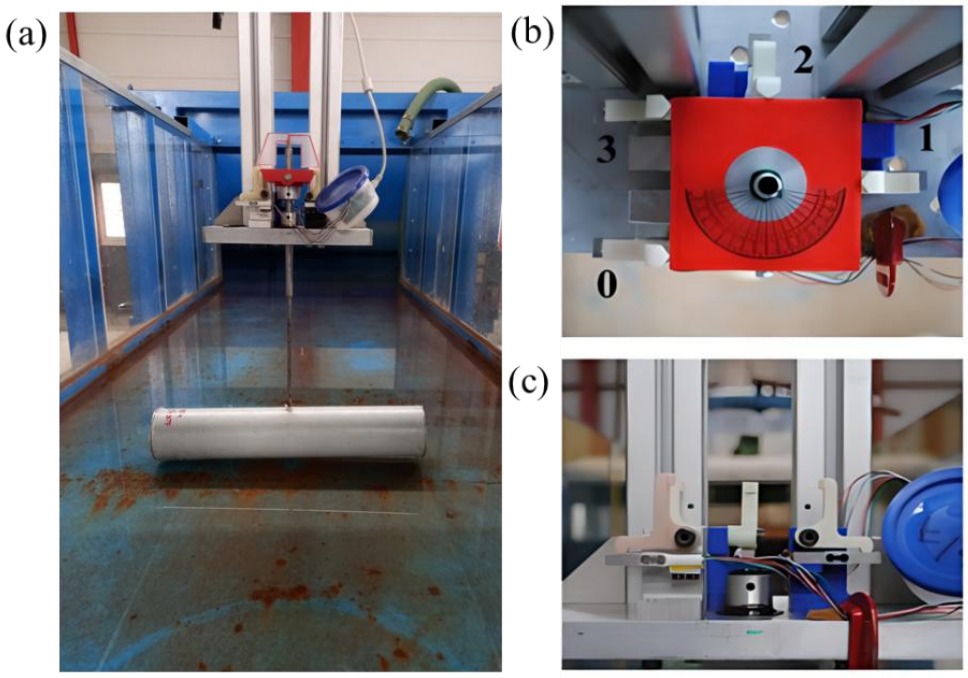

Figure 5.3 (a) the hydrodynamic balance and test model set up; (b) look closer on the configuration of the load cells; (c) the presser with cells that measure the drag and side forces.

5.2.3. Configuration of the experiment

The experimental setup employed a smooth plastic cylindrical model with a length of $L = 0.42\ m$ and a diameter of D = 0.08 m. Throughout the campaign, flow conditions in the flume were kept constant, maintaining a steady, subcritical regime. The cylinder was tested at different orientations relative to the main flow direction: 0° (axis parallel to the flow), 20°, 45°, 70°, and 90° (axis perpendicular to the flow). These yaw angles were selected to capture the effect of orientation on the hydrodynamic forces. The cylinder was suspended above the flume bed (Figure 5.4), leaving a gap $g = 1$ cm between the model and the bottom: this was essential to reproduce conditions as close as possible to those of a log moving in contact with the channel bed, while avoiding direct mechanical interference. Placing the cylinder directly on the bed would have introduced static friction and potential irregular contact points, which would compromise the accuracy of force measurements. By maintaining a small clearance, the cylinder behaved as a semi submerged body in very shallow water conditions in proximity of a boundary element, isolating the hydrodynamic contribution of the flow itself.

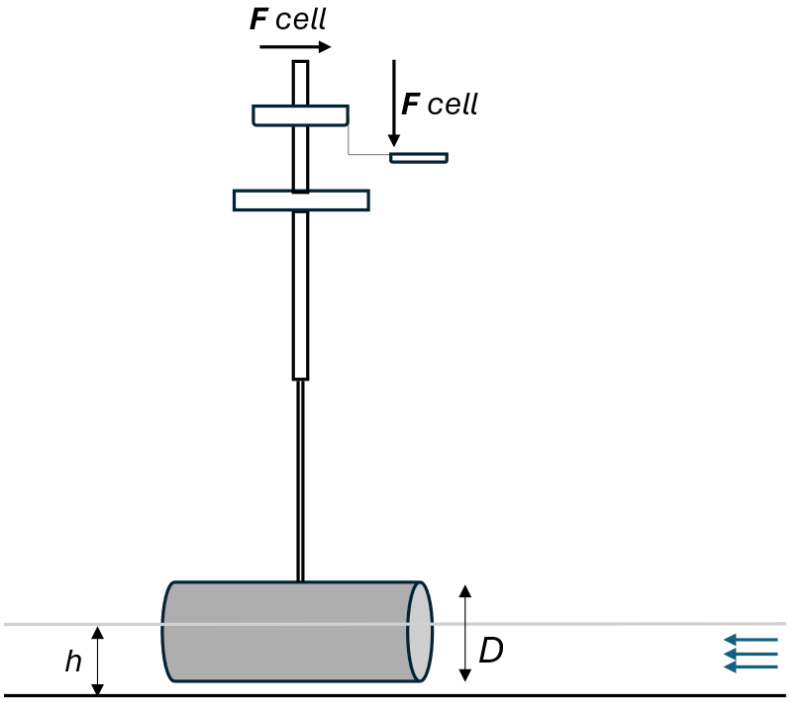

Figure 5.4 Configuration of the experimental setup.

5.3. Experimental campaign

The evaluation of the hydrodynamic coefficients was conducted under well-controlled laboratory conditions, maintaining a constant discharge and uniform flow depth while systematically changing the orientation of the cylindrical model. Prior to the measurement phase, the hydrodynamic balance underwent calibration through the application of known static loads in predefined directions, which ensured both the correct alignment of the system and the activation of the individual load cells. From this procedure, calibration curves were derived, providing a linear correspondence between the electrical response of the cells (mV/V) and the applied force. Once this relationship had been established, the actual experiments were carried out: the hydrodynamic forces acting on the cylinder were recorded in real time, and these values were subsequently used to calculate the drag and side force coefficients.

5.3.1. Hydrodynamic balance calibration

Prior to testing, all four load cells of the hydrodynamic balance were calibrated individually. The calibration was done under static, stable conditions (with the balance fixed and no water flow) to avoid any transient or vibrational effects. Known masses (in increments, 10 g, 20 g, 50 g, 100 g and 200 g) were applied at each cell lever arm, and the cell output voltage was recorded (normalized per volt of excitation, in mV/V) for each load. In each trial the signal was let to stabilize and was averaged (over ~30 s). This process establishes a one-to-one correspondence between applied force and measured voltage. The calibration curves exhibit a high degree of linearity and repeatability. For instance, the results obtained for Cell 1 (Figure 5.5) show that all five calibration runs fall almost perfectly along a single straight line, confirming that the sensor response remains consistent across repeated trials. The scatter of data points is minimal, and the linear regressions yield coefficients of determination of approximately $R^2 \approx 0.9895$. The calibration results for the four load cells are reported in Table 5.1.

Table 5.1 Calibration equations, with y is the cell response in mV/V and x is the applied force in N.

Cell ID	Fitting Equation	R^2
0	$y = 0.4015x + 0.2168$	0.9992
1	$y = 0.3344x + 0.1718$	0.9895
2	$y = 0.3172x - 0.0456$	0.9999
3	$y = 0.3624x + 0.0528$	0.9997

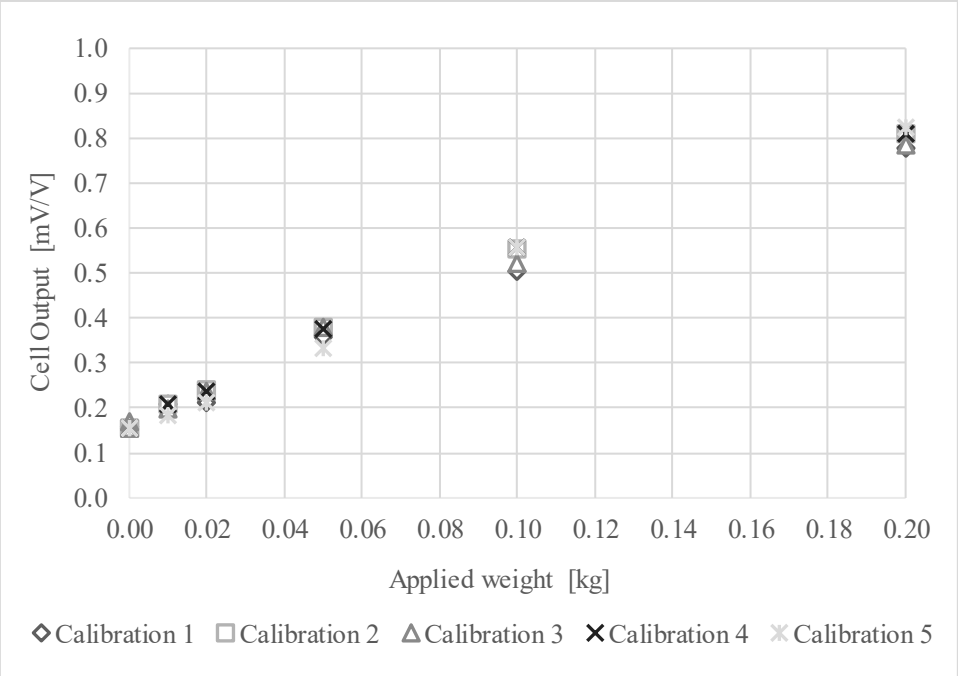

Figure 5.5 Calibration curves for hydrodynamic balance Cell 1 (output voltage vs. applied weight) from five separate static calibration trials.

5.3.2. Drag and side force measurements

Drag (F_{drag}) and side (F_{side}) forces on the test cylinder were recorded at each yaw orientation (0°, 10°, 45°, 70°, and 90°) under the same steady flow conditions. In this setup, one load cell (Cell 2) directly measured the force component aligned with the flow (drag), while two lateral cells (Cells 1 and 3) measured transverse forces. The voltage signals from the balance were converted to physical forces using the calibration curves, and the net side force was obtained from the calibrated difference of the lateral-cell responses. As previously reported, the test cylinder (L = 0.42 m, diameter D = 0.08 m) was mounted in a semi-submerged position and suspended above the smooth metallic bed of the flume, leaving a gap G= 1 cm. During each test run, the hydraulic parameters were held constant as summarized in Table 5.2. These fixed parameters ensured that all measurements were taken under identical hydraulic conditions. In particular, the submergence rate $S = \frac{h-G}{D}$ of the log was kept fixed at a value of 0.375.

Table 5.2 Experimental flow conditions.

Discharge	Q [$\boldsymbol{m^3 s^{-1}}$]	0.0068
Water level	h [m]	0.0400
Water velocity	V [$m\,s^{-1}$]	0.1723
Blockage ratio	B [%]	0.4286
Froude number	Fr [-]	0.2750
Particle Reynolds number	Rep [-]	13780

For each yaw angle, drag and side forces were averaged over the steady portion of the acquisition window. The mean voltage outputs were converted to forces via the calibration equations, and the resulting F_{drag} and F_{side} values were then used to compute the corresponding coefficients. The non-dimensional coefficients were determined using the standard definitions:

$$C_D = \frac{F_{drag}}{\frac{1}{2}\rho_f V^2 A_b} \tag{5.3}$$

$$C_S = \frac{F_{side}}{\frac{1}{2}\rho_f V^2 A_b} \tag{5.4}$$

where ρ_f is the water density, V is the mean velocity, A_b is the longitudinal section area of the entire cylinder (diameter times length, not only the submerged part). Note that F_{side} was computed as the difference between the measured forces $F_1 - F_3$, thus providing positive side coefficient if the resulting force is directed towards the hydraulic right.

5.4. Analysis of the results

The experiments yielded clear evidence of the strong dependence of hydrodynamic coefficients on the yaw orientation of the cylindrical log model. Forces were measured at the five tested angles (0°, 20°, 45°, 70°, and 90°) under identical flow conditions. Table 5.3 reports the mean drag and side coefficients, while Figures 5.6–5.7 present their distribution and variability.

Table 5.3 The resulting mean drag and side coefficients with respect to the orientation relative to the flow.

Orientation relative to the Flow (°)	Mean C_D	Mean C_S
0	0.23	0.05
20	0.63	1.29
45	1.08	1.47
70	1.56	0.86
90	1.82	0.03

The drag coefficient increased monotonically with angle (Figure 5.6), from a minimum of 0.23 at 0° to a maximum of 1.82 at 90°. This trend directly reflects the variation in projected frontal area exposed to the flow: when the cylinder is parallel, only the edge section interacts with the flow, whereas at 90° the entire length is exposed, producing much higher resistance. Intermediate values of C_D (0.63 at 20° and 1.08 at 45°) show a nonlinear rise, with the most pronounced growth occurring between 45° and 70°. The boxplots (Figure 5.8) confirm this behavior. At 0° and 90°, the interquartile range (IQR) is narrow, and variability is low, indicating highly repeatable measurements in symmetric configurations. At 20°–70°, the IQR widens, showing that drag is more sensitive to small fluctuations

in flow alignment and turbulence when the cylinder is oblique. The side coefficient displayed a markedly different pattern, characterized by a bell-shaped distribution (Figure 5.7). At 0° and 90°, values were negligible (≈ 0.0), as the flow around the cylinder is symmetric. At intermediate orientations, significant lateral forces developed, peaking at 45° ($C_S = 1.45$). At 70°, C_S decreased to 0.86, reflecting a partial restoration of symmetry as the cylinder approached the perpendicular configuration. The boxplots (Figure 5.9) highlight variability of these oblique-angle forces. At 20° and 45°, the medians are high but the IQRs are broad, indicating that small misalignments or transient vortices can substantially alter the magnitude of the side force. At 70°, the IQR narrows, but occasionally negative outliers appear, corresponding to momentary force reversals.

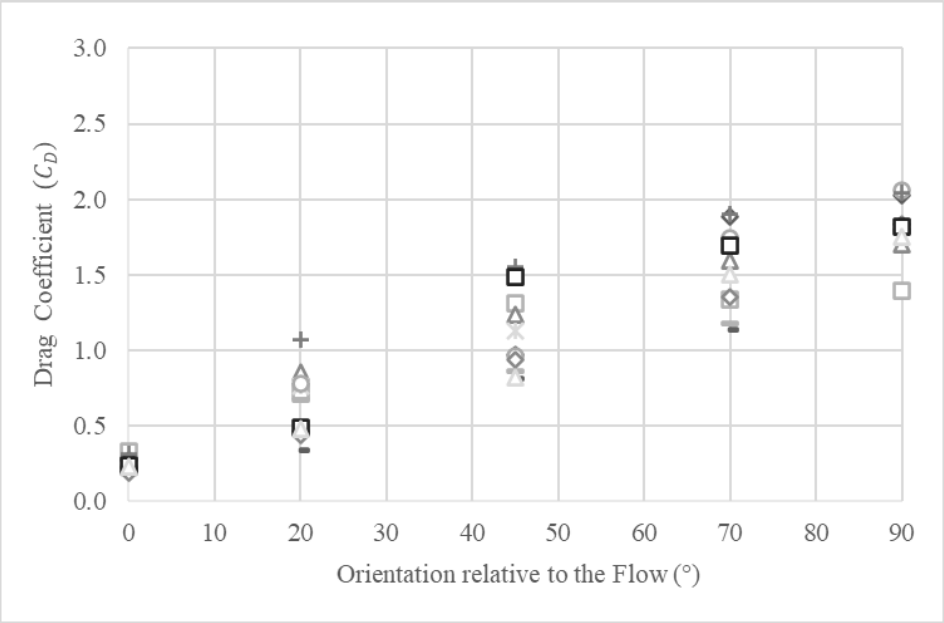

Figure 5.6 Measured drag coefficients for the different experimental trials as a function of the orientation relative to the flow.

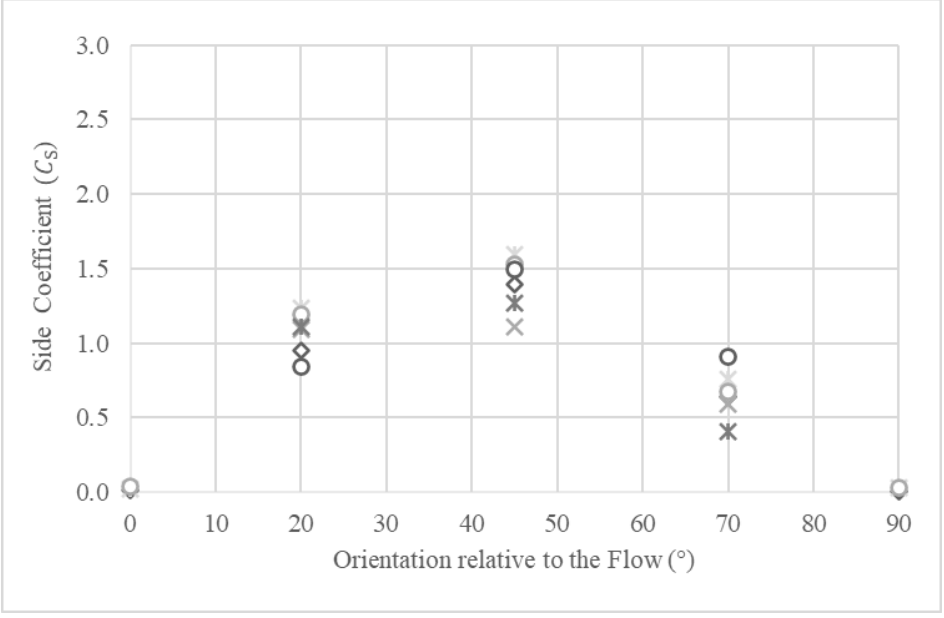

Figure 5.7 Measured side coefficients for the different experimental trials as a function of orientation relative to the flow.

The one-way ANOVA confirmed that the orientation angle has a statistically significant effect on both drag and side coefficients. For C_D, the analysis yielded $F = 118.37$ with $p < 10^{-27}$, far exceeding the critical value $F_{crit} = 2.53$, confirming that drag systematically increases with angle. For C_S, the ANOVA also showed a highly significant dependence on the orientation relative to the flow ($F = 36.50$ with $p < 10^{-13}$), consistent with the observed bell-shaped distribution. The larger within-group variance for C_S reflects the stronger sensitivity of lateral forces to small perturbations at oblique orientations. These results statistically validate the visual trends observed in Figure 5.7.

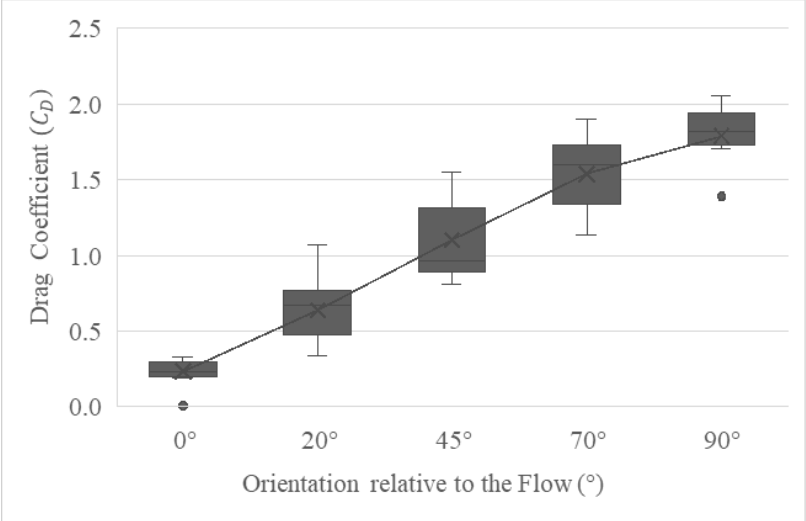

Figure 5.8 Box-and-whisker representation of experimental drag coefficient at different orientations relative to the flow.

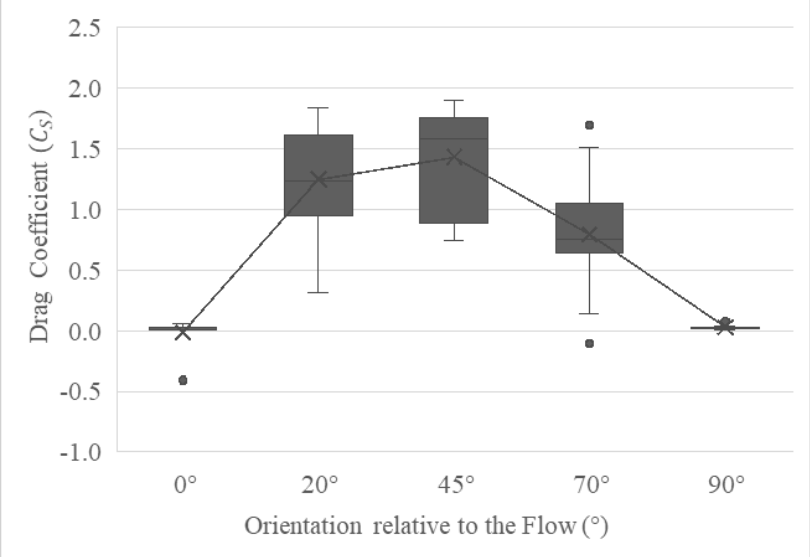

Figure 5.9 Box-and-whisker representation of experimental side coefficient at different orientations relative to the flow.

5.5. Discussion and Validation

The experimental results presented in Section 5.4 demonstrate a consistent dependence of hydrodynamic coefficients on the orientation of the cylindrical model, confirming the fundamental role of yaw angle in controlling the onset of rolling–sliding motion of LW (Bocchiola et al., 2006). The hydrodynamic force coefficients depend strongly on flow depth, LW orientation, and bed proximity. Measured drag coefficients (C_D) for floating logs or surface-piercing cylinders vary widely in the literature, typically from 0 (0.1) to several units, reflecting differences in submergence, geometry and flow condition (Persi, 2018; Persi et al., 2019a). For smooth cylinders under steady open-channel flow, studies report $C_D \approx 0.2$–1.3 (aligned to transverse to flow) for moderate Froude numbers. For example, Persi *et al.* (2019a) measured C_D rising from ≈ 0.2 at 0° to ≈ 1.25 at 90° yaw for half-submerged cylinders. Shields and Alonso (2012) summarize similar laboratory findings: simple cylindrical logs have C_D up to ≈ 1.3–1.5 (higher values occur only for complex branching logs). Field measurements often report higher apparent C_D (e.g. Hygelund and Manga (2003) found values as high as 3.0 for partially buried logs), but these include additional form and blockage effects. Side force (lateral) coefficients (C_S) are less frequently tabulated, but yaw-angle tests indicate that C_S can be of order unity for oblique orientations. Alamayreh et al. (2021) and Persi et al. (2019a) report C_S values peaking near 45° (oblique cylinder) with magnitudes ~0.5–1.5. Therefore, orientation (yaw angle) exerts a dominant control on both drag and transverse forces. Almost all studies find that in-line drag increases monotonically with yaw angle: C_D is smallest when the cylinder axis is aligned with the flow (0°) and largest at crossflow (90°). This trend reflects the changing projected area: when $\theta = 0°$ the cylinder presents only its small end section to the flow, whereas at $\theta = 90°$ its full side it is exposed. Persi et al. (2019a) explicitly observed this behavior under varying submergence, noting that the drag coefficient is at its maximum for a configuration perpendicular to the flow, due to maximum flow deviations. By contrast, the transverse or side-force coefficient C_S exhibits a nonmonotonic (bell-shaped) dependence on yaw. At $\theta = 0°$ or $\theta = 90°$ the flow is symmetric, and the side force is essentially zero; at intermediate yaw the flow around the cylinder is asymmetric, producing a net lateral force. Experiments consistently show a peak C_S around $\theta \approx 45°$. Persi et al. (2019a) reported that the side coefficient reach its max value at 45° orientation, where the flow is most asymmetrical. In the present tests C_S peaked at ~1.47 at θ = 45° (Table 4.3) and declined toward zero at 0° and 90°. This agrees with the literature trend: oblique cylinders generate the largest lateral force. The magnitude of C_S in experiments is typically on the order of 0.5–1.5 for moderate yaw; our values (≈1.3 at 20°, ≈1.5 at 45°) are in line with these observations. Shields and Alonso (2012) likewise noted that aligned logs exhibit very low drag and lateral forces, whereas tilted logs can encounter much larger forces due to the increased frontal area and asymmetric wake. Statistical

analysis of our data (ANOVA) confirms the strong, significant effect of yaw on both C_D and C_S. In summary, both past studies and our experiments find that: (a) drag increases monotonically from 0° to 90°, and (b) side force peaks near 45°. Our measured coefficients don't fall within the ranges of reported coefficients for semi submerged cylinders mainly due to differences in bed proximity: e.g., D'Aoust and Millar (2000) assumed C_D≈0.3 for logs aligned with flow, and laboratory studies report C_D≈0.2 at 0° and C_D≈0.6 at 90° (Persi et al., 2019a) for the case of floating semi submerged cylinders. Likewise, maximum C_S in the order of 0.3-0.5 is a common finding (Alamayreh et al., 2021; Hoang et al., 2015; Persi et al., 2019a). The consistency of these trends across different experiments supports the validity of our results. Furthermore, many studies also emphasize that proximity to the bed strongly modifies hydrodynamic coefficients. Two main effects arise: bed shielding when the cylinder is close to or touching the bed, and flow blockage when the flow depth is shallow relative to the cylinder diameter. In the case of fully submerged cylinders, the drag coefficient generally decreases as the gap between the body and bed plane decreases. Tong et al. (2018) report that C_D grows with increasing gap G, reaching an upper plateau equal to the free-flow value, and that C_D actually peaks at a moderate gap (G ≈ 0.5D) before dropping sharply to below 50% of the free-water value when G ≈ 0. In other words, a cylinder fully in contact with the bed experiences much lower drag (only around a half) than the same cylinder lifted above the bed. Similarly, Sumer and Fredsøe (1997) describe a "sheltering" effect: a pipe embedded in a trench can suffer a significant drop in drag because the bed shields it from flow. These findings suggest that logs that are fully submerged resting on the bed will experience reduced C_D relative to floating cases. The same trend was observed from the experiments conducted by Persi (2018) when comparing her results of a fully submerged circular cylinder with *G/D*=3.2 and *G/D*=5, respectively. When the cylinder was parallel to the flow, the gap didn't really affect the drag coefficient ($C_D \approx 0.2$), however in the case of a cylinder perpendicular to the flow, the effect of the gap from the bed plane was evident, with drag coefficient increasing with increased gap. In contrast, the present experiment investigated a semi-submerged cylinder positioned close to the bed with a shallow depth ratio (h/D = 0.5 and G/D = 0.12). Under these conditions, the results reveal the opposite trend: both drag and side force coefficients increase when the cylinder is near the bed compared to values reported for floating or half-submerged cylinders in deeper flow as by Persi et al. (2019a). Figures 5.10 and 5.11 compare the current results with the latter, the measured values being consistently higher under similar orientations. The drag coefficients increase with the decreasing depth ratio, this effect being especially pronounced when the cylindrical element is perpendicular to the flow, with an increase of 66%. The same trend is observed for the side coefficient, with a max increment of 79% at 45°. This effect can be attributed to strong near-bed confinement and shallow water effects. This finding is supported by Alamayreh et al. (2021), who proved through

numerical simulations that reducing the depth ratio (h/D) from 6 down to 1 cause both drag and side coefficients to increase more than linearly. They attributed this result to flow constriction beneath the cylinder, which accelerates the flow, intensifies pressure differences, and strengthens vortex shedding. Since our experiments were conducted at $h/D = 0.5$, an even more confined regime than those tested by Alamayreh et al. (2021) the increase in both drag and side coefficients aligns with their conclusions.

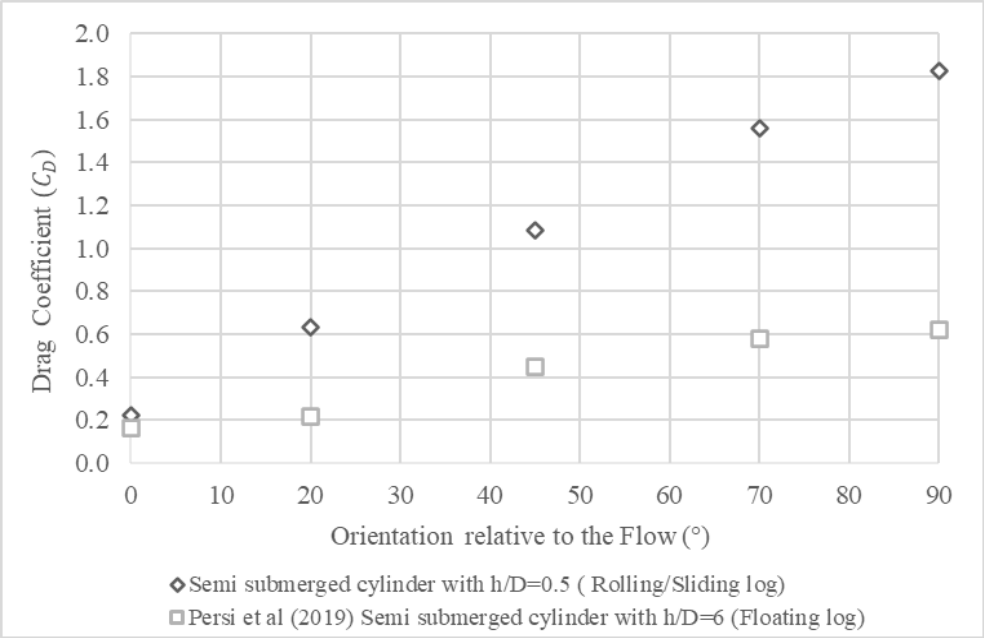

Figure 5.10 Comparison of drag coefficient as a function of orientation angle relative to the flow.

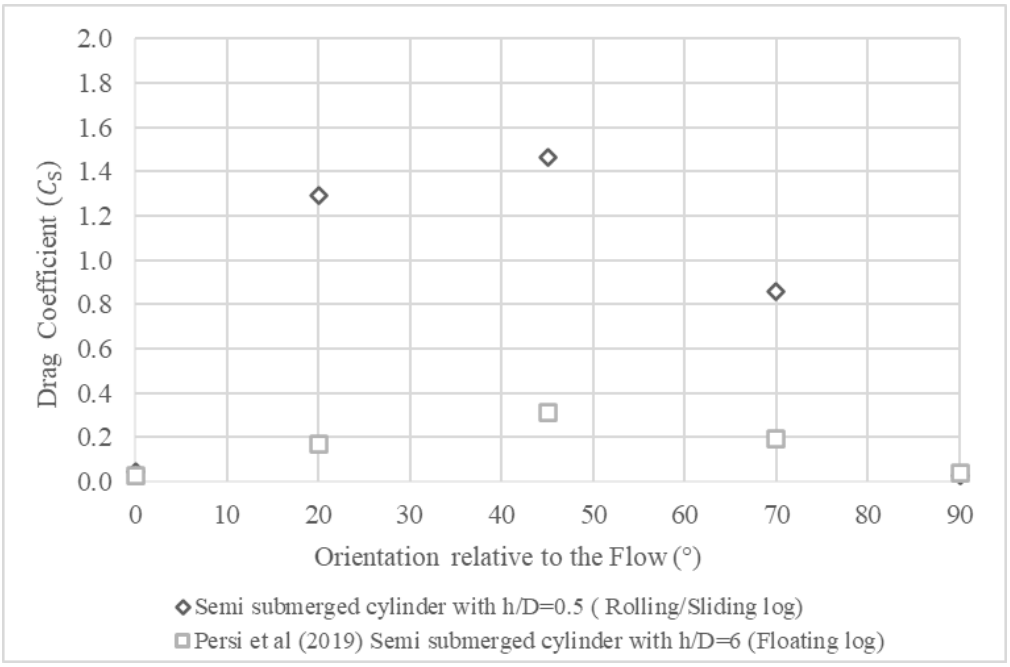

Figure 5.11 Comparison of side coefficient as a function of orientation angle relative to the flow.

5.6. Drag and Side coefficients implemented in ORSA2D_WT

In ORSA2D_WT, the hydrodynamic coefficients implemented for LW transport are conditioned by the prevailing transport mechanism. In situations of very shallow water, when LW elements are predominantly mobilized through sliding or rolling along the bed, the coefficients adopted are those obtained from dedicated laboratory experiments carried out with a semi-submerged cylindrical element near a plane bed. These experimental conditions are representative of near-bed transport, where contact forces and partial immersion strongly influence hydrodynamic behavior.

For the drag coefficient, the variation with respect to the angle of incidence of the element is represented by a linear interpolation of the experimental data:

$$C_D(\vartheta) = \ 0.0179\vartheta + 0.2565 \tag{5.5}$$

as shown in Figure 5.12. This approach ensures a continuous transition between measured values while maintaining consistency with observed physical behavior. To allow for full angular representation during simulations, Eq. (5.5) is extended beyond the experimental range of $0° \leq \vartheta \leq 90°$, up to 360° (Figure 5.13). This extension assumes periodic symmetry, thereby enabling the model to compute drag for any arbitrary orientation of the LW element within the computational domain.

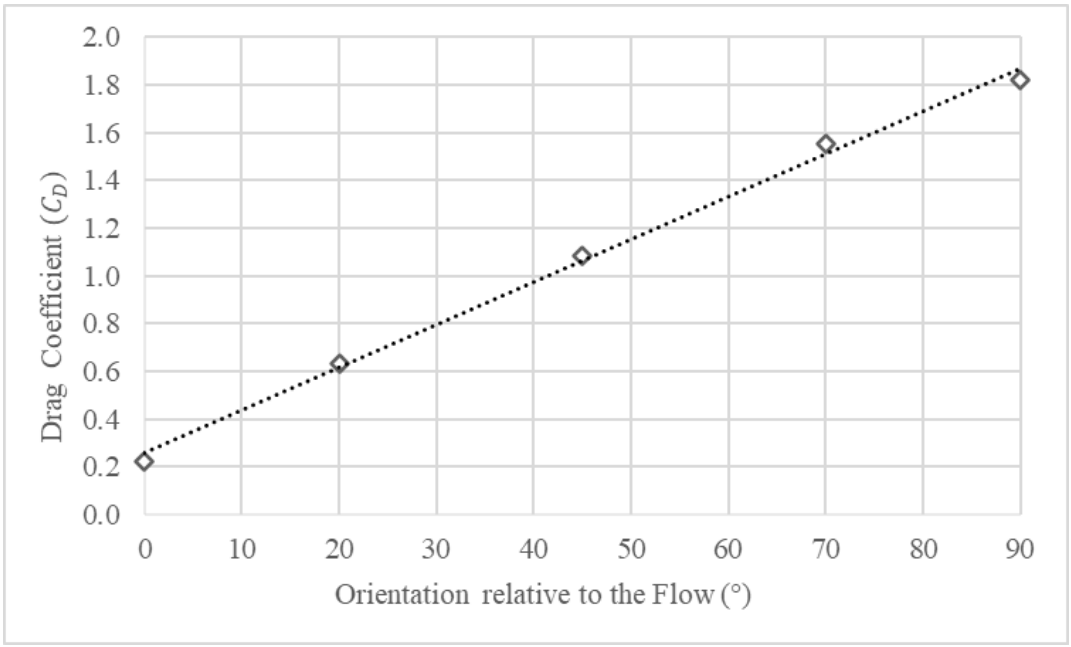

Figure 5.12 Interpolation of the drag coefficient for a semi-submerged body near a plane bed with a linear function.

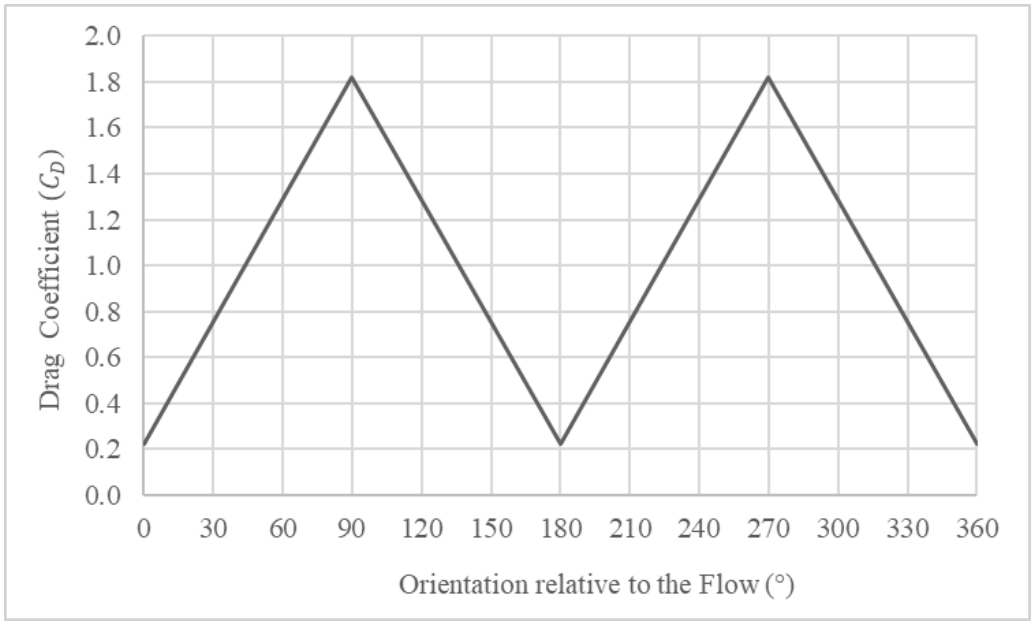

Figure 5.13 Implementation of the drag coefficient for a semi-submerged body near a plane for relative angle from 0° to 360°.

For the side coefficient, the response with orientation is inherently non-linear and exhibits pronounced peaks at intermediate angles. To accurately capture this behavior, a fourth-order polynomial interpolation of the experimental data is employed

$$C_s(\vartheta) = -6 \times 10^{-8}\vartheta^4 + 2 \times 10^{-5}\vartheta^3 - 0.0021\vartheta^2 + 0.0981\vartheta + 0.0478 \qquad (5.6)$$

as shown in Figure 5.14. This method provides a smooth curve across the full angular range while reproducing the observed maxima, thereby ensuring numerical robustness in the implementation. As with the drag coefficient, the side coefficient formulation is extended up to 360° (Figure 5.15). To remain consistent with the physics of the problem, the side coefficient is constrained to zero at angles corresponding to purely parallel (0°, 180°, 360°) or perpendicular (90°, 270°) orientations with respect to the flow, where no net side force is expected.

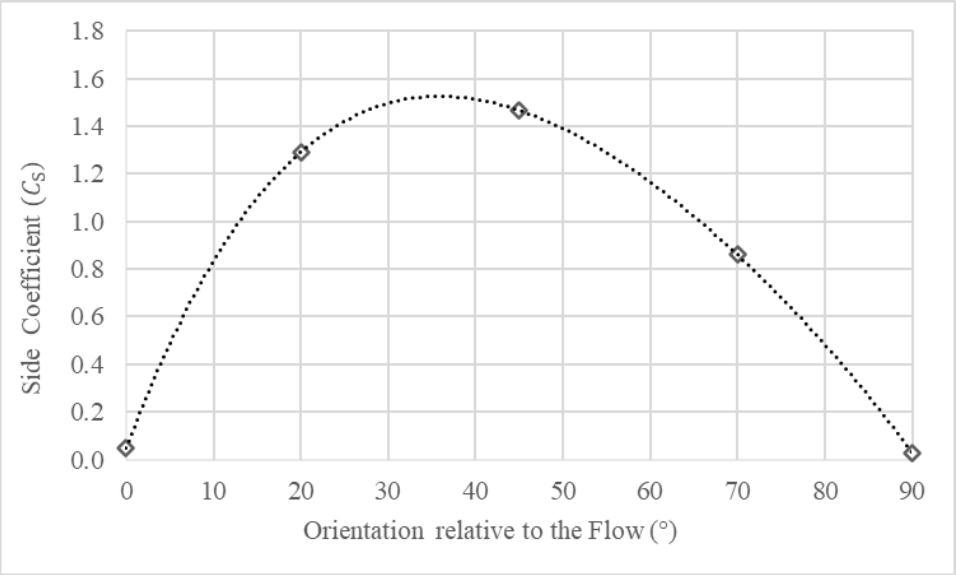

Figure 5.14 Interpolation of the side coefficient for a semi-submerged body near a plane bed with a polynomial interpolation of 4th order.

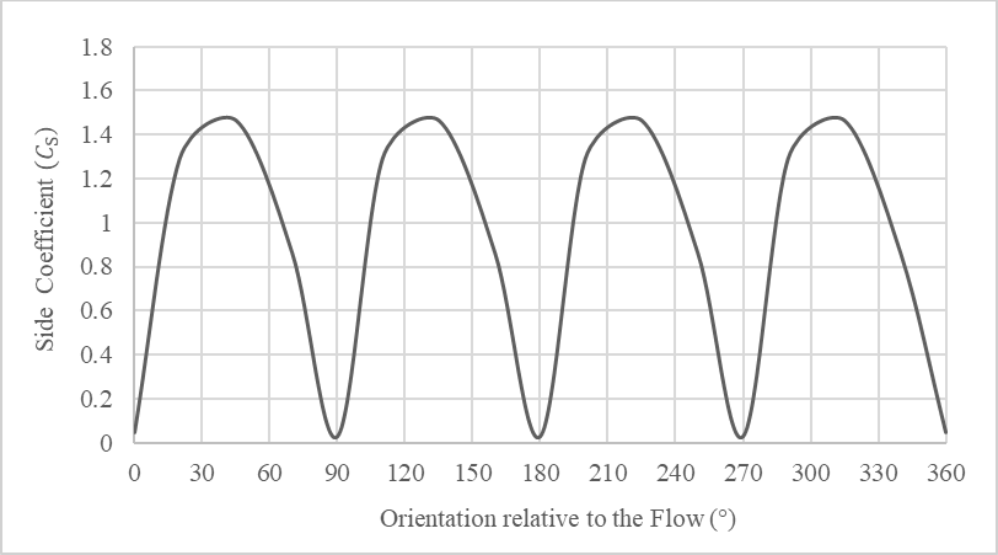

Figure 5.15 Implementation of the side coefficient for a semi-submerged body near a plane for relative angle from 0° to 360°.

Once LW elements transition from rolling or sliding to a floating condition, the hydrodynamic coefficients implemented in ORSA2D_WT are no longer those derived from near-bed, shallow water experiments. Instead, the model adopts the coefficients measured for a semi-submerged cylinder in deep-water conditions, where the element is sufficiently far from the bed plane to neglect bed proximity effects. These coefficients, documented in Persi et al. (2019), are representative of logs that are freely floating and predominantly transported by advection with the flow. In this regime, drag and side forces depend primarily on the body's geometry and orientation relative to the flow. By switching between the two sets of experimentally based coefficients, ORSA2D_WT ensures that the applied

hydrodynamic forces reflect the correct physical regime for LW transport, whether in shallow rolling/sliding conditions or in floating conditions.

The drag coefficient also plays a central role in the formulation of LW entrainment models. Bocchiola et al. (2006) implemented an average value of $C_D = 1.41$ as a representative drag coefficient for entrainment formulation. Chen et al. (2020) employed higher drag coefficients, reaching values up to $C_D = 2.78$ for fine bed material with a median grain size of $D_{50} = 0.005m$. These values are broadly consistent with the range of drag coefficients obtained in our laboratory measurements under near-bed, semi-submerged conditions. In the present implementation of ORSA2D_WT, the drag coefficient used in the entrainment module is not fixed to a constant value but is instead defined as a function of the orientation angle of LW elements with respect to the flow, interpolated directly from Eq. (5.6). This approach provides a more physically grounded representation of entrainment dynamics by explicitly accounting for the variability of hydrodynamic forces with element orientation.

Chapter 6

Entrainment Model Validation

6.1. Abstract

This chapter validates the improved entrainment formulations of the ORSA2D_WT model against controlled laboratory experiments. With the aim of testing the refinements introduced in Chapter 4 and the experimentally derived hydrodynamic coefficients from Chapter 5, a series of flume-based tests was conducted to reproduce the onset of LW motion under different orientations and hydraulic conditions. The experimental campaign employed ultrasonic sensors for water depth measurements, calibrated against known flow depths, and provided precise records of log entrainment thresholds for parallel, oblique, and perpendicular orientations. These data provided a rigorous benchmark against which model predictions were compared. The validation process assessed the model's ability to capture the thresholds for sliding and rolling entrainment mechanisms. Results show that the enhanced ORSA2D_WT model reproduces experimental thresholds with good accuracy, particularly in representing orientation-dependent differences in critical water depths and velocities. Sensitivity analyses further explored the influence of drag coefficients and friction angles on entrainment predictions, identifying the parameters exerting the greatest control and quantifying their uncertainty ranges. These analyses underscore the importance of incorporating both hydrodynamic variability and orientation-dependent resistance into predictive frameworks. By demonstrating consistency between simulations and laboratory observations, this chapter confirms the robustness of the improved entrainment module. This validation represents a step in bridging theoretical model development with experimental evidence, setting the stage for its application to natural river systems in subsequent chapters.

6.2. Experimental set-up

An experimental campaign was conducted in a laboratory flume at the Department of Civil Engineering and Architecture (DICAr) of the University of Pavia. The flume (Figure 6.1) measures 9.40 meters in length and 0.48 meters in width, with a horizontal metallic bottom and Plexiglas sides with a height of 0.80 meters. The bed of the flume is made of steel. The inlet discharge is measured using a triangular weir located at the inlet section, positioned just downstream of a loading tank. The laboratory hydraulic system can deliver a maximum discharge of 0.033 $m^3 s^{-1}$. The water depths were measured using P43-F4V-2D-1C0-220E ultrasonic sensors from "DSPM industria", which employ high-frequency sound waves to provide non-contact water level measurement. With a maximum sensing distance of 1600 mm and a minimum sensing distance of 80 mm, the sensors are well-suited for capturing water level variations within the flume (Figure 6.3).

The study used beech wood cylinders, measuring 15 cm in length and 2.5 cm and 1.9 cm in diameter, to simulate non-rooted, defoliated LW. Beech wood has an average dry density of $\rho_{dry} = 779\ \mathrm{kg\ m^{-3}}$. The standardized dimensions and material properties of the dowels ensured a controlled and repeatable experimental setup, minimizing variability and enabling precise comparisons across trials. Three distinct orientations of a standardized wooden dowel were tested: (a) perpendicular to the flow direction, (b) oblique at approximately 45°, and (c) parallel to the flow. In each configuration, two ultrasonic depth sensors were installed, one upstream and one downstream of the log to measure water depths at the critical moment of the entrainment (Figure 6.2). For each configuration, the experiment was repeated 40 times to ensure statistical robustness and account for variability in entrainment conditions.

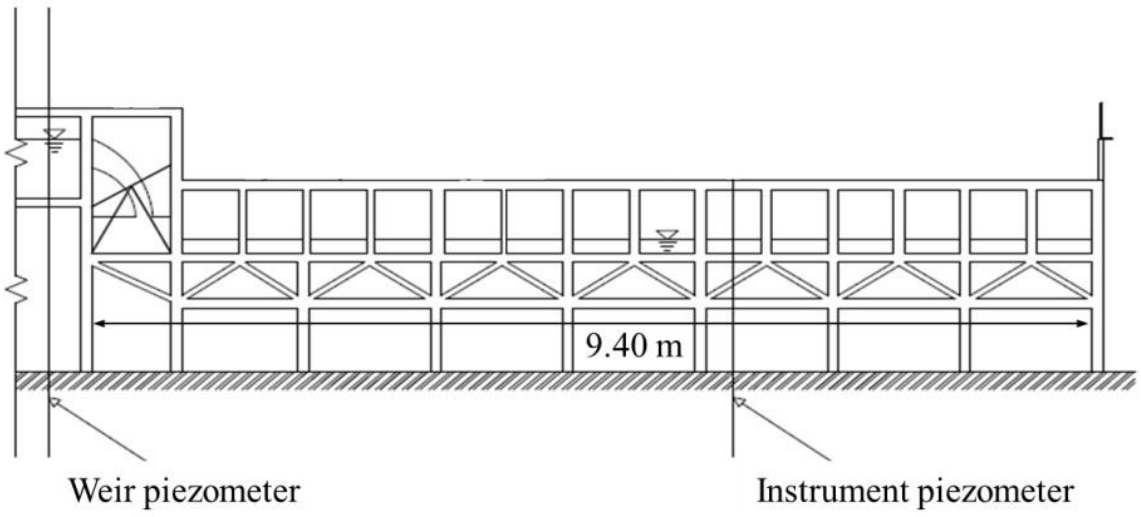

Figure 6.1 The laboratory flume used for the experiment.

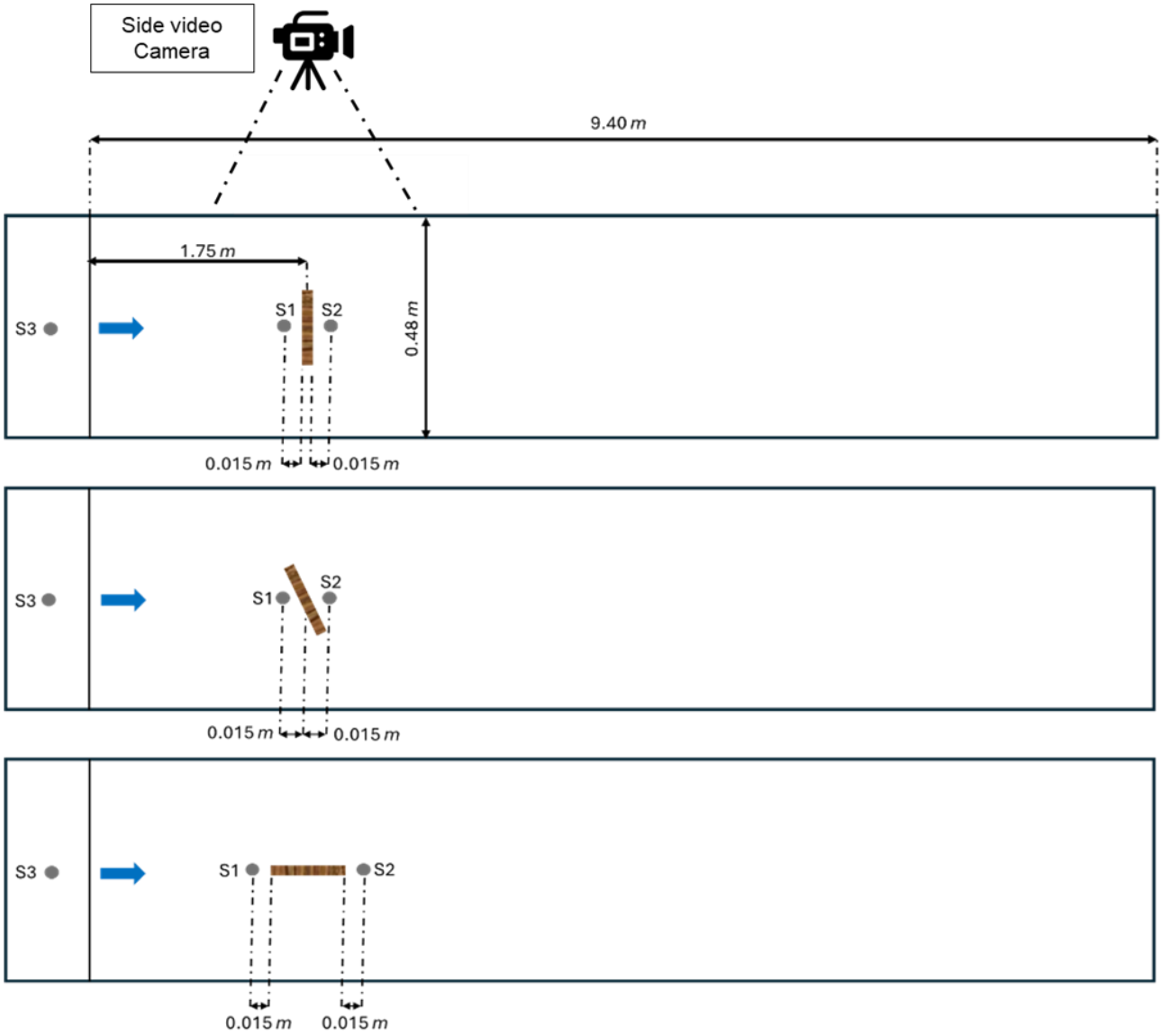

Figure 6.2 Experimental set-up for the 3 configurations (Perpendicular, oblique and parallel to the flow). Sensor S3 is located in the loading tank, upstream of the V-notch weir.

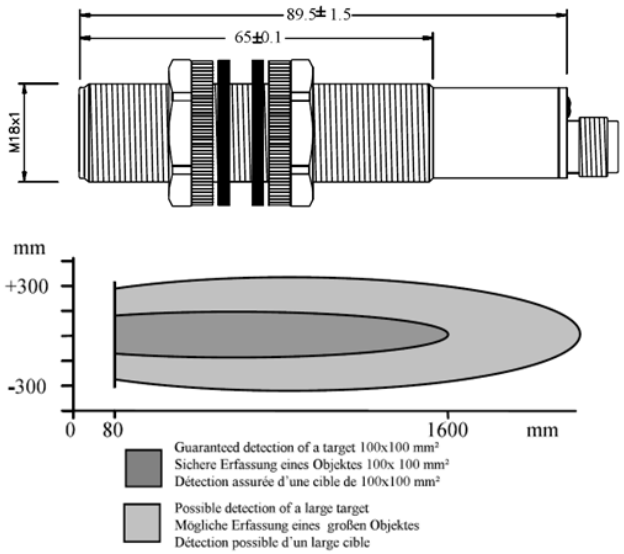

Figure 6.3 Sensor dimensions in mm and detection range of the sensor.

6.3. Experimental campaign

6.3.1. Data acquisition and processing

Raw voltage data were acquired from sensors at regular intervals to capture the temporal variations in the measured parameter. The data were processed using a custom Python script, which applied a Weighted Moving Average (WMA) filter to reduce noise and enhance the signal quality. The weighted moving average is a smoothing technique that assigns different weights to data points within a specified window, giving more importance to recent data points. The WMA is calculated as:

$$WMA = \frac{\sum_{i=1}^{n} \omega_i \, x_i}{\sum_{i=1}^{n} \omega_i} \tag{6.1}$$

where x_i represents the raw voltage data points, ω_i are the weights assigned to each data point and n is the number of data points in the moving window. This smoothing technique allowed for clearer identification of trends and patterns in the voltage measurements over time.

To convert the voltage readings into meaningful physical quantities, water depth was determined using pre-established calibration curves (details in section 6.3.2) that correlate voltage to depth. The relationship between voltage (V) and water depth (h) can be expressed as:

$$h = f(v) \tag{6.2}$$

where $f(v)$ represents the calibration function derived from experimental data.

Finally, discharge (Q) was estimated by applying the V-notch weir equation, which utilized the derived water depth from sensor S3, located upstream of the V-notch weir. The V-notch weir equation is given by:

$$Q = \frac{8}{15} C_q \sqrt{2g} \tan\left(\frac{\theta}{2}\right) h^{\frac{5}{2}} \tag{6.3}$$

Where C_q (which has value 0.6, calibrated from previous experimental campaigns) is the discharge coefficient, g is the acceleration due to gravity, $\theta = 35.8°$ is the angle of the V-notch and h is the water depth above the vertex of the V-notch, as measured by sensor S3.

The resulting discharge hydrograph, obtained by applying Equation (6.3) to the S3 head measurements, is shown in Figure 6.4. This example corresponds to one of the test experiments specifically selected for the calibration of the hydraulic model. The hydrograph illustrates the progressive increase in flow rate during the filling stage, as well as the short-period oscillations induced by the pump system.

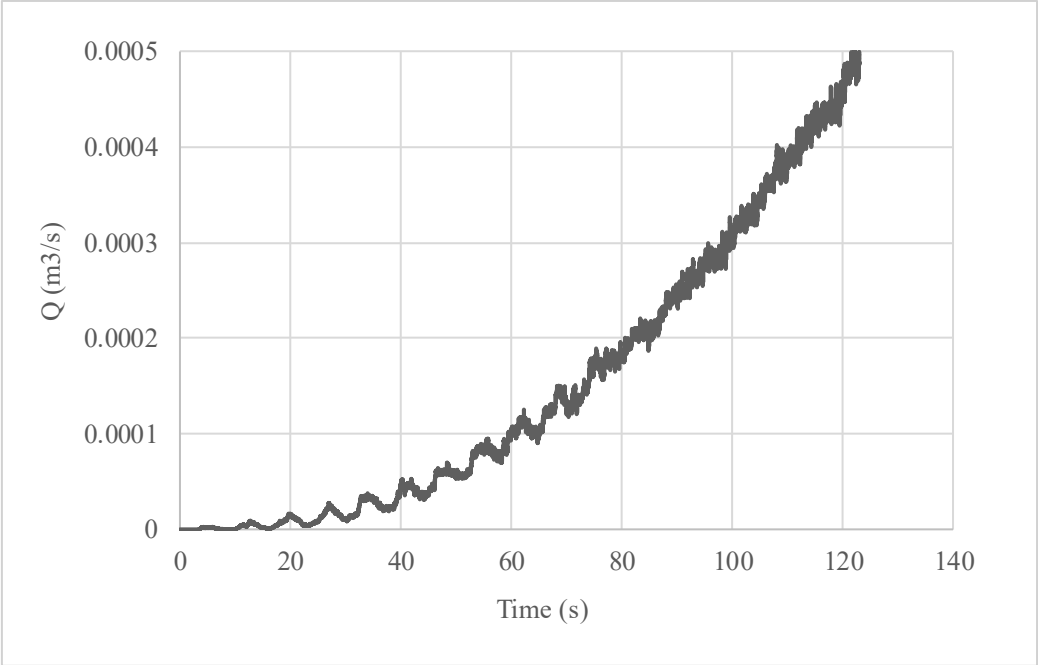

Figure 6.4 Example hydrograph from the calibration test experiment.

6.3.2. Ultrasonic sensors calibration

To ensure accurate measurements of water depth, ultrasonic sensors were calibrated prior to data collection. The calibration process involved establishing a linear relationship between the sensor voltage output and the actual measured water depth. A series of controlled water depth measurements were performed by gradually adjusting the water level in the flume and recording the corresponding sensor output voltage. The reference water depths were measured manually using a ruler with millimetric precision, while the ultrasonic sensor simultaneously provided the voltage readings.

The collected data points were plotted for all the sensors, as shown in Figure 6.5 for sensor S1, where water depth (cm) is expressed as a function of the output voltage (V). A linear regression was applied to the dataset, resulting in the calibration equations shown in Table 6.1.

Table 6.1 Calibration and fitting equations for the three sensors used in the experiments.

Sensor ID	Fitting Equation	R^2
1	$h\ (cm) = -14.863V + 4.0248$	0.9969
2	$h\ (cm) = -19.374V + 4.8297$	0.9985
3	$h\ (cm) = -14.939V + 91.845$	0.9954

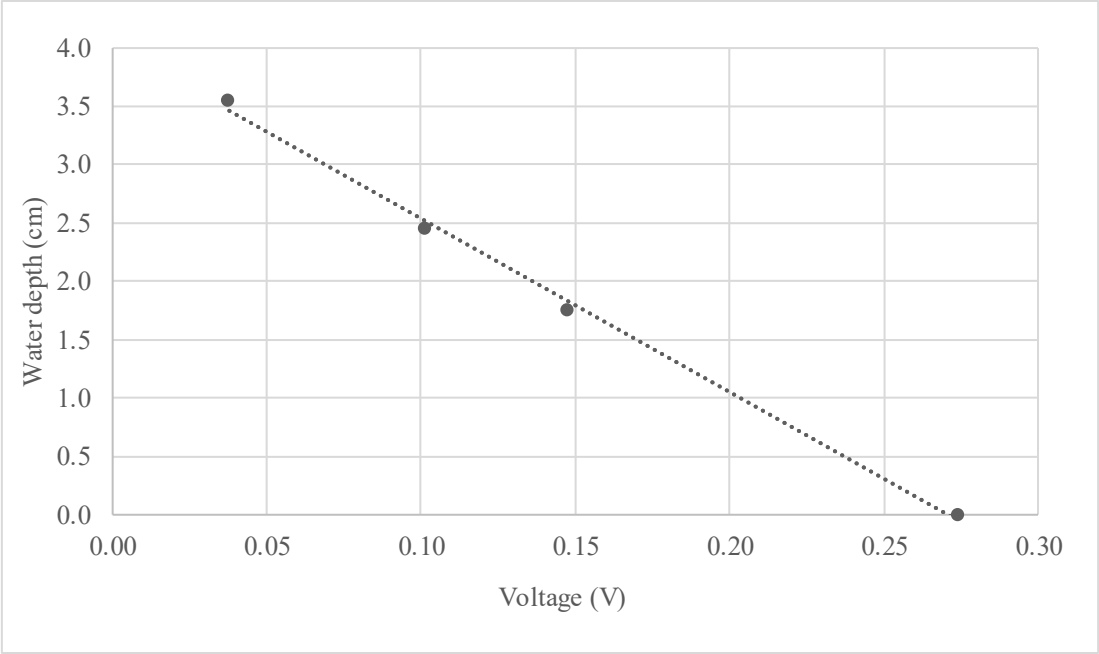

Figure 6.5 Calibration curve for sensor S1.

6.3.3. Friction angles measurement

Since the friction angles on a smooth steel bed flume differ significantly from the friction angles typically used to represent natural river conditions (as described in Chapter 4 for fine and coarse bed materials), tilt tests were conducted in the present study to directly determine the friction angles of wooden elements. These tests were performed for elements positioned at different orientations (parallel, oblique and perpendicular) relative to the slope direction. The procedure involved gradually tilting a smooth steel platform until the wooden element initiated either rolling or sliding. The obtained friction angles are presented in Table 6.2.

Table 6.2 Friction angles measured by means of tilt test for different orientations relative to the flow.

Orientation relative to the Flow (°)	Friction angle (φ)
0	21.04°
45	1.80°
90	1.80°

6.4. Calibration and validation of the hydraulic model

Calibration and validation between laboratory measurements and numerical simulations are fundamental to ensure the accuracy of hydraulic models. In the context of this study, calibration involved adjusting the Manning's roughness coefficient (n) within the hydrodynamic model to best match the measured water surface elevations recorded during flume experiments. This coefficient

reflects the effects of bed friction, turbulence losses, and other small-scale irregularities influencing flow resistance, and therefore plays a critical role in reproducing the observed flow dynamics accurately before proceeding with LW simulations. To conduct the calibration, a range of Manning's *n* values 0.009, 0.010, 0.011, 0.012, 0.013, 0.014, 0.01$\mathrm{m}^{-1/3}\mathrm{s}^{-1}$, were tested within the numerical model. Simulated water depths were then compared against those recorded by the sensors positioned in the flume (Table 6.3). The optimal Manning's *n* value was determined based on the minimization of the root mean square error (RMSE) between simulated and measured water depths. The results indicated that an n = 0.011 $\mathrm{m}^{-1/3}\mathrm{s}^{-1}$ provided the best agreement with the experimental data, accurately reproducing the water surface profile measured by sensor S2. For this configuration, the RMSE was 0.0266 cm. Validation was performed by running the calibrated model against an independent set of 4 measurements not used during the calibration phase. The simulated outputs maintained a good degree of agreement with the measured water depths resulting in RMSE of 0.102 cm, 0.103 cm, 0.125 cm, 0.109 cm for tests 1,2,3 and 4, respectively , reinforcing the transferability of the calibrated Manning's *n* value (Figure 6.6).

Table 6.3 RMSE values for different Manning roughness coefficients based on comparison between simulated and measured water depths.

Manning n	RMSE
0.009	0.0435
0.010	0.0323
0.011	0.0267
0.012	0.0274
0.013	0.0331
0.014	0.0409
0.015	0.0493
0.016	0.0575

After the calibration and validation phases, a further task was carried out to estimate the lag time the time it takes for the discharge measured at the flume inlet to reach the point where the wooden dowel was positioned. Since the only available discharge measurement during the experiments was located upstream of the inlet (sensor S3), it was necessary to determine the delay between the time when a certain discharge value is measured at the inlet and when the same discharge value occurs at the wooden dowel location. This lag time could not be measured directly from the experiments but was instead derived from the results of the hydraulic numerical model. By tracking the propagation of the flow wave through the flume, the model allowed us to quantify the temporal delay between the application of the inlet discharge and the corresponding arrival of the hydraulic response at the log position. The simulation results indicated a lag time of 10.93 seconds under the adopted transient experimental conditions, which were the same for all the runs. This lag time value was then used to

temporally shift the experimental discharge in order to better reflect the actual hydraulic conditions at the wooden dowel location at the moment of entrainment. This adjustment was critical to estimate with higher accuracy the local discharge and velocity influencing the wood entrainment. By aligning the inlet discharge with its effective arrival time at the log, the entrainment analysis could be performed with performed by accounting for the adequate hydraulic variable.

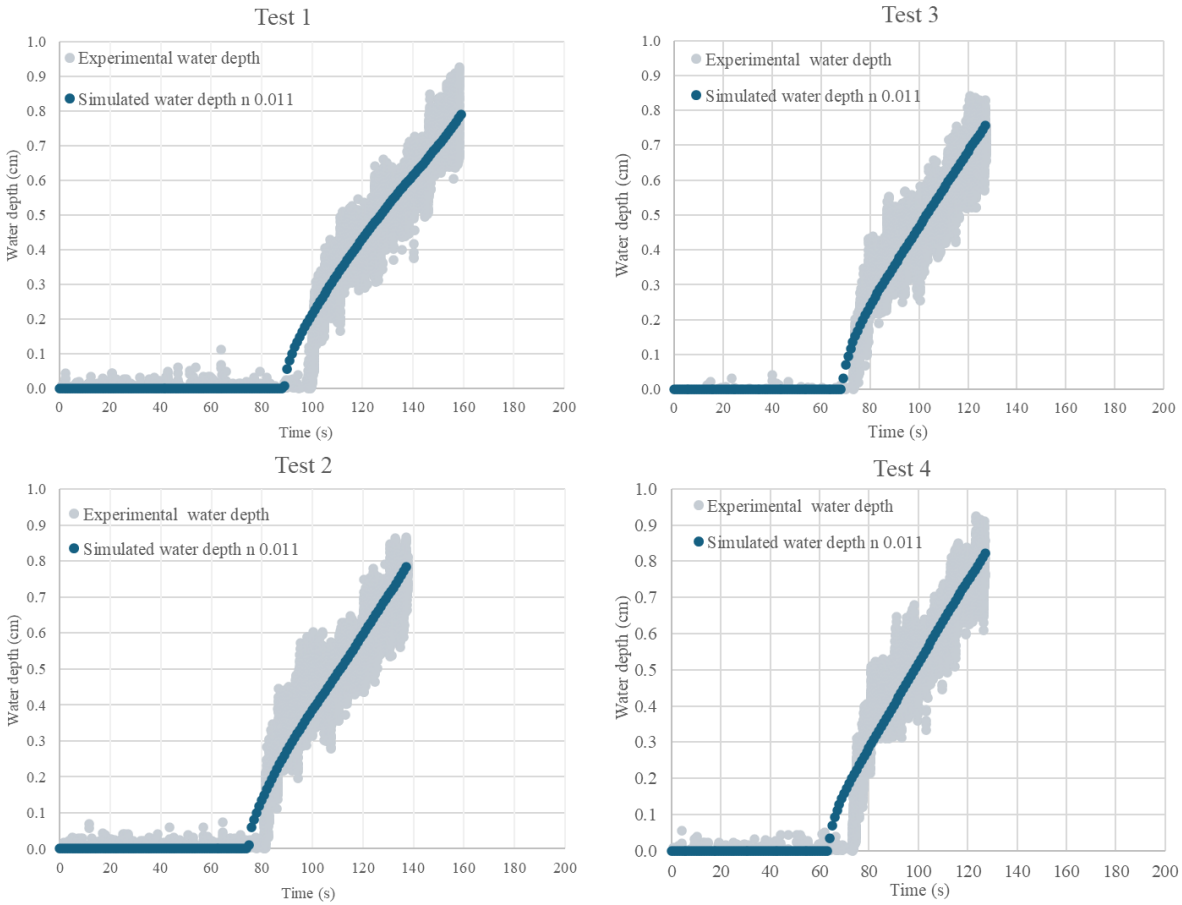

Figure 6.6 Experimental and simulated water depth hydrographs for test 1 to 4.

6.5. Analysis of the experimental results

The experimental results indicate that the orientation of wooden logs relative to flow direction significantly affects their entrainment thresholds, as expressed by the dimensionless critical depth $h_c = h/D_{log}$ (Figure 6.7), where the critical depth, h_c, is defined as the flow depth, measured both upstream and downstream of the dowel (i.e. by sensors S1 and S2, respectively), at the onset of the log motion. As expected, the dimensionless critical depth was highest for logs oriented parallel (0°) to the flow ($h_c/D_{log} \approx 0.42$), and lower for logs at oblique (45°) and perpendicular (90°) orientations ($h_c/D_{log} \approx 0.29 - 0.31$), respectively. These results suggest that logs aligned with the flow are more resistant to entrainment under identical hydraulic conditions. The increased entrainment resistance of parallel-aligned logs is attributed to the minimal projected frontal area in this test configuration, resulting in lower drag forces acting in the direction of the flow. Conversely, logs oriented at 45° or 90° present a larger projected area to the flow, increasing the drag force. This higher hydrodynamic force is able to overcome bed friction at lower water depths. Moreover, oblique orientations introduce asymmetrical drag distributions, which may produce torque that facilitates log pivoting or rolling, reducing the critical depth needed for entrainment. These findings align with what was previously stated by Braudrick and Grant (2000), who highlighted that wood dowels aligned with the flow direction are more stable than those perpendicular or oblique relative to the flow, primarily because of the reduced drag and increased contact with the streambed, which collectively raise the threshold for entrainment. This effect was observed for all tested dowel lengths and diameters. Similarly, Bocchiola et al. (2006) observed that the water depths and velocities required to trigger the motion of a wooden log when it is perpendicular to the flow direction are generally smaller than those required in the case of a wooden log parallel to the flow direction. Moreover, water depth measurements taken upstream and downstream of the log showed a consistent pattern, with upstream depths generally higher than the downstream ones when the log was positioned perpendicular or oblique to the flow. This is attributed to the log acting as an obstruction, causing flow deceleration and a backwater effect upstream, leading to a rise in water surface elevation. Conversely, downstream of the log, the flow accelerates, resulting in a slight drop in water depth due to reduced pressure and energy recovery. Interestingly, when the log was aligned parallel to the flow, the opposite trend was observed: the water depth, always measured along the log axis, was slightly lower upstream and marginally higher downstream. In this configuration, the log imposed minimal frontal resistance, allowing the flow to pass with little upstream disturbance. However, flow interactions along the sides and around the extreme of the dowel induced localized turbulence and wake formation, contributing to a small increase in the local water depth downstream, along the log axis.

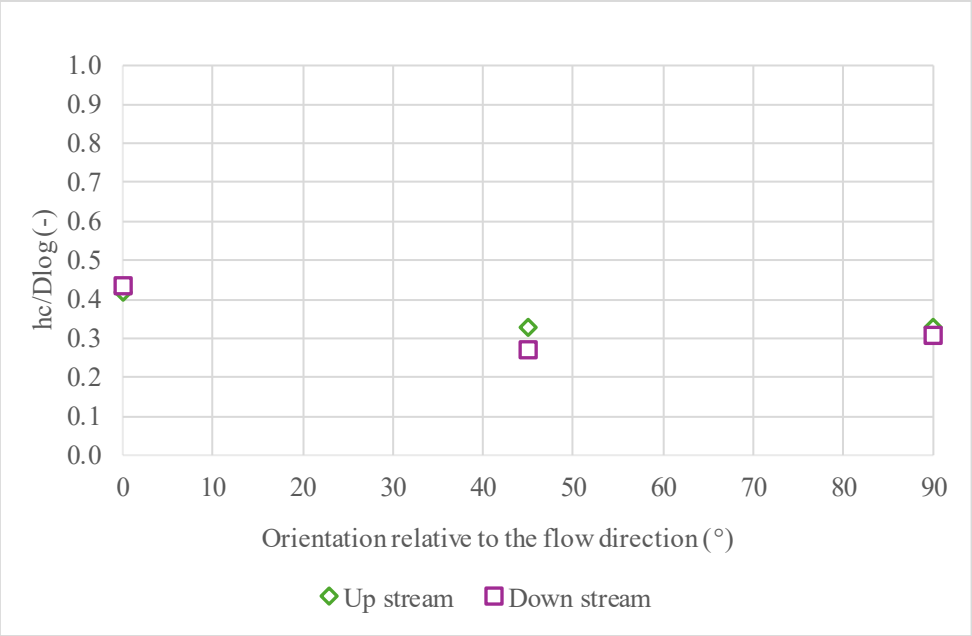

Figure 6.7 Observed critical dimensionless water depth as a function of the wooden dowel orientation relative to the flow.

Figure 6.8 illustrates a broader comparison of our experimental findings with normalized literature data extracted from previous flume studies by Braudrick and Grant (2000) , Bocchiola et al. (2006) and Crosato et al. (2013). When rootwads are attached to the logs, Braudrick and Grant, (2000) report higher critical depth values compared to their measurements without rootwads and to the present experiments: the increase is of the order of 30% and can mainly be ascribed to the increased anchoring effect and flow disturbance caused by the rootwads. Conversely, when comparing our results with those obtained by Braudrick and Grant (2000) without rootwads, we observe a mixed pattern of agreement depending on the log orientation. For the parallel (0°) orientation, our critical entrainment water depth is approximately 7% lower, indicating that in our setup, logs aligned with the flow became mobile under slightly lower hydrodynamic forces. In contrast, for the oblique (45°) orientation, our thresholds were about 8% higher, suggesting that our logs were more resistant to entrainment in this configuration, potentially due to subtle differences in flow attack angle.

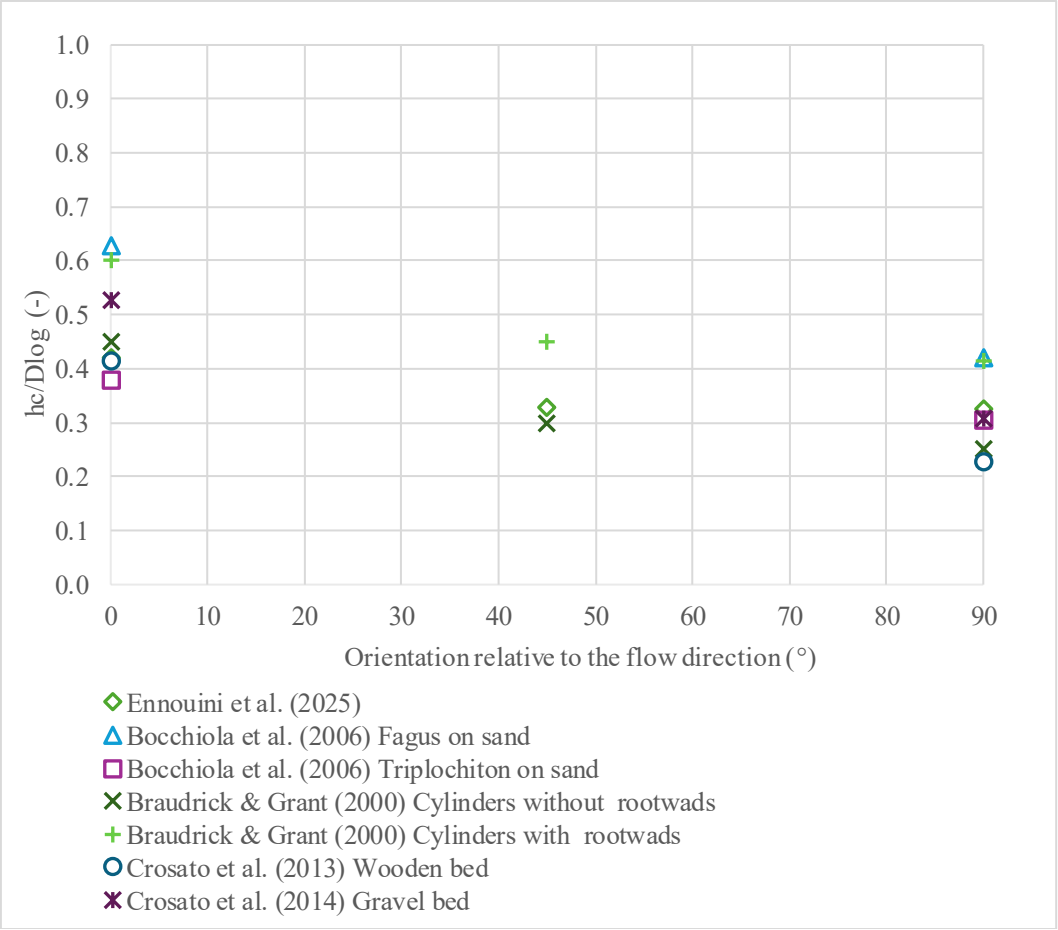

Figure 6.8 Critical Dimensionless Water Depth: Comparison of Our Experiments with Literature Data.

The most pronounced discrepancy appears in the perpendicular (90°) orientation, where the measured critical depth was 23% higher than that reported by Braudrick and Grant (2000) for logs without rootwads. This significant increase in entrainment resistance can be attributed to differences in the density of the wood used. In the conducted experiments, the logs had a density of 779 $kg\ m^{-3}$, compared to 500 $kg\ m^{-3}$ in Braudrick and Grant (2000) study. The higher density increases the submerged weight of the log, increasing the normal force acting on the bed and therefore increasing frictional resistance. As a result, greater flow depth and thus greater drag force is required to initiate the entrainment. This effect is particularly pronounced in the perpendicular orientation, where the entire log length is in contact with the bed, maximizing the influence of submerged weight and friction. The effect of density is more evident in the experiments by Bocchiola et al. (2006) , who measured water depth thresholds at the instant of entrainment on a fixed sand bed, testing two types of wood: *Triplochiton* with a density ranging from 348 kg m-^{3} to 483 kg m-^{3} and *Fagus* with a density values ranging from 706 $kg\ m^{-3}$ to 737 $kg\ m^{-3}$. Their results showed that the normalized entrainment water depths for the denser *Fagus* logs were 28% and 39% higher for the perpendicular and parallel configurations, respectively, compared to *Triplochiton*. Surprisingly, our results aligned more closely with the entrainment thresholds reported for the lower-density *Triplochiton*, with errors of only 10%

(perpendicular) and 7% (parallel), despite our logs having a density much closer to that of *Fagus*. This discrepancy can be explained by the difference in bed conditions: while Bocchiola et al. (2006) used a sand bed with friction range of $n = 0.16{\sim}0.19\ \mathrm{m}^{-1/3}\mathrm{s}^{-1}$, our experiments were conducted on a smooth steel flume bed, where friction was lower, $n = 0.011\ \mathrm{m}^{-1/3}\mathrm{s}^{-1}$. Additional insight comes from the comparison with the results obtained by Crosato et al. (2013), who performed experiments on a gravel bed with wooden dowels having a dry density of 365–368 $kg\ m^{-3}$, significantly lower than the one in our study. Their normalized critical depths are 25% higher than those of the present study for the parallel configuration, reflecting the combined effect of lower log density and higher bed roughness. However, for the perpendicular configuration, our threshold is 7% higher, likely due to the much higher log density in our tests, which increased the submerged weight and resistance to motion. In their follow-up wooden bed experiments, the normalized depth thresholds in the parallel orientation matched closely, with only a 2% error. For the perpendicular orientation, however, our thresholds were 31% higher, again pointing to the influence of the higher log density, which increased frictional resistance. These comparisons confirm that entrainment thresholds are highly sensitive to both log properties (particularly, density and orientation) and bed characteristics (roughness, material type, friction).

The entrainment velocity thresholds can be expressed through a dimensionless critical velocity, $U_c/\sqrt{g\ D_{log}}$, where *Uc* is the flow velocity at the onset of log motion. To estimate *Uc* , the discharge value corresponding to the moment of entrainment shifted by the lag time of 10.93 seconds (as explained in Section 5.4) was extracted from the inlet hydrograph. This discharge was then divided by the cross-sectional flow area at the wooden dowel location, obtained from the numerical model, to calculate the local mean flow velocity:

$$U_c = \frac{Q}{A} \tag{6.5}$$

where Q is the estimated discharge and A is the cross-sectional area at the wooden dowel position. This velocity was then used to compute the dimensionless critical velocity, allowing for comparison across different log configurations and experimental runs.

Figure 6.9 demonstrates a clear dependency of the critical velocity on the orientation of the dowels relative to the flow direction, similarly to the critical water depth. The highest threshold was observed for the parallel orientation (0°), followed by the oblique (45°) and perpendicular (90°) configurations. This trend is consistent with the previously explained hydrodynamic considerations: logs aligned with the flow offer the least projected area, reducing drag and making them more resistant to entrainment

under identical hydraulic conditions. In contrast, logs placed perpendicularly to the flow are subjected to higher drag forces, which more readily overcome bed friction and initiate movement at lower velocities. When compared with previous studies, the normalized critical velocities presented in this study are only 1 % lower than those measured by Crosato et al. (2013) in their wooden bed experiments for the parallel orientation. However, for the perpendicular configuration, our results are significantly higher, showing a 63% difference. A similar overestimation is observed when comparing with Crosato et al. (2013) gravel bed configuration, with a 40% difference for the 90° orientation, whereas the parallel configuration shows a relatively small deviation of -11%.

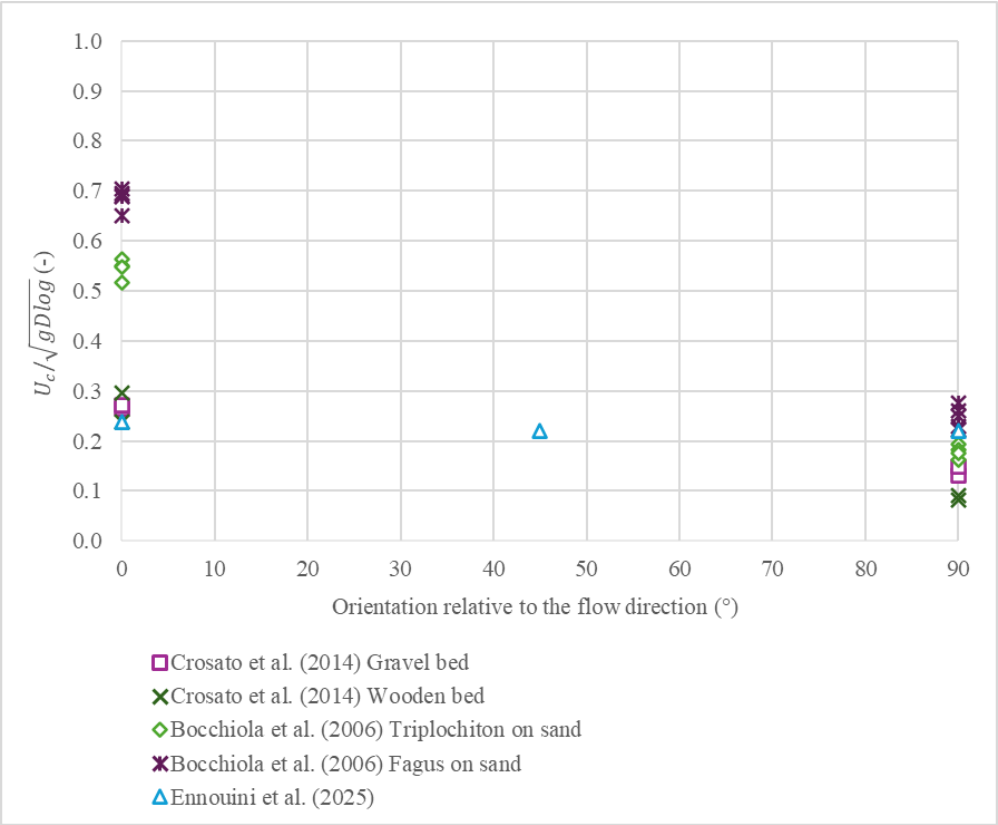

Figure 6.9 Critical Dimensionless Velocity: Comparison of Our Experiments with Literature Data.

6.6. Entrainment model validation against experimental results

To evaluate the predictive capability of the ORSA2D_WT entrainment module, we carried out a simple validation by comparing model outputs against the experimental entrainment thresholds obtained for the three tested log orientations. The validation focused on two primary indicators: dimensionless critical water depth and the entrainment critical velocity at the onset of motion. The model simulations reproduced the laboratory flume conditions by incorporating inputs for channel geometry (the rectangular mesh, extended to the entire flume, presenting 4384 triangular elements), hydraulic input, calibrated bed roughness, log dimensions and orientation, material properties (density and shape), drag coefficients, and friction angles derived from tilt tests. Table 6.4 summarises the corresponding experimental and simulated entrainment thresholds.

Table 6.4 Summary of parameters used in simulations and comparison of experimental vs. simulated critical dimensionless water depth at the entrainment.

Orientation relative to the Flow (°)	Simulated h_c/D_{log}	Experimental h_c/D_{log}	Error percentage
0	0.389	0.420	-7.5%
45	0.366	0.327	11.8%
90	0.325	0.326	-0.5%

The comparison between simulated and experimental dimensionless critical water depth (Figure 6.10) reveals insights into the model accuracy across different orientation configurations. At 45°, the simulation overestimates the experimental value by 11.8%, which can be partly attributed to the complex flow phenomena observed during the experiments. In this oblique configuration, a significant amount of vortex shedding and flow separation was visually evident around the log, leading to increased turbulence and local variations in flow depth effects that are difficult to be fully captured by a 2D numerical model. At 0°, where the log is aligned parallel to the flow, the model slightly underestimates the critical dimensionless water depth by 7.5%. This discrepancy may stem from small uncertainties in the drag coefficient and the effective contact area between the log and the flume bed, both of which influence the resistive forces opposing motion. Finally, for the perpendicular configuration (90°), the model demonstrates excellent agreement with experimental results, showing only a −0.5% error.

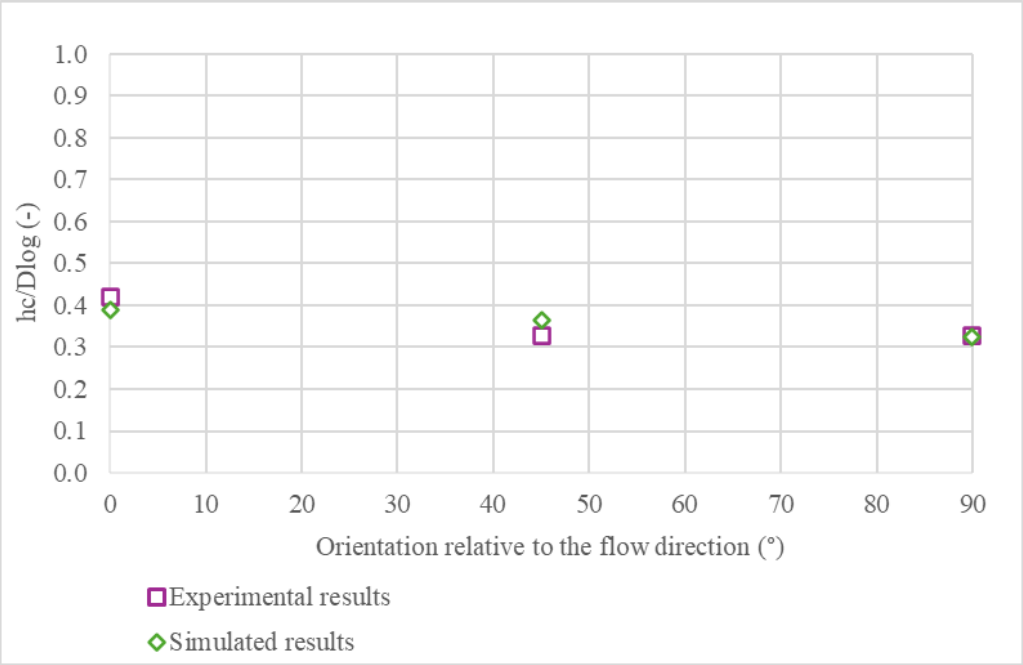

Figure 6.6 Simulated Versus Experimental critical dimensionless water depth as a function of the orientation relative to the flow.

A comparison between the simulated and experimental critical dimensionless velocities (Table 6.5) reveals that the ORSA2D_WT model tends to overestimate the experimental values by +8.4% in the parallel (0°) orientation, +14.4% in the oblique (45°) orientation, and +0.6% in the perpendicular (90°) orientation (Figure 6.11). These results closely align with the trends observed in the dimensionless critical water depth analysis, reinforcing the model consistent predictive behavior across different log orientations. The notable overestimation observed in the 45° configuration further underscores the model limitations in resolving the complex hydrodynamic interactions that characterize oblique alignments. Mainly vortex shedding, flow separation, and asymmetric pressure fields, leading to unsteady localized accelerations in the flow. These phenomena are inherently three-dimensional and are not fully captured by the model two-dimensional framework, which simplifies the spatial variability of flow structures around partially submerged objects. In contrast, the smaller discrepancies in the parallel and perpendicular configurations suggest that the ORSA2D_WT entrainment module provides reliable predictions under both flow-aligned and crossflow conditions.

Table 6.5 Comparison of experimental vs. simulated critical dimensionless velocities.

Orientation relative to the Flow (°)	Simulated Uc/SQRT (gD)	Experimental Uc/SQRT (gD)	Error percentage
0	0.253	0.233	8.4%
45	0.242	0.211	14.4%
90	0.222	0.220	0.6%

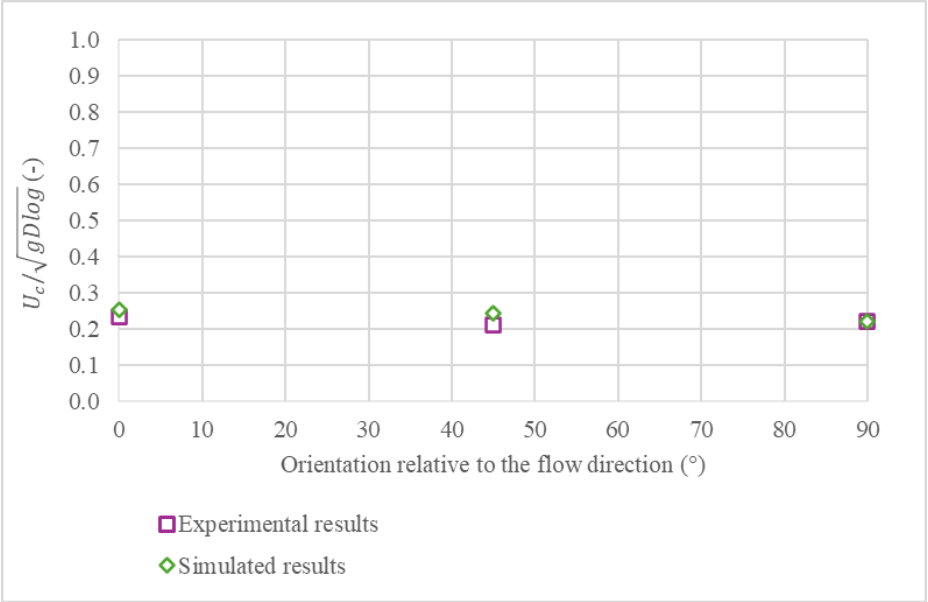

Figure 6.7 Simulated versus Experimental critical dimensionless velocity as a function of the orientation relative to the flow.

6.7. Sensitivity analysis on the drag coefficient

Figure 6.12 illustrates the results of the sensitivity analysis performed for each orientation configuration by varying physical and hydrodynamic parameters in the ORSA2D_WT model. For the perpendicular orientation (Figure 6.12), increasing C_d by +20%, 40%, 60% and +80% resulted in reductions in h_c/D_{log} by 6%, 11%, 15% and 18% respectively. While decreasing C_d by -20%, -40%, -60% and -80% increased the dimensionless critical water depth by 7%, 18%, 32% and 57%, respectively. These trends indicate the dominant influence of frontal drag forces acting on the exposed surface area of the log in this configuration, where the frontal area exposed to the flow is maximized. For the oblique orientation (Figure 6.12), the sensitivity analysis revealed that a decrease of C_d by -20%, -40%, 60% and -80% resulted in an increase of increased the dimensionless critical water depth by 8%, 16%, 29% and 31%, respectively, while an increase of the coefficient led to lower dimensionless critical water depths by 5%, 9%, 13% and 17%, respectively. The parallel orientation (Figure 6.12), unlike the previously described configurations, exhibited minimal sensitivity to variations in C_d. A +80% increase in C_d resulted in only a 0.13% decrease in the dimensionless critical water depth, while a -80% reduction in C_d produced an equally small change. This limited response can be explained by the fact that, in the parallel configuration, the log exposes minimal frontal surface area to the flow. As a result, hydrodynamic drag forces play only a minor role, and the initiation of motion is primarily governed by bed friction and log density (through buoyancy), rather than by variations in drag. Overall, this sensitivity analysis confirms that the model predictions are particularly sensitive to C_d in the perpendicular and oblique orientations, where drag forces are the primary mechanism of entrainment. In contrast, when the log is parallel to the flow, drag effects are secondary. These results highlight the importance of calibrating the drag coefficient, especially for perpendicular and oblique configurations. These findings are in good accordance with prior observations which underscore the sensitivity of LW entrainment to variations in drag coefficient. For example, Buxton (2010) explicitly demonstrated through sensitivity analysis that a reduction in the drag and lift coefficients resulted in a reduction of the error, confirming their critical role in model accuracy. Shields and Alonso, (2012) proposed using Monte Carlo analysis to address uncertainties in input variables such as the drag coefficient acknowledging that the uncertainty related to the computation of the applied forces can be addressed by representing the system through probability density functions. Therefore improving C_d estimation through either refined empirical correlations or CFD simulations would significantly improve the predictive capability of numerical models such as ORSA2D_WT.

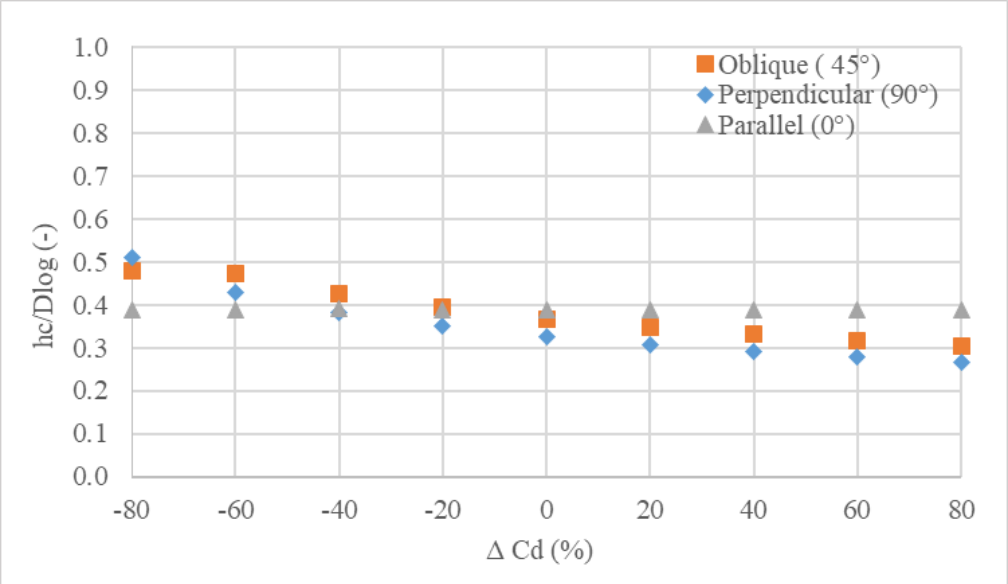

Figure 6.8 Sensitivity analysis of the drag coefficient (Cd) on the dimensionless critical water depth (hc/Dlog) for different log orientations.

6.8. Sensitivity analysis on the friction angle

The friction angle values measured in the base scenario revealed a significant difference between rolling and sliding friction angles: the rolling friction angle was 1.8°, while the sliding friction angle reached 20.04° (Table 6.1). This disparity confirms that logs resist motion much more when sliding than when rolling. Prior studies report similar contrasts: for instance, Chen et al. (2020) measured sliding friction angles in the range ≈17.8–19.3° versus rolling angles ≈6.4–9.1° on coarse beds. Kang and Kimura (2018) likewise used a static friction coefficient of 0.5 (≈26.6°) for sliding but only 0.05 (≈2.9°) for rolling. Bocchiola et al. (2006) found an angle θ≈34° for sliding on sand beds but only 5.6–11° for rolling. Our measured sliding angle (~20°) on a relatively smooth steel bed is consistent with Chen's fine-bed value of ~19.3°, while the extremely low rolling angle (1.8°) matches the expectation of negligible resistance when a log simply rolls on a smooth bed. In short, rolling requires far less force to overcome friction than sliding, in agreement with both theoretical considerations and past flume tests. Figure 6.13 illustrates the relationship between friction angle and predicted dimensionless critical depth for each orientation scenario. In the perpendicular configuration (90°), a clear positive correlation is observed: increasing φ leads to a noticeable increase in h_c/D_{log}. This reflects the dominant role of frictional resistance in counteracting the drag force acting on the full-frontal area of the log. A similar trend is evident in the oblique configuration (45°), where both rolling and sliding mechanisms may contribute to entrainment. Conversely, in the parallel orientation (0°), the model shows a minimal sensitivity to changes in friction angle. Across the tested range, the predicted h_c/D_{log} remains nearly constant. This limited sensitivity can be explained by the fact that,

with the log fully in contact with the bed and aligned with the flow, the exposed frontal area is minimal and hydrodynamic drag forces are very weak. As a result, friction forces though dominant are already large enough to counteract the small drag force, and variations in friction angle produce only minor changes in the overall force balance, while the entrainment is essentially triggered by buoyancy effects.

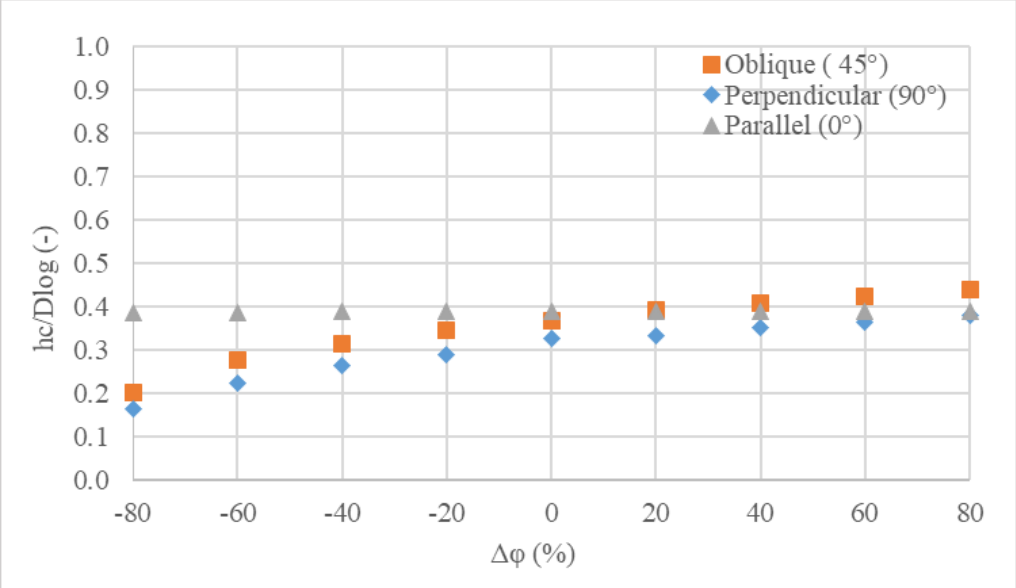

Figure 6.9 Sensitivity analysis of friction angle (°) on the dimensionless critical water depth (hc/Dlog) for different log orientations

A direct cross-comparison of the two sensitivity analyses is presented in Figure 6.14, which plots the dimensionless critical water depth as a function of parameter variation (from -80% to +80%) for both C_d and friction angle on the same axes for each of the three orientations. The total range of the dimensionless critical water depth across the full ±80% variation provides a straightforward measure of relative parameter importance. For the parallel configuration (0°), both parameters produce negligible variation: the friction angle range is only Δ hc/Dlog = 0.004 and the C_d range is 0.001, confirming that predictions for this orientation are insensitive to both parameters and are governed instead by the accuracy of the imposed flow depth. For the oblique configuration (45°), friction angle is the more influential parameter (Δ hc/Dlog = 0.235 versus 0.176 for C_d), reflecting the mixed sliding-rolling entrainment mode in which frictional resistance and torque effects play a comparably important role to drag. For the perpendicular configuration (90°), C_d is marginally the dominant parameter (Δhc/Dlog = 0.243 versus 0.217 for friction angle), consistent with drag being the primary mobilizing force when the maximum projected area of the log faces the flow. These findings support a differentiated calibration strategy: effort should be concentrated on measuring orientation-specific drag coefficients for applications dominated by transverse or oblique log orientations, while tilt-test-derived friction angles provide a reliable and sufficient constraint for parallel-log scenarios.

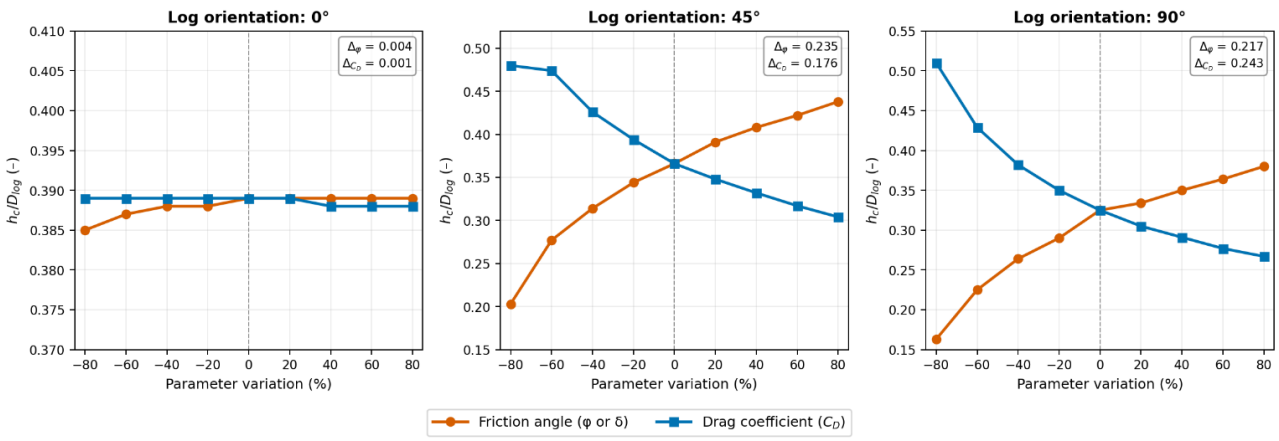

Figure 6.14 Cross-comparison of the sensitivity of the dimensionless critical water depth (hc/Dlog) to drag coefficient (C_d) and friction angle (φ or δ) variations for the three tested log orientations.

Chapter 7

Model Application to the Tagliamento River

7.1. Abstract

This chapter assesses the capabilities of the enhanced ORSA2D_WT model, described in detail in Chapter 3 and 4, in simulating LW transport in the Tagliamento River. The model is applied to two reaches of the Tagliamento River, where field data on LW transport was available (Ravazzolo et al., 2015a). In this application, the vegetation-entrapment procedure was not activated. Despite the limited number of comparisons, as only 2 GPS trajectories and 48 RFID data were available, the model demonstrated an acceptable level of accuracy in replicating LW entrainment. While the model effectively predicted LW dynamics under simplified conditions, discrepancies in trajectories near islands and areas of complex flow dynamics highlighted challenges in capturing intricate LW transport. Sensitivity analysis revealed the significant influence of wood density on LW transport, with wet density conditions showing notable deviations from the observed data. Additionally, the initial orientation of logs was found to significantly affect transport dynamics, with logs alignment affecting the time of entrainment and vicinity to riverbanks. The model displayed an overestimation of LW mobility, compared to field surveys observations, claiming for greater attention in representing LW interactions, partial burial, and structural features such as root wads and branches. These results have been published in Ennouini et al. (2025).

7.2. Study area

The study focuses on the Tagliamento River (northeastern Italy), which drains a 2871 km^2 basin mostly within the Friuli Venezia Giulia Region. The river extends to over 178 *km*, with a gradient ranging between 0.003 and 0.005 *m/m*. The Tagliamento River is a highly dynamic system with significant wood deposits and entrainments during flood events (Bertoldi et al., 2010; Gurnell et al., 2001; Tockner et al., 2003). The numerical modelling of LW transport was performed for two distinct reaches of the Tagliamento River, hereinafter named Cornino and Flagogna (Figure 7.1c and Figure 7.1d). The upstream Cornino reach stretches approximately 3.5 *km* in length and spans 800 *m* in width. It has an average slope of 0.0035 *m/m*, and it is characterized by an extensive bar-braided morphology (Figures 7.1c). The simulated downstream Flagogna reach stretching over 3.5 *km* as well, while having a similar slope, features a narrower active channel width of about 600 *m* (Sitzia et al., 2016) and a predominantly wandering morphology (Figures 7.1d). The Tagliamento River flow regime includes frequent flow pulses (below bankfull level) and less frequent flood pulses (at bankfull or higher), with distinct seasonal variations and low-flow periods in winter and summer. The riverbed comprises a mix of sediments ranging from fine sand to cobbles, with median grain size (D_{50}) of approximately 40 mm and localized armoring in main channels. The riparian zone features continuous woodland along the floodplain margins and dynamic vegetated islands within the braided network, shaped by the river's frequent morphological adjustments during floods (Bertoldi et al., 2010).

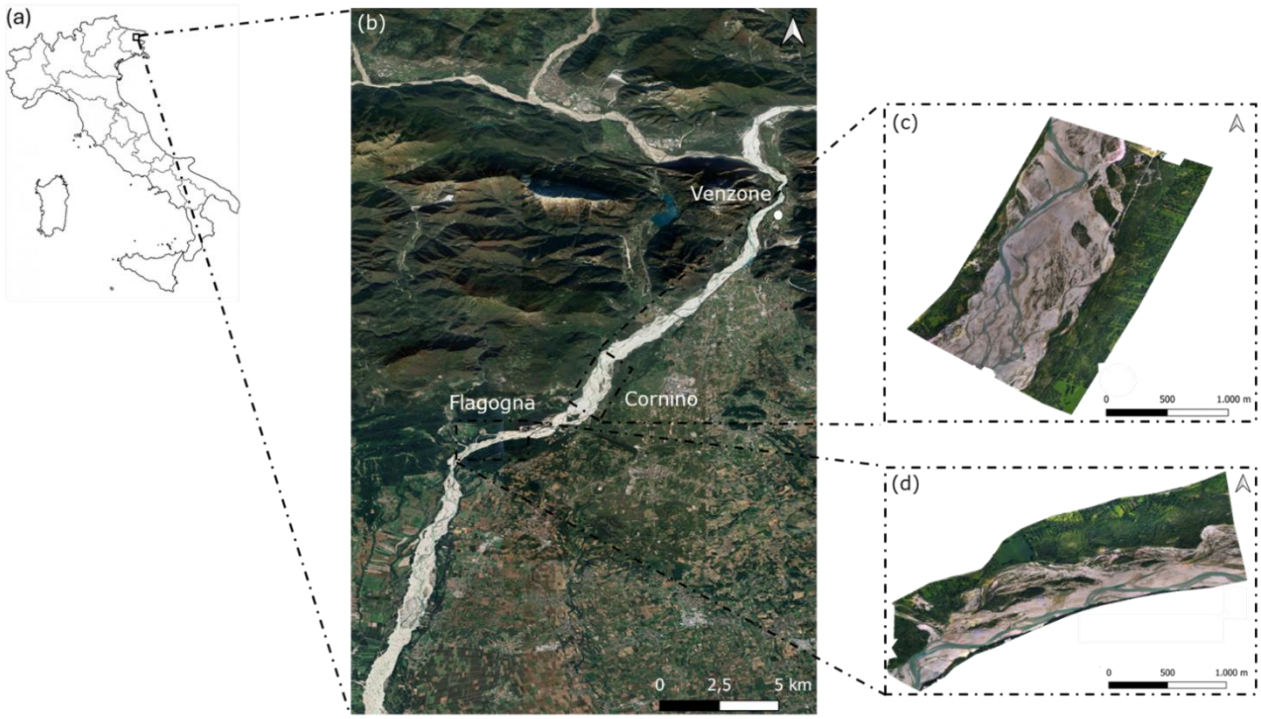

Figure 7.1 (a) Location of the Tagliamento River in Italy. (b) The Tagliamento River with the location of (c) the Cornino reach and (d) the Flagogna reach.

7.3. Field observation of large wood transport during floods

For model application, the field data from (Ravazzolo et al., 2015a) were exploited. The researchers employed active RFID tags and passive GPS tracker devices to monitor LW displacement, length, and velocity in the Cornino and Flagogna reaches of the Tagliamento River. The RFID tags (RF Code Company) were active, battery-powered devices enclosed in polycarbonate cases (47×34×12 mm), emitting signals at 443 MHz every 2 seconds with a detection range of ~200 m. These tags were implanted into log trunks using silicone caulk to ensure stability during floods and enhance waterproofing. The GPS trackers (LandAirSea 3100-EXT) consisted of a GPS antenna receiver, a waterproof plastic case (80×100×40 mm), 4 AA batteries, and an internal data logger. These devices recorded positions at 1-second intervals when activated by movement (triggering a 50-second "warm start") and paused logging after 2 minutes of immobility to conserve battery. GPS trackers were secured to logs using stainless steel chains and included an internal RFID tag to aid recovery. Together, the technologies offered a dual perspective: RFID tags emitted signals detectable with a mobile receiver, while GPS trackers recorded precise location data during movement, providing detailed insights into log displacement trajectories and transport velocities. A total of 113 active RFID tags and 42 GPS trackers were deployed across three field campaigns (June 2010–October 2011), targeting logs representative of in-channel wood dynamics. Logs were selected based on size (median length 11.5 m, diameter 0.19 m), orientation (75% parallel to flow), and structure (70% trees with rootwads/branches; 30% bare trunks). Only 48 LW elements, surveyed between June and July 2010, are here analyzed. In the Cornino reach, a total of 36 logs were surveyed, as shown in Table 7.1. Among these logs, 10 were outfitted with both GPS trackers and RFID tags, allowing for precise monitoring and data collection. The remaining logs were equipped solely with RFID tags. Within the Flagogna reach, 12 logs were monitored and fitted with RFID tags, with 6 of them additionally equipped with GPS trackers (Table 6.1). In Table 6.1, the “Typology” column differentiates between trunks (without branches) and trees (with branches and rootwads), “Length” refers to the total length of the tree, including its crown, “Width” represents the transverse dimension of the tree crown, if present, and “Diameter” is measured at 1.3 *m* from the trunk base or from the rootwads, providing a standardized reference for trunk size. For logs with RFID the initial and final position (acquired during the field surveys) are known, while for those equipped with GPS the entire trajectory (time and coordinates) is available. Among these logs, only 4 of those tracked with GPS moved during the considered event, thus limiting the possibility of comparison of the modelled trajectories. Thanks to the entire dataset, however, it is possible to evaluate the model capability to (1) replicate trajectory and (2) replicate entrainment (moving/not moving).

Table 7.1 LW inventory for Cornino and Flagogna reaches in the Tagliamento River (mod. from Ravazzolo et al., 2015 a).

Log ID	Reach	Tracking device	Typology	Length [m]	Width [m]	Diameter [m]
C1	Cornino	RFID	Tree	12.0	-	0.17
C2	Cornino	RFID	Trunk	2.6	-	0.27
C3	Cornino	RFID	Trunk	8.1	-	0.21
C4	Cornino	RFID	Tree	11.0	1.9	0.15
C5	Cornino	RFID-GPS	Tree	12.5	1.5	0.17
C6	Cornino	RFID	Tree	10.9	3.0	0.27
C7	Cornino	RFID	Tree	11.0	1.3	0.20
C8	Cornino	RFID	Tree	12.0	1.5	0.18
C9	Cornino	RFID-GPS	Tree	10.5	1.4	0.13
C10	Cornino	RFID	Trunk	8.5	-	0.19
C11	Cornino	RFID-GPS	Tree	11.1	-	0.18
C12	Cornino	RFID	Tree	19.7	4.1	0.29
C13	Cornino	RFID	Tree	21.0	2.8	0.18
C14	Cornino	RFID	Tree	13.0	-	0.19
C15	Cornino	RFID-GPS	Tree	17.3	2.9	0.16
C16	Cornino	RFID	Tree	17.5	2.4	0.22
C17	Cornino	RFID-GPS	Tree	18.8	2.1	0.22
C18	Cornino	RFID	Tree	12.0	2.0	0.18
C19	Cornino	RFID	Trunk	11.0	-	0.07
C20	Cornino	RFID	Trunk	13.0	-	0.23
C21	Cornino	RFID-GPS	Tree	14.7	-	0.21
C22	Cornino	RFID	Tree	12.1	-	0.15
C23	Cornino	RFID	Tree	8.6	1.4	0.16
C24	Cornino	RFID-GPS	Tree	16.8	2.9	0.22
C25	Cornino	RFID-GPS	Tree	14.9	2.0	0.27
C26	Cornino	RFID-GPS	Tree	14.8	4.2	0.28
C27	Cornino	RFID	Trunk	1.2	-	0.33
C28	Cornino	RFID	Trunk	8.7	-	0.17
C29	Cornino	RFID	Trunk	3.2	-	0.32
C30	Cornino	RFID	Trunk	9.2	-	0.25
C31	Cornino	RFID	Tree	18.5	4.1	0.30
C32	Cornino	RFID	Tree	11.0	2.3	0.13
C33	Cornino	RFID	Tree	5.0	2.4	0.21
C34	Cornino	RFID	Tree	4.5	3.0	0.10
C35	Cornino	RFID	Tree	8.7	2.9	0.27
C36	Cornino	RFID-GPS	Tree	8.15	3.7	0.20
F1	Flagogna	RFID-GPS	Tree	30.0	4.5	0.45
F2	Flagogna	RFID	Trunk	17.3	-	0.38
F3	Flagogna	RFID	Tree	11.0	-	0.20
F4	Flagogna	RFID	Tree	17.6	-	0.24
F5	Flagogna	RFID	Trunk	11.6	-	0.18
F6	Flagogna	RFID-GPS	Tree	15.9	2.3	0.22
F7	Flagogna	RFID-GPS	Tree	21.2	2.4	0.32
F8	Flagogna	RFID	Tree	13.0	7.2	0.27
F9	Flagogna	RFID-GPS	Tree	20.5	4.0	0.30
F10	Flagogna	RFID	Tree	13.0	4.1	0.23
F11	Flagogna	RFID-GPS	Tree	11.9	-	0.18
F12	Flagogna	RFID-GPS	Tree	18.8	2.1	0.21

7.4. Flood event selection

As reported in (Ravazzolo et al., 2015a), 15 floods occurred during the entire study period (2010-2012), with water levels at Venzone gauging station (approximately 12 *km* upstream from the Cornino reach) ranging between a base level around 0.5 *m* and the bankfull stage (3 m, Bertoldi et al., 2013; Gurnell et al., 2002). To simulate LW entrainment and transport, the first event after the instrumentation campaign was selected, occurring from August 15 to August 16, 2010 (Figure 7.2). First GPS movements were recorded precisely for that event, during which the water level reached 1.5 *m,* half of the bankfull stage. As shown in Figure 7.2, three following events of similar magnitude occurred, which frames the event as a "flow pulse", characteristic of the Tagliamento River (Bertoldi et al., 2010).

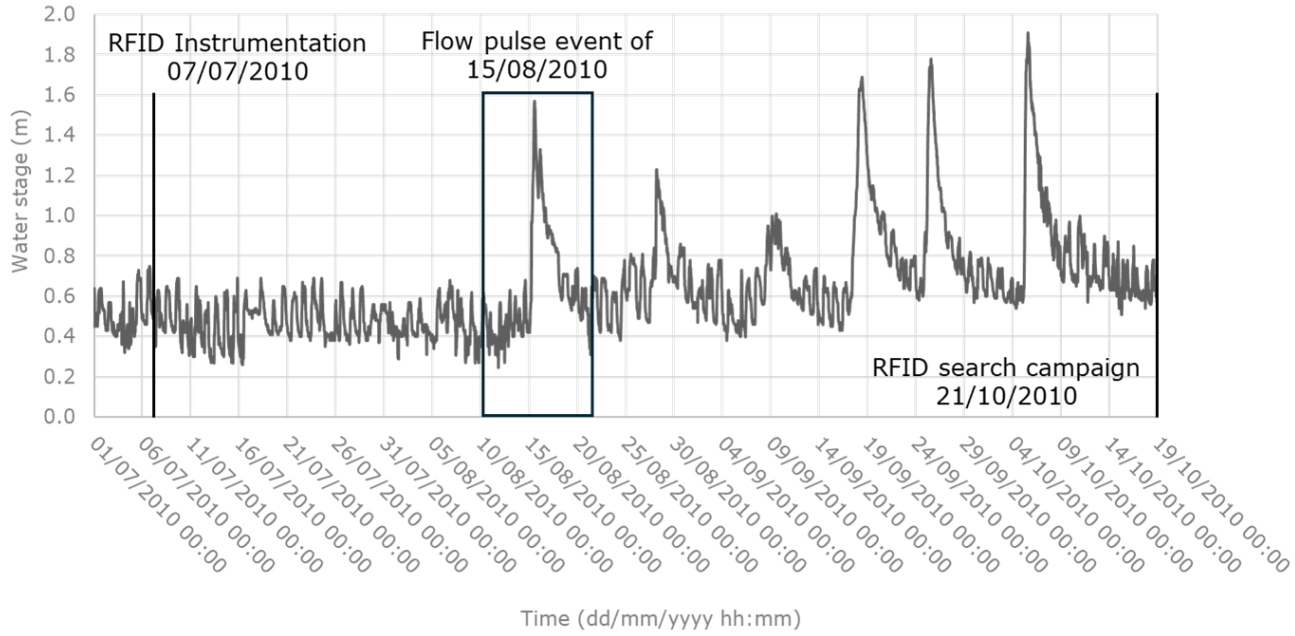

Figure 7.2 Water stage level variations over time during LW tracking in the Tagliamento River measured at the gauging station of Venzone.

The discharge hydrograph used in this simulation was derived by applying a three-segments rating curve obtained by the Regione Friuli Venezia Giulia for the instrumented section in Venzone. The discharge Q, in $m^3\ s^{-1}$, is calculated based on the water depth h, in cm, according to the following equations:

$$Q(h) = 2.562 \times 10^{-4} h^3 + 0.0166 h^2 + 1.117 h + 48.753 \quad \text{if } h < 10\ cm \tag{7.1}$$

$$Q(h) = 53.191 e^{0.015 h} \quad \text{if } 10\ cm < h \leq 151\ cm \tag{7.2}$$

$$Q(h) = 9.144 h - 855.76 \quad \text{if } h > 151\ cm \tag{7.3}$$

The rating curve (Eqs. 7.1,7.2 and 7.3) were applied to hourly water measurements taken on August 15, 2010, at the Venzone gauging station. The resulting hydrograph covers about 16.7 hours duration (Figure 7.3). This specific time window was selected because it aligns with the beginning of log movement recorded by the GPS trackers. By focusing on this specific time frame, the aim was to capture the hydrological conditions that directly triggered the movement of logs within the watershed. For the Flagogna reach, the discharge hydrograph was generated by conducting an unsteady-state simulation using the ORSA2D model (Petaccia et al., 2016) of the previously described event within the Cornino reach. The resulting output hydrograph (Figure 7.3) from the Cornino simulation was utilized as the upstream boundary condition for the Flagogna reach. While this approach is justified by the short distance between the downstream part of the Cornino reach and the upstream part of the Flagogna reach, 3 *km*, it is important to note that a significant confluence occurs between these two reaches, where the Ledra stream flows into the Tagliamento River. This confluence, which discharge is unknown, introduces a variability in the flow characteristics, leading to a certain level of uncertainty. At the Flagogna reach inlet, the Tagliamento River splits into multiple channels, distributing the flow across four inlets: the main channel and three secondary channels. The flow distribution was scaled using the factor $Bh^{5/3}$, which is derived from the Manning formula for uniform flow.

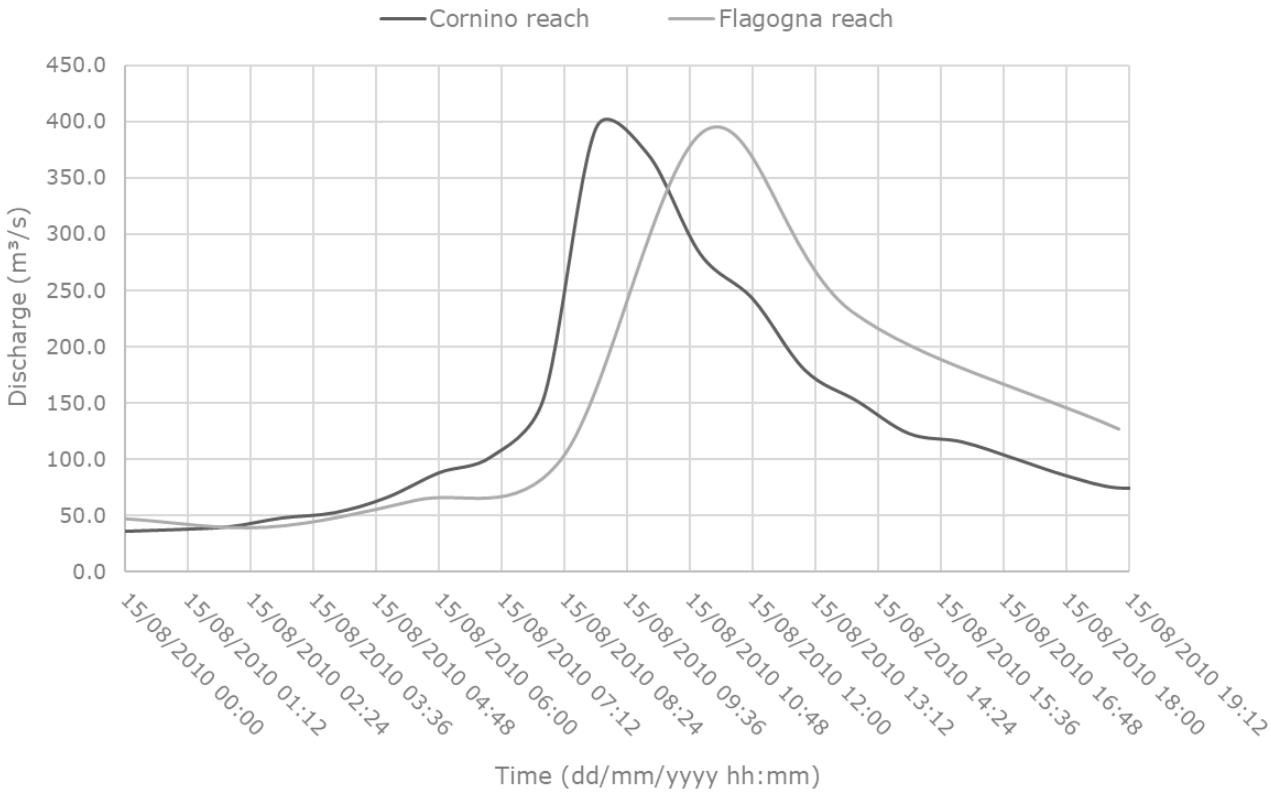

Figure 7.3 Simulated discharge hydrograph for the Cornino reach (in black) and Flagogna reach (in grey).

7.5. Numerical model setup

7.5.1. Topographic data

The ORSA2D_WT model was configured using topographic data, spatially distributed roughness values, and initial boundary conditions for the entire extension of the Cornino and Flagogna reaches (3.5 *km* each). The physical domain's topography was derived from a LiDAR survey (Digital Terrain Model -DTM- 0.5 *m* spatial resolution) conducted in June 2010 (Figures 7.4a, 7.4b). These high-resolution elevation data enabled the generation of an unstructured triangular mesh with a 5 *m* element size for each study reach, resulting in 136,054 elements for Cornino and 126,375 elements for Flagogna. The mesh resolution was selected to resolve terrain variations, ensuring accurate representation of morphological features such as bars, channels, and banks while optimizing computational time. Roughness coefficients were assigned based on two criteria: (1) channel bed grain size and (2) land use characteristics. For the channel bed, grain size distributions were obtained from (Bertoldi et al., 2010), which identified gravel as the dominant sediment (mean grain size = 40 mm; sand fraction ≈ 20%). The Manning's roughness coefficient (n) for the channel was calculated using the Federal Highway Administration (FHWA) empirical relationship for gravel-bed rivers, where n is expressed as a function of the median grain size (D_{50}). This yielded a channel bed roughness coefficient of 0.027 s $m^{-1/3}$. For floodplain areas, roughness values were assigned according to land use classifications following Cowan's (1956) methodology. The Manning's coefficients for distinct land cover types are summarized in Table 7.2. While the assigned Manning's coefficients reflect channel and floodplain heterogeneity, the influence of roughness uncertainties on LW entrainment thresholds was not explicitly assessed. This decision stemmed from constraints in field data resolution, particularly the absence of localized measurements for bed roughness variations.

The model's initial conditions were established through an initial steady-state simulation using a constant discharge of $Q = 27\ m^3\ s^{-1}$, corresponding to the discharge calculated based on the pre-flood water level recorded at the hydrological station of Venzone (Eqs. 7.1,7.2 and 7.3). The unsteady simulation was then initiated from these steady-state conditions, incorporating the time-varying hydrographs shown in Figure 7.3. LW transport dynamics were integrated into the unsteady simulation framework. To be consistent with the field data, all the 36 logs surveyed in the Cornino reach, and the 12 logs in the Flagogna reach were included in the model. The logs were modelled as solid cylindrical shapes, with their barycenter at the position detected during the June 2010 campaign. To parameterize LW transport, the model requires input data on log quantities, physical dimensions (diameter, length), initial positions (coordinates of the center of mass), wood density, and orientation with respect to the flow direction. Most of these data were directly available from the field survey by

(Ravazzolo et al., 2015a), apart from the wood density and the initial orientation. To provide a value for these parameters, estimates were performed based on additional information, as described in the next paragraphs.

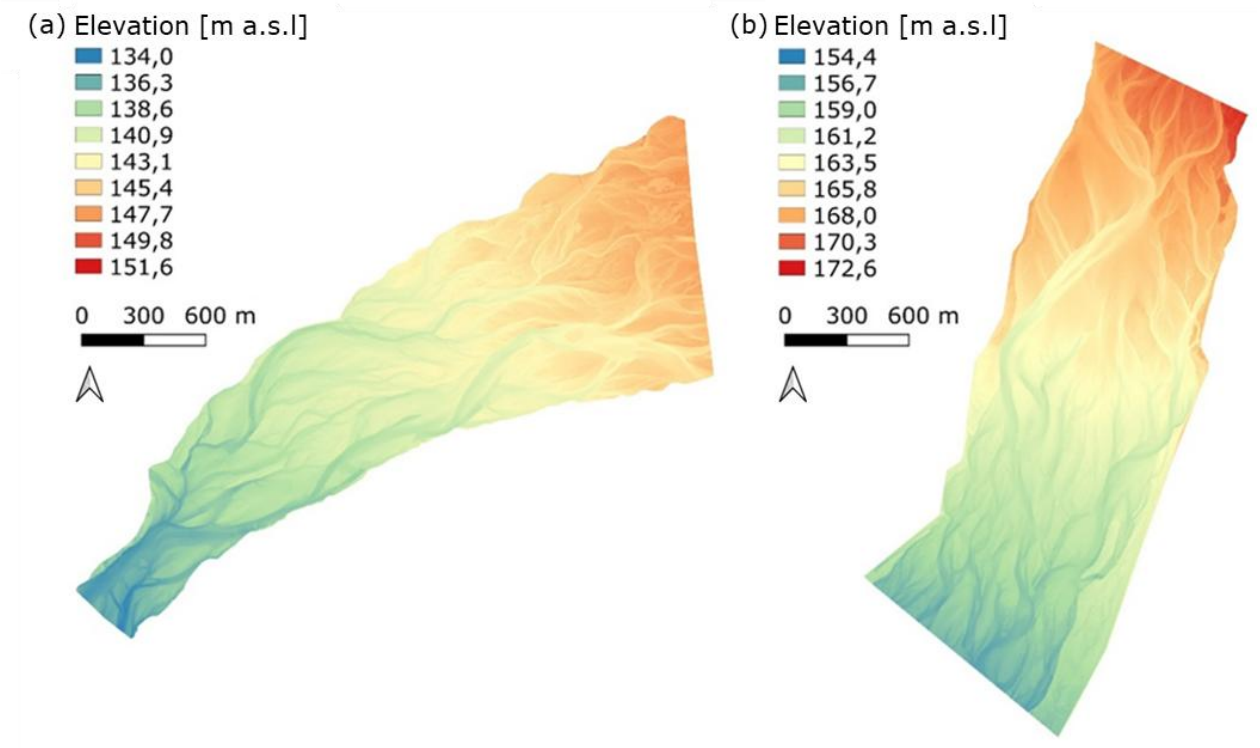

Figure 7.4 (a) DTM of Flagogna reach; (b) DTM of Cornino reach.

Table 7.2 Manning coefficients assigned based on land use.

Land Use	Manning's *n* (s m$^{-1/3}$)
Active channel	0.027-0.030
Pioneer island (Medium-density vegetation)	0.055
Established island (High-density vegetation)	0.100
High bars (Low vegetation)	0.040

7.5.2. Estimation of wood density and initial orientation

Wood density significantly influences buoyancy and transport, requiring accurate estimation to avoid over- or under-predicting log motion (Ruiz-Villanueva et al., 2016a). Although not directly measured during the field survey, wood density was estimated based on data from the most widespread species in the area (*Populus nigra*, *Salix Elaeagnos*, and *Alnus incana*) as documented by Francis et al. (2008). *Populus nigra* and *Salix Elaeagnos* are more commonly found on the islands and floodplains of the Tagliamento River (Sitzia et al., 2016), while *Alnus incana* is prevalent along headwater streams (Gurnell and Petts, 2006). The density values for these species are 616 kg m^{-3} for *Populus nigra*, 789 kg m^{-3} for *Salix Elaeagnos*, and 667 kg m^{-3} for *Alnus incana*, with an average density of 690 kg m^{-3}. Although visual species identification of tagged logs was challenging due to decay and lack of branches, morphological traits and habitat context suggested a predominance of *Alnus incana*.

Consequently, its density (667 kg m^{-3}) was assigned uniformly to model elements. This value falls slightly below the study-area average (690 kg m^{-3}) but aligns with instream wood characteristics. Regarding initial orientation, a general indication of LW orientation relative to the flow direction was provided. To enhance the accuracy of these estimates, orthophotos from the same period (Picco et al., 2015) were used to determine the orientations. If orthophotos were unsuitable, we assumed an initial orientation parallel to the flow direction for the simulation. While this approach provides consistency, it is a simplified representation and may not accurately reflect the true orientation of the logs in the field. Consequently, it is important to note that the proposed orientation values carry a certain degree of uncertainty.

7.5.3. Sensitivity analysis of wood density and initial orientation

To assess the impact of density and initial orientation on LW entrainment and transport a sensitivity analysis was conducted. The analysis focused on logs F1 and F12, which were equipped with GPS trackers, enabling the monitoring of LW trajectory throughout the study. The initial orientation of these logs was also documented during field observations, ensuring greater accuracy in the reference simulations. To evaluate the influence of wood density uncertainty on numerical simulations, we considered two extreme scenarios: a potential decrease in density due to decay and an increase due to water absorption. Based on experimental data from *Alnus incana* (Ruiz-Villanueva et al., 2016a), we assigned wood densities of 530 kg m^{-3} (dry density, representing the lower bound after drying) and 928 *kg* m^{-3} (wet density, representing the upper bound after prolonged water exposure). These values allowed us to assess the range of variability in wood transport behavior due to density changes. Hereafter, dry density, standard density, and wet density will be referenced as DD, SD, and WT, respectively. The influence of initial log orientation was analyzed by testing 5 distinct configurations: recorded field orientation (baseline scenario), parallel to flow, perpendicular to flow, and oblique to flow (45° and 135°). By systematically varying the initial positioning angle, we aimed to determine its effect on entrainment patterns and transport dynamics under natural flow conditions. This approach enhances our understanding of how orientation-dependent hydrodynamic forces influence LW movement.

7.6. Analysis of the results

7.6.1. Cornino Reach

According to the field campaign, 7 logs moved (only RFID tagged), while 29 remained stationary (18 RFID and 10 RFID-GPS equipped). The enhanced ORSA2D_WT model correctly predicted the entrainment of 5 out of the 7 mobilized LW, while correctly simulating the stationary behavior of 24 out of 29 non-moving LW. Since all the GPS-equipped logs in this reach remained stationary during the August event, it is not possible to directly compare simulated and monitored trajectories. For this reach, we can only compare the simulated trajectories to the "RFID supposed trajectories", based on RFID initial and deposition points, respectively recorded in July and October 2010. It is worth noting that the "RFID supposed trajectories" were estimated following the path of the main flow, or the most probable one, between the initial and the deposition points by (Ravazzolo et al., 2015a) following their field campaign in 2010. Furthermore, the RFID travelled distance was derived based on this path, and not on the initial-deposition points distance. The ORSA2D_WT model demonstrates reasonable agreement with RFID-measured distances (limited to the study area) for most logs, particularly for C1, C27, C31, and C33, where differences (Table 7.3) are ≤ 16.8%. However, significant discrepancies were observed for log C24, for which the simulated distance (102.81 m) underestimated the RFID-estimated distance limited to the study area (509.41 m) by 79.8%. The simulated paths for logs C1 and C32 closely matched the RFID-estimated trajectories, based on channel morphology, as illustrated in Figure 7.5 Additionally, the absence of movement of the remaining logs was further validated by the logs tracked with the GPS devices (i.e., C5, C9, C11, C15, C17, C21, C26 and C35) which remained still during the event, consistently with the simulation results.

Table 7.3 RFID supposed trajectories derived travelled distances versus Simulated travelled distances.

Log ID	RFID Supposed trajectories Travelled Distance [m]	Simulated Travelled Distance [m]	Relative Error Percentage [%]
C1	1914.981	1690.94	-11.7
C24	509.415	102.81	-79.8
C27	1195.251	1208.472	1.1
C31	433.272	421.26	-2.8
C33	896.909	746.05	-16.8

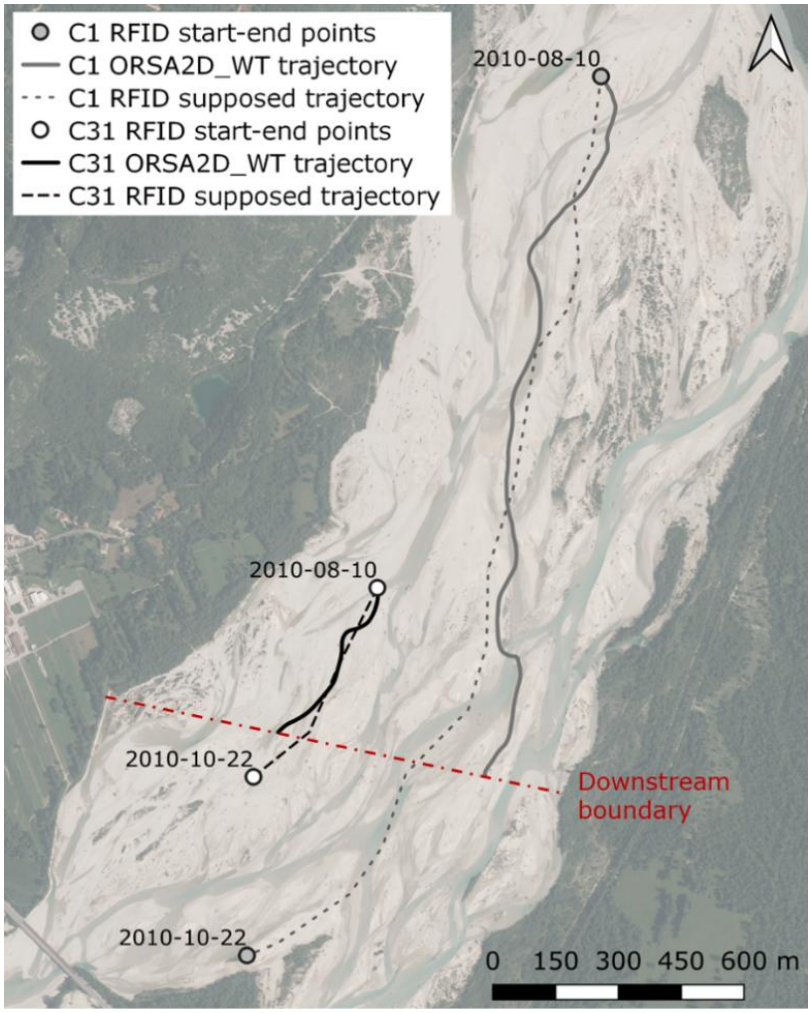

Figure 7.5 Comparison of simulated trajectories with RFID start and ending positions, and "RFID supposed trajectories" for logs C1 and C31. The orthophoto on the background was taken on July 2nd, 2011 (Italian National Geoportal).

7.6.2. Flagogna reach

In Flagogna reach, 12 logs were monitored using RFID tags and GPS trackers. Of these, 4 LW exhibited movement during the event while 8 remained stationary. Regarding entrainment, the simulation correctly identified 3 of the 4 moving logs, resulting in one false negative. Conversely, among the 8 stationary logs, 5 were correctly simulated as stationary while 3 were mistakenly predicted to move (false positives). Overall, the model achieved an accuracy of around 67%, meaning that two-thirds of the logs were correctly classified regarding their initial movement behavior. LW elements F2, F5, F6, F7, and F10 remained motionless throughout the simulation, consistent with both the RFID data and GPS tracker data. The comparison of GPS and simulated trajectories provides further insights. For log F1 (in grey in Figure 7.6), the trajectories were aligned for the first 1300 *m* with Euclidean distances ranging between 5 *m* and 15 *m*. The alignment was maintained until the simulated trajectory drifted toward the hydraulic right in correspondence with a flooded bar, the maximum divergence reaching 68 m. Ultimately, the trajectories converged again with a final

Euclidean distance of less than 8 m. For log F12 (Figure 7.6 in black), the 2 trajectories (GPS vs Simulated) showed variable alignment. For the initial 780 *m,* the Euclidean distance fluctuated between 4 and 35 *m,* indicating a close match. However, as the log approached the upstream section of an island, the trajectories diverged, peaking at a maximum separation of 100 *m* before converging downstream (reducing to a maximum of 30 m). A further divergence occurred 600 *m* before the study area's boundary limit, with the distance peaking at 98 m. These variations suggest that while the simulation effectively captures overall movement patterns, discrepancies are expected near bars or islands, due to complex flow dynamics, including velocity variations, turbulence, and eddies and potential morphological discrepancies between the real riverbed and the numerical domain that influence the log's path. Additionally, an analysis of average velocities (Table 7.4) revealed that the simulated mean velocities of 0.76 $m\ s^{-1}$ and 1.03 $m\ s^{-1}$ for logs F1 and F12, respectively, were generally lower than those recorded by GPS, with discrepancies of 13.6% for log F1 and 7.2% for log F12. This underestimation indicates that the simulation may not fully account for the intricate hydrodynamic forces, especially in regions where the trajectories diverged as logs exit the main flow path. Nonetheless, the similarity between measured and simulated velocities supports the validity of the hydraulic conditions used to replicate the flood event of August 15th, 2010, despite inherent uncertainties in these parameters. Importantly, the log maintained continuous motion throughout the reach, mirroring the GPS-tracked trajectory. An evaluation of the travelled distances further informs the simulation's performance (Table 7.5). For log F1, a minimal relative error of around 2% was found. Similarly, log F12 exhibited a close match, with a relative error of 6.5%. In contrast, log F4 (with RFID tag) displayed a significant discrepancy, yielding a relative error of 33.4%.

Table 7.4 Comparison of the mean velocity of GPS data and simulated values for logs F1 and F12.

Log ID	GPS mean velocity [m s-1]	Simulated mean velocity [m s-1]	Relative Error Percentage [%]
F1	0.880	0.760	-13.6
F12	1.110	1.030	-7.2

Table 7.5 Travelled RFID-GPS derived Distance versus Simulated travelled distances.

Log ID	RFID-GPS Derived Traveled Distance [m]	Simulated Travelled Distance [m]	Relative Error Percentage [%]
F1	2155.171	2113.364	-2.0
F4	2981.135	1983.518	-33.4
F12	3414.170	3191.584	-6.5

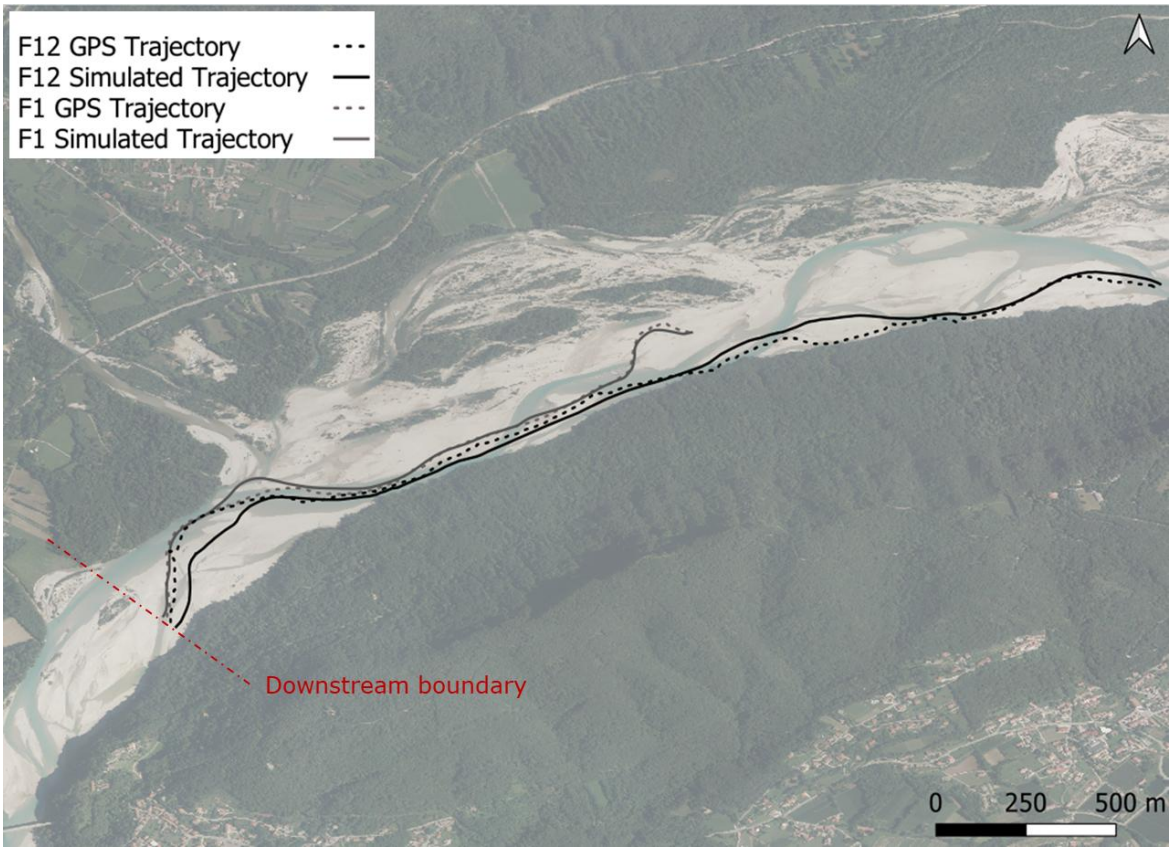

Figure 7.6 Comparison of simulated versus GPS-trajectories (Ravazzolo et al., 2015a) for logs F1 and F12. The orthophoto on the background was taken on July 2nd, 2011 (Italian National Geoportal).

7.6.3. Sensitivity analysis on wood density

The sensitivity analysis of wood density on log transport simulations was conducted by comparing GPS-derived velocities and travelled distances with simulated results under three density conditions: standard (SD), dry (DD), and wet (WD) wood density, for logs F1 and F12, for which the complete GPS trajectory was available. The GPS mean velocity for log F1 was 0.88 $m\ s^{-1}$, while the simulated velocity varied, showing a reduction as wood density increased. Table 7.6 illustrates that under SD conditions, the simulated velocity was 0.76 $m\ s^{-1}$, resulting in a -13.6 % relative error, whereas under DD conditions, it increased to 0.83 $m\ s^{-1}$, lowering the relative error to -5.7 %. However, under WD conditions, the simulated velocity dropped drastically to 0.01 $m\ s^{-1}$, leading to a -98.9 % relative error. Similarly, for log F12, the GPS mean velocity was 1.11 $m\ s^{-1}$, and the simulated velocity under SD and DD was 1.03 $m\ s^{-1}$, yielding a 7.2 % relative error, whereas under WD, the simulated velocity declined to 0.96 $m\ s^{-1}$, increasing the relative error to 13.5 %. Traveled distance followed a similar pattern (Table 6.7), with a reference travelled distance within the study area for log F1 of 2155.17 *m,* and the simulated distance under SD and DD conditions being 2113.36 *m*, resulting in a -1.9% relative error in both cases. However, under WD conditions, the travelled distance reduced drastically to 40.97 *m,* leading to a -98.1% relative error. Likewise, for log F12, the reference travelled distance was 3414.17 *m,* while the simulated distance with SD and DD conditions resulted in 3191.58 *m,*

corresponding to a -6.5% relative error, while WD conditions reduced the travelled distance to 903.24 *m,* increasing the relative error to -73.5%. Figure 8 shows a comparison between GPS trajectories (Ravazzolo et al., 2015a) and simulated trajectories under different wood density conditions, showing the spatial variation in log movement. The simulated trajectories for the lowest densities DD align closely with the simulations based on the standard densities SD and the GPS-recorded trajectory (Figures 7.7a and 7.7b). The trajectories for the highest density WD (Figure 7.7c), although following the same initial path, are much shorter. Overall, the results demonstrate that increased wood density significantly reduces both velocity and travelled distance in simulations, with wet conditions causing the most pronounced discrepancies due to higher resistance to movement.

Table 7.6 GPS mean velocity versus Simulated mean velocity.

Log ID	GPS mean velocity [m s-1]	Simulated mean velocity [m s-1]	Relative Error Percentage [%]
F1 SD	0.880	0.760	-13.6
F1 DD		0.830	-5.7
F1 WD		0.010	-98.9
F12 SD	1.110	1.030	-7.2
F12 DD		1.030	-7.2
F12 WD		0.960	-13.5

Table 7.7 GPS observed Travelled Distance versus Simulated travelled distances.

Log ID	GPS Travelled Distance [m]	Simulated Travelled Distance [m]	Relative Error Percentage [%]
F1 SD	2155.171	2113.364	-1.9
F1 DD		2113.364	-1.9
F1 WD		40.970	-98.1
F12 SD	3414.170	3191.584	-6.5
F12 DD		3191.584	-6.5
F12 WD		903.240	-73.5

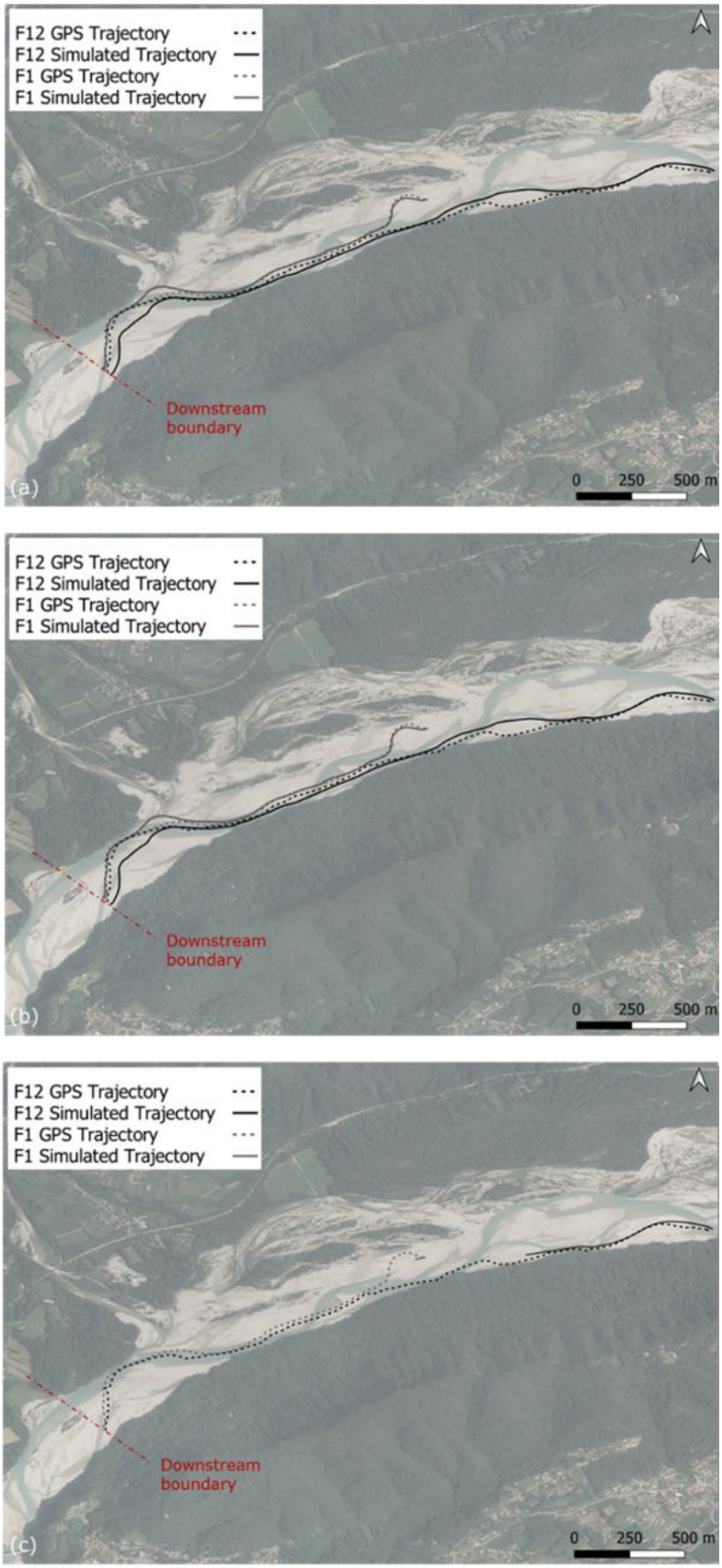

Figure 7.7 Comparison of the GPS trajectories (Ravazzolo et al., 2015a) with the simulated trajectories using (a) dry-wood density, (b) standard density, and (c) wet-wood density for logs F1 and F12. The background orthophoto belongs to the 2012 collection from the Italian National Geoportal (taken on July 2nd, 2011).

7.6.4. Sensitivity analysis on the initial orientation

For log F12, the initial orientation relative to the flow direction had a clear and significant impact on both the timing of entrainment and the total travel distance. Simulations showed that when the log was oriented perpendicular to the flow, it was entrained earlier than in other configurations. This earlier initiation of movement can be attributed to the higher hydrodynamic drag forces acting on the log's surface in this position, making it more susceptible to mobilization. However, despite this early entrainment, the perpendicular orientation resulted in the shortest travel distance, approximately -75.4% lower than the displacement tracked by the GPS device (Table 7.8). In contrast, when the log was oriented parallel to the flow direction matching the original position recorded during instrumentation, it travelled the farthest. This scenario produced a travel distance closely aligned with the GPS data, with only a -6.5% error, indicating strong agreement. Oblique orientations (45° and 135°) resulted in intermediate travel distances, approximately -26.2% lower than the reference. These results suggest that while a perpendicular orientation may promote earlier entrainment due to increased drag, it may also lead to reducing the transport, whereas a parallel orientation, despite delayed mobilization, favors longer displacement. In contrast to log F12, the results for log F1 showed that the initial orientation had a minimal effect on the overall travel distances. The following orientations were tested: the registered original orientation during the LW instrumentation, 30°; 0° with the log parallel to the flow; oblique orientations of 45° and 135°, and 90° with the log perpendicular to the flow. Across all these scenarios, the differences in planar displacement were negligible. The simulated trajectories were nearly superimposed, and only minor variations in travel distance were observed (1.9%).

Table 7.8 Observed GPS Travelled Distance versus Simulated travelled distances for log F12.

Orientation scenario	GPS Travelled Distance [m]	Simulated Travelled Distance [m]	Relative Error Percentage [%]
Baseline	3414.170	3191.584	-6.5
Parallel to flow		3191.584	-6.5
Perpendicular to flow		837.900	-75.4
Oblique to flow		2518.723	-26.2

7.7. Discussion

The numerical simulations of LW transport during August 15th, 2010, in the Tagliamento River, provided valuable insights into the dynamics of log movement and entrainment. Despite the limited number of logs modelled, across both reaches-36 and 12 respectively- the model successfully predicted the entrainment of 8 out of 11 logs that were observed to move during the event, with an error rate of around 27% for entrained logs. Additionally, the model accurately simulated the stationary behavior of 29 out of 37 logs that remained immobile, resulting in an error rate of around 22% for non-entrained logs. Overall, the model achieved a mean error rate of 24%, indicating a reasonable level of accuracy in replicating LW dynamics giving the simplification of the LW elements' representation in the model, highlighting areas where the model's predictive capabilities can be improved in the future.

The comparison between simulated and RFID- supposed trajectories derived travel distances (limited to the downstream boundary line) revealed an average error of 26% across both reaches. This deviation in travel distances can be attributed to the fact that the second RFID survey was conducted on October 21st, 2010, after three additional flood events comparable to the simulated one. These subsequent events may have caused secondary movements of the LW elements. Since this study focused on replicating the behavior of logs during a single event, the potential influence of multiple flood events on log dynamics was not fully captured. To address the overall motion of LW more comprehensively, future simulations should incorporate all events capable of log entrainment, eventually extending the numerical domain to include the entire area crossed by LW. This approach would help reduce uncertainties caused by the underestimation of cumulative log movements. However, such multi-event simulations require careful planning due to the significant enlargement of the domain and to the computational time involved. Some logs, i.e., C8, C13, C25, C28, C33, F8, F9, and F11 remained stationary throughout the whole investigation period according to the RFID or GPS data, while they moved in our simulations. The reasons for the stillness of the surveyed logs can be identified through the analysis of the field monitoring data from June 2010, and of the orthophotos of the same period. The stationary logs in the Cornino reach were part of wood accumulations of variable size, each consisting of multiple elements in contact with each other. The logs in the Flagogna reach (F8, F9 And F11) were entire trees, acting as key-logs (Collins and Montgomery, 2002) of accumulations comprised of buried material interspersed with fine surface branches (Figure 7.8). In the numerical model these logs were considered as single LW, thus disregarding the connection with other elements and their partial burial. Cadol and Wohl (2010) suggest that logs in wood accumulations tend to resist movement and remain stationary for extended periods. Moreover, their

mobilization would require a flood event of higher magnitude than the one considered in the simulation, since the presence of multiple logs clustered together creates additional friction and resistance to movement, making them less susceptible to displacement by moderate flood flows. In addition, it appears that the partial burial effectively immobilizes the logs despite the flood flow. This is consistent with the observations by Ravazzolo et al. (2015b) that in the Tagliamento River the frequency of the fluctuations in the flow discharge causes an increase in local scour and deposition around LW elements, which increases their resistance to entrainment. Furthermore, Merten et al. (2010) highlight the role of buried material and surface branches in anchoring wood pieces and impeding their movement during flood events. Additionally, the presence of root wads and branches further anchors the logs to the riverbed, making them more prone to remain stationary. This observation is supported by Gurnell (2003) and Welber et al. (2013), which emphasize the influence of root wads and branches in stabilizing wood accumulations and preventing their mobilization. Therefore, these discrepancies in LW behavior are produced by a poor replication in the numerical model of the attachment of the logs to other elements, or of their partial burial. Although in this specific case study such discrepancies could have been reduced by artificially imposing restrictions on the non-moving logs, in other real-case simulations where such information is not available, an alternative approach is required. This approach should consider the possibility that some logs may be attached to other elements, making them unavailable or more resistant to entrainment. Further factors contributing to the uncertainty in predicting LW movement include the under- or over-estimation of wood density. Wood density varies significantly depending on the tree species and waterlogging , and can be far from that of fresh dry wood because of mass loss from decay processes or water absorption (Hlavňa et al., 2024), In the Tagliamento River, the simplified assumption of a single density value for all the modelled LW elements could have caused some of the discrepancies between simulated and observed behavior, as denser logs would be more resistant to movement and less likely to be entrained by the flow.

The Tagliamento River is a highly dynamic braided system, where morphodynamic processes such as sediment transport, channel shifting, and local scour play a crucial role during flood events (Bertoldi et al., 2010). These processes can influence LW dynamics by reshaping the channel morphology, forming new deposition areas, and altering flow patterns (Ruiz-Villanueva et al., 2016c). In this study, we adopted a fixed-bed configuration, sediment transport, bank erosion, and bedform evolution were not accounted for dynamically during the simulation of the flood event. However, such changes in channel morphology can influence LW transport by affecting local flow velocities, modifying potential retention zones, and shifting entrainment thresholds. While the dynamic simulation of morphologic evolution would provide a more realistic representation of LW behavior,

it was beyond the scope of our model. Moreover, incorporating morphodynamic evolution remains a complex task, particularly in terms of calibration and validation, and would introduce additional sources of uncertainty to the results presented here.

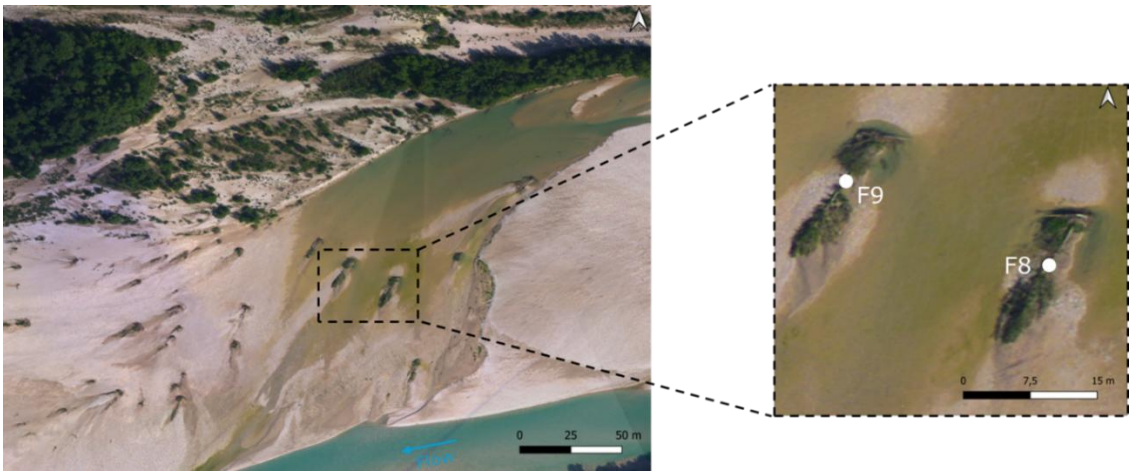

Figure 7.8 Presence of root wads and branches for logs F8 and F9. The background orthophotos were taken in 2010 (Picco et al., 2015).

Hydrological data can be a source of uncertainty in LW transport modelling as well (Ruiz-Villanueva et al., 2014b), especially in dynamic river systems like the Tagliamento River. The lack of reliable discharge measurements, compounded by the active gravel bed of the Tagliamento, makes it challenging to obtain precise flow data. In braided river systems, such as the Tagliamento River, complex morpho dynamics, shallow branching flows, and mobile bed topography further complicates the collection of accurate hydraulic data (Williams et al., 2013). These systems frequently experience shifts in channel patterns, resulting in highly variable flow conditions that are difficult to capture with conventional methods. Additionally, the absence of a hydrological station and the resulting uncertainty in the generated hydrograph, which served as the upstream boundary condition for the Flagogna reach, aggravate the issue, as simulations without accurate, high-resolution hydraulic data may fail to reflect the real-world behavior of wood movement, leading to discrepancies between predicted and observed behavior. All the factors discussed above collectively represent a significant source of uncertainty on LW trajectories, entrainment and deposition modelling.

The sensitivity analysis of wood density provides additional insight into how density variations influence LW transport, particularly in terms of velocity, travel distance, and entrainment timing. Simulations using standard (SD), dry (DD), and wet (WD) density scenarios, compared with GPS-tracked data for logs F1 and F12, demonstrate that SD and DD conditions yield the most accurate results, with lower relative errors. In contrast, the WD scenario leads to shorter trajectories and reduced velocities, underscoring the impact of higher moisture content on transport behavior. The

earlier entrainment of logs under the DD scenario reflects the lower buoyancy of drier wood, making it more susceptible to mobilization. This observation is consistent with the findings of Braudrick and Grant (2000) who stated that a decrease in LW density reduces the water depth required for entrainment, leading to earlier movement. This highlights the importance of incorporating realistic density values in transport models. Even small deviations in wood density can alter model outcomes, emphasizing the need for precise parameterization to improve predictive accuracy. Our findings align with the findings of Wilcox and Wohl (2006), who demonstrated that increased LW density significantly enhances resistance to movement, suggesting that as wood density increases, its mobility decreases. Similarly, emphasized the impact of wood density on LW buoyancy and mobility, underscoring the importance of accounting for density variability in LW dynamics models. Wood density plays a critical role in determining the movement and final disposition of logs in river systems. While lighter logs may travel further due to their lower density, other factors such as entrainment timing, flow velocity, and log rotation also significantly influence LW behavior. The earlier entrainment of logs with dry density (DD) further highlights the complex interplay between density, buoyancy, and hydrodynamic forces in shaping log transport dynamics.

The analysis of initial log orientation revealed contrasting behaviors between the two modelled logs, underscoring the context-dependent nature of LW transport. Log F1 exhibited minimal variation in trajectory across different initial orientations, primarily due to its starting position near the main flow. Upon entrainment, it quickly entered the zone of maximum velocity, enabling it to rotate and align parallel to the flow direction. This alignment was maintained throughout its transport, effectively reducing the influence of its initial orientation.

On the other hand, log F12 experienced varying entrainment and transport modes, depending on its initial orientation. When positioned parallel to the flow, log F12 faced minimal drag due to its streamlined alignment, which enabled it to remain in the high-velocity zone, avoiding areas prone to deposition. This orientation facilitated a more efficient downstream movement, allowing the log to navigate with fewer interruptions. Conversely, when it was oriented perpendicular or oblique to the flow, the increased drag caused by the larger frontal area limited its movement. The log remained in a low-velocity zone near the riverbank, where various factors such as obstacles and shallow water increased the likelihood of early deposition. These findings are in line with Ruiz-Villanueva et al. (2014a), who observed that LW pieces aligned parallel and oblique to the flow direction exhibit a tendency to be carried along the path of maximum velocity in their original orientation. Additionally, Schalko (2018) stated that LW pieces transported with an orientation parallel to the flow direction exhibit a notably lower probability of deposition compared to other orientations therefore higher

travel distances. Although direct field evidence of entrainment mechanisms was lacking, simulation results suggest that orientation also affects how motion initiates. Perpendicular logs tended to roll and initiate movement earlier, while parallel logs were more likely to slide and entrain later. These outcomes are consistent with the experimental findings of Bocchiola et al. (2006), offering indirect support for the simulated motion types. In summary, while initial orientation plays a key role during entrainment particularly in determining the onset and mechanism of motion its influence decreases during transport, where flow velocity and channel positioning become the dominant controls.

Chapter 8

Field monitoring of Large Wood Transport in the Allier River

8.1. Abstract

This chapter presents the field monitoring campaign undertaken on the Allier River (France) to provide empirical data for understanding LW dynamics under natural flood conditions. Unlike controlled flume experiments, field-scale observations capture the complexity of wood recruitment, transport, and deposition processes in morphologically diverse and vegetated rivers. The study, carried out by (Hortobágyi et al., 2024a) employed radio-frequency identification (RFID) technology to tag and track individual logs. During the PhD stay abroad in 2024, I took part in a field campaign for tracking LW post a flood event, supported by complementary measurements of sediment grain size distribution and wood density The activities for this specific field campaign were planned together with the research group of Environment, city and society laboratory located at ENS de Lyon and Veodis 3D a consultancy expert in fluvial geomorphology . These methods enabled the collection of spatially and temporally explicit datasets on LW mobilization, travel distances, deposition sites, and stabilization mechanisms. The monitoring campaign carried out by (Hortobágyi et al., 2024a), from 2020 to now, spans multiple flood seasons, capturing both moderate and high-flow events, and revealing critical insights into the behavior of LW in a large, dynamic river system. Results highlight the influence of channel morphology, flood magnitude, and wood characteristics on entrainment and deposition patterns. Tagged logs exhibited a wide range of mobilities, from short-distance displacements to several-kilometer-scale transport, often with repeated phases of motion and rest. Deposition was frequently associated with geomorphic features such as point bars, islands, and floodplain vegetation, and was enhanced by processes such as partial burial and snagging. Sediment analyses provided context on bed roughness and channel resistance, while density measurements confirmed the heterogeneity of buoyancy conditions among wood pieces. The outcomes of this field monitoring will directly inform the application of the enhanced ORSA2D_WT model to the Allier River in the subsequent chapter.

8.2. Study area

Between August 2024 and September 2024, I took part to the preparation and field monitoring on the lower Allier River in central France (Figure 8.1a), focusing on a ~50 *km* meandering reach situated partially in the Val d'Allier Natural National Reserve, region limited upstream by the Contigny bridge and downstream by “le Veurdre”.” (Figure 8.1b). The Allier River is a major tributary of the Loire, originating in the Massif Central at an elevation of 1485 *m* and flowing 410 *km* northward to join the Loire at about 140 *m* elevation. Throughout the study area, the river exhibits a dynamic planform with active lateral migration and a well-developed floodplain. The channel is typically about 60 *m* wide on average, with a sinuous to locally braided pattern featuring multiple gravel bars and vegetated islands. Bank erosion is frequent due to the river’s natural mobility, yielding lateral channel shifts on the order of 0.2–0.9 hectares per *km* of bank per year. This active geomorphic setting is largely free of major engineering structures, aside from legacy infrastructure such as the Contigney rail bridge at the upstream end. The riparian corridor, much of which lies within the nature reserve, is characterized by a heterogeneous mosaic of vegetation ages, reflecting the river’s active dynamics. Mature poplar, willow, and oak stands occur alongside recently rejuvenated patches and eroding margins, together supplying LW through bank undercutting and channel avulsion during floods (Hortobágyi et al., 2024c).

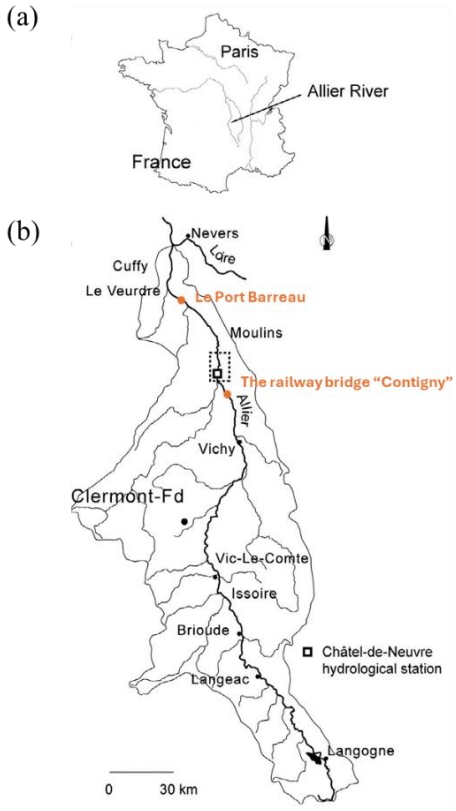

Figure 8.1 Location of the Allier River catchment in France, including major tributaries, towns, and the Châtel-de-Neuvre hydrological station (from Hortobágyi et al., 2024b , modified by the author) .

Hydrologically, the Allier is characterized by a flashy pluvial regime with high flows in winter and spring. The mean annual discharge at the Châtel-de-Neuvre gauging station (drainage area ~12,400 km^2) is approximately 114 $m^3\ s^{-1}$. Floods of 2-year recurrence (Q2) reach around 560 $m^3\ s^{-1}$, and 10-year floods (Q10) give a discharge around 940 $m^3\ s^{-1}$. Bankfull conditions are typically associated with the dominant flood (approximately the 1.5-year flood, Q1.5), which in this reach is on the order of a few hundred $m^3\ s^{-1}$ and corresponds to the stage at which the river begins to inundate its floodplain (Hortobágyi et al., 2024c). Overbank flooding is relatively frequent due to the minimal incision of the channel, allowing large floods to disperse into the floodplain and interact with riparian forests. The study period (2020–2024) included several notable floods, including a March 2024 event that reached a peak discharge of 690 $m^3\ s^{-1}$ (a moderate to large flood for this river) and caused extensive inundation of the active corridor (Figure 8.2). Hydrological conditions create a highly dynamic wood regime: LW is recruited during bank erosion episodes and can be transported downstream or stored locally depending on the magnitude of the flood, duration, and the presence of trapping features. Hortobágyi et al. (2024) performed surveys using aerial imagery and field inventories and they documented wood piece densities on the order of 59–164 trunks per *km* in the lower Allier. Hortobágyi et al. (2024) attributed this to the river's energetic lateral erosion and avulsion processes, which recruit an estimated 58 m^3 of LW per *km* of river length annually. The combination of plentiful wood supply and frequent overbank floods leads to numerous log accumulations. Furthermore, Hortobágyi et al. (2024) report log-jam frequencies of approximately 3–12 jams per *km* on the Allier, often formed when entrained logs snag on channel banks or island vegetation. Once deposited, wood may be partly buried in sediments or entangled in vegetation, increasing its residence time until sufficiently large flows occur.

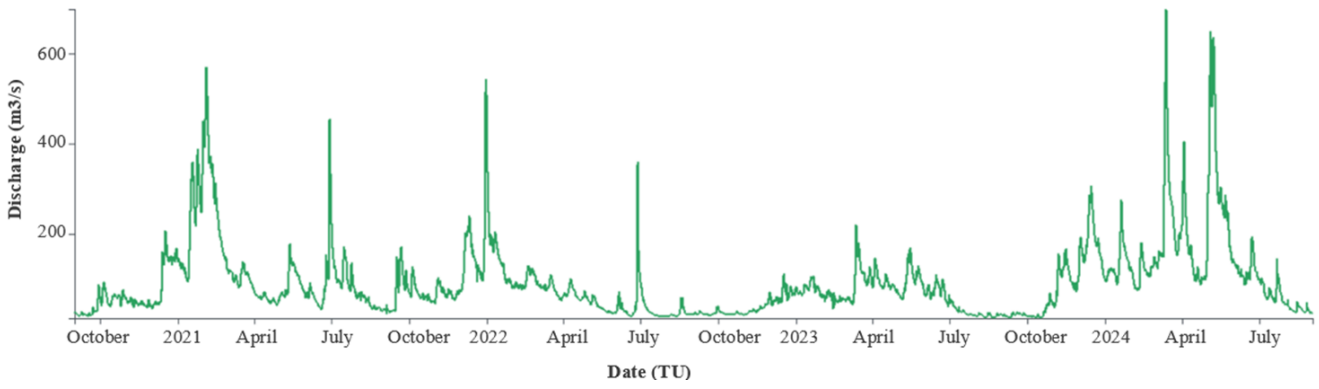

Figure 8.2 Discharge time series from September 2020 to September 2024 obtained from the French Hydro-Portal (https://hydro.eaufrance.fr/).

8.3. Methodology

Ongoing monitoring efforts by Hortobágyi et al. (2024) has been conducted since 2020 along a 50 *km* reach of the Allier River downstream of the Contigny railway bridge. The campaigns focused on tracking LW dynamics following major floods through annual post-event RFID search campaigns. In each campaign, RFID-tagged logs were relocated and their new coordinates systematically recorded, enabling the reconstruction of transport distances and deposition sites. The present PhD research included participation in the fieldwork and post-flood data analysis carried out in summer 2024, following the March 2024 Q5 flood event. The contribution included assisting with RFID search and recovery of tagged logs within the floodplain and active channel, as well as recording detailed wood characteristics. These included log dimensions, presence of roots or branches, degree of burial in sediments, and whether the piece was integrated into a jam structure. To acquire additional information useful for LW numerical modelling, grain-size analyses on representative bar surfaces and wood density estimations from sampled logs were also carried out, to provide additional insights into the depositional context and buoyancy properties of the transported material. In addition to field measurements, data analysis to quantify displacement distances and evaluate deposition patterns was also performed. This combined approach provided first-hand insight into how floods mobilize stored wood and redistribute them across bars, banks, and floodplain zones. By systematically documenting both positional changes and morphological attributes of the logs, it was possible not only to estimate transport rates but also to assess how wood form, density, and condition influenced stability, mobility, and the likelihood of entrapment.

8.3.1. Field monitoring and preliminary simulations

In 2020, an initial set of naturally occurring LW pieces (primarily tree trunks and large branches exceeding 1 *m* in length and 0.1 *m* in diameter, in addition to standing trees) within the active channel and flood plain were equipped with passive RFID tags (Hortobágyi et al., 2024a). Each tag (Figure 8.3) was embedded into the wood by drilling and inserting. This tagging technique has been successfully applied in other rivers to track log displacement during floods (Ravazzolo et al., 2015a). A total of 280 logs were tagged upstream the 50 *km* study reach, just downstream of the Contigny railway bridge, focusing on pieces situated on bar surfaces, mid-channel islands, or concave banks subject to erosion that were likely to be mobilized by future floods. The geographic coordinates of each tagged log initial position were recorded with an RTK (Real-time kinematic positioning) GPS unit (± 1 *cm* accuracy) at the time instrumentation while a handheld GPS was used later on during the search campaigns (± 2-3 *m* accuracy). Key attributes such as log length, diameter, and orientation relative to flow were noted during this baseline survey.

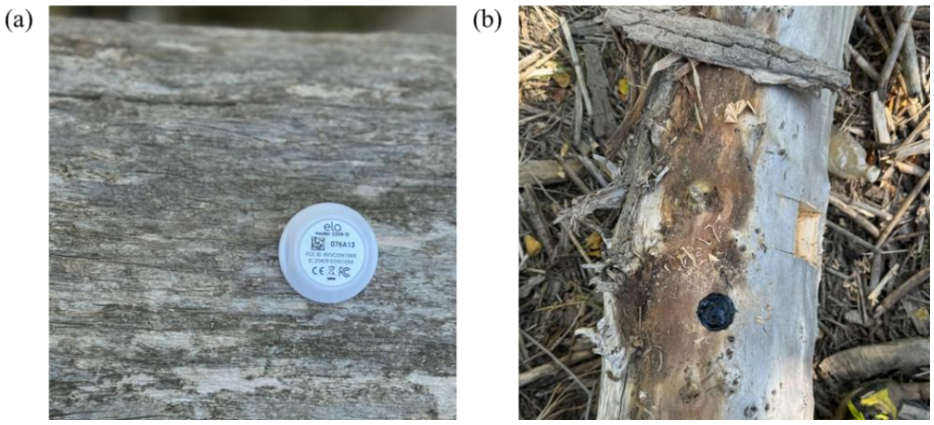

Figure 8.3 (a) RFID tag used for LW tracking and (b) its insertion into a log (photos taken by the author during the field survey conducted in August 2024).

Following the instrumentation, field surveys were conducted inter-annually during low flow seasons, to locate and recover the tagged logs, according to the timeline below:

- Campaign 1: June 2021
- Campaign 2: October 2021
- Campaign 3: February 2022
- Campaign 4: September 2023
- Campaign 5: August 2024

Specifically, during the August 2024 field campaign the research methodology consisted of traversing the river corridor on foot (Figure 8.4a) and by boat equipped with portable RFID receivers (Figure 8.4b). The RFID reader antenna, when passed within a few meters of a tagged log, detects the unique tag ID, emitting an audible signal.

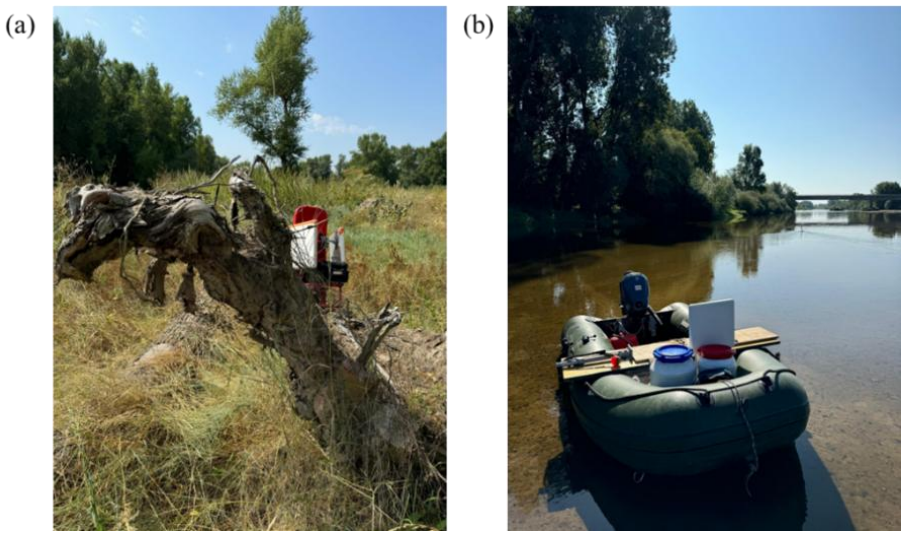

Figure 8.4 (a) Portable RFID detection system carried in a backpack equipped with an antenna and (b) inflatable boat equipped with portable RFID receivers for LW tracking (photos taken by the author during the field survey in August 2024).

To aid with the RFID search, hydraulic modeling was used to simulate flood conditions and identify likely zones of wood movement. A two-dimensional unsteady flow model was set up for the study reach using HEC-RAS 2D (Version 6.7) to replicate the March 2024 (Figure 8.2) flood hydrograph, which was the largest event during the 2023-2024 interval. The model domain covered approximately 32 *km* of the river, centered on the most active portion of the reach (this length was chosen to balance resolution and computational load). The topographical domain was obtained by integrating two topographic data sources: recent LiDAR surveys (0.5 *m* DEM from 2023, Figure 8.5a), and ground-surveyed cross-sectional profiles of the channel (at ~200 *m* spacing along bends from 2023, Figure 8.5b). These data were merged to produce a continuous elevation model of the channel and floodplain, with break lines used along high banks to enforce terrain edges. A computational mesh (Figure 8.5c) was generated with variable grid resolution: a fine cell size (2 *m* grid spacing) was used in the active channel and primary overbank areas to capture flow detail, and coarser cells (10–20 m) on the outer floodplain extents. The resulting mesh contained about 2.5 million cells covering the 32 *km* reach. The model was driven by the recorded flood hydrograph from the upstream gauge. The March 2024 event was modelled using as input the rising limb, peak, and falling limb flows (peak discharge on 12 March 2024 on the order of 700 $m^3\ s^{-1}$) at the upstream boundary, and imposing normal depth or a stage-discharge relation at the downstream boundary (far enough downstream to avoid backwater effects in the area of interest). The simulation was run in unsteady mode over the entire flood duration (~5 days) with a 1-2 second step to ensure numerical stability. Channel roughness (Manning's n) was assigned spatially: initial values around 0.035–0.045 $m^{-1/3}s^1$, for the active channel (gravel bed) and higher (0.08–0.15 $m^{-1/3}s^1$) for vegetated floodplain areas, adjusted iteratively. This initial simulation was not calibrated; rather, it was conceived as a preliminary tool to support the field search campaign. Its primary purpose was to provide indicative insights into the flow dynamics, particularly by approximating the velocity field, thereby guiding and optimizing the planning and execution of the on-site activities. Once in the field, by systematically sweeping likely deposition zones (guided the preliminary simulation results), we pinpointed the new positions of as many RFID-tagged logs as possible. For each relocated piece, a GPS position was recorded and registered, and the log condition was documented (e.g. whether it was part of a jam, buried in sediment, or stranded singly, length, diameter, orientation relative to the flow…).

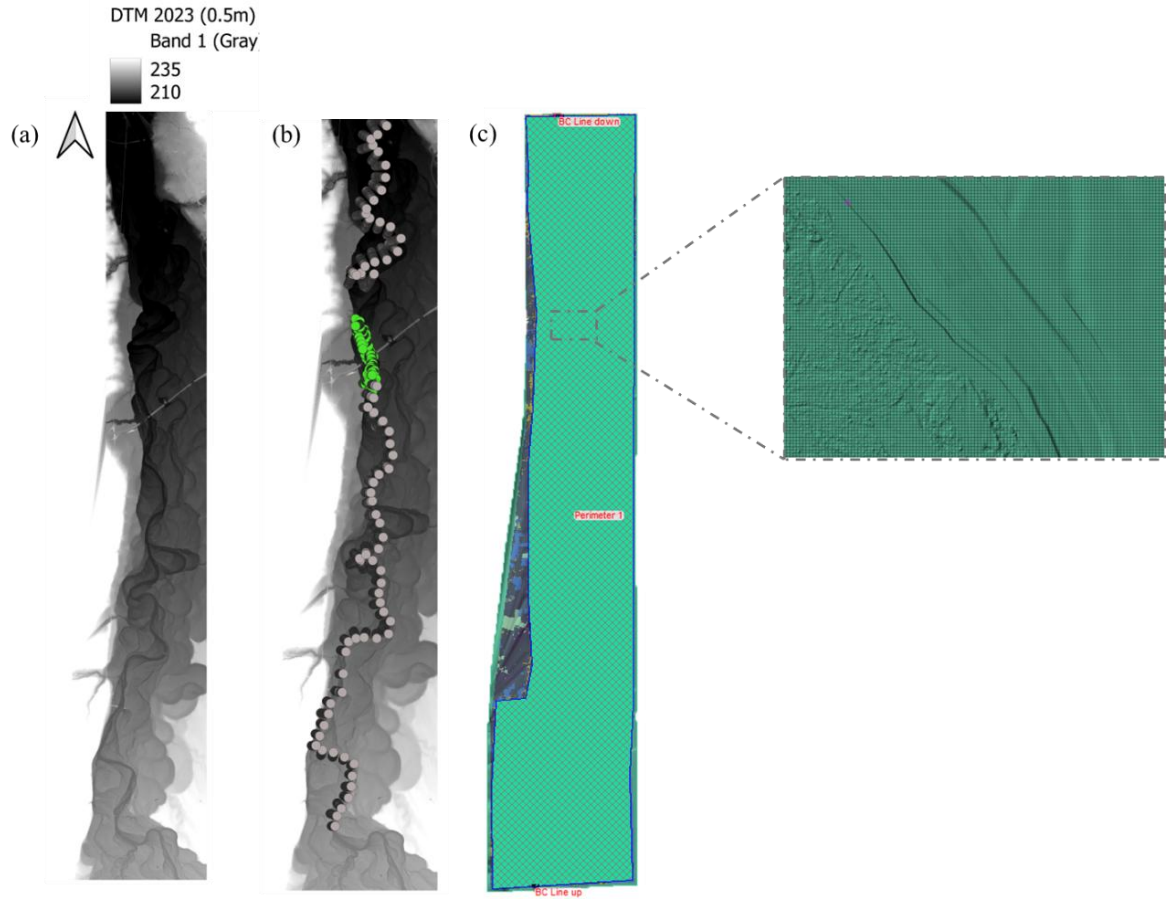

Figure 8.5 (a) Digital Terrain Model (DTM) from 2023 at 0.5 *m* resolution, (b) bathymetric surveys with data from 2020 (grey) and 2023 (green), and (c) computational mesh generated for hydraulic modelling.

8.3.2. Sediment grain size analysis

In parallel with wood tracking, the surface sediment texture of river bars and banks, where LW tends to deposit, was also characterized. Grain-size distributions of bar sediments were determined using a combination of digital image analysis and traditional Wolman pebble counts (Wolman, 1954). These data were used to derive more accurate estimates of Manning's roughness coefficients, providing essential input for the coupled hydraulic–wood transport simulations. It is important to note that sediment analysis was not carried out across the entire 50 *km* monitoring reach but was instead focused on an 8 *km* stretch immediately downstream of the Châtel-de-Neuvre hydrological station (Figure 8.6). This sub-reach was selected because it constitutes the core area of interest for LW transport simulations, which will be discussed in detail in Chapter 9. Six representative point bars within this section were sampled to capture the variability in bar surface textures (Figure 8.6). The Wolman pebble count was carried out at two representative sites (point bar 1 and 4), a transect-based sampling design was implemented (Figure 8.7a). Each transect was established using a tape measure, with a fixed length and fixed sampling interval so that point spacing remained constant along the entire transect. At each point the surface clast located directly under the toe of the sampler's boot or

a marked rod was selected, thereby minimizing sampling bias. The intermediate axis (b-axis) was measured to the nearest millimeter using a gravel template or caliper. This procedure was repeated until at least 100 clasts per site were recorded, a sample size widely considered sufficient to obtain reliable estimates of median grain-size (D_{50}). Clasts larger than 256 mm (boulders) were recorded as "greater than 256 mm," while particles finer than 2 mm (sand fraction) were noted as "less than 2 mm," as these are below the resolution of the method. In addition, high-resolution photographs of the gravel surface were taken vertically downward at multiple locations per plot. A rigid meter of known dimensions was placed to provide scale in each image (Figure 8.7b). Using these images, automated grain size analysis techniques was applied: the photographs were processed with the image analysis software MIPAR to detect individual grains and calculate their sizes based on the scaling (Figure 8.8). The digital photo method allowed capture of smaller size fractions and a continuous grain size distribution, complementing the manual counts which are typically biased toward coarser clasts.

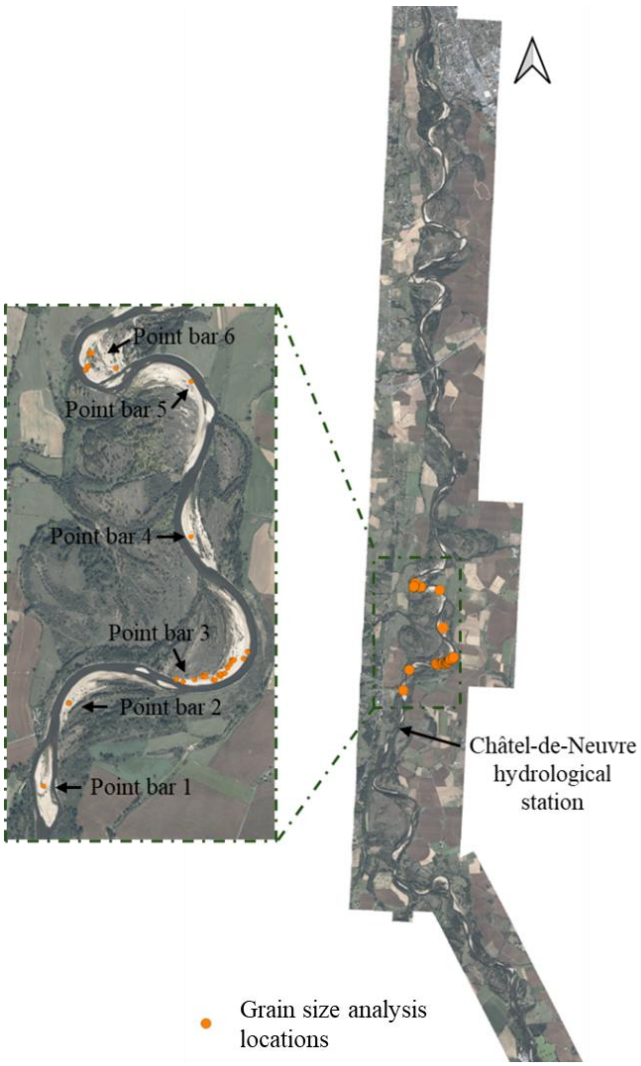

Figure 8.6 Location of pebble count surveys along the Allier River with highlighted point bars (1–6) and the Châtel-de-Neuvre hydrological station.

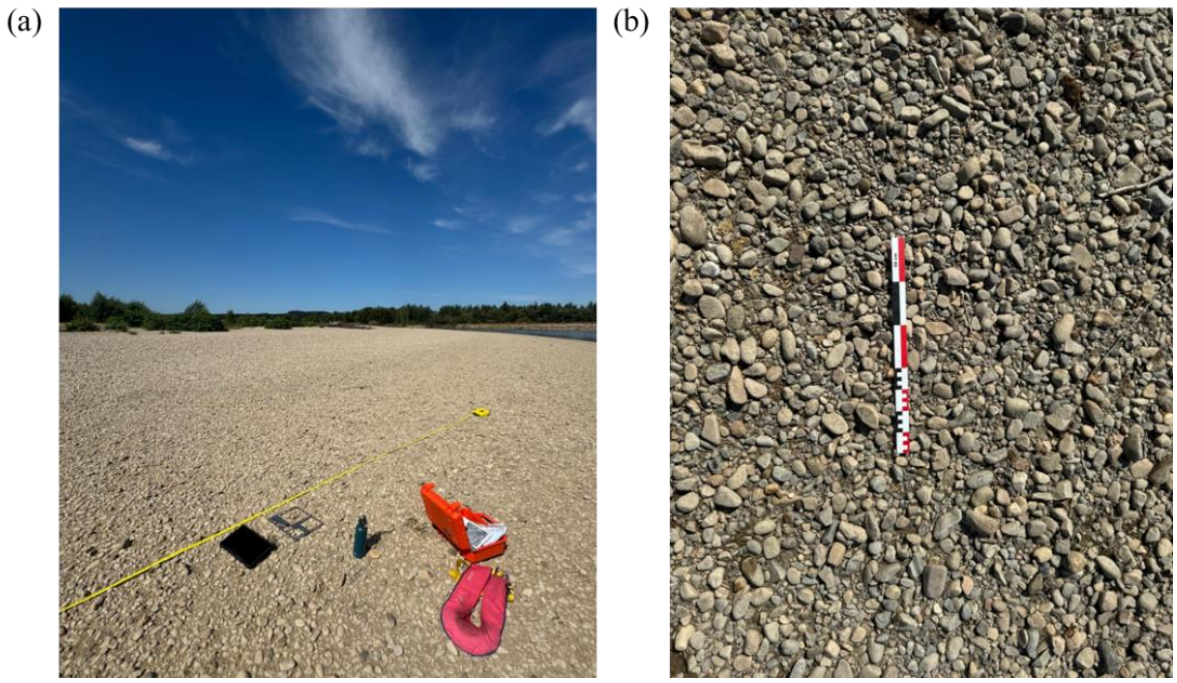

Figure 8.7 (a) Field setup for performing a traditional Wolman count and (b) digital photograph acquisition for automated grain-size analysis (photos taken by the author during the field survey in August 2024).

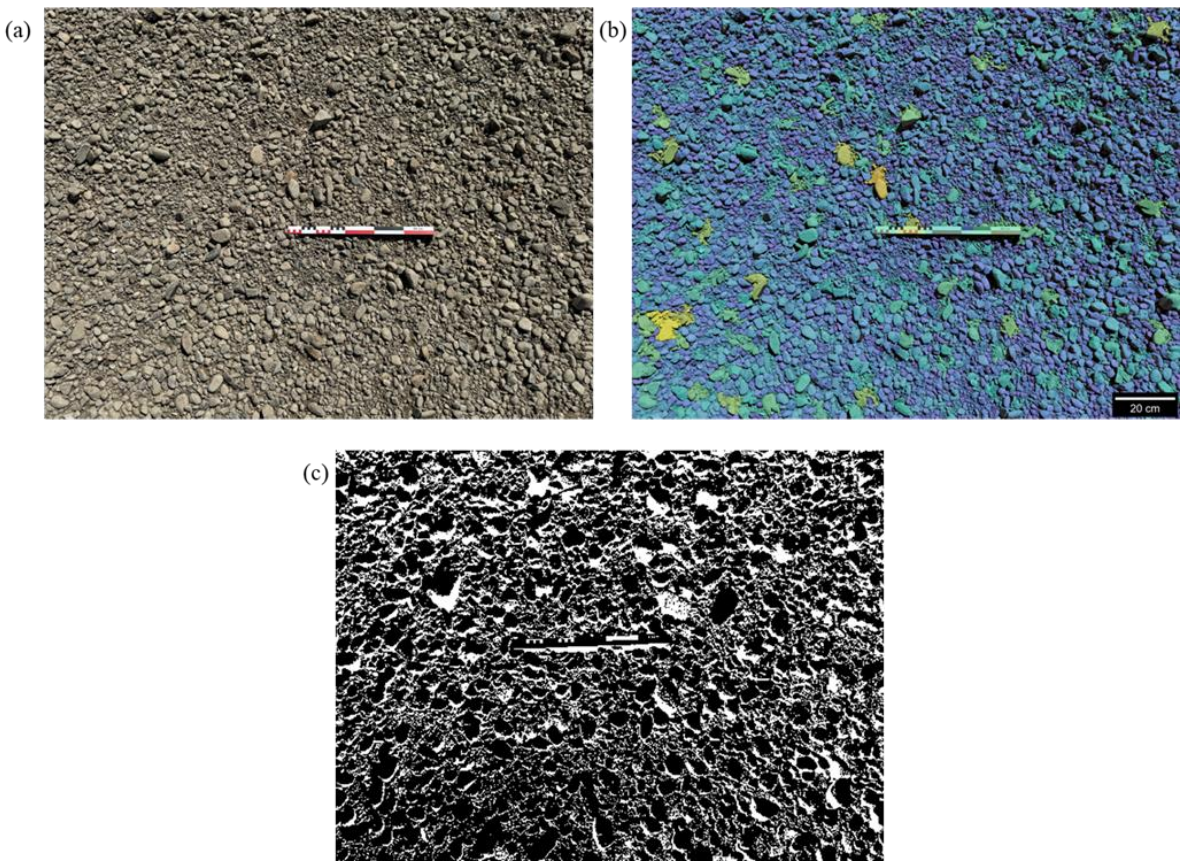

Figure 8.8 Example of digital grain-size analysis using MIPAR software from field photographs: raw image (a), classified image (b), and segmented output (c).

8.3.3. Wood density sampling

To evaluate the buoyancy properties of LW, we determined the density of wood samples collected from 9 representative logs. Small blocks were extracted from tagged elements and subsequently analyzed in the laboratory (Figure 8.9a). The procedure followed a gravimetric approach based on the principle of Archimedes. Each sample was first weighed in air using a precision electronic balance to obtain its dry weight in field-moisture condition. This procedure was performed one/two days after the field survey, to ensure the minimum variation of moisture, so that the samples are representative of the conditions of wood during the field survey. Each sample was then suspended in water with the aid of a thin support bar (Figure 7.9b), ensuring that it was fully submerged without touching the beaker walls or bottom. The apparent submerged weight allowed the displaced water volume to be calculated, corresponding to the sample's volume. From these measurements, the effective density of each wood sample (ρ, g cm^{-3}) was derived as:

$$\rho = \frac{W_{in\ air}}{V} \tag{8.1}$$

Where $W_{in\ air}$ is the sample weight in air (g), and V is the displaced volume of water (cm^3).

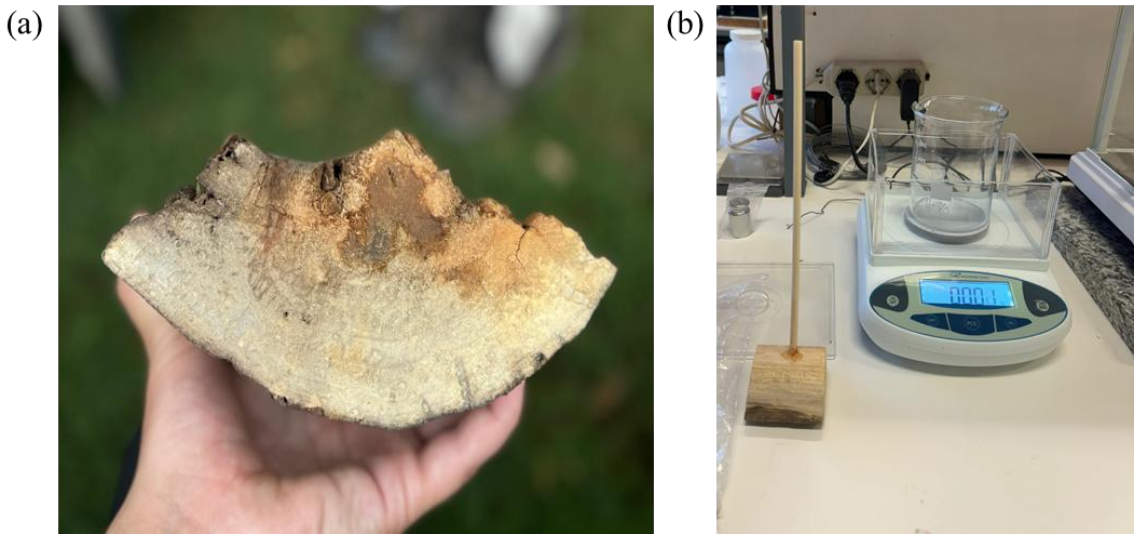

Figure 8.9 (a) An example of a wood core extracted from a tagged log for laboratory density analysis and (b) experimental setup using a precision balance and water immersion method based on Archimedes' principle to determine sample volume.

8.4. Results and Discussion

8.4.1. Insights from tracking large wood in the Allier River

A first-order depiction of floodplain hydraulics throughout the 32 *km* study reach is provided by the uncalibrated HEC-RAS 2D simulation of the March 2024 flood event. The depth-averaged velocity field (b) and simulated water depth distribution (a) at peak discharge (~700 $m^3 s^{-1}$ on March 12, 2024) are shown in Figure 8.10. The water depth results show that the active channel and the adjacent floodplain are heavily inundated. Depending on local topography and connectivity, floodplain inundation typically ranged from 0.5 to 2 *m,* while maximum depths within the main channel exceeded 6–7 m. Potential bypass zones for the transport of LW are indicated by the simulation's depiction of the development of secondary flow pathways across low-lying agricultural fields and deserted meanders. These locations are crucial because they offer new paths for LW fragments during intense flows, which could make recovery plans more difficult. The velocity distribution provides further insight into potential zones of wood entrainment and deposition. Locally higher values were concentrated along outer bends and constrictions, with velocities in the main channel generally ranging between 1 and 2.5 $m\ s^{-1}$. In contrast, over a large portion of the flooded floodplain, velocities fell below 0.5 $m\ s^{-1}$. The high-velocity bends and thalweg sections serve as preferential transport corridors, while the low-velocity floodplain pockets serve as depositional traps. The simulation results further indicate transitional zones along channel margins characterized by moderate velocities (0.5–1.0 $m\ s^{-1}$) that correspond to shallow depths. These zones are significant, as they may represent areas of partial mobilization where logs can be displaced but not effectively transported downstream. This has direct implications for RFID-based searches, as wood elements may accumulate near channel-floodplain junctions, levee breaches, or secondary inlets.

Due to the model preliminary and uncalibrated status, absolute values of depth and velocity must be approached with caution. The observed patterns align with anticipated fluvial dynamics in a meandering river during overbank flooding. The simulation effectively achieved its purpose by informing the design of the field campaign and pinpointing priority areas for search and recovery. The velocity field offered a spatially explicit framework for predicting areas of probable entrainment (outer bends, constricted reaches) and areas of likely deposition (inundated floodplain depressions).

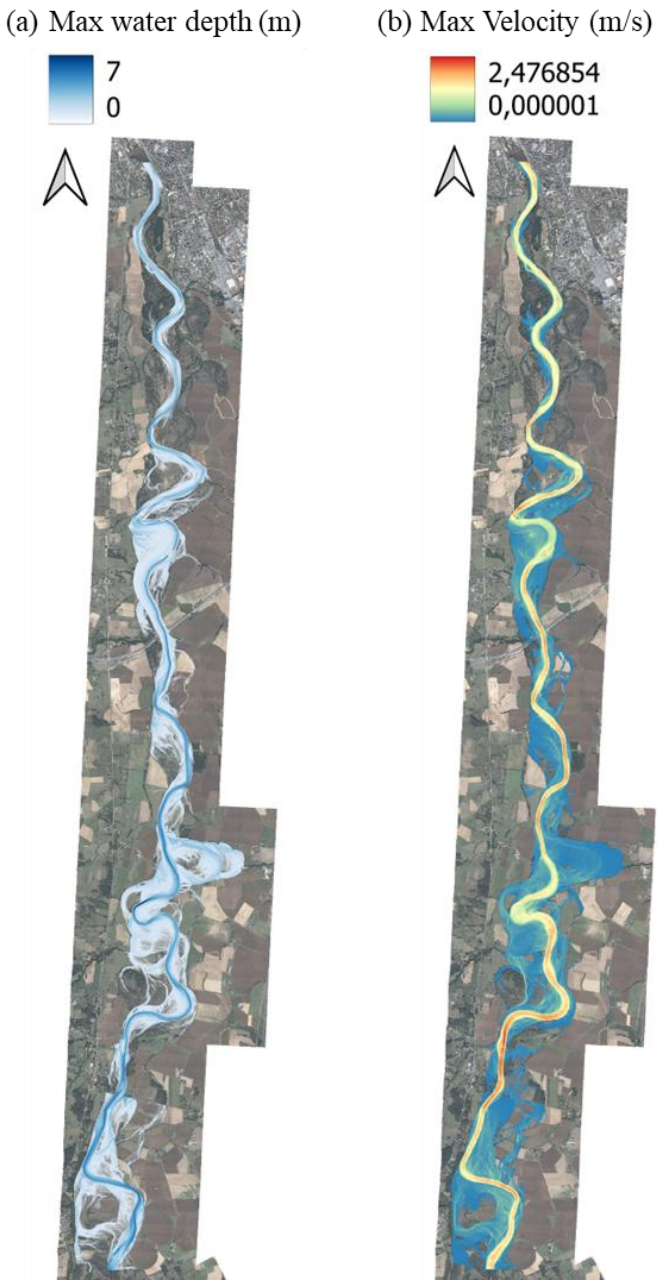

Figure 8.10 Spatial distribution of hydraulic parameters in the Allier River reach: (a) water depth (m), and (b) flow velocity (m s^{-1}).

The field monitoring of tagged LW in the Allier River, carried out by the research group of CNRS, ENS de Lyon and funded by "Véodis-3D" and the French office of biodiversity since 2020, provides a basis for comparing wood mobility under different flood magnitudes. This section focuses on the results from the 2024 campaign following a March 2024 Q5 flood (690 m^3 s^{-1}, ~5-year return period) and compares them to the 2023 campaign after a Q1.5 flood (218 m^3 s^{-1}, ~1.5-year return period). Although long-term monitoring is ongoing, these two consecutive flood events offer a clear contrast between a near-threshold flow and a higher-magnitude event. Key outcomes from the two campaigns are summarized in Table 8.1, highlighting differences in log recovery, stability and transport.

Table 8.1 Comparative statistics of LW mobilization and transport between 2023 and 2024 campaigns.

	Campaign 2023	**Campaign 2024**
Flood magnitude	Q1.5	Q5
Total logs (tagged in 2020)	280	280
Found logs	110	69
Lost logs	170	216
Stable logs	90	30
Entrained logs	20	34
Recovery rate (overall)	39%	23%
Loss rate (overall)	61%	77%
Transport rate (based on found logs)	18%	53%
Stability rate (based on found logs)	82%	47%
Stable logs (overall)	32%	11%
Entrained logs (overall)	7%	12%
Max transported distance (m)	30463	54152
Min transported distance (m)	73	91
Average transported distance (m)	7824	12712
Average diameter of mobilized logs (m)	0.22	0.32
Average length of mobilized logs (m)	10.47	12.06

Following the Q5 flood event in March 2024, the recovery rate (the percentage of tagged logs detected after the flood) was significantly lower at 24% compared to 39% following the Q1.5 event. This discrepancy implies that, in addition to mobilizing more logs, the higher magnitude flood probably carried many of them further downstream, outside the search area. In contrast, more than one-third of the logs in the Q1.5 flood were detected within the monitored reach, suggesting that wood export was more restricted (Figure 8.11). The stability versus transport of recovered logs also shifted markedly with flood size: In the near-threshold Q1.5 event, the majority of recovered logs (82%) remained in place (stable), with only a small fraction (18%) exhibiting evidence of transport, while more than half (53%) of the recovered logs in the larger Q5 event had been transported downstream, suggesting that a significantly higher percentage of wood was mobilized as the flood magnitude increased.

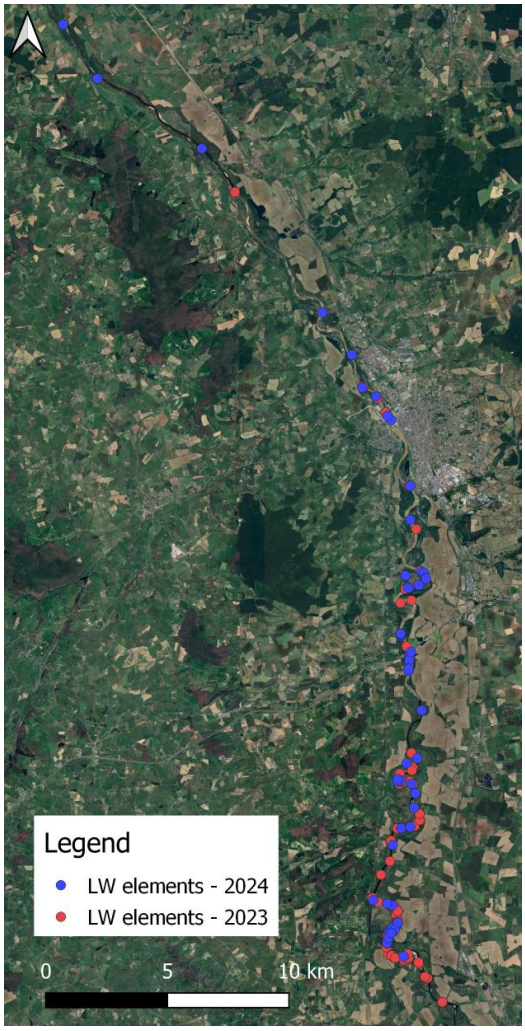

Figure 8.11 LW elements detected during the 2023 search campaign in red and during the 2024 campaign in blue.

This pattern supports the hypothesis that the Q5 flood surpassed the threshold of widespread wood mobilization and entrained many pieces that had previously remained stationary, while the Q1.5 flood was only at the threshold and only enlisted the more easily movable pieces. The main factor influencing wood mobility is flood magnitude; once flows exceed a certain threshold, a significant amount of wood is put into motion (Hortobágyi et al., 2024b, 2024a; Kramer and Wohl, 2017; MacVicar et al., 2009; Ravazzolo et al., 2015a). This threshold behavior is supported by previous research; for instance, larger flows (i.e. higher flow depths and greater velocities) can mobilize logs that smaller floods cannot, particularly logs with a large diameter or those anchored by rootwads (Bocchiola et al., 2006; Braudrick and Grant, 2001; Chen et al., 2020; Kramer and Wohl, 2017). Field evidence from the Allier River supports this: the average diameter and length of mobilized logs during the 2023 Q1.5 flood were 0.22 m and 10.47 m, respectively, while those transported during the 2024 Q5 flood were significantly larger on average (0.32 m in diameter and 12.06 m in length), suggesting that the higher flow conditions overcame size- and drag-related thresholds for entrainment (Bocchiola et al., 2006; Chen et al., 2020). Furthermore, this idea of transport thresholds is demonstrated by the

Q5 event capacity to mobilize almost twice as much wood compared to the Q1.5 event, causing a surge in wood export. The 1.5-year flood, which is roughly equivalent to a bankfull discharge, seems to have been close to the critical entrainment threshold; it mobilized some wood but left a sizeable residual stock in place. Notably, after the Q1.5 event, the system's overall log stability (as a percentage of all tagged logs) decreased from about 32% to just about 11% following the Q5 event. This dramatic drop is a result of the larger flood, which caused many logs that had been stable during smaller flows to mobilize from their original locations. After the Q 5 flood event, 77% of the logs were lost compared to 61% during the Q 1.5 flood event, this can be either due to being carried further downstream outside the study area or maybe because they were broken and washed away. Meanwhile, the small subset of logs that remained stable during the Q5 flood were mainly extremely large pieces, part or key logs in jams (Figure 8.12 a and b) or partially/totally buried under sediment (Figure 8.12c). These highly stable logs represent only ~11% of the total, indicating that nearly nine in ten logs were either transported or lost during the Q5 event – a striking contrast to the Q1.5 event where roughly one-third stayed in place. The persistence of any stable logs even under a Q5 flow suggests variability in site conditions and log characteristics: certain pieces may require floods of even greater magnitude to move, due to favorable anchoring or size. Overall, the comparison of stability and mobility between the two monitoring campaigns clearly demonstrates how a moderate flood versus a higher-magnitude flood differentially affect in-stream wood: the smaller, near-bankfull event primarily tested the system’s threshold (mobilizing a fraction of wood), whereas the larger event effectively reset much of the wood storage by transporting the majority of pieces downstream.

(a)

(b)

(c)

Figure 8.12 Stable LW elements observed during the August 2024 field survey, illustrating different stabilization mechanisms: (a) part of a wood jam, (b) stabilization by riparian vegetation and part of a jam, and (c) anchoring through partial burial in sediments. (Photos taken by the author during the field survey in August 2024).

In addition, the Q5 flood not only mobilized more logs but also, on average, carried wood much further downstream. The average displacement (~7.8 *km*) for transported logs in the 2023 (Q1.5) campaign is about 1.5 times smaller than the average travel distance (~12.7 *km*) for logs entrained in 2024 with the maximum recorded distance was about 40.8 *km* in 2024.

The greater transport distances observed in 2024 are consistent with the higher flow velocities, depths, and flood durations associated with the Q5 event. A larger flood can sustain wood transport over longer times and distances before deposition, especially when the floodplain is connected. Some logs likely rode the peak flow into the mainstem river or onto the floodplain far downstream. In contrast, the Q1.5 event, certainly corresponding to lower water levels on the study area, resulted in shorter travel distances for most logs. This aligns with literature on flood-driven wood dynamics: extreme events tend to produce disproportionate wood export, moving material much farther, whereas smaller events primarily redistribute wood locally (Comiti et al., 2016; Gurnell et al., 2002; Kramer and Wohl, 2017; Lucía et al., 2015; Pavlowsky et al., 2023). These results prove that the Q5 flood effectively exported a significant portion of the reach wood stock downstream in a single event. Many of the logs that were missing (not recovered) are presumed to have been carried out of the study area. Such a pulse of wood export can contribute to LW loading in downstream reaches, with both positive and negative consequences. On one hand, mobilized wood contributes to river corridor dynamics and habitat formation downstream: periodic influxes of wood help replenish woody structures that provide ecological functions as cover for aquatic organisms, substrate for biological growth, and promoters of geomorphic complexity (Wohl et al., 2024). The downstream redistribution of wood by large floods is a natural process that maintains a dynamic equilibrium in wood budgets, preventing any single reach from indefinitely accumulating all its wood and ensuring that habitat features are rejuvenated over time (Abbe and Montgomery, 2003; Gurnell et al., 2002; Wohl et al., 2024). On the other hand, exported wood during major floods can pose hazards. When large quantities of logs are released and transported, they can accumulate against bridges, weirs, or other infrastructure, increasing flood risks or causing structural damage (Zischg et al., 2018). The 2024 Q5 event exported nearly an order-of-magnitude more wood (in terms of both quantity and distance traveled) underscoring the need to anticipate such wood pulses in flood management. Another aspect that was analyzed is the mechanisms of LW deposition. Field monitoring of LW after the March 2024 flood revealed distinct patterns of deposition and entrapment. Cross-checking each recovered position against orthophotos and site photos show a clear dominance of vegetation- and jam-mediated arrest. As summarized in Table 8.2, 65% of the entrained pieces were trapped directly against living trees or shrubby stands, often at the heads or margins of vegetated islands or along forested banks. A further 12% were incorporated into, or blocked by, pre-existing log jams with little or no surrounding

vegetation, typically at bar heads. The remaining 23% were deposited as single pieces on gently sloping banks, on low-vegetation bars/islands, or locally within the channel where shallow depths promoted grounding during the hydrograph recession. Examples of captures against trees include logs 074A9C, 074BE0, 074B35, and 074B38 (Figure 8.13), while an example of deposition against a largely unvegetated jam is log 074ACC (Figure 8.14).

Table 8.2 Deposition and entrapment patterns of tracked LW following the March 2024 flood in the Allier River.

Deposition/Entrapment Type	Percentage of Logs	Description
Tree-mediated entrapment	65%	Logs blocked directly against riparian trees; often formed jams on vegetated islands or forested banks.
Entrapment by logjams	12%	Logs blocked by pre-existing log jams with little or no surrounding vegetation.
Isolated deposition (banks/bars)	23%	Single logs deposited on exposed banks, gravel bars, or low-vegetation islands; often during flood recession

These findings imply that the primary retention mechanism in the Allier River is riparian vegetation, and a tree-mediated trapping is well documented in the literature. For instance, (Kramer and Wohl, (2017) confirmed that live, rooted vegetation on banks has an effective role in trapping mobile LW on bars and overbank areas. Similarly, Sear et al. (2003) stated that in forested floodplains flood LW is frequently transported onto the floodplain surface and trapped against trees and bushes. In the present field survey the strong role of vegetation is consistent with the idea that live trees and shrubs can trap LW early in a flood, causing wood flux to peak before the discharge peak (Kramer and Wohl, 2017) while, in practice, logs are typically entrained during the rising limb of the flow hydrograph and then deposited as flows decrease. In short, the present analysis confirmed that riparian live wood is a key anchor for flood-carried logs, especially in forested floodplains. The complementary role of pre-existing wood structures is highlighted by 12% of arrests against primarily unvegetated logjams. Once established, jams increase local capture probabilities even in the absence of vegetation (Davidson and Eaton, 2015; Kramer and Wohl, 2017). Similarly, Beckman and Wohl (2014b) show that stable “key pieces” can nucleate jams which then trap additional wood flux, increasing wood storage even when living vegetation is limited. The remaining 23% of logs were found singly deposited on bars or banks with sparse vegetation cover. These isolated deposits are common when floods are in their declining stages. Gurnell et al. (2002) found that only 20% of LW on braided gravel bars forms crescent shapes at forested edges, with the majority (approximately 80%) being deposited in straight-line piles during falling-stage flows. This is in contrast to the present findings, where only 24% of tracked logs were stranded singly on bars or low-vegetation islands, whereas 65% of the logs were directly trapped by riparian trees. This further implies that, in contrast to more open braided

systems where bar stranding predominates, the high density of riparian vegetation along the Allier River encourages tree-mediated entrapment as the predominant deposition mechanism.

Figure 8.13 Examples of tree-mediated entrapment of LW after the March 2024 flood in the Allier River. (Photos taken by the author during the field survey in August 2024).

Figure 8.14 Example of a log entrapped within a log jam without significant vegetation after the March 2024 flood in the Allier River. (Photos taken by the author during the field survey in August 2024).

8.4.2. Insights for the 8 *km* reach selected for modeling

To complement the tracking results, we conducted a focused analysis on the 8 *km* study reach that will be the subject of hydraulic modeling in Chapter 9. During the pre-flood field survey, in September 2023, a total of 110 logs were identified across the 50 *km* corridor, 29 of which were located within this specific 8 *km* segment (Figure 8.15). Following the March 2024 flood, only 13 of these 29 logs were re-detected within the reach. Specifically, 9 logs were entrained, 4 remained stable, and the remaining 16 could not be found. Given the intensity of the flood and the downstream monitoring limit of 42 *km*, it is reasonable to assume that the missing logs were exported beyond the monitored corridor. Among the 9 entrained logs, the deposition mechanisms were strongly skewed toward vegetation-mediated retention. Approximately 78% of the entrained logs were trapped against riparian trees or shrubs, while 11% became part of pre-existing wood jams, and another 11% were deposited as single, isolated pieces on the bank without major entrapment structures. This again emphasizes the critical role of riparian vegetation as the dominant capture agent in the Allier system.

When comparing the initial (2023) positions of tagged logs within the 8 *km* reach with their post-flood (2024) deposition points, and assuming that logs that were not recovered, have exited the monitored corridor, we estimate that the retention rate of this 8 *km* reach is 34%. In other words, roughly one-third of the entrained wood that passed through this reach remained stored locally after the flood, while the rest was exported downstream. This retention efficiency aligns with previous findings that show localized vegetation and existing log structures strongly influence the persistence of wood within short river segments (Gurnell et al., 2002; Kramer and Wohl, 2017) . Such field-based

quantification of reach-scale retention will provide a valuable benchmark for the numerical simulations of LW dynamics in this segment in Chapter 9, where hydraulic conditions and vegetation distributions will be explicitly simulated to assess how they control wood storage dynamics during flood events.

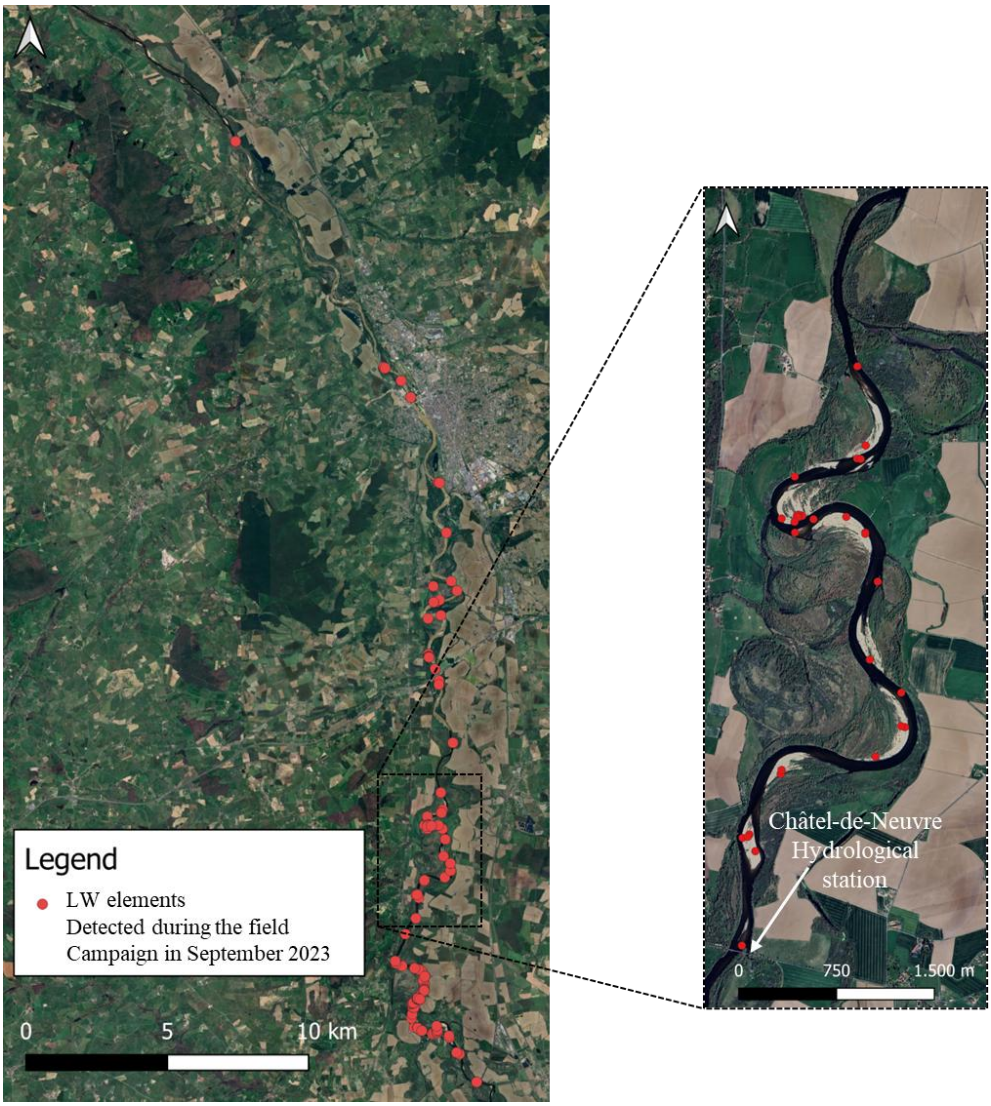

Figure 8.15 Distribution of tagged LW elements in the Allier River in September 2023. (a) Locations of all tagged logs along the 50 *km* monitored corridor. (b) Zoom on the 8 *km* study reach downstream the Châtel-de-Neuvre hydrological station, which was later selected for detailed hydraulic modeling in Chapter 9.

8.4.3. Sediment grain size and roughness estimation

Grain-size surveys carried out on the five representative point bars in the 8 *km* reach downstream of the Châtel-de-Neuvre hydrological station revealed considerable spatial variability in surface textures. At Point Bar 1, the median grain size (D_{50}) was around 16 mm, indicating a coarse gravel surface. A similar value was obtained at Point Bar 4, where the bar surface was likewise dominated by coarse gravels. In contrast, Point Bar 2 showed a much finer texture, with a D_{50} of only 7 mm, reflecting the presence of sand and fine gravels deposited under lower-energy flow conditions. Point Bar 3 exhibited intermediate values, with D_{50} ranging between 9 and 11 mm at different sampling points, while Point Bar 5 was somewhat more heterogeneous, with values varying between 9 and 12 mm depending on location across the bar, and finally Bar Point 6 with D_{50} ranging between 13-14 mm. Overall, the D_{50} values ranged from 7 mm on the finest bar to 16 mm on the coarsest one, with an average of about 11.5 mm and a standard deviation of roughly 3.5 mm. This twofold difference in median grain size between bars highlights the strong influence of local hydraulic and geomorphic conditions on sediment sorting. The coarser textures observed at Bars 1 and 4 are consistent with their position on outer bends, where higher flow competence promotes the winnowing of fine fractions and the persistence of a gravel armoring layer. By contrast, the finer sediments at Bar 2 suggest a depositional setting associated with reduced velocities or increased sand supply, typical of inner bends or low-energy secondary channels. Bars 3 and 5 illustrate the transitional character of many active bars, where lateral accretion processes and flood variability generate a patchy surface texture with both fine and coarse facies. The variability in grain size observed across these bars is consistent with earlier descriptions of the Allier River as a mixed sand–gravel system with strong local contrasts in sediment texture. For example, Corenblit et al. (2016) describe the point bar surfaces near Châtel-de-Neuvre as being "dominated by a mixture of sand, gravel and pebbles", reflecting a broad grain-size ranges. In detailed analyses of the active channel upstream of Moulins (which includes the Châtel-de-Neuvre reach), Van Dijk et al. (2014) report a median grain diameter (D_{50}) on the order of 5–8 mm, with the 90th-percentile size D_{90} around 9–20 mm, depending on location. These values indicate a predominantly fine-gravel bed with a substantial sand fraction. Indeed, the Allier's bed material is heterogeneous, during low flows an immobile coarse surface "pavement" forms, while finer sand/gravel moves in patches (Kleinhans et al., 2002; Van Dijk et al., 2014). Furthermore, it is worth highlighting the differences in accuracy between Wolman pebble counts and digital image. Wolman counts, carried out directly in the field, remain a widely used and straightforward approach, but they are inherently constrained by human bias in clast selection and measurement. Operators often tend to measure larger, more visible clasts while overlooking finer sediments, leading to an overrepresentation of coarse particles. As a result, Wolman counts in this study yielded systematically

coarser medians (D_{50} ≈ 16 mm), Figure 8.16 presents an example of the cumulative grain-size distribution measured on Point Bar 1 using the Wolman method, illustrating the coarse gravel-dominated texture of this site with only around 30% of the sediments are < 8 mm. Digital grain-size analysis, by contrast, is able to process high-resolution images and identify thousands of particles automatically, providing statistically robust and repeatable results while reducing human bias (Garefalakis et al., 2023). The method captures finer fractions (< 8 mm) more effectively than field counts, as obvious in Figure 8.17, which shows an example of the digital photo-derived distribution for Point Bar 3, emphasizing the finer component of the surface sediments compared to manual counts with 48% of the sediments < 8 mm. This explains why the photo-based analysis produced lower median values (D_{50} ≈ 11 mm). However, digital methods are not free of limitations. One major drawback is that clasts that are partially buried or overlapping may appear smaller in two-dimensional images than their actual size, causing systematic underestimation of grain diameters (Buscombe et al., 2010; Garefalakis et al., 2023). This effect is particularly relevant on bar surfaces where finer sediments partially fill the gaps between larger gravels, masking their true dimensions. Furthermore, image-based analysis is sensitive to factors such as lighting, shadowing, and algorithm calibration, all of which influence the precision of the automated detection.

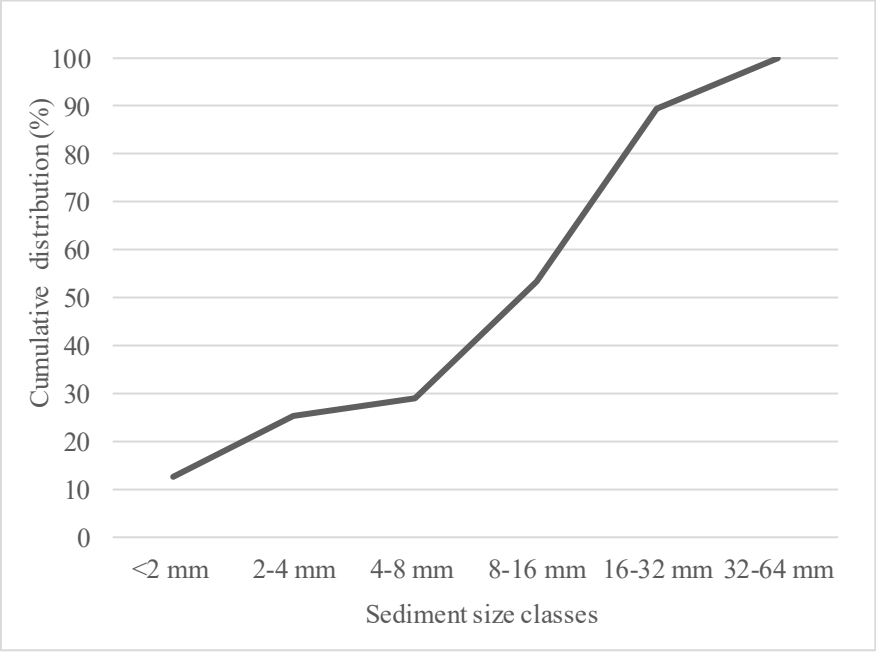

Figure 8.16 An example of cumulative grain-size distribution of sediments obtained from Wolman pebble count analysis.

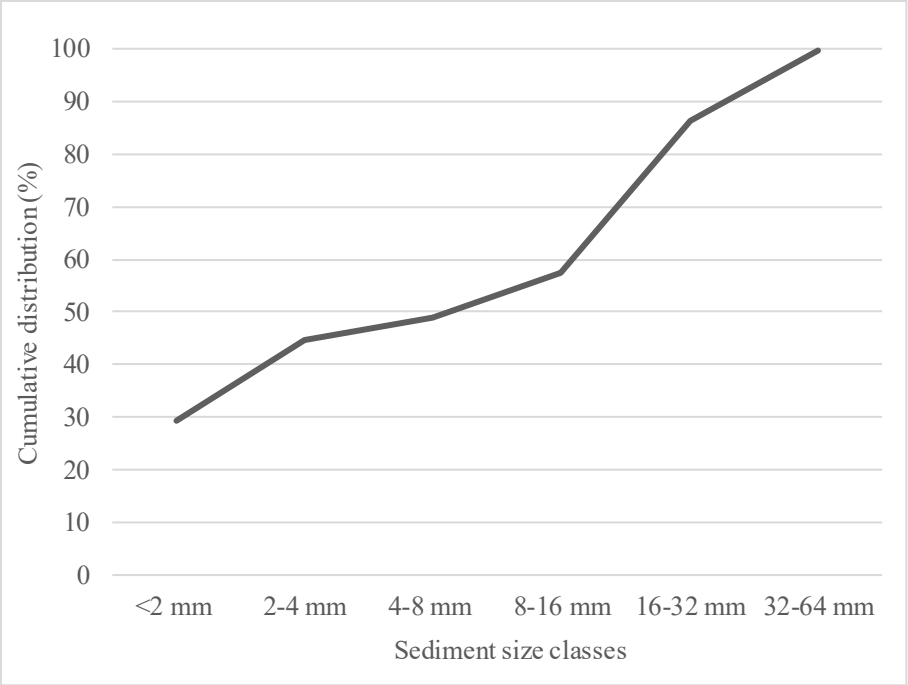

Figure 8.17 An example of cumulative grain-size distribution of sediments obtained from digital pebble count analysis using MIPAR software.

The average D_{50} value derived for each point bar was subsequently transformed into n_0, the base component of the Manning's roughness coefficient, representing the contribution of bed material alone to overall hydraulic resistance. This conversion was carried out using the Federal Highway Administration (FHWA) grain-roughness equation, a Strickler-type relationship expressed as:

$$n_0 = 0.048 D_{50}^{\frac{1}{6}} \tag{8.1}$$

Where D_{50} is the median grain size expressed in m.

The calculated values of n_0 based on the FHWA grain-roughness equation (Table 8.2) highlight systematic differences in base roughness across the sampled point bars. Coarser bars such as Bars 1 and 4, with $D_{50} \approx 16$ mm, yielded the highest base Manning coefficients ($n_0 \approx 0.0242$), while finer bars such as Bar 2 ($D_{50} \approx 7$ mm) produced the lowest ($n_0 \approx 0.0211$). Intermediate bars, with D_{50} values between 10 and 13.5 mm (Bars 3, 5, and 6), showed n_0 values in the range of 0.0224–0.0235. These n_0 values represent the grain roughness component of Manning's coefficient and serve as the baseline for further adjustments. In particular, they were used as the starting point for calculating Manning's n modified for vegetation density, which constitutes the dominant additional source of resistance in the study reach. As a result, the Manning's coefficients applied in the simulations (more details in Chapter 9) consist of the base roughness derived from sediment size (as quantified in Table 7.2), systematically adjusted to reflect spatial variability in riparian vegetation density, while relying on

the 2D framework itself to capture form resistance linked to channel morphology (Costabile and Macchione, 2015).

Table 8.3 Summary of the median grain size (D_{50}) and the estimated base Manning's roughness coefficient (n_0) for the six surveyed point bars.

Point Bar	Average D_{50} (mm)	n_0 $(m^{-1/3}s^{-1})$
1	16.0	0.0242
2	7.0	0.0211
3	10.0	0.0224
4	16.0	0.0242
5	10.5	0.0226
6	13.5	0.0235

8.4.4. Wood Density Sampling

A total of nine wood samples were extracted from tagged logs to determine density under natural saturation conditions. Measured values ranged from approximately from 396 to 1147 kg m^{-3}, with an average of about 565 kg m^{-3} (Figure 8.18). Most samples clustered between 450 and 650 kg m^{-3}, a range that indicates positive buoyancy under normal river conditions, consistent with values reported in the literature. For example, Mallqui et al. (2025) note that wood density may range from as low as ~250 kg m^{-3} up to beyond 1000 kg m^{-3} under different conditions. This range spans extremely light, dry/decayed wood to fully water-saturated or inherently dense wood. Furthermore, (Ruiz-Villanueva et al., (2016a) found that pieces of instream wood (logs retrieved from a river reservoir) initially ranged ~408 to 1054 kg m^{-3} (median ~651 kg m^{-3}). Notably, these values include natural moisture content at extraction. In contrast, freshly cut green wood of various species had higher densities (averaging around 800–900 kg m^{-3} when freshly cut with sap moisture). The instream wood was on average ~16–24% less dense than fresh wood of the same species, likely because decay processes reduce wood's solid mass (making it less dense). The average density of the sampled logs in the Allier River (~565 kg m^{-3}) falls somewhat on the lower side of the reported instream range. This suggests the sampled logs may have been relatively decayed or of inherently light species (e.g. poplar or willow), resulting in lower densities consistent with a moderate decay class. Indeed, decay tends to lower the dry-matter density of wood (Ruiz-Villanueva et al., 2016a), increasing the potential of buoyancy. Moreover, water content has an important effect on wood density. Fully water-saturated wood can approach or exceed the density of water (~1000 kg m^{-3}). In laboratory wetting experiments, Ruiz-Villanueva et al. (2016a) observed that previously dry wood samples could absorb water until their density rose to ~1100–1200 kg $m^{-3}$for certain species like *Populus* (poplar) and *Acer*, and around 1000 kg m^{-3} for others (e.g. *Fraxinus*, *Abies*). Out of the 9 sampled logs, one outlier log (ID 074BD2)

with density ~1147 kg m^{-3} fits this scenario well, its density is well above the density of freshwater. This piece was observed to be semi submerged during the field campaign (Figure 8.19), it behaved as a negatively buoyant log, unlikely to float during floods and instead it would be transported as submerged LW along the channel bed by sliding or rolling (Kimura et al., 2021) or it will stay stable, which is the most probable scenario. According to the RFID tracking post the March 2024 Q5 flood event this specific log remined stable. Its behavior stands in contrast to the majority of sampled logs, which remained positively buoyant and would typically move as floating driftwood.

In summary, comparing the Allier River wood density findings with existing literature revealed strong agreement: most river wood has a saturated density well below water's density (hence it floats), typically in the 400–800 kg m^{-3} range (Mallqui et al., 2025; Ruiz-Villanueva et al., 2016a), but fully waterlogged or very dense wood can occasionally exceed 1000 kg m^{-3} and lose buoyancy (Ruiz-Villanueva et al., 2016a). Our results reinforce these known patterns. The positive-buoyancy logs in our sample are expected to mobilize as floating driftwood during floods, consistent with the behavior of driftwood. In contrast, the single negative-buoyancy log in our sample provides a case study of the sinking-wood phenomenon described in the literature: once saturated past the buoyancy threshold, it travels along the bed as a submerged hazard, potentially impacting bridge piers or scouring the channel (Kimura et al., 2021). This dual behavior within the nine samples highlights the variability in wood transport dynamics and the importance of wood density as a key parameter.

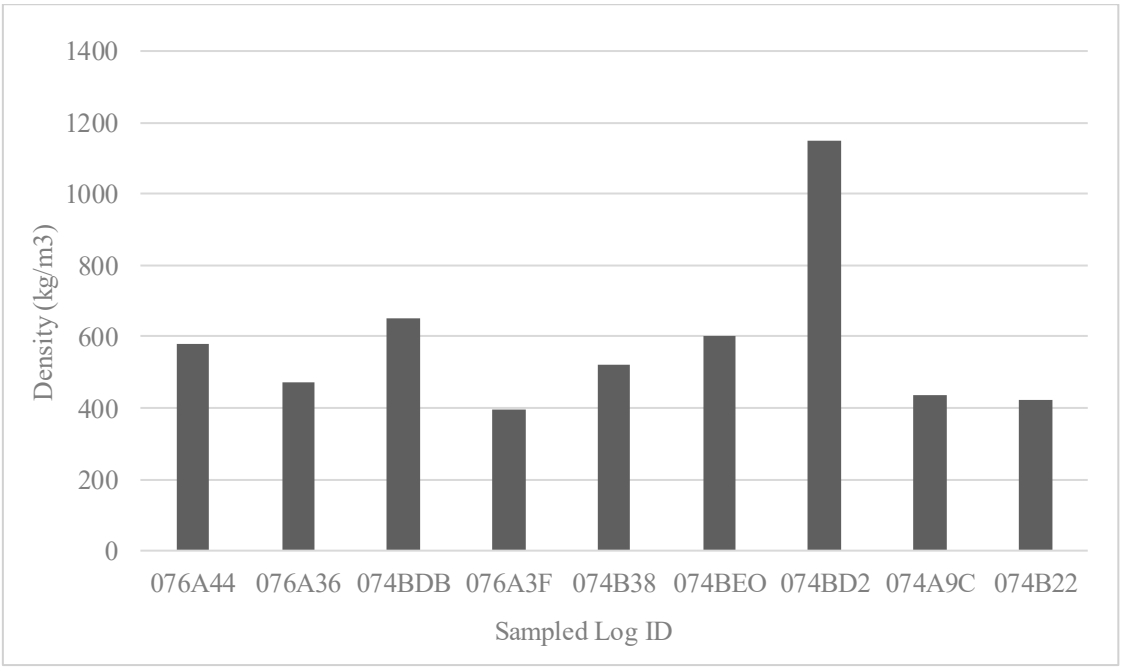

Figure 8.18 Density distribution of tagged logs sampled in the Allier river.

Figure 8.19 Negatively buoyant log (ID 074BD2) observed fully submerged in the Allier river (the photo is taken by the author during the field survey in August 2024).

Chapter 9

Model application to the Allier River

9.1. Abstract

This chapter applies the enhanced ORSA2D_WT model to the Allier River (France) to investigate LW transport and retention processes during a real flood event. The objective is to evaluate how riparian vegetation influences LW dynamics under natural hydraulic and morphological conditions. The March 2024 flood was selected as a representative event for model testing, supported by field data that include tracked logs equipped with RFID tags, LiDAR-derived vegetation information, and hydrodynamic calibration based on observed water levels. Two simulation scenarios were performed: a baseline case considering only hydraulic entrainment and transport of the monitored logs, and a second configuration where the vegetation entrapment routine was activated to account for log–vegetation interactions derived from the LiDAR dataset. To improve the robustness of the analysis, the dataset was expanded beyond the RFID-monitored logs by identifying additional LW elements visible in pre-flood (September 2023) orthophotos. This process increased the total number of simulated logs to 50, including both filed-monitored and imagery-digitized wood. Comparison between these scenarios enables a detailed evaluation of how riparian vegetation modulates LW mobility, entrainment thresholds, and trapping efficiency. The results contribute to understanding the role of riparian corridors as natural retention systems and highlight their potential as nature-based solutions for mitigating LW-related flood hazards.

9.2. Study reach for modelling

As anticipated in Chapter 8, the selected modelling domain extends over an 8 *km* segment of the Allier River downstream the Châtel-de-Neuvre hydrological station (Figure 9.1). This reach was chosen primarily because of its representative morphological complexity and the availability of high-resolution topographic and hydrological data necessary for two-dimensional hydraulic modelling. Morphologically, the segment is characterized by a meandering planform with multiple cutoffs, vegetated islands, and alternating gravel bars. Such a setting provides diverse hydraulic environments ranging from fast-flowing thalwegs to shallow marginal zones, thereby offering a realistic testbed for simulating LW transport under flood conditions. The abundance of riparian vegetation and LW structures also makes the reach particularly relevant for studying interactions between flow, morphology, and wood retention natural structures. As anticipated in Chapter 8, hydrological input data are available from the Châtel-de-Neuvre gauging station. The availability of detailed airborne LiDAR dataset including mapped vegetation cover further supports the model parameterization as will be described in details in Sections 9.3. The combination of complex hydraulics, active morphodynamics, and high-quality monitoring data makes this reach especially suited for the coupled Eulerian–Lagrangian modelling framework presented in Chapters 3 and 4. The 8 *km* segment thus serves as a test environment to evaluate how LW is entrained, transported, and deposited during flood events, with insights that are scalable to longer sections of the Allier River and comparable highly vegetated gravel-bed rivers.

Figure 9.1 The 8 *km* study reach of the Allier river downstream Châtel-de-Neuvre.

9.3. Numerical model setup

9.3.1. Topographic data

The base terrain model (DTM) was built based on the latest (0.5 m resolution). To represent the riverbed, this bare-earth DTM (Figure 9.2 a) was merged with surveyed bathymetry: cross-section measures collected in 2020 were interpolated along the river axis to reconstruct a continuous riverbed surface. Islands and vegetated bars within the active corridor were also explicitly modelled in the terrain dataset. Their inclusion was essential because they influence local hydraulic gradients and flow division, therefore increasing the overall accuracy of the hydraulic model. From this combined topography, a 2D triangular mesh was generated using SMS software (Figure 9.2 b), consisting of approximately 178,600 cells. The mesh was refined to 2 m resolution within the active channel to resolve steep hydraulic gradients and complex morphology around islands, while a coarser spacing (up to ~20 m) was applied along the outer floodplain.

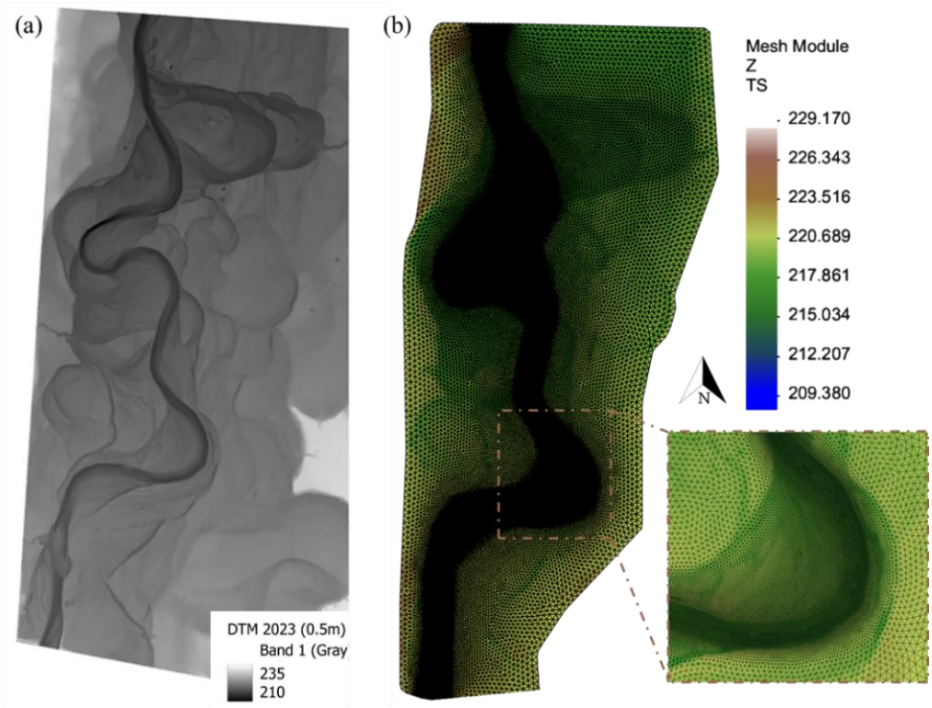

Figure 9.2 (a) Digital terrain model and (b) Computational mesh of an 8 km segment of the Allier River downstream of the Châtel-de-Neuvre hydrological station.

Manning's roughness coefficients were assigned according to land use, grain size, and vegetation density, then refined through calibration with observed flood marks (Section 9.4). The main and secondary channels were set to n = 0.038 $s/m^{1/3}$, consistent Manning's roughness values for gravel-bed channels (Thomason, 2019). For the floodplain, the roughness coefficients were derived using a combination of grain-size analysis and the Cowan (1956) method. First, an initial estimate of the base roughness $n_0$was calculated from the median grain size D_{50} obtained in Chapter 8, using a Strickler-

type relationship, with $n_0 \approx 0.021–0.024\ s/m^{1/3}$. This base roughness represents the hydraulic resistance associated solely with the surface material. To more accurately represent floodplain conditions, this value was then adjusted according to the Cowan methodology, which expresses the final Manning's coefficient as:

$$n = (n_0 + n_1 + n_2 + n_3 + n_4)m$$

With, n_1 accounts for the effect of channel surface irregularities, n_2 accounts for variation in channel cross section shape and size, n_3 accounts for obstructions, n_4 accounts for vegetation and m is a correction factor for channel meandering. However, due to the two-dimensional nature of the model, several of these correction terms are already implicitly represented by the spatially distributed topography. Surface irregularities (n_1), cross-sectional variability (n_2), and localized obstructions (n_3) are resolved directly through the DEM. Therefore, these terms were not applied in the present work. Only the vegetation-related component $n_4$was retained, as sub-grid-scale vegetation density and structure are not explicitly captured by the 2D mesh but exert a significant influence on floodplain roughness. The meandering factor m was set to 1.0, since planform curvature and secondary circulation are inherently represented in a 2D modelling framework. The resulting floodplain Manning's coefficients therefore reflect a combination of grain-size-derived base roughness and vegetation induced resistance, providing a physically consistent parameterization that was subsequently refined during hydraulic calibration (more details in section 9.4). The initial roughness values adopted for each land-use category are reported in Table 9.1.

Table 9.1 Manning's roughness coefficients assigned to different land use classes.

Land Use	**Manning's coefficients ($s/m^{1/3}$)**
Main channel	0.0380
Secondary channel	0.0380
periodically herbaceous	0.0500
Permanent herbaceous	0.0800
Dense forest	0.2000
Low density forest	0.1000
Sealed	0.0130
bare gravel bar 1	0.0242
bare gravel bar 2	0.0210
bare gravel bar 3	0.0223
bare gravel bar 4	0.0242
bare gravel bar 5	0.0225
bare gravel bar 6	0.0235

9.3.2. Vegetation data

Previous research has shown that riparian vegetation plays a critical role in controlling LW dynamics, with tree stands and shrubs often providing the primary trapping elements during floods (Gurnell et al., 2002; Ruiz-Villanueva et al., 2014b; Piégay and Gurnell, 1997). In this study, incorporating LiDAR-derived vegetation structure therefore provides a spatially explicit way to represent these trapping mechanisms in the modeling framework. Vegetation structure was derived from airborne LiDAR data using the IGN's LiDAR-HD (National Geographic & Forest Institute) product (Figure 9.3a), which provides a cloud points data across the territory of France. The raw point cloud was processed into a 0.5 *m* Digital Surface Model (DSM), from which only medium and high vegetation classes were retained (Figure 9.3b). Following the methodology detailed in Section 4.5, we generated a canopy height model (CHM) by subtracting the ground DTM from the DSM and then interpolated the resulting raster onto the ORSA2D_WT computational grid. This ensured that each grid cell (x, y) was assigned a representative CHM value, enabling the model to account for vegetation structure in subsequent simulations.

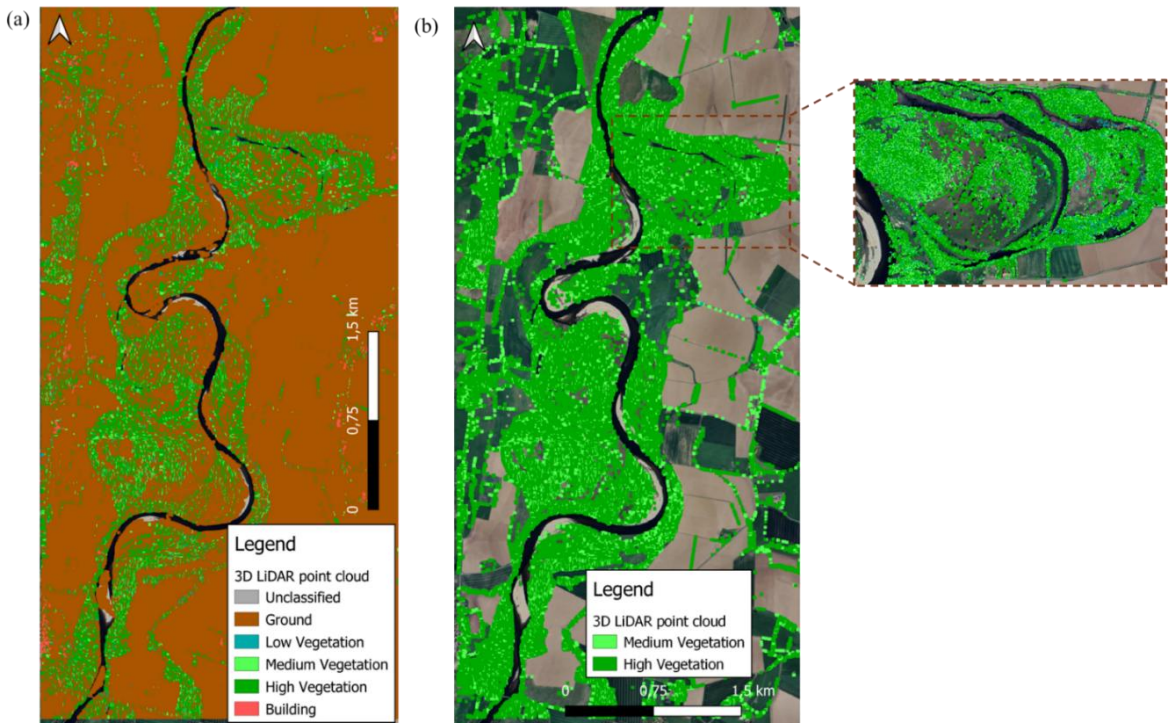

Figure 9.3 Airborne LiDAR-HD dataset provided by the French National Institute of Geographic and Forest Information (IGN). (a) Classified point cloud from the IGN LiDAR-HD product, including ground, low/medium/high vegetation, and buildings, (b) Retained vegetation layers.

9.3.3. Hydraulic and calibration data

Two steady-state flow scenarios were first simulated on the Allier reach using the calibrated 2D hydrodynamic model. The low-flow condition was set at Q = 20 $m^3 s^{-1}$, corresponding to the baseflow on 26 September 2023. This steady-flow run provided a reference water surface profile and extent that could be directly compared with contemporaneous orthophoto imagery to verify the modelled inundation area under low-flow conditions. A second steady-state run at Q = 120 $m^3 s^{-1}$ was then carried out to represent the pre-flood initial condition. The higher discharge ensured full conveyance through the channel without overflow, yielding initial water levels and velocities for the ensuing unsteady simulation. In practice, the upstream flow was held constant, and the model solved the steady varied-flow equation for the specified discharges, providing the initial depth distribution. This approach follows standard practice in two-dimensional river modelling, where steady simulations are used to establish initial conditions for flood routing (Jeppson, 1974). The March 2024 flood was then simulated in unsteady mode. The prescribed upstream hydrograph was obtained from the Châtel-de-Neuvre hydrological station, with a peak flow of 690 $m^3 s^{-1}$ (Figure 9.4) corresponding to a flood event of a 5 years return period. At the downstream boundary, a Froude number condition enforcing subcritical flow was applied. The unsteady run was initialized using the water surface and flow field from the 120 $m^3 s^{-1}$ steady simulation as its starting conditions. The March 2024 event simulation served as the calibration baseline, it provided time-series of water depths and velocities against which observations could be compared.

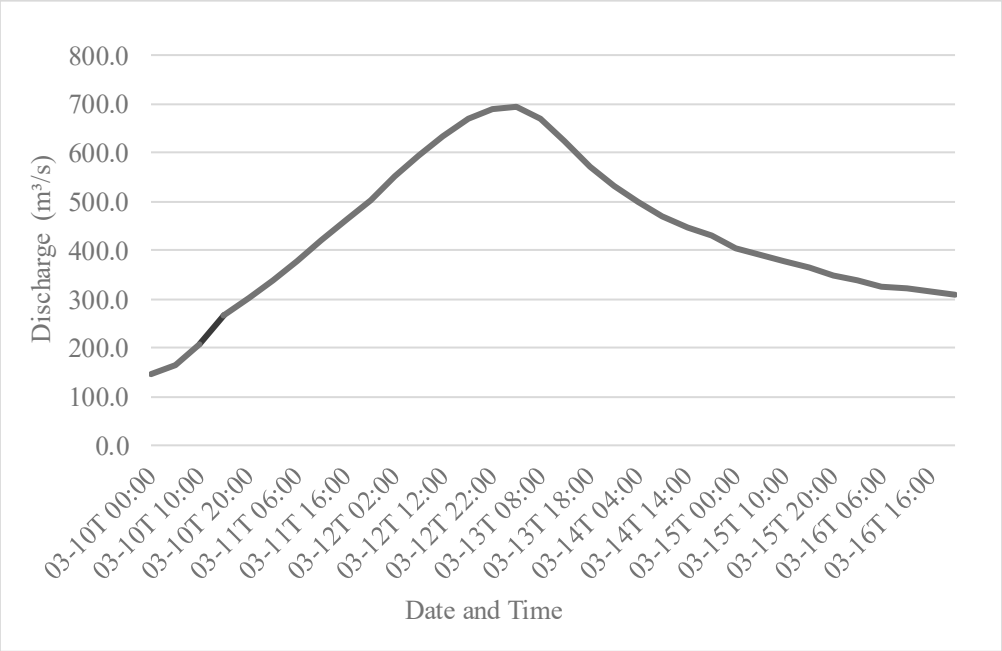

Figure 9.4 Observed discharge ($m^3 s^{-1}$) from March 10 to March 16, 2024, showing a flood peak of approximately 690 measured at the Châtel-de-Neuvre hydrological station.

Model calibration was performed by comparing simulated flood elevations to field-measured high-water marks. In August 2024 fieldwork, seven distinct flood marks were identified on tree trunks within the study reach (Figure 9.5), from which the peak water depths were determined. At these calibration points, the water depth error was computed as the difference between simulated and observed water levels. The calibration goal was to minimize these point-wise depth errors by adjusting hydraulic parameters. In practice, only the spatially distributed Manning's roughness coefficients were varied, since topography and boundary inputs were prescribed. Initial roughness values for each land-cover class (Section 9.3.1) were then refined iteratively. Specifically, the calibration procedure involved computing the depth error at each mark, then slightly increasing or decreasing the Manning n-values to improve agreement and re-running the unsteady model. This manual trial-and-error approach – adjusting channel and overbank *n* until simulated high-water marks match the measured marks with lower error – is a standard technique in flood modelling when high-water observations are available (Garrote et al., 2021; Iroume et al., 2022). Indeed, previous studies have used this method of "flood mark calibration" (for example, using silt lines on trees as proxy flood heights) to tune HEC-RAS and similar models (Gholami, 2022).

Figure 9.5 Location of surveyed flood marks along the Allier River study reach downstream of the Châtel-de-Neuvre hydrological station.

9.3.4. Large wood data

The LW inventory for the 8 *km* segment of the Allier River was derived from post-flood field surveys and pre-flood imagery. In total 29 logs were re-detected after the March 2024 flood: nine had been mobilized ("entrained"), four remained in place ("stable"), and sixteen were not found. These field observations form the baseline dataset for model input (Section 8.4.2). Each log was characterized by its initial position, measured diameter, length, and wood density (the latter measured as described in Section 8.4.4 or, if unavailable, set to the average of all measurements 580 $kg\ m^{-3}$) and by its initial orientation relative to flow. September 2023 orthophotos (EVS and Veodis3D) provided the pre-flood alignment of each log relative to the flow direction. In the first simulation trial, only the nine entrained logs were introduced into the hydraulic model under the March 2024 flood hydrograph, without including vegetation as an entrapment mechanism, thus serving as a baseline scenario for comparison. In the second stage, vegetation entrapment was activated, using the LiDAR-derived vegetation structure described in Section 9.3.2, to evaluate the influence of riparian vegetation on wood trapping. For each log, the input parameters were its length, diameter, density, and initial orientation and are summarized in Table 9.2.

Table 9.2 Physical characteristics of RFID-tagged LW elements across the 8 *km* segment of the Allier River downstream the Châtel-de-Neuvre hydrological station.

ID RFID	D (m)	L (m)	Density (kg m-³)	Initial orientation
074B38 (LW1)	0.20	6	519.50	90.00
074AAC (LW2)	0.33	9	580.00	20.00
074ADA (LW3)	0.22	15	580.00	70.00
074B35 (LW4)	0.30	4.6	580.00	54.00
074B3C (LW5)	0.22	12	580.00	125.00
074A9C (LW6)	0.26	10	436.86	130.00
076A26 (LW7)	0.34	5.1	580.00	130.00
076A20 (LW8)	0.39	12	580.00	51.00
076A35 (LW9)	0.24	9	580.00	100.00

In a subsequent step, the dataset was extended by detecting additional logs visible in September 2023 pre-flood orthophotos (Figure 9.6). This process increased the total number of simulated LW elements to 50 logs, combining both RFID-monitored logs and logs digitized from imagery. To ensure that the selected orthophoto-derived logs formed a representative and unbiased sample of the reach, a clear

and consistent selection procedure was followed. First, only logs whose full length and orientation could be confidently identified in the imagery were retained, excluding pieces partially obscured by shadows, dense canopy, or LW-jams. Second, logs were digitized from both vegetated and non-vegetated areas (e.g., channel margins, gravel bars, secondary channels, vegetated islands). For these additional logs, the lengths and orientation were directly obtained from the orthophotos using GIS tools. Since diameters could not be reliably inferred from orthophotos, a randomized distribution of diameters between 10 and 40 cm was assigned, corresponding to the observed range of diameters recorded for the LW monitored within the study reach. The wood density for these extended set of LW was assumed constant, using the mean value of all samples analyzed during the post-flood field campaign (580 $kg\ m^{-3}$). This procedure ensured that the extended dataset preserved realistic variability in geometry and orientation while maintaining consistency with the measured physical properties of the surveyed wood. By integrating both directly monitored and digitized logs, the enlarged dataset allowed for a more comprehensive analysis of entrainment thresholds, trapping mechanisms, and overall retention probabilities within the 8 *km* study reach.

Figure 9.6 pre-March 2024 flood event initial positions of the 50 LW elements simulated in this study.

9.4. Analysis of the results

9.4.1. Hydraulic modelling and model calibration

The first comparison refers to the river condition on September 26, 2023. The water extent derived from the orthophoto and the simulated flooded area, obtained with the input hydrograph of that specific day derived from Chatel-de--- gauging station, are compared. Both areas of agreement and sources of discrepancy in the model's performance are highlighted. To quantitatively assess the correspondence between the two datasets, the simulated, observed, and intersected water-extend areas were computed (Table 9.3). These values were then used to derive performance metrics based on the confusion matrix approach (Figure 9.7), which provides a structured framework for evaluating model accuracy. The metrics are defined as follows:

$$Precision = \frac{TP}{TP + FP} \tag{9.1}$$

$$Recall = \frac{TP}{TP + FN} \tag{9.2}$$

$$F1 = 2 \cdot \frac{Precision \cdot Recall}{Precision \times Recall} \tag{9.3}$$

$$Intersection\ over\ Union\ (IoU) = \frac{TP}{TP + FP + FN} \tag{9.4}$$

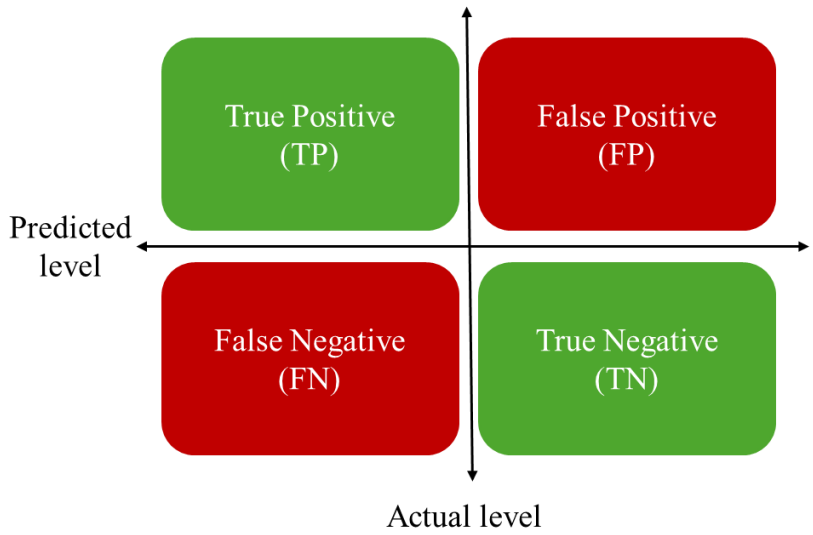

Figure 9.7 Confusion matrix categories for model validation against observed inundation extent.

Table 9.3 Quantitative comparison of simulated and observed flood extents (September 26, 2023, flow conditions).

Simulated Area (km^2)	49.44
Observed Area (km^2)	45.38
True Positive (km^2)	37.34
False Positive (km^2)	12.10
False Negative (km^2)	8.04

The results show a precision of 76%, indicating that the majority of the simulated wet areas correctly represent actual inundation. Nonetheless, the model exhibits false positives, particularly in flat or transitional topographic zones, where the representation of micro-topography and hydraulic connectivity is inherently challenging. Similarly, a recall of 82% confirms that the model successfully captures most of the observed inundation; however, some wet areas visible in the orthophoto remain underrepresented in the simulation, corresponding to false negatives. Beyond these two complementary indicators, the F1-score of 78.7% provides a balanced measure of accuracy by combining precision and recall, suggesting that the model achieves a solid compromise between correctly identifying observed floods and minimizing overprediction. The Intersection over Union (IoU), or Jaccard Index, of 65.6% further quantifies the spatial agreement between the two datasets, indicating that approximately two-thirds of the total inundated area (considering both model and observation) is correctly reproduced by the simulation. Despite this generally accepted performance, some discrepancies are evident. The visual comparison of the flooded areas (Figure 9.8) shows that mismatches are most pronounced near riverbanks, meandering reaches, and floodplain transition zones, where uncertainties in the bathymetric representation and, possibly, roughness parameterization can affect simulated water distribution. Limitations in the orthophoto data must also be acknowledged, particularly the difficulty in detecting shallow, transient, or vegetation-obscured flooded areas, which may partly explain the apparent overprediction by the model.

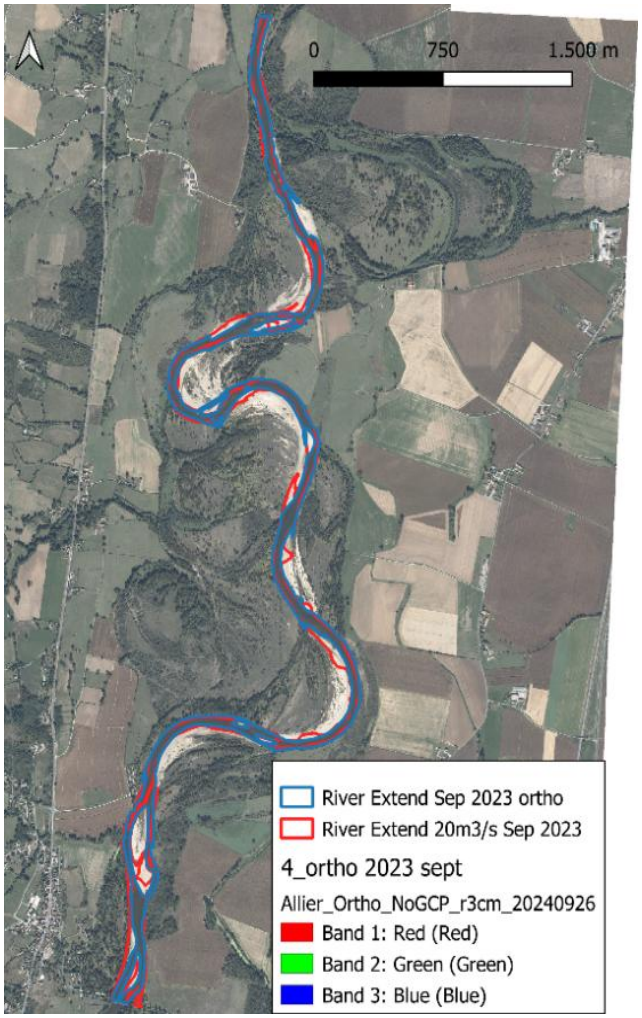

Figure 9.8 Overlay of modelled flood extent (20 $m^3 s^{-1}$) and observed water extent from orthophoto for September 26, 2023.

Figure 9.9 illustrates the steady state "warm-up" simulation results representing the pre-flood hydraulic conditions with a constant discharge of Q = 120 $m^3 s^{-1}$ and a simulation duration of 30 hours, that ensures that steady conditions are obtained along the entire reach. This scenario establishes the baseline flow distribution and water surface profile before the flood event. With water depth values ranging between 0.001 *m* and 4 *m*, depending on local channel morphology. Deeper zones are observed along the thalweg and at meander bends, reflecting the expected hydraulic behavior under normal flow conditions. The resulting pre-flood conditions serve as an initial condition for the subsequent unsteady-state flood event simulation. Figure 9.10 presents the results of the unsteady-state flood simulation corresponding to the March 2024 flood event, driven by the discharge hydrograph in Figure 9.4. The hydrograph spans a one-week period, with a peak discharge of 690 $m^3 s^{-1}$. Figure 9.10 shows the maximum simulated water depth throughout the event, highlighting the extent of inundation and the spatial variability of flow depths across the floodplain. The maximum water depths reach up to approximately 7 *m* along the main river channel, particularly within the

meandering reaches. Shallower depths are recorded in overbank and floodplain areas, indicating lateral water spreading and potential gradual attenuation of flow energy.

Figure 9.9 Simulated water depth from steady-hydraulic model of the Allier River on September 26, 2023.

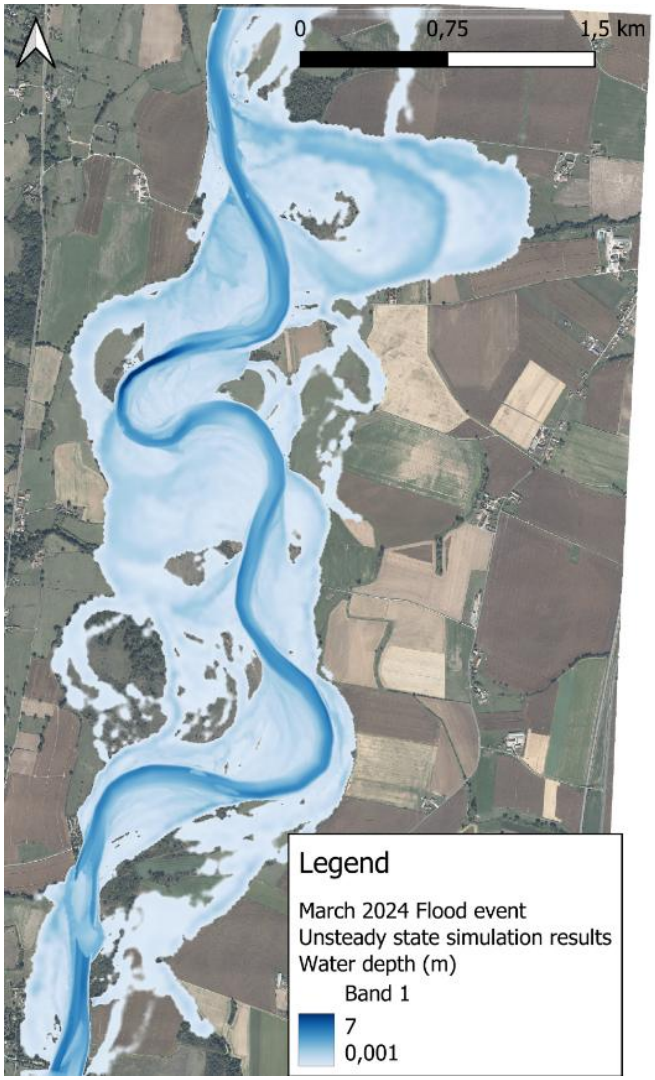

Figure 9.10 March 2024 flood event – unsteady-state water depth simulation results.

Model validation was carried out using observed flood marks collected during a field campaign in August 2024 (Figure 9.5). These marks, measured on trees using a tape measure and referenced to the ground elevation at each tree. This procedure provided water depth marks with an estimated vertical precision of approximately ± 5-10 cm, depending on local surface irregularities. The comparison between observed flood-mark elevations and simulated water depths prior to calibration (Table 9.4) showed variable agreement, with absolute errors ranging from 2% to 57%. The model adequately reproduced the flood stage at some locations (e.g. LC2 and LC7, both 2 %), but significant overestimations were observed at others, particularly LC4 (57 %) and LC3 (34 %). This overprediction trend indicates that the model initially overestimated water levels, especially within floodplain areas. Several factors can explain these discrepancies. First, inaccuracies in the representation of the riverbed geometry can substantially affect flow conveyance. When the model underestimates channel depth or cross-sectional area, the flow capacity of the main channel decreases, forcing excess discharge onto the floodplain and artificially raising the simulated water surface

(Czech et al., 2016; Neal et al., 2012). Second, the mesh resolution (≈ 10-20 *m* at the floodplain) can smooth localized terrain variability, leading to an inaccurate depiction of small depressions and levees that control over bank flow. This effect has been widely documented in flood modeling research: for instance, Fewtrell et al. (2008) demonstrated that coarse digital elevation models tend to elevate the floodplain surface and produce overestimated inundation depths. Furthermore, the roughness parameterization influences hydraulic resistance and simulated water levels. Overestimated Manning's coefficients in the main channel or floodplain increase energy losses, resulting in higher simulated stages (Bhargav et al., 2024; Sharma and Regonda, 2021). In the initial uncalibrated model, this likely contributed to the general overestimation trend observed at most validation points. To reduce these discrepancies, Manning's roughness coefficients were adjusted for both the main channel and vegetated areas within the floodplain (Table 9.5). The calibration significantly improved the agreement between observed and simulated water levels, decreasing the average percentage error from approximately 27 % to 15 % (Table 9.4). For example, the error at LC3 dropped from 34 % to 13 %, and at LC6 from 33 % to 11 %. These improvements are consistent with the findings of Horritt and Bates, (2002), who reported that refining roughness values can markedly enhance flood prediction accuracy. The post-calibration simulation preserved the expected hydraulic behavior, deep flows along the main channel and shallower floodplain inundation, while achieving substantially improved agreement with field measurements. The model performance now falls within the typical range of accepted flood-model accuracy, with residual pointwise errors of 10–20 %, comparable to those reported by Zhao et al. (2019). However, some localized discrepancies remain, especially at LC2 and LC4, primarily due to the mesh resolution that smooths microtopography and neglects fine-scale terrain features. Such resolution-related limitations have been highlighted in several studies as a key source of model uncertainty (Bilgili et al., 2023; David and Schmalz, 2021). Nevertheless, after calibration, the model demonstrates a good ability to reproduce both the magnitude and spatial distribution of water depths during the flood event.

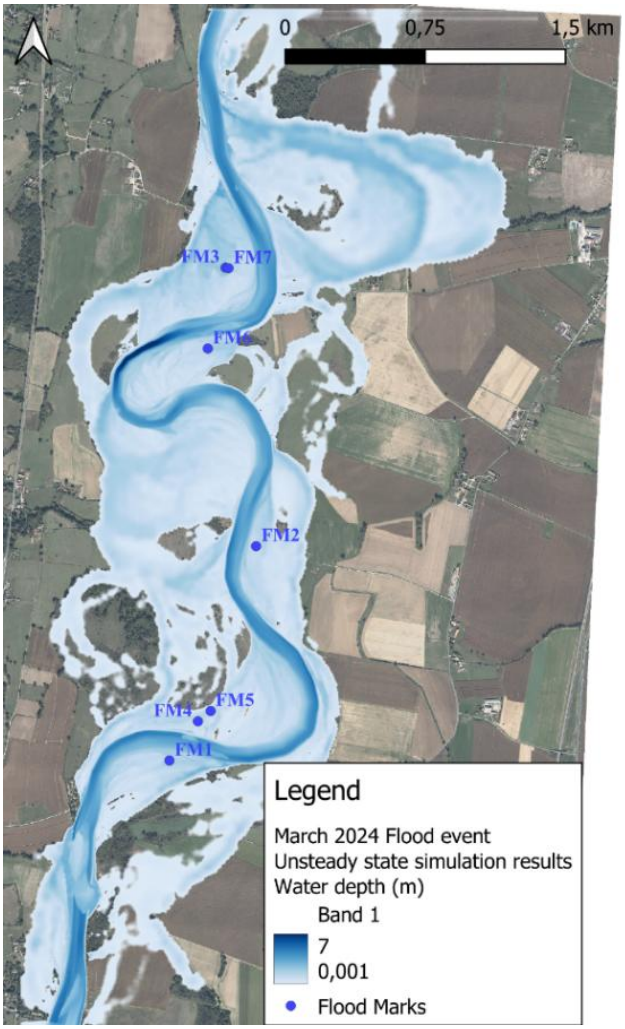

Figure 9.11 Unsteady-state simulation results showing water depth and flood marks during the March 2024 flood event.

Table 9.4 Comparison between observed flood marks and simulated water depths pre- and post-calibration, for the March 2024 flood event.

Point ID	Observed flood marks (m)	Max simulated pre -calibration water depth (m)	Max simulated post-calibration water depth (m)	Pre-calibration absolute error (%)	Post-calibration absolute error (%)
LC1	1.00	1.50	1.19	50 %	19 %
LC2	1.00	0.98	0.72	2 %	28 %
LC3	1.50	2.01	1.69	34 %	13 %
LC4	0.70	1.10	0.83	57 %	19 %
LC5	1.20	1.35	1.21	13 %	1 %
LC6	1.00	1.33	1.11	33 %	11 %
LC7	1.60	1.64	1.35	2 %	16 %

Table 9.5 Calibrated Manning's roughness coefficients for different land use classes.

Land use	Manning's coefficients ($s/m^{1/3}$)
Main channel	0.030
Secondary channel	0.030
periodically herbaceous	0.025
Permanent herbaceous	0.060
Dense forest	0.100
Low density forest	0.080

9.4.2. Large-Wood transport and retention dynamics

To isolate the effect of riparian vegetation on log entrapment, two simulation scenarios were performed for the nine logs that were observed to have changed their position between the 2023 and 2024 field surveys, thus mobilized by the hydraulic events that occurred during that period, with the March 2024 flood being the dominant event. In the bare-channel scenario (Scenario 1), where vegetation was entirely removed from the model domain, no entrapment occurred (0%), with all logs transported downstream without encountering obstacles. In contrast, the inclusion of mapped vegetation patches (Scenario 2) resulted in an entrapment rate of 57% (4 out of 7 logs), nearer to the 78 % entrapment rate observed in the field (considering only the 9 modelled logs). This improvement highlights the key role of riparian vegetation in limiting downstream transport and promoting in-channel storage of wood. The difference between the two scenarios is also evident in the travelled-distance errors between observed and simulated deposition points. Without vegetation, predicted deposition points were significantly displaced, with absolute errors reaching up to 6.6 *km*, while when vegetation was included, errors decreased to less than 100 *m* for the 9 analyzed logs (Table 9.6), yielding a substantially closer agreement with field observations. Only three logs are included in Table 9.6. Although four logs were entrapped in Scenario 2, one of these was a false entrapment: the model entrapped a log that was not entrapped in the field and whose ID does not correspond to any of the observed entrapped logs. This log was therefore excluded from the comparison to ensure that the evaluation focuses solely on logs that were entrapped both in the model and in reality. Overall, the reduction in displacement errors and the higher entrapment success in Scenario 2 confirm that the representation of riparian vegetation markedly improves the reproduction of observed LW retention dynamics within the study reach.

Table 9.6 Comparison of simulated LW travel distances absolute errors between Scenario 1 and Scenario 2.

Log ID	Scenario 1	Scenario 2
	Traveled distance absolute error (m)	**Traveled distance absolute error (m)**
LW 4	6620.13	32.32
LW 5	1154.41	81.08
LW 6	2518.70	57.83

Once the initial validation confirmed that including vegetation improved model performance, the simulation framework was extended to a larger dataset consisting of 50 LW elements, as described in Section 9.3.4. The model entrainment rate was 84%, in excellent agreement with the 86% calculated from monitored logs in the modeled segment, confirming the ability of the model to replicate the high mobility of wood under flood conditions. Among the entrained logs, 69% were deposited through entrapment by vegetation, closely reproducing the 78% field estimate of logs trapped against riparian trees and shrubs. This strong correspondence indicates that the implementation of the simplified vegetation–LW interaction routines successfully captured the role of riparian vegetation as a key control on wood deposition and local storage. The analysis of travelled distances provided further insight into the spatial dynamics of LW movement. Simulated travelled distances varied by more than two orders of magnitude, ranging from a few meters up to over 5,000 *m,* highlighting the inherent heterogeneity of wood transport processes. A clear trend emerged between logs that were entrapped by vegetation and those that remained free-floating. Logs not entrapped exhibited much greater downstream displacement, with median distances of approximately 1,500 *m* and maximum values exceeding 5,000 *m*, consistent with long-range transport typically associated with unobstructed flow corridors. In contrast, entrapped logs displayed markedly reduced mobility, with median travelled distances below 300 *m* and several cases showing deposition within the first 100 m from their initial position. The statistical test (Figure 9.12) revealed a difference ($p < 0.05$, Mann–Whitney U test) between the two groups, confirming that vegetation entrapment acts as the dominant factor limiting log displacement. On the contrary, weak negative correlations were found between travelled distance and both log's diameter ($r = 0.30$) and length ($r = 0.21$), confirming that during intense floods log's geometric properties are secondary compared to the influence of vegetation. The relationship between log geometry and travelled distance is however weakly negative, suggesting that larger or longer logs can be more mobile if not trapped, but entrapment effectively negates this potential.

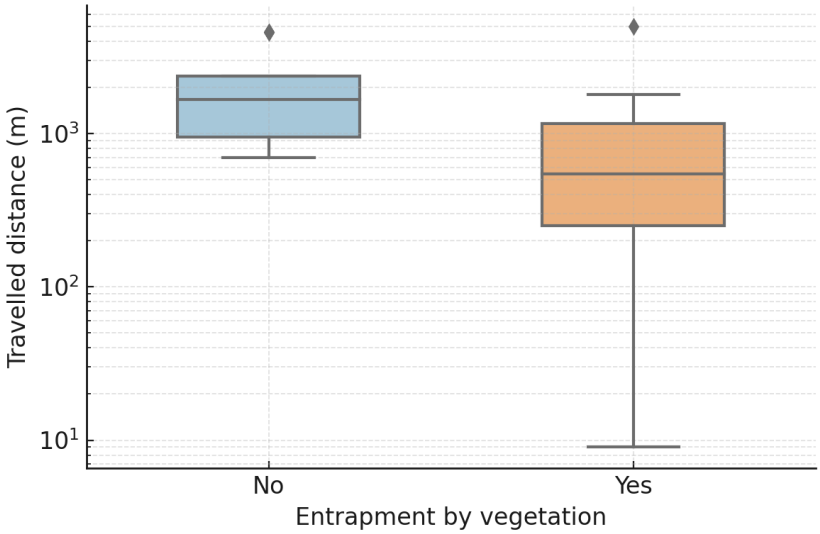

Figure 9.12 Boxplot of travelled distance by vegetation entrapment.

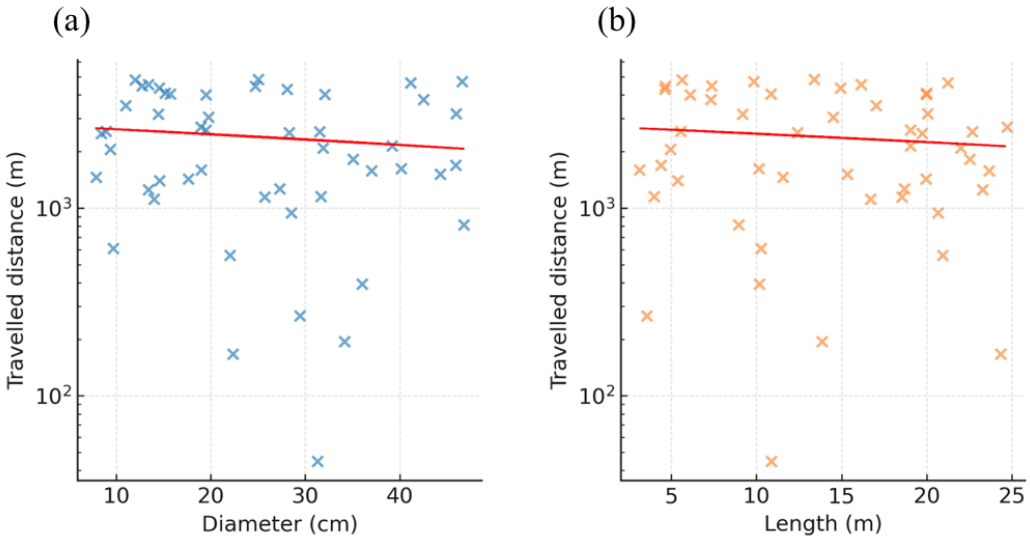

Figure 9.13 Relationship between LW dimensions and travelled distance. (a) Diameter versus travelled distance, (b) Length versus travelled distance.

When comparing the overall retention and export behavior of the study area, the model reproduced the general tendencies observed in the field, though with some differences in magnitude. In the field, of the 29 logs originally present in the reach, approximately 34% were retained after the flood and 66% were exported downstream, assuming that the 16 unrecovered logs exited the reach. Conversely, the simulation predicted that 72% of the initial 50 logs were retained within the modelled segment and only 28% were exported, suggesting an overestimation of the total retention. However, when restricting the comparison to the subset of logs with known fate from field monitoring, the effective field retention increased to 77%, while export decreased to 23%, values that align remarkably well with the 72% retained and 28% exported predicted by the model. This convergence indicates that

much of the apparent discrepancy stems from uncertainties in field detection rather than model bias. Spatially, LW deposition within the modelled meander reach is predominantly concentrated along the inner bends, where clusters of six to nine retained logs were observed (Figure 9.14). This spatial pattern suggests that wood retention is strongly controlled by local hydraulic and morphological conditions. The inner bends are characterized by low-velocity zones and shallow flow depths, which promote the gradual deceleration and deposition of floating logs. In these zones, vegetated point bars and riparian plants further enhance wood trapping by providing physical barriers against which the logs can lodge. In contrast, the outer bends, dominated by high velocities and greater shear stress, favor continued transport rather than deposition. Overall, the observed clustering pattern highlights the role of secondary flow circulation and energy dissipation in promoting preferential wood storage along the inner banks of meandering rivers.

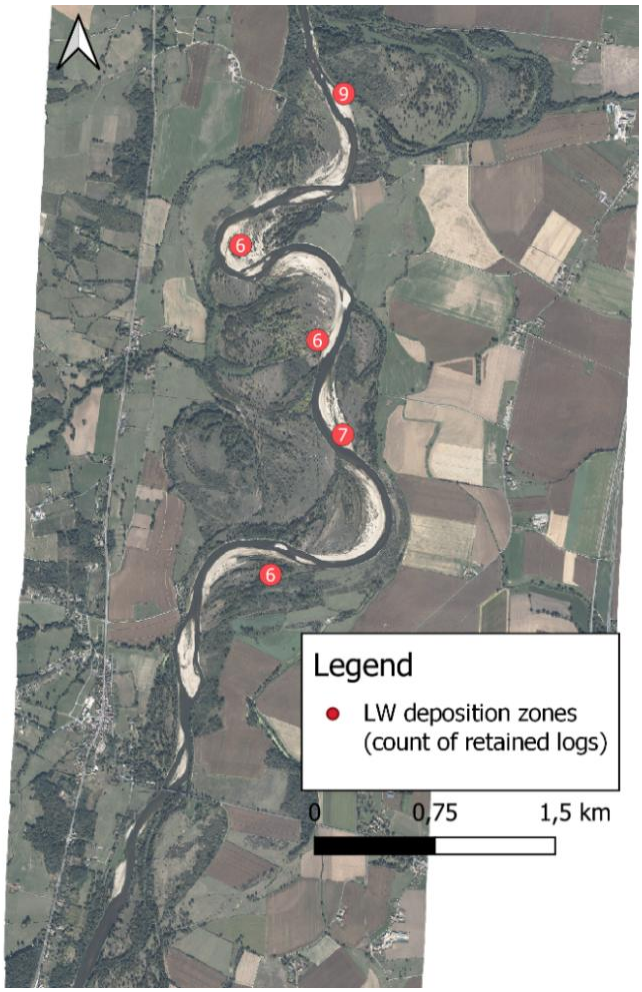

Figure 9.14 LW deposition zones and counts of retained logs.

9.5. Discussion

Flood magnitude exerts the primary control on the mobilization and export of LW in river corridors. In the case of the March 2024 event, the peak discharge reached 690 $m^3\ s^{-1}$, corresponding to an estimated return period of 5 years, was sufficient to entrain the majority of the initially present LW. Consistent with thresholds reported in experimental and field studies. Braudrick and Grant (2001) demonstrated that wood movement begins when flow depth exceeds a log's buoyant depth. These findings align with our observations, most monitored logs began to move during the rising limb of the hydrograph, once local water depths exceeded their estimated flotation thresholds.

LW dynamics are highly variable among rivers, but consistent trends emerge regarding entrainment, retention and export. Under ordinary flow conditions, only a small fraction of total in-stream wood is exported annually. Senter et al. (2017) estimated that merely 0.3–5.6% of total wood stock typically leaves a system each year, implying strong internal retention. Long-term tracking in forested mountain streams has confirmed this, showing less than 2% annual export under normal flows, with substantially higher mobilization occurring only during extreme events. For example, following the 1996 flood, approximately 8% of logs were exported from an old-growth reach and 22% from a second-growth reach. Such evidence underscores that high wood retention is the norm, and significant export occurs primarily during rare, high-magnitude floods capable of mobilizing previously stable wood deposits (Ruiz-Villanueva et al., 2016c).

In our study, 86% of identifiable logs were entrained, representing near-complete mobilization of the monitored LW set, consistent with the simulated mobilization rate of 84% and falls within the range observed during other large floods. For instance, Kramer and Wohl (2017) reported that during very large flood events, mobilization / remobilization of fluvial LW could approach ~80–90 %, particularly for new recruits or in areas undergoing strong morphological change. Meanwhile, under bankfull floods can potentially mobilize up to 30-40% (Kramer and Wohl, 2017; Merten et al., 2010). Thus, while flood magnitude dictates the scale of entrainment, the fate of mobilized LW, whether exported or retained, depends largely on channel characteristics and vegetation structure.

Vegetation acts as a mechanical barrier that intercepts and traps floating LW, thereby reducing downstream export potential. Numerous field studies have demonstrated this mechanism. Galia and Máčka (2023) found that standing woody vegetation can retain 15–30% of total in-channel wood, while Beckman and Wohl (2014b) reported that up to 80% of logs can be incorporated into jams in systems with abundant vegetation and wood supply. Likewise, Pettit and Naiman (2006) observed that large floods deposit LW around riparian vegetation, forming accumulations that later facilitate

plant regeneration. Our simulations and field data fall within these reported ranges, confirming that the 8 *km* reach of the Allier River functions as an efficient wood retention zone. Despite widespread entrainment (86%), approximately three-quarters of mobilized logs were retained within the 8 *km* modeled reach, with only a small fraction exported downstream. These retention rates are consistent with those observed in other wood-rich rivers during major floods (Galia and Máčka, 2023; Warren and Kraft, 2008). Such findings confirm that riparian vegetation plays a central role in retaining LW, promoting local storage even during high-energy flood events. Overall, model results mirrored field observations closely. The simulated entrainment rate (84%) nearly matched the observed one (86%), indicating that the model realistically captured which logs became mobile. When not accounting for lost logs, the model predicted 77% retention versus 72% observed (28% exported), confirming its accuracy in reproducing overall retention–export ratios. However, discrepancies arose in the mechanisms and locations of retention. Field observations showed that approximately 78% of transported logs were trapped by vegetation, often forming clumps around trees or shrubs, whereas the simulation obtained 69% vegetation entrapment. This underestimation likely reflects how vegetation was represented in the model. In the present modelling framework, the spatial distribution of riparian vegetation is derived from remote sensing datasets, specifically from the difference between the Digital Surface Model (DSM) and the Digital Terrain Model (DTM), which provides a canopy height model used to represent vegetated areas along the river corridor. This approach allows the integration of vegetation information over large spatial scales and provides a practical method for identifying potential trapping zones where transported large wood may interact with vegetation. However, this representation introduces several simplifications that should be considered when interpreting the model results. Remote sensing techniques such as airborne LiDAR or photogrammetric DSMs primarily detect rigid canopy structures, typically associated with mature trees. In contrast, flexible vegetation elements such as shrubs, young trees, or partially submerged branches may not be reliably detected, especially when surveys are conducted under leaf-off conditions or when vegetation is submerged during flood events. In natural river systems, these flexible vegetation structures can play a significant role in filtering and trapping transported wood elements, particularly during the rising stages of floods when floating logs interact with low vegetation layers along the channel margins or floodplains. As a result, the DSM-based vegetation representation used in the model may underestimate the actual trapping capacity of vegetated areas. This simplification may therefore lead to a systematic bias toward increased wood mobility, as some vegetation structures capable of retaining wood elements are not explicitly represented in the numerical model. Consequently, simulated wood elements may travel longer distances than those observed, particularly in river reaches characterized by dense riparian vegetation.

Such limitations are common in deterministic wood-transport modelling. As highlighted by Bertoldi and Ruiz-Villanueva (2017) wood–vegetation interactions are highly stochastic and depend strongly on small-scale structural complexity, which is difficult to reproduce in simplified numerical frameworks. In our model, vegetation is implemented as a set of static, solid obstacle cells with an ON/OFF trapping behavior: once a log enters a vegetated cell, it is considered entrapped. While this binary approach is necessary for computational efficiency, it does not account for partial obstructions, branch networks, or the cumulative effects of multiple adjacent stems, all of which play a critical role in real retention processes. Flume studies (e.g., Bocchiola et al., 2008; Braudrick and Grant, 2001) show that logs can be trapped by wedging, pinning, or leaning against small branches and rootwads, mechanisms that cannot be reproduced when vegetation is represented only by simplified cell-based obstacles. Despite these limitations, the adopted approach provides a practical compromise between physical realism and data availability, enabling the integration of vegetation effects into reach-scale simulations of wood transport. Future developments of the modelling framework could improve the representation of vegetation characteristics by integrating additional datasets such as high-resolution terrestrial LiDAR, UAV-based photogrammetry, or field-based vegetation surveys, which can provide more detailed information on vegetation density, flexibility, and structural complexity.

Furthermore, a significant source of uncertainty arises from the "lost" logs in the field data. 16 of 29 tagged logs were not recovered post-flood. While excluded from the comparative analysis, some may have been retained but went undetected (e.g. buried or lost their RFID tags). Thus, even when simulated and observed retention rates align closely, differences in detectability and data completeness must be acknowledged. Another limitation involves how models handle submergence and overtopping. The current simplified approach assumes that once water depth exceeds vegetation height, the modelled LW element will float over, and when flows are shallower, vegetation acts as a solid barrier. In reality, even submerged vegetation can trap wood, and logs sometimes dive beneath partially submerged obstacles. Braudrick and Grant (2001) introduced the concept of "debris roughness," noting that deposition likelihood depends on the relationship between flow depth and log buoyant depth. Although such threshold approaches offer first-order predictions, they remain static and neglect the dynamic feedback between flow and vegetation. In reality, those interactions are far more complex: logs can be caught by submerged crowns, or flexible stems can rebound and pin them after flow recession. In summary, the close correspondence between modeled and observed LW entrainment and retention-export rates confirms that including vegetation significantly improved the realism of ORSA2D_WT model. However, the underestimation of vegetation trapping highlights the need for more detailed representations of riparian vegetation. Future modeling should integrate dynamic vegetation behavior, consider flexible morphology, and refine snagging criteria to better

imitate natural trapping efficiency. Incorporating these improvements will enhance predictions of LW retention and support more accurate assessments of flood-related LW transport in vegetated river systems.

9.6. Implications for river management

The current study findings in terms of retention potential highlight that riparian trees can serve as highly effective natural barriers for LW during flood events. In fact, dense stands of floodplain trees and shrubs act as "natural filter" that intercept and retain drifting LW. This means that LW mobilized by flood events could get captured on vegetated floodplains before it can travel further downstream. Indeed, literature confirms that when flood carry LW into a forested floodplain, the standing trees tend to trap the woody material; LW pieces deposited among riparian vegetation are unlikely to remobilize once the flood recedes (Wohl et al., 2016). These natural trapping processes observed in the field reinforce the value of preserving vegetated areas along rivers. The LW trapping capacity of riparian vegetation may have direct benefits for infrastructure safety. LW transport is a known hazard in rivers (Mazzorana et al., 2018; Ruiz-Villanueva et al., 2014c; Schalko, 2018; Schalko et al., 2020; Wohl et al., 2016) if uncontrolled, logs can jam against bridges, block culverts, or collide with other structures, often causing severe damage or flooding upstream (Schalko, 2018). By maintaining or restoring vegetated zones in strategic locations to enhance trapping, river managers can create natural filters that intercept LW before it reaches these vulnerable points. During overbank flow conditions, widely spaced floodplain trees encourage the formation of log jams on the floodplain, effectively storing wood outside the main channel (Kramer and Wohl, 2017), thus preventing hazardous accumulations at downstream critical zones. Furthermore, the energy of floating debris also dissipates in a controlled manner. A notable example comes from a managed river corridor in Colorado, where a reach with a broad gravel bar and healthy riparian woodland was deliberately used as a wood retention zone where flood-mobilized LW elements accumulate among the trees, providing environmental benefits while avoiding any risk to the downstream footbridge (Wohl et al., 2016). Such an example illustrates how nature-based solutions can complement traditional engineering approaches in river management.

Within this context, the modelling framework developed in this thesis provides a valuable tool to support eco-engineering approaches and nature-based river management strategies. By simulating the transport pathways, deposition patterns, and trapping probabilities of LW elements during flood events, the enhanced ORSA2D_WT model can help identify locations where wood accumulation is most likely to occur. These predictions allow river managers to distinguish between areas where LW accumulation may pose a potential hazard and areas where wood can be safely retained within the

river corridor to enhance habitat complexity and ecological functioning without significantly increasing downstream risk.

Such capabilities are particularly relevant in the context of international environmental policies such as the European Union Water Framework Directive, which encourages the restoration of natural hydro morphological processes and the improvement of ecological conditions in river systems. Instead of systematically removing wood from channels, river management strategies can therefore move toward more balanced approaches that combine flood risk management with ecological restoration objectives.

From an operational perspective, the modelling framework can support decision-making in several management contexts. For example:

- **Bridge and infrastructure risk management:** Hydraulic structures such as bridges represent critical locations where large wood accumulation may increase flood risk by obstructing the flow section. The modelling framework can help identify river reaches where transported wood elements are more likely to interact with such structures during flood events. Although the current model does not provide a quantitative prediction of accumulation probability, it allows for the identification of areas potentially prone to wood retention near bridge piers and other hydraulic infrastructures. These insights can support infrastructure management by highlighting priority areas for monitoring, maintenance operations, or the implementation of debris retention measures upstream.
- **Riparian vegetation management:** riparian vegetation plays an important role in trapping and retaining large wood elements during flood events. By analyzing the interaction between wood transport pathways and vegetated areas, the model can help identify sections of the river corridor where vegetation acts as a natural retention system, reducing the probability that wood reaches downstream infrastructure. This information can support vegetation management strategies aimed at maintaining or enhancing the retention capacity of riparian corridors.
- **Floodplain planning and river restoration:** in river restoration projects, large wood is increasingly used as a nature-based solution to improve morphological diversity and ecological functioning. The modelling framework can help identify floodplain areas or channel reaches where wood deposit is likely to occur naturally and where restoration interventions involving wood placement may be implemented without significantly increasing flood hazard.

Several results derived from the simulations can be particularly informative for river managers and decision-makers. Through post-processing and spatial analysis of the model outputs using GIS tools, it is possible to generate maps indicating potential large wood (LW) retention zones, identify areas prone to wood accumulation, and reconstruct transport pathways under different flood scenarios. These derived results provide spatially explicit information that can support the identification of suitable zones for natural wood retention and the assessment of potential risk areas near critical infrastructure.

Designing and implementing natural LW filters therefore involves identifying and maintaining areas within the river corridor that can safely trap LW elements. In practice, this means preserving existing floodplain forests and encouraging the development of robust riparian vegetation in locations prone to LW deposition. These areas should ideally be located upstream of critical infrastructure and away from densely populated zones, allowing them to function as buffer zones that intercept transported wood before it reaches vulnerable locations.

The adoption of these nature-based strategies should be accompanied by appropriate monitoring and management practices. Following major flood events, inspections should be conducted to evaluate the stability of trapped wood accumulations (Wohl et al., 2016). Wood pieces that are firmly wedged among trees are generally stable and may be left in place, whereas elements that could potentially become remobilized during subsequent floods may need to be selectively removed or repositioned. Periodic monitoring and maintenance are therefore essential to ensure the continued effectiveness of these natural retention zones.

Overall, these findings suggest that preserving and strategically managing riparian vegetation can provide a cost-effective and environmentally sustainable approach to mitigating LW-related hazards. By integrating natural trapping processes into river management strategies, it is possible to reduce flood risks while simultaneously enhancing the ecological value and resilience of river systems.

Conclusions and recommendations

LW plays an important role in river systems. While it contributes to morphological diversity and ecological habitat formation, it can also increase hydraulic risks during floods by blocking bridge openings and constricting flow. This thesis investigated the dynamics of LW in rivers through a combination of experimental, numerical, and field approaches. The study aimed to improve the understanding and predictive modelling of the processes governing LW entrainment and deposition under flood conditions. To achieve this, the work updated the two-dimensional Eulerian–Lagrangian model ORSA2D_WT (Persi 2018), incorporating more accurate formulations for LW entrainment and arrest, and validating these improvements across scales, from laboratory experiments to field-scale applications. The motivation for this research stems from the persistent uncertainty in predicting when and how LW initiates motion, how it propagates through complex flow fields, and how it is retained by channel morphology and riparian vegetation. Addressing these challenges requires integrating theoretical developments, controlled laboratory experiments, and field observations.

Advances in the understanding and modelling of LW dynamics

The first part of the thesis reviewed the state of knowledge on LW dynamics, emphasizing the wide range of approaches used in both experimental and field studies. It identified the principal mechanisms controlling wood recruitment, entrainment, transport, and deposition and examined how these are influenced by wood geometry, density, and channel morphology. The review also discussed the ecological and hydraulic implications of LW, highlighting the need to balance risk mitigation with the preservation of its beneficial functions. A critical outcome of the review was the identification of three major research needs:

(i) the implementation of a physically based entrainment formulation that can represent rolling and sliding motion,
(ii) empirical data on near-bed hydrodynamic forces acting on logs under shallow flows, and
(iii) an explicit treatment of vegetation as a component influencing wood retention. These priorities guided the experimental and modelling developments that followed.

The subsequent model development focused on improving the entrainment and arrest routines of ORSA2D_WT. The earlier version relied on simplified flotation-based criteria, which underestimated the flow conditions required for initiation of motion. In this thesis, the model was reformulated following the theoretical approach of Bocchiola et al. (2006), in which entrainment is expressed as the equilibrium between hydrodynamic forces (drag) and resisting forces (gravity, buoyancy, and bed friction). This formulation allowed explicit simulation of sliding and rolling motion, extending

applicability to shallow conditions typical of initial mobilization. Representation of orientation and friction variability was added to account for natural heterogeneity as suggested by Chen et al. (2020). A vegetation entrapment sub-module was also included to simulate the arrest of transported LW in areas with mature vegetation. Together, these improvements enhanced the physical realism of the model while maintaining numerical stability and computational efficiency.

Laboratory experiments provided the empirical basis for these developments. Controlled experiments were performed to measure drag and side-force coefficients for semi-submerged cylindrical bodies near the bed, under different orientations. The results confirmed the strong dependence of hydrodynamic forces on bed proximity and orientation, validating theoretical expectations and offering new empirical relationships suitable for modeling near-bed wood motion. These coefficients were directly implemented in ORSA2D_WT, strengthening the linkage between experimental evidence and numerical representation. The accurate quantification of these coefficients is fundamental for realistic prediction of entrainment thresholds and transport dynamics.

Validation of the enhanced ORSA2D_WT model against the laboratory results demonstrated that simulated thresholds of entrainment closely matched experimental observations, confirming the reliability of the theoretical entrainment model and the appropriateness of the newly measured hydrodynamic coefficients. Sensitivity analyses revealed that both drag coefficient and bed friction angles exert strong control on the onset of motion, emphasizing the need for accurate parameterization. The validation demonstrated that the enhanced model could replicate the physical processes observed in the flume, thereby providing confidence for its application to field-scale environments.

The first real-scale application was conducted in the Tagliamento River, a braided Alpine River with well-documented LW transport data (Ravazzolo et al., 2015a). This case study tested the model's capacity to reproduce wood mobility under flood conditions. The vegetation entrapment routine was excluded, allowing the study to isolate purely hydraulic and morphological controls. This choice was justified by the characteristics of the Tagliamento river, where vegetation plays a comparatively minor role in wood retention. Ravazzolo et al. (2015a) showed that the transported LW in the Tagliamento river were deposited in roughly equal proportions as isolated pieces or within wood jams formed primarily on unvegetated bars. These observations indicate that, in this specific river, wood retention is governed mainly by hydraulic conditions and bar morphology rather than by riparian vegetation, making the vegetation routine less relevant for this application. Field data from GPS- and RFID-tracked logs provided reference trajectories for comparison. The model captured the general transport patterns, with simulated trajectories closely consistent with field observations. The

sensitivity analysis revealed the significant influence of wood density on log behavior. Simulations of wet density conditions showed notable deviations from observed data, while those employing dry density conditions resulted in earlier entrainment. These findings underscore the complex interplay among density, buoyancy and hydrodynamic forces, emphasizing the need for precise density measurements in LW transport modelling. The initial orientation of logs was also found to affect transport dynamics. However, the impact of LW orientation on entrainment and travel distance appears less significant than that of density. Additionally, the model's treatment of immobile LW as isolated entities led to an overestimation of mobility. In reality, such logs are often part of larger accumulations or partially buried, which increases their resistance to entrainment. This limitation suggests that future models must better represent interactions among LW, as well as the effects of partial burial and structural elements like root wads and branches.

The field monitoring campaign in the Allier River formed a critical link between controlled experimentation and modelling applications. The campaign provided a board dataset on LW dynamics to support model validation. Conducted along a 50 *km* reach of the Allier River, characterized by alternating forested and open banks, the study involved multiple flood events during which wooden elements were equipped with RFID tags and recovered after transport (Hortobágyi et al., 2024a). In 2024 supplementary data were collected on sediment size, channel geometry, and vegetation structure, while a LiDAR survey provided high-resolution maps of tree density and canopy height. The field observations yielded several important insights. Even moderate floods were able to mobilize stored wood, indicating that entrainment can occur below traditional bankfull thresholds. Retention was closely associated with vegetated zones and root structures, and deposition frequently occurred near islands and floodplain margins where local flow decelerated. The recovery data showed strong variability in transport distances emphasizing the stochastic nature of wood motion in natural settings. Partial burial and entrapment with vegetation were observed as common stabilizing mechanisms.

Building on this dataset, the enhanced ORSA2D_WT model was applied to the Allier River to simulate LW transport and retention during the March 2024 flood event. The objective was to evaluate the model's ability to reproduce field-observed wood behavior under natural conditions and to test the influence of vegetation on wood dynamics. The hydraulic modelling and calibration reproduced the main characteristics of the flood event with satisfactory accuracy: the comparison between simulated and observed inundation extents indicated that the model captured the general spatial pattern of flooding, although some discrepancies remained near channel margins and low-relief floodplain areas. These mismatches were mainly related to uncertainties in the digital terrain representation, roughness parameterization, and limitations in detecting shallow or vegetation-

obscured water surfaces from aerial imagery. Calibration of Manning's coefficients improved the agreement between simulated and observed water levels, bringing the model performance within the expected range for reach-scale hydraulic applications. Overall, the calibrated model provided a reliable representation of both steady and unsteady flow conditions and served as a basis for LW transport simulations. LW modelling confirmed the critical influence of riparian vegetation on wood retention. In simulations without vegetation, most logs were transported downstream, whereas including vegetation produced realistic entrapment patterns and deposition zones consistent with field observations. Vegetation enhanced model agreement by promoting wood storage along inner bends and floodplain margins, reflecting the physical role of trees as obstacles to LW movement. The extended simulations using additional logs reproduced the observed high entrainment and retention during the flood, supporting the applicability of the enhanced ORSA2D_WT framework at the reach scale. Despite these promising results, several uncertainties persist. Vegetation was represented as rigid, static elements, while natural riparian vegetation is flexible and structurally complex. The model also simplifies wood–wood interactions and does not simulate jam formation or breakage, processes that can influence local retention. Limited RFID recovery introduced further uncertainty into validation. Nevertheless, the combined hydraulic-LW modelling provides a coherent picture of floodplain inundation and wood dynamics during the March 2024 flood, demonstrating that the enhanced ORSA2D_WT model can reproduce observed trends of entrainment and deposition.

Across all components of this research, a coherent picture emerges. LW entrainment is governed by the balance between driving and resisting forces, strongly influenced by log orientation, density, and friction conditions. Transport behavior depends on local hydraulic gradients and channel morphology, while retention is controlled primarily by vegetation density and structure. The enhanced ORSA2D_WT model provides a physically consistent tool for simulating these processes, effectively linking experimental observations with field-scale applications. Its results align with the patterns observed in both flume and natural settings, demonstrating that the combination of theoretical modelling and empirical data can yield credible predictions of LW motion.

Compared with existing two-dimensional Eulerian–Lagrangian models for LW transport, the enhanced ORSA2D_WT model developed in this thesis introduces several methodological improvements that strengthen the physical representation of wood entrainment and retention processes. Previous modelling approaches have successfully coupled depth-averaged hydraulic solvers with Lagrangian descriptions of wood motion (e.g., Ruiz-Villanueva et al., 2014a; Kang and Kimura, 2018; Persi et al., 2018), allowing simulation of wood trajectories and deposition patterns within river reaches. However, many of these models rely on simplified entrainment criteria,

empirical parameterizations of hydrodynamic forces, or limited representation of vegetation–wood interactions.

The first improvement introduced in this thesis is the implementation of a physically based entrainment formulation derived from the theoretical framework proposed by Bocchiola et al. (2006). The enhanced ORSA2D_WT model explicitly computes the balance between hydrodynamic forces and resisting forces acting on individual logs. This approach enables the simulation of rolling and sliding mechanisms that govern the initial mobilization of wood elements under shallow flow conditions depending on their orientation relative to the flow. As a result, the model provides a more realistic representation of the physical processes controlling entrainment in natural rivers. A second contribution concerns the experimental characterization of hydrodynamic coefficients acting on near-bed wood elements. Many existing modelling frameworks rely on assumed or indirectly calibrated drag coefficients, which introduces uncertainty in the representation of hydrodynamic forces acting on LW elements. In contrast, this thesis integrates empirically derived drag and side-force coefficients obtained from controlled laboratory experiments on semi-submerged cylindrical bodies in near bed conditions. This experimental calibration strengthens the physical consistency of the model and improves the prediction of entrainment thresholds and transport dynamics. Another important advancement introduced in this work is the explicit representation of vegetation-induced LW retention. Although the influence of riparian vegetation on wood trapping has been widely documented in field studies, it is rarely explicitly represented in numerical LW transport models. In the enhanced ORSA2D_WT framework, a vegetation entrapment routine was implemented using vegetation information derived from digital surface models. This allows the model to simulate the interaction between transported wood elements and riparian vegetation stands, thereby improving the representation of deposition processes in vegetated floodplains and channel margins. These developments collectively enhance the ability of the model to reproduce the physical mechanisms governing entrainment, transport, and retention of individual wood elements, while maintaining the computational efficiency typical of two-dimensional shallow-water hydrodynamic models. Overall, ORSA2D_WT framework remains suitable for reach-scale applications and scenario-based analyses relevant to river management and flood risk assessment.

Nevertheless, some modelling limitations and trade-offs remain inherent to the approach and are discussed in greater detail in the "Domain of Applicability and Modelling Limitations" section of the Conclusions. Overall, the enhanced ORSA2D_WT framework advances the current state of the art by integrating physically based entrainment processes, experimentally derived hydrodynamic parameters, and vegetation-driven trapping mechanisms within a computationally efficient two-dimensional hydraulic modelling framework validated across laboratory and field scales.

Domain of applicability and modelling limitation

The ORSA2D_WT model is a two-way coupled Eulerian–Lagrangian framework designed to simulate the transport of LW elements in river environments. In this approach, the flow field is computed using a depth-averaged hydrodynamic solver based on the two-dimensional shallow water equations, while individual wood elements are represented as discrete rigid bodies whose motion is computed through Newton's second law. This coupling allows the model to simulate the translation, rotation, entrainment, and deposition of wood pieces while accounting for interactions between the flow and transported elements. The model is intended for high-Reynolds-number open-channel flows typical of natural river floods, where inertial and gravitational forces dominate over viscous effects. The hydrodynamic forces acting on the wood elements are therefore expressed through empirical drag and side force coefficients, which are appropriate under turbulent conditions where Reynolds numbers exceed approximately 10^4. In terms of river morphology, the ORSA2D_WT model is particularly applicable to gravel-bed and mixed-bed river systems, where large wood recruitment and mobility frequently occur during flood events. Such environments are typically characterized by heterogeneous hydraulic conditions, including fast-flowing channels, shallow marginal zones, and morphologically complex areas such as bars, islands, and secondary channels. These conditions are representative of many European river systems and correspond to the environments analyzed in this thesis. The enhanced version of the model developed in this thesis further extends the domain of applicability of ORSA2D_WT by incorporating additional physical processes controlling LW mobility. In particular, the introduction of rolling and sliding entrainment thresholds allows the model to represent the initiation of motion for logs under shallow flow conditions. Previous studies have shown that wood entrainment can occur not only by flotation but also through rolling or sliding mechanisms depending on log orientation and bed friction conditions. The incorporation of these mechanisms therefore enables the model to simulate wood mobilization across a wider range of hydraulic conditions, including the early stages of flood events when water depths may still be limited.

However, several modelling assumptions constrain the range of conditions for which the framework can be reliably applied. In particular, large wood elements are represented as rigid cylindrical bodies, which simplifies their natural geometry and neglects structural features such as branches, root wads, and irregular surface roughness. In natural river systems, these features often increase the likelihood of mechanical anchoring or interlocking with bed material, vegetation, or existing wood accumulations, thereby reducing wood mobility. By neglecting these structural complexities, the model may systematically overestimate the mobility and transport distance of wood elements, effectively representing a conservative scenario in which wood remains mobile for longer distances.

A similar limitation arises in the representation of riparian vegetation. Vegetation is derived from DSM-based canopy height information, which primarily captures the upper structure of mature trees but may not adequately represent flexible vegetation elements such as shrubs, young trees, or partially submerged branches. These lower and more flexible vegetation structures can play a significant role in trapping floating wood during flood events, particularly along floodplain margins and secondary channels. Consequently, the simplified vegetation representation may lead to an underestimation of the actual trapping capacity of vegetated floodplains, further contributing to simulated transport distances that may exceed those observed in natural conditions.

Furthermore, the coupling between LW transport, sediment transport, and morphological change was beyond the scope of this work, although such interactions are fundamental for understanding long-term river evolution. These simplifications, while necessary for computational tractability, limit the model's applicability under conditions where fine-scale structural complexity or strong wood–morphology feedback dominate. Addressing these aspects in future developments will be essential to improve the predictive capacity and realism of two-way coupled LW transport models.

Uncertainty also arises from the limited availability of field data. Tracking individual wood pieces during floods is inherently challenging, and recovery rates are often incomplete. Positional accuracy and timing uncertainties can influence comparisons with model results. Although the combination of RFID and LiDAR techniques improved spatial coverage, broader datasets encompassing multiple events and rivers would enhance model calibration. Continued development of automated and remote monitoring methods is therefore essential for advancing predictive capability.

Implications for river management and eco-engineering

The results of this thesis have important implications for river management and eco-engineering approaches. Riparian vegetation was shown to play a key role in controlling LW retention, acting as a natural filter that intercepts floating wood during flood events. Rather than systematically removing wood from river corridors, management strategies may therefore benefit from preserving or restoring vegetated floodplains capable of safely trapping LW. The modelling framework developed in this thesis provides a tool to support such strategies. By analyzing simulated transport pathways and spatial patterns of wood–flow interactions, it is possible to identify areas where wood is more likely to be retained within the river corridor without increasing risks to downstream infrastructure. These capabilities are consistent with international environmental policies such as the European Union Water Framework Directive, which encourages the restoration of natural river processes and ecological functions. The model can support decision-making in several contexts, including bridge risk assessment, riparian vegetation management, and floodplain restoration planning.

Future research directions

Looking forward, several research directions can be proposed. In the short term, improving the representation of wood geometry by accounting for branches, root wads, and partial burial would significantly enhance predictions of entrainment and retention. Refinement of vegetation representation, including flexible and multi-layered structures rather than static canopy-based obstacles, is a second priority, given its demonstrated influence on LW retention. In the present framework, vegetation is derived primarily from DSM-based canopy height information, which captures mature tree structures but may underrepresent flexible vegetation elements such as shrubs, young trees, and partially submerged branches. These components can act as highly effective filters for floating wood during flood events. Future research should therefore explore improved vegetation characterization methods, potentially integrating higher-resolution remote sensing data such as UAV photogrammetry, terrestrial LiDAR surveys, or detailed field inventories. In the medium term, explicit modelling of jam formation would allow simulation of accumulation processes that strongly affect local hydraulics and flood risk. Wood jams can alter flow patterns, promote sediment deposition, and create significant backwater effects, yet their formation and evolution remain difficult to predict numerically. Developing algorithms capable of simulating jam formation, growth, and potential breakage would therefore represent an important advancement in large wood transport modelling.

From a computational perspective, future development should prioritize model parallelization. As applications extend to longer river reaches, finer spatial resolutions, and large ensembles of LW elements, computational demand will increase substantially. Parallel implementation of the LW module would improve scalability and enable practical use of the model

From an applied perspective, another promising avenue for future research concerns the response of LW transport processes to changing flood regimes associated with climate change. In many river basins, flood events are increasingly characterized by longer periods of sustained high discharge rather than short, sharply peaked hydrographs (Blöschl et al., 2019; Woods et al., 2023). Such conditions may lead to repeated cycles of mobilization, temporary deposition, and remobilization of wood elements along the river corridor, potentially favoring congestion processes and the formation of large wood accumulations. Exploring how different hydrograph shapes, durations, and flood sequences influence LW transport dynamics will therefore be important for improving flood risk assessments under evolving climatic conditions.

Another promising direction for future research is the integration of Graph Neural Network (GNN) models with the physically based simulations produced by the enhanced ORSA2D_WT framework.

River systems are inherently network-based structures in which hydraulic and geomorphological processes propagate through spatially connected channel and floodplain elements. GNNs are particularly well suited to modelling such systems because they explicitly represent spatial relationships between nodes and allow information to propagate along network connections.

In this context, the computational grid of the hydraulic model could be represented as a graph structure, where each grid cell corresponds to a node and the hydraulic connectivity between neighboring cells defines the edges of the graph. For each node, a set of input features could be derived from the hydrodynamic simulations and terrain characteristics, including variables such as flow depth, velocity magnitude, bed slope, terrain elevation, distance from the main channel, vegetation density, and flood duration and intensity. The target variable could be defined as the probability of LW deposition or trapping at a given location, obtained from the ORSA2D_WT simulations.

The ORSA2D_WT model could therefore serve as a physics-based generator of labelled training data, producing large datasets of LW trajectories and deposition locations under different hydraulic scenarios. These datasets could then be used to train a GNN model capable of learning the spatial patterns that control wood retention processes. Architectures such as Graph Convolutional Networks (GCN) or Graph SAGE could be explored to capture the propagation of LW through the river network and to predict zones with high probability of wood accumulation.

Once trained, such a model could provide rapid predictions of potential LW deposition zones across large river networks, significantly reducing the computational cost associated with repeated hydraulic simulations. This type of hybrid framework, combining physics-based simulations with graph-based machine learning models, could therefore support large-scale screening analyses aimed at identifying critical accumulation zones, bridge blockage risks, or natural wood retention areas.

More broadly, integrating GNN-based predictive tools with physically based hydrodynamic modelling could contribute to the development of operational decision-support systems for river management, enabling rapid assessment of LW-related hazards while maintaining consistency with the underlying physical processes governing wood transport.

In conclusion, this thesis provides a physically grounded, multi-scale contribution to the study of LW's dynamics in river systems. By combining theoretical formulations, controlled laboratory experiments, and field observations, it demonstrates the feasibility of representing LW entrainment, transport, and retention processes within an improved hydrodynamic modelling framework. The developments implemented in the ORSA2D_WT model, namely the Bocchiola-based entrainment

formulation and the vegetation-entrapment routine, establish the foundation for a practical modelling tool that can support flood-risk assessment and river-management applications.

For the model to be applied effectively, high-quality input data are essential, particularly high-resolution topographic information and realistic representations of riparian vegetation. When such datasets are available, the modelling framework can be used to evaluate LW-related hazards, explore alternative management scenarios, such as clearing, thinning, or restoring vegetated corridors and assessing the effectiveness of nature-based mitigation strategies aimed at enhancing natural wood retention within river corridors.

Although certain simplifications remain, and further integration will be necessary to improve predictive capability, the results of this work demonstrate the potential of the enhanced ORSA2D_WT framework as a valuable tool for analyzing LW dynamics in natural river systems. Importantly, the model should be interpreted and applied primarily as a decision-support tool rather than a deterministic predictive system, acknowledging the inherent variability and uncertainty that characterize natural river processes. Within this perspective, the modelling framework developed in this thesis provides a solid basis for incorporating LW dynamics into river-management planning and for supporting more informed and adaptive decision-making in the context of flood-risk mitigation and ecosystem-based river management.

References

Abbe, T.B., Montgomery, D.R., 2003. Patterns and processes of wood debris accumulation in the Queets river basin, Washington.

Addy, S., Wilkinson, M., 2016. An assessment of engineered log jam structures in response to a flood event in an upland gravel-bed river. Earth Surf. Process. Landf. 41, 1658–1670. https://doi.org/10.1002/esp.3936

Addy, S., Wilkinson, M.E., 2019. Representing natural and artificial in-channel large wood in numerical hydraulic and hydrological models. WIREs Water 6. https://doi.org/10.1002/wat2.1389

Alamayreh, M.I., Fenocchi, A., Petaccia, G., Sibilla, S., Persi, E., 2021. Numerical analysis of fluid flow dynamics around a yawed half-submerged cylinder inside an open channel. Journal of Hydrodynamics 33, 111–119. https://doi.org/10.1007/s42241-021-0005-0

Amicarelli, A., Albano, R., Mirauda, D., Agate, G., Sole, A., Guandalini, R., 2015. A Smoothed Particle Hydrodynamics model for 3D solid body transport in free surface flows. Comput. Fluids 116, 205–228. https://doi.org/10.1016/j.compfluid.2015.04.018

Anlanger, C., Attermeyer, K., Hille, S., Kamjunke, N., Koll, K., König, M., Schnauder, I., Nogueira Tavares, C., Weitere, M., Brauns, M., 2022. Large wood in river restoration: A case study on the effects on hydromorphology, biodiversity, and ecosystem functioning. Int. Rev. Hydrobiol. 107, 34–45. https://doi.org/10.1002/iroh.202102089

Beckman, N.D., Wohl, E., 2014a. Carbon storage in mountainous headwater streams: The role of old-growth forest and logjams. Water Resour. Res. 50, 2376–2393. https://doi.org/10.1002/2013WR014167

Beckman, N.D., Wohl, E., 2014b. Effects of forest stand age on the characteristics of logjams in mountainous forest streams. Earth Surf. Process. Landf. 39, 1421–1431. https://doi.org/10.1002/esp.3531

Bertoldi, W., Gurnell, A.M., Welber, M., 2013. Wood recruitment and retention: The fate of eroded trees on a braided river explored using a combination of field and remotely-sensed data sources. Geomorphology 180–181, 146–155. https://doi.org/10.1016/j.geomorph.2012.10.003

Bertoldi, W., Ruiz-Villanueva, V., 2017. Physical and Numerical Modelling of Large Wood and Vegetation in Rivers, in: Gravel-Bed Rivers. Wiley, pp. 729–753. https://doi.org/10.1002/9781118971437.ch27

Bertoldi, W., Zanoni, L., Tubino, M., 2010. Assessment of morphological changes induced by flow and flood pulses in a gravel bed braided river: The Tagliamento River (Italy). Geomorphology 114, 348–360. https://doi.org/10.1016/j.geomorph.2009.07.017

Bhargav, A.M., Suresh, R., Tiwari, M.K., Trambadia, N.K., Chandra, R., Nirala, S.K., 2024. Optimization of Manning's roughness coefficient using 1-dimensional hydrodynamic modelling in the perennial river system: A case of lower Narmada Basin, India. Environ. Monit. Assess. 196, 743. https://doi.org/10.1007/s10661-024-12883-w

Bilgili, E., Bomers, A., van Lente, G.J., Huthoff, F., Hulscher, S.J.M.H., 2023. The effect of a local mesh refinement on hydraulic modelling of river meanders. River Res. Appl. 39, 832–846. https://doi.org/10.1002/rra.4110

Blanckaert, K., Han, R., Pilotto, F., Pusch, M., 2014. Effects of large wood on morphology, flow and turbulence in a Lowland River, in: River Flow 2014. CRC Press, pp. 2493–2501. https://doi.org/10.1201/b17133-332

Blöschl, G., Hall, J., Viglione, A., Perdigão, R.A.P., Parajka, J., Merz, B., Lun, D., Arheimer, B., Aronica, G.T., Bilibashi, A., Boháč, M., Bonacci, O., Borga, M., Čanjevac, I., Castellarin, A., Chirico, G.B., Claps, P., Frolova, N., Ganora, D., Gorbachova, L., Gül, A., Hannaford, J., Harrigan, S., Kireeva, M., Kiss, A., Kjeldsen, T.R., Kohnová, S., Koskela, J.J., Ledvinka, O., Macdonald, N., Mavrova-Guirguinova, M., Mediero, L., Merz, R., Molnar, P., Montanari, A., Murphy, C., Osuch, M., Ovcharuk, V., Radevski, I., Salinas, J.L., Sauquet, E., Šraj, M., Szolgay, J., Volpi, E., Wilson, D., Zaimi, K., Živković, N., 2019. Changing climate both increases and decreases European river floods. Nature 573, 108–111. https://doi.org/10.1038/s41586-019-1495-6

Bocchiola, D., Rulli, M.C., Rosso, R., 2008. A flume experiment on the formation of wood jams in rivers. Water Resour. Res. 44. https://doi.org/10.1029/2006WR005846

Bocchiola, D., Rulli, M.C., Rosso, R., 2006. Flume experiments on wood entrainment in rivers. Adv. Water Resour. 29, 1182–1195. https://doi.org/10.1016/j.advwatres.2005.09.006

Braudrick, C.A., Grant, G.E., 2001. Transport and deposition of large woody debris in streams: a flume experiment, Geomorphology.

Braudrick, C.A., Grant, G.E., 2000. When do logs move in rivers? Water Resour. Res. 36, 571–583. https://doi.org/10.1029/1999WR900290

Buscombe, D., Rubin, D.M., Warrick, J.A., 2010. A universal approximation of grain size from images of noncohesive sediment. J. Geophys. Res. Earth Surf. 115. https://doi.org/10.1029/2009JF001477

Buscombe, D., Warrick, J., Ritchie, A., East, A., McHenry, M., McHenry, M., Foxgrover, A., Wohl, E., 2024. Remote sensing large-wood storage downstream of reservoirs during and after dam removal: Elwha River, Washington, USA. https://doi.org/10.31223/X5DQ4W

Buxton, T.H., 2010. Modeling entrainment of waterlogged large wood in stream channels. Water Resour. Res. 46. https://doi.org/10.1029/2009WR008041

Cadol, D., Wohl, E., 2010. Wood retention and transport in tropical, headwater streams, La Selva Biological Station, Costa Rica. Geomorphology 123, 61–73. https://doi.org/10.1016/j.geomorph.2010.06.015

Caldatto, I.R., Becker, A.C.C., Bleninger, T., Polli, B.A., Daru, R.L., Penteado, R., Freitas, C., 2024. Characterization of woody material transport on the Madeira River at the Jirau Hydroelectric Power Plant: a study using a three-dimensional particle model. RBRH 29. https://doi.org/10.1590/2318-0331.292420230128

Charles, F., Laveissière, L., Groc, M., Magdalou, J.-A., Garrigue, J., Garrigue RFID, J., n.d. RFID tracking for monitoring deadwood mobility in a small coastal Mediterranean mountainous river: implementation and preliminary results.

Chen, S.C., Tfwala, S.S., Wang, C.R., Kuo, Y.M., Chao, Y.C., 2020. Incipient motion of large wood in river channels considering log density and orientation. Journal of Hydraulic Research 58, 489–502. https://doi.org/10.1080/00221686.2019.1625816

Collins, B.D., Montgomery, D.R., 2002. Forest Development, Wood Jams, and Restoration of Floodplain Rivers in the Puget Lowland, Washington. Restor. Ecol. 10, 237–247. https://doi.org/10.1046/j.1526-100X.2002.01023.x

Comiti, F., Lucía, A., Rickenmann, D., 2016. Large wood recruitment and transport during large floods: A review. Geomorphology 269, 23–39. https://doi.org/10.1016/j.geomorph.2016.06.016

Corenblit, D., Vidal, V., Cabanis, M., Steiger, J., Garófano-Gómez, V., Garreau, A., Hortobágyi, B., Otto, T., Roussel, E., Voldoire, O., 2016. Seed retention by pioneer trees enhances plant diversity resilience on gravel bars: Observations from the river Allier, France. Adv. Water Resour. 93, 182–192. https://doi.org/10.1016/j.advwatres.2016.02.015

Costabile, P., Macchione, F., 2015. Enhancing river model set-up for 2-D dynamic flood modelling. Environmental Modelling & Software 67, 89–107. https://doi.org/10.1016/j.envsoft.2015.01.009

Cowan, 1956. Estimating hydraulic roughness coefficients. Agricultural Engineering 37, 473–475.

Crosato, A., Rajbhandari, N., Comiti, F., Cherradi, X., Uijttewaal, W., 2013. Flume experiments on entrainment of large wood in low-land rivers. Journal of Hydraulic Research 51, 581–588. https://doi.org/10.1080/00221686.2013.796573

Czech, W., Radecki-Pawlik, A., Wyżga, B., Hajdukiewicz, H., 2016. Modelling the flooding capacity of a Polish Carpathian river: A comparison of constrained and free channel conditions. Geomorphology 272, 32–42. https://doi.org/10.1016/j.geomorph.2015.09.025

David, A., Schmalz, B., 2021. A Systematic Analysis of the Interaction between Rain-on-Grid-Simulations and Spatial Resolution in 2D Hydrodynamic Modeling. Water (Basel). 13, 2346. https://doi.org/10.3390/w13172346

Davidson, S.L., Eaton, B.C., 2015. Simulating riparian disturbance: Reach scale impacts on aquatic habitat in gravel bed streams. Water Resour. Res. 51, 7590–7607. https://doi.org/10.1002/2015WR017124

Davidson, S.L., MacKenzie, L.G., Eaton, B.C., 2015. Large wood transport and jam formation in a series of flume experiments. Water Resour. Res. 51, 10065–10077. https://doi.org/10.1002/2015WR017446

Elisabetta Persi, 2018. Eulerian-Lagrangian modelling of large floating debris transport during floods.

Elliot, R.C., Froehlich, D.C., MacArthur, R.C., 2012. Calculating the Potential Effects of Large Woody Debris Accumulations on Backwater, Scour, and Hydrodynamic Loads, in: World Environmental and Water Resources Congress 2012. American Society of Civil Engineers, Reston, VA, pp. 1213–1222. https://doi.org/10.1061/9780784412312.123

Elosegi, A., Elorriaga, C., Flores, L., Martí, E., Díez, J., 2016. Restoration of wood loading has mixed effects on water, nutrient, and leaf retention in Basque mountain streams. Freshwater Science 35, 41–54. https://doi.org/10.1086/684051

Ennouini, W., Persi, E., Petaccia, G., Ravazzolo, D., Picco, L., Mao, L., Sibilla, S., 2025. Exploiting GPS and RFID field data to validate numerical modelling of large wood transport in the Tagliamento River (Italy). Earth Surf. Process. Landf. 50. https://doi.org/10.1002/esp.70163

Erpicum, S., Poppema, D., Burghardt, L., Benet, L., Wüthrich, D., Klopries, E.-M., Dewals, B., 2024. A dataset of floating debris accumulation at bridges after July 2021 flood in Germany and Belgium. Sci. Data 11, 1092. https://doi.org/10.1038/s41597-024-03907-8

Erskine, W.D., Saynor, M.J., Chalmers, A., Riley, S.J., 2012. Water, Wind, Wood, and Trees: Interactions, Spatial Variations, Temporal Dynamics, and their Potential Role in River Rehabilitation. Geographical Research 50, 60–74. https://doi.org/10.1111/j.1745-5871.2011.00731.x

Fewtrell, T.J., Bates, P.D., Horritt, M., Hunter, N.M., 2008. Evaluating the effect of scale in flood inundation modelling in urban environments. Hydrol. Process. 22, 5107–5118. https://doi.org/10.1002/hyp.7148

Follett, E., Wohl, E., 2024. Channel-Spanning Logjams and Reach-Scale Hydraulic Resistance in Mountain Streams. Geophys. Res. Lett. 51. https://doi.org/10.1029/2024GL110126

Francis, R.A., Tibaldeschi, P., McDougall, L., 2008. Fluvially-deposited large wood and riparian plant diversity. Wetl. Ecol. Manag. 16, 371–382. https://doi.org/10.1007/s11273-007-9074-2

Galia, T., Máčka, Z., 2023. Living woody vegetation as a storage element for large wood in the channel. Science of The Total Environment 892, 164717. https://doi.org/10.1016/j.scitotenv.2023.164717

Galia, T., Poledniková, Z., Škarpich, V., 2024. Impact of large wood on sediment (dis)connectivity in a meandering river. Geomorphology 453, 109153. https://doi.org/10.1016/j.geomorph.2024.109153

Garefalakis, P., do Prado, A.H., Mair, D., Douillet, G.A., Nyffenegger, F., Schlunegger, F., 2023. Comparison of three grain size measuring methods applied to coarse-grained gravel deposits. Sediment. Geol. 446, 106340. https://doi.org/10.1016/j.sedgeo.2023.106340

Garrote, J., González-Jiménez, M., Guardiola-Albert, C., Díez-Herrero, A., 2021. The Manning's Roughness Coefficient Calibration Method to Improve Flood Hazard Analysis in the Absence of River Bathymetric Data: Application to the Urban Historical Zamora City Centre in Spain. Applied Sciences 11, 9267. https://doi.org/10.3390/app11199267

Gholami, V., 2022. Prediction of flood discharge and flood flow depth using a hydraulic model and flood marks on the trees in ungauged forested watersheds. J. For. Sci. (Prague). 68, 190–198. https://doi.org/10.17221/6/2022-JFS

Gippel, C.J., O'neill, I.C., Finlayson, B.L., Schnatz, I., 1996. HYDRAULIC GUIDELINES FOR THE RE-INTRODUCTION AND MANAGEMENT OF LARGE WOODY DEBRIS IN LOWLAND RIVERS. Regulated Rivers: Research & Management 12, 223–236.

Grabowski, R.C., Gurnell, A.M., Burgess-Gamble, L., England, J., Holland, D., Klaar, M.J., Morrissey, I., Uttley, C., Wharton, G., 2019. The current state of the use of large wood in river restoration and management. Water and Environment Journal 33, 366–377. https://doi.org/10.1111/wej.12465

Gurnell, A., 2003. Wood storage and mobility , in: Ecology and Management of Wood in World Rivers . American Fisheries Society Symposium 37 , pp. 75–91.

Gurnell, A., Petts, G., 2006. Trees as riparian engineers: the Tagliamento river, Italy. Earth Surf. Process. Landf. 31, 1558–1574. https://doi.org/10.1002/esp.1342

Gurnell, A.M., Corenblit, D., García de Jalón, D., González del Tánago, M., Grabowski, R.C., O'Hare, M.T., Szewczyk, M., 2016. A Conceptual Model of Vegetation–hydrogeomorphology Interactions Within River Corridors. River Res. Appl. 32, 142–163. https://doi.org/10.1002/rra.2928

Gurnell, A.M., Petts, G.E., Hannah, D.M., Smith, B.P.G., Edwards, P.J., Kollmann, J., Ward, J. V., Tockner, K., 2001. Riparian vegetation and island formation along the gravel-bed Fiume Tagliamento, Italy. Earth Surf. Process. Landf. 26, 31–62. https://doi.org/10.1002/1096-9837(200101)26:1<31::AID-ESP155>3.0.CO;2-Y

Gurnell.A.M., Piegay, H., Swanson, F.J., Gregory, S. V., 2002. Large wood and fluvial processes. Freshw. Biol. 47, 601–619. https://doi.org/10.1046/j.1365-2427.2002.00916.x

Haga, H., Kumagai, T., Otsuki, K., Ogawa, S., 2002. Transport and retention of coarse woody debris in mountain streams: An in situ field experiment of log transport and a field survey of coarse woody debris distribution. Water Resour. Res. 38, 1-1-1–16. https://doi.org/10.1029/2001wr001123

Harmon, Anderson, Franklin, Cline, Swanson, Aumen, Sollins, Sedell, Gregory, Lienkaemper, lattin, cromack Jr, n.d. Ecology of Coarse Woody Debris in Temperate Ecosystems.

Hinwood, J.B., McLean, E.J., 2017. Large wood in the Snowy River estuary, Australia. Geomorphology 279, 209–225. https://doi.org/10.1016/j.geomorph.2016.10.023

Hlavňa, M., Máčka, Z., Záthurecký, J., 2024. Numerical Modeling of Potential Large Wood Entrainment in Rivers: Application of Hybrid Modeling in the Inter-Dam Reach of the Dyje River, Czechia. Water Resour. Res. 60. https://doi.org/10.1029/2023WR035145

Hoang, M.C., Laneville, A., Légeron, F., 2015. Experimental study on aerodynamic coefficients of yawed cylinders. J. Fluids Struct. 54, 597–611. https://doi.org/10.1016/j.jfluidstructs.2015.01.002

Horritt, M.S., Bates, P.D., 2002. Evaluation of 1D and 2D numerical models for predicting river flood inundation. J. Hydrol. (Amst). 268, 87–99. https://doi.org/10.1016/S0022-1694(02)00121-X

Hortobágyi, B., Melun, G., Petit, S., Piégay, H., 2024a. Dynamique des bois flottés en rivière-Éléments de synthèse des travaux de recherche 2020-2024.

Hortobágyi, B., Petit, S., Marteau, B., Melun, G., Piégay, H., 2024b. A high-resolution inter-annual framework for exploring hydrological drivers of large wood dynamics, in: River Research and Applications. John Wiley and Sons Ltd, pp. 958–975. https://doi.org/10.1002/rra.4242

Hyatt, T.L., Naiman, R.J., 2001. THE RESIDENCE TIME OF LARGE WOODY DEBRIS IN THE QUEETS RIVER, WASHINGTON, USA. Ecological Applications 11, 191–202.

Hygelund, B., Manga, M., 2003. Field measurements of drag coefficients for model large woody debris.

Igarashi, Y., Tanaka, N., 2024. Experimental Study on the Transport and Trapping of Floating Debris by Standing Trees during a Flood Event.

Iroume, J.Y.-A., Onguéné, R., Djanna Koffi, F., Colmet-Daage, A., Stieglitz, T., Essoh Sone, W., Bogning, S., Olinga Olinga, J.M., Ntchantcho, R., Ntonga, J.-C., Braun, J.-J., Briquet, J.-P., Etame, J., 2022. The 21st August 2020 Flood in Douala (Cameroon): A Major Urban Flood Investigated with 2D HEC-RAS Modeling. Water (Basel). 14, 1768. https://doi.org/10.3390/w14111768

Jeppson, R.W., 1974. Simulation of Steady and Unsteady Flows in Channels and Rivers.

Kang, T., Kimura, I., 2018. Computational modeling for large wood dynamics with root wad and anisotropic bed friction in shallow flows. Adv. Water Resour. 121, 419–431. https://doi.org/10.1016/j.advwatres.2018.09.006

Kimura, I., Kang, T., Kato, K., 2021. 3D–3D Computations on Submerged-Driftwood Motions in Water Flows with Large Wood Density around Driftwood Capture Facility. Water (Basel). 13, 1406. https://doi.org/10.3390/w13101406

Kleinhans, M.G., Wilbers, A.W.E., De Swaaf, A., Van Den Berg, J.H., 2002. Sediment Supply-Limited Bedforms in Sand-Gravel Bed Rivers. Journal of Sedimentary Research 72, 629–640. https://doi.org/10.1306/030702720629

Kramer, N., Wohl, E., 2017. Rules of the road: A qualitative and quantitative synthesis of large wood transport through drainage networks. Geomorphology 279, 74–97. https://doi.org/10.1016/j.geomorph.2016.08.026

Lai, Y., Bountry, J., 2022. Robust Eco-Hydraulic 3D Modeling Tools for Rivers with Complex In-Stream Structures Lead Researcher.

Lai, Y.G., Bandrowski, D.J., 2014. Large Wood Flow Hydraulics: A 3D Modelling Approach.

Latterell, J.J., Naiman, R.J., 2007. SOURCES AND DYNAMICS OF LARGE LOGS IN A TEMPERATE FLOODPLAIN RIVER. Ecological Applications 17, 1127–1141. https://doi.org/10.1890/06-0963

Lucía, A., Comiti, F., Borga, M., Cavalli, M., Marchi, L., 2015. Dynamics of large wood during a flash flood in two mountain catchments. Natural Hazards and Earth System Sciences 15, 1741–1755. https://doi.org/10.5194/nhess-15-1741-2015

Lyn, D., Cooper, T., Yi, Y.-K., 2003. Debris Accumulation at Bridge Crossings: Laboratory and Field Studies. https://doi.org/10.5703/1288284313171

MacVicar, B., Piégay, H., 2012. Implementation and validation of video monitoring for wood budgeting in a wandering piedmont river, the Ain River (France). Earth Surf. Process. Landf. 37, 1272–1289. https://doi.org/10.1002/esp.3240

MacVicar, B.J., Piégay, H., Henderson, A., Comiti, F., Oberlin, C., Pecorari, E., 2009. Quantifying the temporal dynamics of wood in large rivers: field trials of wood surveying, dating, tracking, and monitoring techniques. Earth Surf. Process. Landf. 34, 2031–2046. https://doi.org/10.1002/esp.1888

Mallqui, R., Claros, E., Cabrera, J., 2025. Influence of Wood Density on Backwater Rise due to Wood 3 Accumulations. Journal of Coastal and Hydraulic Structures 5. https://doi.org/10.59490/jchs.2025.0046

Martin, D.J., Benda, L.E., 2001. Patterns of instream wood recruitment and transport at the watershed scale. Trans. Am. Fish. Soc. 130, 940–958.

Martin, D.J., Harden, C.P., Tran, L., Pavlowsky, R.T., 2018. Investigating patterns of in-channel wood deposition locations in a low-gradient, variably-confined alluvial river system. Progress in Physical Geography: Earth and Environment 42, 139–161. https://doi.org/10.1177/0309133318759613

Mazzorana, B., Ruiz-Villanueva, V., Marchi, L., Cavalli, M., Gems, B., Gschnitzer, T., Mao, L., Iroumé, A., Valdebenito, G., 2018. Assessing and mitigating large wood-related hazards in mountain streams: recent approaches. J. Flood Risk Manag. 11, 207–222. https://doi.org/10.1111/jfr3.12316

Mazzorana, B., Zischg, A., Largiader, A., Hübl, J., 2009. Hazard index maps for woody material recruitment and transport in alpine catchments. Natural Hazards and Earth System Sciences 9, 197–209. https://doi.org/10.5194/nhess-9-197-2009

Merten, E., Finlay, J., Johnson, L., Newman, R., Stefan, H., Vondracek, B., 2010. Factors influencing wood mobilization in streams. Water Resour. Res. 46. https://doi.org/10.1029/2009WR008772

Merten, E.C., Finlay, J., Johnson, L., Newman, R., Stefan, H., Vondracek, B., 2011. Environmental controls of wood entrapment in upper Midwestern streams. Hydrol. Process. 25, 593–602. https://doi.org/10.1002/hyp.7846

Mitchell, D.M.W., Entrekin, S.A., Adams, G.L., 2012. Structure and function of large wood in Ozark headwater streams and its relationship to fish community structure. J. Freshw. Ecol. 27, 335–349. https://doi.org/10.1080/02705060.2012.658655

Moulin, B., 2005. Variabilité spatiale et temporelle du bois mort dans le réseau hydrographique de l'Isère à l'amont de Grenoble.

Murakami, Y., Shimizu, O., Sato, H., Yamada, T., 2008. Sediment-related Disaster Caused by Typhoon 0310 (Etau) in Hidaka Region of Hokkaido, Japan. International Journal of Erosion Control Engineering 1, 30–37. https://doi.org/10.13101/ijece.1.30

Nakagama, H., Takahashi, T., 2001. BEHAVIOR OF DRIFTWOOD DEBOUCHED FROM THE OHNO RIVER INTO THE BAY OF BEPPU DURING THE 1990 FLOOD. PROCEEDINGS OF HYDRAULIC ENGINEERING 45, 931–936. https://doi.org/10.2208/prohe.45.931

National Geographic & Forest Institute, n.d. GeoServices IGN portal [WWW Document].

Neal, J., Schumann, G., Bates, P., 2012. A subgrid channel model for simulating river hydraulics and floodplain inundation over large and data sparse areas. Water Resour. Res. 48. https://doi.org/10.1029/2012WR012514

Okamoto, T., Takebayashi, H., Sanjou, M., Suzuki, R., Toda, K., 2020. Log jam formation at bridges and the effect on floodplain flow: A flume experiment. J. Flood Risk Manag. 13. https://doi.org/10.1111/jfr3.12562

Omidvar, P., Stansby, P.K., Rogers, B.D., 2013. SPH for 3D floating bodies using variable mass particle distribution. Int. J. Numer. Methods Fluids 72, 427–452. https://doi.org/10.1002/fld.3749

Panici, D., de Almeida, G.A.M., 2018. Formation, Growth, and Failure of Debris Jams at Bridge Piers. Water Resour. Res. 54, 6226–6241. https://doi.org/10.1029/2017WR022177

Pascal, F.-G., Marc, etier, Antoine, R., 2023. Numerical modelling of large debris transport during floods.

Pavlowsky, R.T., Hess, J.W., Martin, D.J., Dogwiler, T., Bendix, J., 2023. Large wood loads in channels and on floodplains after a 500-year flood using UAV imagery in Mark Twain National Forest, Ozark Highlands, Missouri. Geomorphology 431, 108672. https://doi.org/10.1016/j.geomorph.2023.108672

Persi, E., Petaccia, G., Fenocchi, A., Manenti, S., Ghilardi, P., Sibilla, S., 2019a. Hydrodynamic coefficients of yawed cylinders in open-channel flow. Flow Measurement and Instrumentation 65, 288–296. https://doi.org/10.1016/j.flowmeasinst.2019.01.006

Persi, E., Petaccia, G., Sibilla, S., 2019b. Analysis of a two-way coupled model for Large Wood transport, Geophysical Research Abstracts.

Persi, E., Petaccia, G., Sibilla, S., Brufau, P., García-Navarro, P., 2019c. Calibration of a dynamic Eulerian-lagrangian model for the computation of wood cylinders transport in shallowwater flow. Journal of Hydroinformatics 21, 164–179. https://doi.org/10.2166/hydro.2018.085

Petaccia, G., Leporati, F., Torti, E., 2016. OpenMP and CUDA simulations of Sella Zerbino Dam break on unstructured grids. Comput. Geosci. 20, 1123–1132. https://doi.org/10.1007/s10596-016-9580-5

Petaccia, G., Natale, E., 2013. ORSADEM: A ONE-DIMENSIONAL SHALLOW WATER CODE FOR FLOOD INUNDATION MODELLING. Irrigation and Drainage 62, 29–40. https://doi.org/10.1002/ird.1802

Petaccia, G., Natale, L., 2020. 1935 Sella Zerbino Dam-Break Case Revisited: A New Hydrologic and Hydraulic Analysis. Journal of Hydraulic Engineering 146. https://doi.org/10.1061/(asce)hy.1943-7900.0001760

Petaccia, Gabriella, Natale, Luigi, Natale, L, Petaccia, G, 2010. ORSADEM: an interactive tool for dam break studies.

Pettit, N.E., Naiman, R.J., 2006. Flood-deposited wood creates regeneration niches for riparian vegetation on a semi-arid South African river. Journal of Vegetation Science 17, 615–624. https://doi.org/10.1111/j.1654-1103.2006.tb02485.x

Picco, L., Tonon, A., Rainato, R., Lenzi, M.A., 2016. Bank erosion and large wood recruitment along a gravel bed river. Journal of Agricultural Engineering 47, 72. https://doi.org/10.4081/jae.2016.488

Picco, L., Tonon, A., Ravazzolo, D., Rainato, R., Lenzi, M.A., 2015. Monitoring river island dynamics using aerial photographs and lidar data: the tagliamento river study case. Applied Geomatics 7, 163–170. https://doi.org/10.1007/s12518-014-0139-7

Piégay, H., Thévenet, A., Citterio, A., 1999. Input, storage and distribution of large woody debris along a mountain river continuum, the Drôme River, France. Catena (Amst). 35, 19–39. https://doi.org/10.1016/S0341-8162(98)00120-9

Piton, G., Cohen, M., Flipo, M., Nowak, M., Chapuis, M., Melun, G., Robert, Y., Andréis, N., Liebault, F., 2024. Large in-stream wood yield during an extreme flood (Storm Alex, October 2020, Roya Valley, France): Estimating the supply, transport, and deposition using GIS. Geomorphology 446, 108981. https://doi.org/10.1016/j.geomorph.2023.108981

Poledniková, Z., Galia, T., 2021. Ecosystem Services of Large Wood: Mapping the Research Gap. Water (Basel). 13, 2594. https://doi.org/10.3390/w13182594

Pöppl, R.E., Fergg, H., Wurster, M.T., Schuchardt, A., Morche, D., 2021. The effects of large wood (LW) on water and sediment connectivity in river systems: a new LW dis-connectivity index and its application in sediment management contexts. https://doi.org/10.5194/egusphere-egu21-14342

Poupeau, G., Bladé, E., Cea, L., Lara, Á., 2010. Iber, a river dynamics simulation tool.

Rabinowicz, E., 1951. The Nature of the Static and Kinetic Coefficients of Friction. J. Appl. Phys. 22, 1373–1379. https://doi.org/10.1063/1.1699869

Rasche, D., Reinhardt-Imjela, C., Schulte, A., Wenzel, R., 2019. Hydrodynamic simulation of the effects of stable in-channel large wood on the flood hydrographs of a low mountain range creek, Ore Mountains, Germany. Hydrol. Earth Syst. Sci. 23, 4349–4365. https://doi.org/10.5194/hess-23-4349-2019

Ravazzolo, D., Mao, L., Picco, L., Lenzi, M.A., 2015a. Tracking log displacement during floods in the Tagliamento River using RFID and GPS tracker devices. Geomorphology 228, 226–233. https://doi.org/10.1016/j.geomorph.2014.09.012

Ravazzolo, D., Mao, L., Picco, L., Sitzia, T., Lenzi, M.A., 2015b. Geomorphic effects of wood quantity and characteristics in three Italian gravel-bed rivers. Geomorphology 246, 79–89. https://doi.org/10.1016/j.geomorph.2015.06.012

Ruiz-Villanueva, V, Bladé, E., Sánchez-Juny, M., Marti-Cardona, B., Díez-Herrero, A., Bodoque, J.M., 2014a. Two-dimensional numerical modeling of wood transport. Journal of Hydroinformatics 16, 1077–1096. https://doi.org/10.2166/hydro.2014.026

Ruiz-Villanueva, V, Bodoque, J.M., Díez-Herrero, A., Bladé, E., 2014b. Large wood transport as significant influence on flood risk in a mountain village. Natural Hazards 74, 967–987. https://doi.org/10.1007/s11069-014-1222-4

Ruiz-Villanueva, V., Díez-Herrero, A., Bodoque, J.M., Bladé, E., 2014c. Large wood in rivers and its influence on flood hazard. Cuadernos de Investigación Geográfica 40, 229–246. https://doi.org/10.18172/cig.2523

Ruiz-Villanueva, Piégay, H., Gaertner, V., Perret, F., Stoffel, M., 2016a. Wood density and moisture sorption and its influence on large wood mobility in rivers. Catena (Amst). 140, 182–194. https://doi.org/10.1016/j.catena.2016.02.001

Ruiz-Villanueva, V., Piégay, H., Gurnell, A.M., Marston, R.A., Stoffel, M., 2016b. Recent advances quantifying the large wood dynamics in river basins: New methods and remaining challenges. Reviews of Geophysics 54, 611–652. https://doi.org/10.1002/2015RG000514

Ruiz-Villanueva, Virginia, Wyżga, B., Zawiejska, J., Hajdukiewicz, M., Stoffel, M., 2016c. Factors controlling large-wood transport in a mountain river. Geomorphology 272, 21–31. https://doi.org/10.1016/j.geomorph.2015.04.004

Ruiz-Villanueva, V., Wyżga, B., Mikuś, P., Hajdukiewicz, M., Stoffel, M., 2017. Large wood clogging during floods in a gravel-bed river: the Długopole bridge in the Czarny Dunajec River, Poland. Earth Surf. Process. Landf. 42, 516–530. https://doi.org/10.1002/esp.4091

Ruiz-Villanueva, V., Badoux, A., Rickenmann, D., Böckli, M., Schläfli, S., Steeb, N., Stoffel, M., Rickli, C., 2018. Impacts of a large flood along a mountain river basin: the importance of channel widening and estimating the large wood budget in the upper Emme River (Switzerland). Earth Surface Dynamics 6, 1115–1137. https://doi.org/10.5194/esurf-6-1115-2018

Sansen, D., Archambeau, P., Pirotton, M., Erpicum, S., Dewals, B., 2025. Lagrangian description for the drift of large floating debris in rivers during floods. https://doi.org/10.5194/egusphere-egu24-17477

Schalko, 2018. MODELING HAZARDS RELATED TO LARGE WOOD IN RIVERS. ETH ZURICH.

Schalko, I., Schmocker, L., Weitbrecht, V., Boes, R., 2017. Backwater rise due to large wood accumulations: Effect of organic fine material, in: Geophysical Research Abstracts. Copernicus.

Schalko, I., Schmocker, L., Weitbrecht, V., Boes, R.M., 2020. Risk reduction measures of large wood accumulations at bridges. Environmental Fluid Mechanics 20, 485–502. https://doi.org/10.1007/s10652-019-09719-4

Schalko, I., Weitbrecht, V., 2022. Wood blockage and sediment transport at inclined bar screens. Journal of Hydraulic Research 60, 164–172. https://doi.org/10.1080/00221686.2021.1903588

Schenk, E.R., Moulin, B., Hupp, C.R., Richter, J.M., 2014. Large wood budget and transport dynamics on a large river using radio telemetry. Earth Surf. Process. Landf. 39, 487–498. https://doi.org/10.1002/esp.3463

Sear, D.A., Newson, M.D., Thorne, C.R., 2003. Guidebook of Applied Fluvial Geomorphology. Defra Flood Management Division.

Senter, A., Pasternack, G., Piégay, H., Vaughan, M., 2017. Wood export prediction at the watershed scale. Earth Surf. Process. Landf. 42, 2377–2392. https://doi.org/10.1002/esp.4190

Seo, J. Il, Nakamura, F., Akasaka, T., Ichiyanagi, H., Chun, K.W., 2012. Large wood export regulated by the pattern and intensity of precipitation along a latitudinal gradient in the Japanese archipelago. Water Resour. Res. 48. https://doi.org/10.1029/2011WR010880

Sharma, V.C., Regonda, S.K., 2021. Two-Dimensional Flood Inundation Modeling in the Godavari River Basin, India—Insights on Model Output Uncertainty. Water (Basel). 13, 191. https://doi.org/10.3390/w13020191

Shields, F.D., Alonso, C. V., 2012. Assessment of flow forces on large wood in rivers. Water Resour. Res. 48. https://doi.org/10.1029/2011WR011547

Sitzia, T., Picco, L., Ravazzolo, D., Comiti, F., Mao, L., Lenzi, M.A., 2016. Relationships between woody vegetation and geomorphological patterns in three gravel-bed rivers with different intensities of anthropogenic disturbance. Adv. Water Resour. 93, 193–204. https://doi.org/10.1016/j.advwatres.2015.11.016

Skagit Watershed Council, 2017. SKAGIT RIVER LARGE WOODY DEBRIS ASSESSMENT Connecting LWD to the 2005 Skagit Chinook Recovery Plan .

Soukal, R., Málková, M., Kolingerová, I., 2012. Walking algorithms for point location in TIN models. Comput. Geosci. 16, 853–869. https://doi.org/10.1007/s10596-012-9305-3

Spreitzer, G., Gibson, J., Tang, M., Tunnicliffe, J., Friedrich, H., 2019. SmartWood: Laboratory experiments for assessing the effectiveness of smart sensors for monitoring large wood movement behaviour. Catena (Amst). 182. https://doi.org/10.1016/j.catena.2019.104145

Spreitzer, G., Schalko, I., Boes, R.M., Weitbrecht, V., 2024. SmartWood: field-based analysis of large wood movement dynamics using inertial measurement units (IMUs). Environ. Sci. Eur. 36, 94. https://doi.org/10.1186/s12302-024-00916-7

Stewart, P.M., Bhattarai, S., Mullen, M.W., Metcalf, C.K., Reátegui-Zirena, E.G., 2012. Characterization of large wood and its relationship to pool formation and macroinvertebrate metrics in southeastern coastal plain streams, USA. J. Freshw. Ecol. 27, 351–365. https://doi.org/10.1080/02705060.2012.679322

Thomason, C., 2019. Hydraulic Design Manual.

Tockner, K., Ward, J. V., Arscott, D.B., Edwards, P.J., Kollmann, J., Gurnell, A.M., Petts, G.E., Maiolini, B., 2003. The Tagliamento River: A model ecosystem of European importance. Aquat. Sci. https://doi.org/10.1007/s00027-003-0699-9

Tong, F., Cheng, L., An, H., Griffiths, T., 2018. Hydrodynamics on Circular Cylinder Close to a Wall: Effects From Wall Boundary Layers, in: Volume 5: Pipelines, Risers, and Subsea Systems. American Society of Mechanical Engineers. https://doi.org/10.1115/OMAE2018-77518

Van Dijk, W.M., Schuurman, F., Van De Lageweg, W.I., Kleinhans, M.G., 2014. Bifurcation instability and chute cutoff development in meandering gravel-bed rivers, Bifurcation instability and chute cutoffs.

Vera, M., Jara, C., Iroumé, A., Ulloa, H., Andreoli, A., Barrientos, S., 2014. Reach scale ecologic influence of in-stream large wood in a Coastal Mountain range channel, Southern Chile. Gayana (Concepción) 78, 85–97. https://doi.org/10.4067/S0717-65382014000200002

Warren, D.R., Kraft, C.E., 2008. Dynamics of large wood in an eastern U.S. mountain stream. For. Ecol. Manage. 256, 808–814. https://doi.org/10.1016/j.foreco.2008.05.038

Welber, M., Bertoldi, W., Tubino, M., 2013. Wood dispersal in braided streams: Results from physical modeling. Water Resour. Res. 49, 7388–7400. https://doi.org/10.1002/2013WR014046

Wilcox, A.C., Wohl, E.E., 2006. Flow resistance dynamics in step-pool stream channels: 1. Large woody debris and controls on total resistance. Water Resour. Res. 42. https://doi.org/10.1029/2005WR004277

Williams, R.D., Brasington, J., Hicks, M., Measures, R., Rennie, C.D., Vericat, D., 2013. Hydraulic validation of two-dimensional simulations of braided river flow with spatially continuous aDcp data. Water Resour. Res. 49, 5183–5205. https://doi.org/10.1002/wrcr.20391

Wohl, E., 2020. Wood process domains and wood loads on floodplains. Earth Surf. Process. Landf. 45, 144–156. https://doi.org/10.1002/esp.4771

Wohl, E., Bledsoe, B.P., Fausch, K.D., Kramer, N., Bestgen, K.R., Gooseff, M.N., 2016. Management of Large Wood in Streams: An Overview and Proposed Framework for Hazard Evaluation. JAWRA Journal of the American Water Resources Association 52, 315–335. https://doi.org/10.1111/1752-1688.12388

Wohl, E., Goode, J.R., 2008. Wood dynamics in headwater streams of the Colorado Rocky Mountains. Water Resour. Res. 44. https://doi.org/10.1029/2007WR006522

Wohl, E., Uno, H., Dunn, S.B., Kemper, J.T., Marshall, A., Means-Brous, M., Scamardo, J.E., Triantafillou, S.P., 2024. Why wood should move in rivers. River Res. Appl. 40, 976–987. https://doi.org/10.1002/rra.4114

Woods, D., Kirstetter, P.-E., Vergara, H., Duarte, J.A., Basara, J., 2023. Hydrologic evaluation of the global precipitation measurement mission over the U.S.: Flood peak discharge and duration. J. Hydrol. (Amst). 617, 129124. https://doi.org/10.1016/j.jhydrol.2023.129124

Wyss, A., Schalko, I., Weitbrecht, V., 2021. Field study on wood accumulation at a bridge pier. Water (Switzerland) 13. https://doi.org/10.3390/w13182475

Wyżga, B., Mikuś, P., Zawiejska, J., Ruiz-Villanueva, V., Kaczka, R.J., Czech, W., 2017. Log transport and deposition in incised, channelized, and multithread reaches of a wide mountain river: Tracking experiment during a 20-year flood. Geomorphology 279, 98–111. https://doi.org/10.1016/j.geomorph.2016.09.019

Xiong, Y., Liang, Q., Zheng, J., Stolle, J., Nistor, I., Wang, G., 2022. A fully coupled hydrodynamic-DEM model for simulating debris dynamics and impact forces. Ocean Engineering 255, 111468. https://doi.org/10.1016/j.oceaneng.2022.111468

Yano, S., Tsuchihashi, S., Dozono, S., Kazama, K., Kita, T., 2016. ASSESSMENT OF WOODY DEBRIS DISASTER RISK AT ALL BRIDGES ALONG THE KAGETSU RIVER ACCORDING TO ITS GENERATION POTENTIAL CONCEPT. Journal of Japan Society of Civil Engineers, Ser. B1 (Hydraulic Engineering) 72, I_289-I_294. https://doi.org/10.2208/jscejhe.72.I_289

Zhang, W., Nistor, I., Rennie, C.D., Almansour, H., 2022. Influence of Dynamic Woody Debris Jam on Single Bridge Pier Scour and Induced Hydraulic Head. J. Mar. Sci. Eng. 10, 1421. https://doi.org/10.3390/jmse10101421

Zhang, W., Rennie, C.D., Nistor, I., 2023. Experimental investigation of the hydrodynamic field around a half-cone woody debris jam on a bridge pier. Journal of Hydraulic Research 61, 866–879. https://doi.org/10.1080/00221686.2023.2259859

Zhao, G., Xu, Z., Pang, B., Tu, T., Xu, L., Du, L., 2019. An enhanced inundation method for urban flood hazard mapping at the large catchment scale. J. Hydrol. (Amst). 571, 873–882. https://doi.org/10.1016/j.jhydrol.2019.02.008

Zischg, A.P., Galatioto, N., Deplazes, S., Weingartner, R., Mazzorana, B., 2018. Modelling Spatiotemporal Dynamics of Large Wood Recruitment, Transport, and Deposition at the River Reach Scale during Extreme Floods. Water (Basel). 10, 1134. https://doi.org/10.3390/w10091134